University of Southampton
Faculty of Engineering and the Environment
Institute of Sound and Vibration Research (ISVR)

Dynamic analysis of a nonlinear parametrically excited system using electromagnets

by

Bahareh Zaghari

A thesis for the degree of Doctor of Philosophy

December 2016

UNIVERSITY OF SOUTHAMPTON

ABSTRACT

FACULTY OF ENGINEERING AND THE ENVIRONMENT
INSTITUTE OF SOUND AND VIBRATION RESEARCH (ISVR)

Doctor of Philosophy

DYNAMIC ANALYSIS OF A NONLINEAR PARAMETRICALLY EXCITED SYSTEM USING ELECTROMAGNETS

Bahareh Zaghari

Parametrically excited systems, where defining system parameters vary periodically with an independent variable (time), are a popular research topic in engineering. Cable-stayed bridges, free hanging marine flexible risers, planetary gear systems and other engineering structures are often subject to parametric excitation. Due to the high amplitude of responses as a result of parametric amplification, parametric excitation can be disastrous if not account. Parametric amplification in mechanical and electrical systems can be exploited for designing vibration energy harvesters and electrical filters.

This thesis contains various work on Linear and Nonlinear Parametrically Excited (LPE) and (NPE) systems. The system of interest is a clamped-free cantilever beam which is modelled as a single degree of freedom system. An electromagnetic system is used to generate time-periodic stiffness and control nonlinearities. The forces applied from the electromagnetic system are found analytically in order to compare this work to similar systems and to conduct parametric studies. The nonlinear electromechanical coupling, electrical damping, and the induced current is implemented in the analytical model. The free responses of LPE and NPE systems are investigated analytically with the method of averaging and harmonic balance, with particular attention paid to the stability of these systems. The effect of cubic and cubic parametric nonlinearity on the NPE systems is demonstrated through some analytical and experimental investigations. This study on the NPE system is employed to show the effect of time-periodic stiffness and stiffness nonlinearities on attenuating or amplifying the response. Increasing the response amplitude of amplifiers and filters with an electromagnetic system can be achieved by tuning the system at the parametric resonance. Furthermore, the electromagnetic system can be configured to reduce the electrical damping, or to control the nonlinearities and consequently increase the parametric amplification.

The responses and stability of the NPE system subject to a harmonic base excitation are investigated analytically and experimentally. Unlike previous studies, the parametric excitation is independent of the base excitation. A careful selection of system parameters, such as parametric amplitude, relative phase and cubic parametric nonlinearity, can result in significant parametric amplification, and can prevent the jump between stable solutions. Parametric attenuation can also be achieved by controlling the phase difference between the base and the parametric excitation. This study has successfully demonstrated the importance of nonlinearity in parametrically excited systems.

Contents

List of Figures

List of Tables

Declaration Of Authorship

I, **Bahareh Zaghari**, declare that the thesis entitled *Dynamic analysis of a nonlinear parametrically excited system using electromagnets* and the work presented in the thesis are both my own, and have been generated by me as the result of my own original research. I confirm that:

- this work was done wholly or mainly while in candidature for a research degree at this University;
- where any part of this thesis has previously been submitted for a degree or any other qualification at this University or any other institution, this has been clearly stated;
- where I have consulted the published work of others, this is always clearly attributed;
- where I have quoted from the work of others, the source is always given. With the exception of such quotations, this thesis is entirely my own work;
- I have acknowledged all main sources of help;
- where the thesis is based on work done by myself jointly with others, I have made clear exactly what was done by others and what I have contributed myself;
- parts of this work have been published as referenced in [1–4].

Signed: *Bahareh Zaghari*

Date:

Acknowledgements

I would like to express my deep and sincere gratitude to my supervisors, Dr. Maryam Ghandchi Tehrani and Dr. Emiliano Rustighi at the Institute of Sound and Vibration Research (ISVR) at the University of Southampton. Also I would like to thank Prof. Brian Mace from my visit to University of Auckland for his support during the visit and his valuable suggestions through my PhD. Also from my visit to the University of Auckland, I would like to thank Dr. Till Jochen Kniffka. I would especially like to thank Dr. Scott Walker for allowing me to use a shaker in the National Oceanography Centre and Dr. Dibin Zhu for his assistance during the experiments for the energy harvesting tests. I would like to thank the technicians at the University of Southampton who were supporting me through the experimental work.

My gratitude goes also to Dr. Fadi Dohnal for letting me to adopt and change the electromagnetic system which he designed in 2008 at the University of Southampton, and for his feedback to improve the quality of this thesis.

I would like to acknowledge my studentship from the University of Southampton. This contribution towards my tuition fees has been very helpful.

A special thanks to my friends and family. Words cannot express how grateful I am to my parents and my siblings, my in-laws and my husband for all of the sacrifices that you have made on my behalf. I would like to dedicate my thesis to my mother who thought me to be patient, creative and strong to never give up on what I really love.

Nomenclature

Latin Symbols

a	amplitude of the response
$a_{0,1}$	averaged amplitude of the response, stable response
$a_{0,2}$	averaged amplitude of the response, unstable response
$\mathbf{B}$	magnetic field
b_b	width of the beam
$\mathbf{B}_{\mathrm{ez1}}$	magnetic field generated from moving the magnet around the coil
B_{r}	residual magnetic flux density of the permanent magnet
$\mathbf{B}_{\mathrm{x}}$	magnetic field in the direction of x
$\mathbf{B}_{\mathrm{z}}$	magnetic field in the direction of z
c_{e}	electrical viscous damping coefficient
c_{es}	electrical viscous damping coefficient for the coils connected in series
c_{m}	mechanical viscous damping coefficient
c_{t}	total viscous damping coefficient
D_{w}	diameter of the coil
E	Young's Modulus
F_e	external excitation force
F_{mag}	force applied from one magnet
F_{us}	external force on a dipole magnet
F_{z}	force applied to the magnet from a magnetic field generated by a pair of coils
h	distance between the magnet and the coil

h_{coil}	height of the permanent coil, including the shield
I	total current in the coils
i	the imaginary unit
I_{AC}	AC current through the coils
I_{c}	input current in the coils
I_{DC}	DC current through the coils
i_{ep}	induced current in the coils connected in parallel
i_{es}	induced current in the coils connected in series
I_m	area moment of inertia
k_1	static stiffness of the beam with the electromagnetic system
k_3	cubic stiffness
k_{b}	static stiffness of the beam without the electromagnetic system
k_{ext}	external stiffness applied by the DC current
k_{l}	linear stiffness
k_{n}	nonlinear stiffness
k_{p1}	parametric stiffness
k_{p3}	cubic parametric stiffness
k_{t}	electromechanical coupling coefficient of an electromechanical system with two coils
$k_{\mathrm{t1,2}}$	electromechanical coupling coefficient of an electromechanical system with one coil
l_1	distance of the magnet and the coils with respect to the fixing point
l_{b}	length of the cantilever beam
L_{coil}	inductance of the coil
l_{w}	length of wire in one rotation
m_b	mass of the cantilever beam
m_m	total mass of the magnets
m_{t}	total mass

N	number of turns in the coil
$\mathbf{R}$	monodromy matrix
r_1	inner radius of the coil
r_2	outer radius of the coil
R_3	additional resistance
r_c	radius of the coil
R_coil	internal resistance of the coil
r_m1	inner radius of the magnet
r_m2	outer radius of the magnet
T	period of the signal
t_b	thickness of the beam
U	potential function
V	voltage across the coils
V_m	volume of the magnet
w	width of the transition curve
$x(t)$	mass displacement
$y(t)$	base excitation
Y_0	amplitude of the base excitation
$z(t)$	displacement of the cantilever beam
Z_coil	total impedance of the coils connected in series

Greek Symbols

Δ	detuning parameter
Γ	normalised external force
Ω	parametric frequency
α	normalised cubic stiffness
δ	normalised parametric stiffness

δ_{es}	normalised nonlinear parameter for the coils connected in series
δ_{th1}	instability threshold at the first natural frequency
δ_{th2}	instability threshold at parametric resonance
γ	normalised cubic parametric stiffness
γ_{es}	normalised nonlinear parameter for the coils connected in series
κ	frequency ratio
λ	eigenvalues
λ_b	wavelength
$\mathbf{\Psi}$	Fundamental matrix
μ	magnetic dipole moment
μ_0	permeability of free space
ω	base excitation frequency
ω_N	natural frequency of the nonlinear parametrically excited system
ω_{n2}	second natural frequency
ω_{n}	first natural frequency
ϕ	phase difference between the base excitation and the parametric excitation
ϕ_{m}	magnetic flux generated from moving the magnet around the coil
τ	time domain in averaging method
ε	small parameter
φ	averaged response phase
ς	fill factor
ζ	total damping ratio
ζ_{es}	electrical damping ratio for the coils connected in series
ζ_{m}	mechanical damping ratio
μ	magnetic dipole moment

Chapter 1

Introduction

1.1 Motivation

Understanding the dynamic behaviour of an engineering structure or system will provide an intuitive understanding of its stability. This thesis is focused on understanding the dynamics of Linear Parametrically Excited (LPE) and Nonlinear Parametrically Excited (NPE) systems and hence their stability. Examples of such systems include slender columns under axial loading, bridges, and aircraft structures under wind loading. These systems exhibit stiffness and inertia nonlinearities due to large deflections [5]. When a dynamic loading is applied to the structure, the entire system can be parametrically excited under certain conditions (direction of excitation, amplitude of excitation, etc.) [6]. If the dynamic loading acts at twice the resonance frequency of the system, Parametric Resonance (PR) is known to occur [7, 8]. This is often a disastrous phenomenon resulting in parametric instability, an exponential and uncontrollable growth of the response of the system known as parametric amplification [9]. Failures of engineering structures due to high vibrations, for example in cable-stayed bridges, have been caused by PR despite damping measures being implemented. However, parametric amplification can also be used beneficially in some engineering systems. Microelectrical resonators use parametric amplification to perform electrical filtering or sensing, without considerably amplifying noise [10, 11]. Parametric amplification is also exploited in the design of vibration energy harvesters to maximise the motion of the harvester at parametric resonance [12].

In this thesis, beneficial parametric excitation is studied as a way of controlling the response amplitude. A clamped-free cantilever beam with an electromagnetic system is considered for designing a NPE system. The electromagnetic system is employed for generating time-varying and nonlinear stiffness. Dohnal and Mace [13] and Schmidth et al. [14] investigated the feasibility of generating time-varying stiffness with an electromagnetic system. The performance and the design of the electromagnetic system is improved from the previous studies [13–16]. In this contribution, nonlinear forces generated by the electromagnetic system and their effect on parametric amplification is investigated. The effect of stiffness nonlinearities generated by the electromagnetic system for NPE systems has not been studied in the past (see [13–16] and the literature cited therein). Controlling the response amplitude in a wide frequency range can increase the efficiency of the electrical filters and vibration energy harvesters. Hence, the design of the electrical filters and vibration energy harvesters can be optimised by conducting a parametric study for the NPE systems.

1.2 Methodology and objectives

This study aims to answer these research questions:

- In SDOF linear and nonlinear parametrically excited systems, which parameters can cause parametric amplification? In contrast, how the response can be attenuated?
- Can experimental tests validate the theory of SDOF nonlinear parametrically excited systems? Which design criteria should be considered for the best predictions?
- What assumptions in the theory are not valid in the experiments for the stability and free responses of the NPE system?
- In SDOF linear and nonlinear parametrically excited systems subject to harmonic base excitation, which parameters can cause parametric amplification or suppression?
- What are the benefits and limitations of a cantilever beam with an electromagnetic system in comparison with a vertically excited cantilever beam?
- Which nonlinearities are observed from an electromagnetic system and how can they be included in SDOF model of the PE system?
- What are the benefits of using an electromagnetic system for parametric excitation in designing filters, amplifiers and vibration energy harvesters?

The present research aims to develop methodologies for the design of LPE and NPE systems. In this thesis the dynamic of LPE and NPE systems are investigated analytically and experimentally. Several single or multi Degree of Freedom (DOF) systems with time-varying coefficients are introduced in the literature to demonstrate the dynamic of PE systems [6, 17–20]. In this study a LPE system is modelled as a Single Degree of Freedom (SDOF) system with a time-varying stiffness coefficient. For the NPE system the cubic and cubic parametric stiffness nonlinearities are considered as well as the time-varying stiffness. An experimental model of the PE system is created using a cantilever beam with an additional electromagnetic system to contribute time-varying coefficients to the differential equation. With the electromagnetic system it is possible to alter the parametric amplitude (time-varying stiffness) and its frequency (parametric frequency). The aim is to determine the effect of parametric amplification at twice the first natural frequency of the cantilever beam. Hence, a SDOF model is sufficient for this study.

Dependency of the response amplitude on system parameters is studied including linear damping, parametric amplitude, stiffness nonlinearities, and parametric frequency. The parametric study on the effect of each parameter on the response amplitude is conducted independently. The aim is to determine the possibility of increasing the response amplitude for a wide frequency range using analytical approaches and experimental investigations.

In order to achieve the above goals, the free response of the LPE and NPE systems is analysed analytically using the methods of averaging and harmonic balance. The stability and responses of the LPE systems demonstrate the potential for increasing the response amplitude. For the LPE system, when a certain threshold for the parametric amplitude is achieved, the response at the parametric frequency is unbounded. Hence, the cubic stiffness nonlinearity is applied to reduce the response amplitude at parametric resonance. However, the cubic stiffness nonlinearity results in an increase of the response amplitude for the wider range of parametric frequencies. In order to understand the influence of the stiffness nonlinearities, the stability and responses of the NPE system are investigated using the method of averaging. For the LPE and NPE systems, the analytical stable solutions are compared with the numerical results.

The LPE and NPE systems can be subjected to harmonic base excitations. This is an interesting investigation to find the effect of base excitation amplitude and frequency on the response amplitude. Findings from this study can be a motivation for designing a vibration energy harvester that is subject to a base excitation. Also, the effect of phase difference between the base excitation and parametric excitation and its influence on the response amplitude and the phase is investigated. For the NPE system, the phase difference between the base excitation and the parametric excitation can affect stable branches. Hence, controlling the amplitude of the stable branches with this phase difference is investigated. The stability and responses of the NPE system with base excitation is achieved with the method of averaging, and the stable solutions are compared with the numerical solutions.

NPE system responses change with damping, parametric amplitude, and stiffness nonlinearities. Hence, different design configurations are considered to understand the influence of electromagnetic forces on system parameters. These parameters are calculated and measured. For example, the coil's configuration in electromagnetic system can affect the damping of the cantilever beam. The influence of coils connected in parallel or series on electrical damping is investigated. The natural frequencies of the cantilever beam are also varied with the electromagnetic system set-up. The DC current in coils can change the natural frequencies of the beam and can generate cubic stiffness nonlinearity. However, AC current influences the parametric amplitude and can generate the cubic parametric stiffness nonlinearity. The relation between the DC/AC current and system parameters can be defined analytically and measured experimentally.

The effect of induced current in NPE systems are also modelled analytically. The induced current can affect the electrical damping and parametric amplitude. Hence, better approximation of the experimental set-up is achieved. The NPE systems are also subjected to harmonic base excitations using a shaker. The response of the NPE system is obtained experimentally and analytically for strong cubic nonlinearity. This is achieved by controlling the DC current. The AC current in the coils is controlled to generate parametric amplitude with the phase difference between the shaker and parametric excitation. Altering the phase difference between the shaker and the parametric excitation can influence the stable solutions and the jump between the higher stable and lower stable branch. The feasibility of increasing the response amplitude with different base excitation amplitudes, parametric amplitudes and phase differences is investigated analytically and experimentally.

1.3 Contributions of the thesis

This work has produced original understanding and knowledge in the area of the nonlinear parametrically excited systems. Novel contributions of this study are summarised:

- In Chapter 3, the stability of nonlinear parametrically excited systems with cubic parametric nonlinearity as well as cubic nonlinearity is presented with the method of averaging and it is compared with numerical simulations. The relation between the transition curves and the amplitude-frequency response of the nonlinear system is presented. It is shown that the nonlinear parametrically excited transition curves are a function of parametric amplitude, the amplitude of the steady-state response, and the parametric frequency. The free responses of the NPE system with the stiffness nonlinearities are presented experimentally and analytically. In this novel contribution, the system parameters, including parametric excitation and nonlinearities are varied, and good agreement between the experimental and analytical results are shown. These results are presented in Chapter 6.

- In Chapter 4, the responses and the stability of the NPE system subject to harmonic base excitations with the phase difference are presented analytically with the method of averaging. The stability of the response is determined by Jacobian eigenvalues. The phase difference for the stable and unstable branches of solutions are examined. It is demonstrated that the phase difference variation can amplify or suppress the response amplitude. The effect of phase difference on reducing or increasing the amplitude of the stable upper branch and the lower branch is presented in this thesis as a novel work. Also, the effects of parametric amplitude are demonstrated experimentally and analytically in Chapter 7. The phase control allows us to increase the response amplitude and frequency bandwidth. By adjusting the phase it is possible to control the jumps between the upper stable branch and lower stable branch. This can be useful for designing filters or vibration energy harvesters when expanding the frequency bandwidth is essential, and a jump from the upper branch to the lower branch is not ideal.

- In Chapter 5, a NPE system with an electromagnetic system is introduced, which has several advantages compared to a vertically excited cantilever beam or a pendulum. For example, the effects of damping, parametric amplitude and cubic nonlinearity for the NPE system can be demonstrated independently. An accurate analytical model for the response of the NPE system with an electromagnetic system is implemented. The electromechanical coupling factor between the pair of coils and magnets, and the induced current generated by the coils are included in the model of the NPE system. The nonlinear electromechanical coupling shows the relation between the velocity of the moving magnet and the current generated in the coils as a result of this motion. The induced current in the coils affects the shape of the branches, which is important to include in the model. This effect of the induced current was neglected in previous work, and its importance is highlighted in this thesis. Also, several design configurations are considered to reduce the effect of damping. Reduction in electrical damping has a significant effect on parametric amplification. Since the full model of the electromagnetic system is considered, the results provided from the experimental tests is in good agreement with the analytical analysis.

1.3.1 Awards and publications

- **Worldwide Universities Network (WUN) award**
  The work presented in Chapter 3 was initiated from the visit to the University of Auckland in 2014 to work with Prof. Brian Mace's research group on studying the effect of cubic nonlinearity for nonlinear parametrically excited harvesters.

- **Conference proceedings**
  Part of Chapters 3 and 4 have been published in several conference proceedings as cited in [1, 3, 4]. The linear parametrically excited system with a piezoelectric harvester is presented in [2].

1.4 Outline of the thesis

The thesis is organised into eight chapters. The order of the chapters follows the introduction to PE systems and the modelling tools to prepare the reader for practical problems related to the NPE system with an electromagnetic actuator. The appendices are provided to explain the analytical methods and to improve relevant derivations.

PE systems are introduced in Chapter 2 with some examples. Parametric excitation in dynamic systems can be exploited for parametric amplification or suppression. Some relevant examples are presented in Section 2.2. Dynamic systems can be addressed from engineering disciplines as well as physics, chemistry, biology and medical sciences. Often the behaviour of these systems is complex due to their nonlinear and time-varying nature. Stability and solutions of these systems are presented in the literature with analytical and numerical approaches. Some of the methods are mentioned briefly in Section 2.1.

In Chapter 3, the free response study of the LPE and NPE systems is presented. The analytical model of a PE system as a SDOF system is presented. The methods of averaging and harmonic balance for finding the solutions of the LPE system are explained. The stability of the dynamic system is illustrated based on definitions of stability, and is explained using Floquet theory, the method of averaging and harmonic balance. The analytical model of the NPE system is explained in Section 3.4. This nonlinear system has cubic and cubic parametric stiffness nonlinearities. The method of averaging is also used to find the free response solution of the nonlinear system. The stability of the nonlinear parametrically excited system is defined by studying the solutions of the system. The eigenvalues for a linearised system are found to show the stability of the nonlinear parametrically excited system. Transition curves are used to explain the stability of the linear parametrically excited system. The comparison between the method of averaging and harmonic balance for calculating the transition curves is presented in Section 3.5.1. This chapter is concluded by a parametric study to determine the effects of damping, cubic stiffness, cubic parametric stiffness nonlinearity on stability and response amplitude.

In Chapter 4, the responses of the LPE and NPE systems subject to harmonic base excitation are demonstrated. The response of the NPE system is obtained using the method of averaging, and is presented in Section 4.2. The solutions of the LPE system are found based on the harmonic balance method and the method of averaging. In this chapter, the parametric frequency is tuned at twice the base excitation frequency. In Section 4.4 several cases are presented to show the effect of system parameters on system responses. The stability and solutions of each system are demonstrated. For the LPE system the effect of phase difference between the base excitation and parametric excitation is illustrated. The gain associated with the LPE system is compared when the phase difference and the parametric frequency is varied. Similarly, for the NPE system the gain is compared when the phase difference and the parametric frequency are altered. These results are shown in Section 4.6. The effect of relative phase between the base excitation and parametric excitation for each stable and unstable branches of solutions are demonstrated in Section 4.6.

In Chapter 5, the experimental set-up is described and the configuration of the electromagnetic system is explained. Appendix E provides complementary information on electromagnetic system design assumptions and limitations. In Chapter 5.4, the time-periodic stiffness, the cubic stiffness, and the cubic parametric nonlinearity are presented as a function of electromagnetic system parameters. These parameters are used in Chapters 6 and 7. A novel approach is demonstrated to find the electrical damping and induced current generated from the electromagnetic system.

In Chapter 6, the free responses of the NPE system are presented experimentally and analytically. The effects of damping, parametric amplitude, and nonlinearities on the response of the NPE system are demonstrated. The change in response amplitude as a result of parametric amplification is investigated, and the experimental and analytical results are presented in Section 6.3. The effects of cubic stiffness nonlinearity in the NPE system for a fixed position between the coils are presented in Section 6.4.

In Chapter 7, the cantilever beam and the electromagnetic system are excited with a shaker. The model presented in Chapter 4 is improved to fit to the experimental set-up. In this chapter the effect of the relative phase on the response amplitude is considered. The mechanism used to vary the phase difference between the base excitation and the current generated in the coils is presented in Section 7.2.1. The system parameters such as cubic nonlinearity, parametric amplitude, phase difference, and the base excitation amplitude are altered. The system responses are found experimentally and analytically in Sections 7.4.1, 7.4.2 and 7.4.5, respectively.

Finally, the thesis is concluded with a short summary and evaluation of the analytical and experimental approaches used to study the dynamic of LPE and NPE systems.

Chapter 2

Introduction to parametrically excited systems

Parametrically Excited (PE) systems, where defining system parameters vary periodically with an independent variable (time), are known since the late 19th century. One of the first documents in observing a PE system was released by Faraday in 1831 [21]. He observed parametric excitation in a vertically oscillating cylinder on the surface of a fluid which had half the frequency of the excitation. Lord Rayleigh in 1883 [22] devised an experiment to show the PE system behaviour. The experiment was based on a taut string attached to a tuning fork. When the tuning fork vibrated vertically the fundamental vibration frequency in string was observed to be half the tuning fork frequency.

A playground swing-set is a simple example of parametric excitation in a physical system. The swing is like a pendulum, whose moment of inertia changes with time in a periodic manner. The frequency of this change is called parametric frequency. The user of the swing will squat to increase the swing height without being pushed. If the frequency of the periodic oscillation of the user is equal to twice the frequency of the periodic oscillation from the swing, the amplitude will increase progressively. This large movement happens at Parametric Resonance (PR).

A PE system with time-varying stiffness is presented in literature [9, 18] by

$$\ddot{\mathbf{z}} + 2\boldsymbol{\zeta}\dot{\mathbf{z}} + \boldsymbol{\omega}^2\mathbf{z} + \boldsymbol{\delta}\cos(\Omega t)\mathbf{z} = 0 \quad \text{with} \quad \mathbf{z} = [z_1, z_2, ..., z_n]^{\mathrm{T}} \tag{2.1}$$

where $\mathbf{z}$ is the displacement, and $(k \times k)$ matrices $\boldsymbol{\zeta}$ and $\boldsymbol{\delta}$ correspond to damping and parametric amplitude, respectively. Ω is the parametric frequency. A PE system may exhibit PR if the parametric frequency is

$$\Omega_{n,j}^{PR} = \frac{2\omega_n}{j}, \qquad \forall j \in \mathbb{N}_+, \tag{2.2}$$

where ω_n is the natural frequency of the undamped system. For Multi Degree of Freedom (MDOF) systems, Parametric Combination Resonances (PCR) may occur when

$$\Omega_{n,m,j}^{PCR} = \frac{|\,\omega_n \pm \omega_m\,|}{j}, \qquad \forall j \in \mathbb{N}_+ \text{ and } (n \neq m), \tag{2.3}$$

where ω_n and ω_m denote the n-th and m-th natural frequency of undamped system. ω_n and ω_m are the n-th and m-th element of the diagonal $(k \times k)$ matrix $\boldsymbol{\omega}$. The denominator j denotes the order of the parametric resonance. In this thesis the first-order resonance $j = 1$ for a SDOF system is considered. There are several publications on SDOF with time-varying coefficients [6, 17, 18] and MDOF systems with time-varying coefficients [19, 20].

2.1 Linear and nonlinear systems with time-periodic coefficients

Dynamic systems governed by ordinary differential equations with periodically varying coefficients have been studied since one and a half centuries ago [7, 18, 23, 24]. In 1868, Mathieu [25] introduced a differential equation with periodic coefficient. In 1886, Hill [26] presented the first ever solution technique of linear periodic equations. This approach is called the Hill's method of infinite determinants which is a suitable tool to obtain the stability of time-periodic system. In 1892, Poincaré [27] published the proof of convergence of Hill's method. After Hill in 1883, Floquet [28] developed the complete study for stability of linear time-periodic differential equations. Based on Floquet theory the stability of the linear system with time-periodic coefficients can be determined from the eigenvalues of the monodromy matrix [9]. These eigenvalues are often called Floquet multipliers. If all Floquet multipliers have magnitude less than one, the linear system with time-periodic coefficient is asymptotically stable. Lyapunov in 1896 [29] demonstrated the Lyapunov-Floquet transformation for autonomous systems. The Lyapunov-Floquet transformation is a technique to transform a linear periodic system into a dynamically equivalent time-invariant form.

2.1.1 Analytical methods

The method of averaging, perturbation methods, point mapping techniques and the theory of normal modes have all been recently used for nonlinear analysis with and without time-periodic coefficients. For example, multi body problems such as dynamics of the solar system are very complex, and these systems were unsolvable until perturbation techniques were introduced. The averaging and perturbation methods were developed to provide approximate solutions. Averaging method was presented by Clairaut in 1754 [30] and it was demonstrated as a clear methodology by Lagrange in 1788 [31]. The idea of averaging as a computational technique is well presented by Verhulst [32]. In 1892, Poincaré [27] extended the method introduced by Lagrange in 1788. Poincaré also introduced other techniques for nonlinear systems such as point mapping and the theory of normal forms [33].

Averaging methods and perturbation methods, such as multiples scales, are based on the idea that if a solution of the system can be found without the problematic part (normally the time-periodic or nonlinear term) then we can consider the problematic part is small and the solutions will be the same. Hence the time-periodic and nonlinear terms are considered small compared to the time-invariant linear part. In the averaging method, the system is transformed to a standard form, then the periodic and nonlinear part are averaged out over the principle period (period of the time-varying part). In perturbation methods, the solution is assumed to be expanded into series of small parameters, which can define the order of the method. In this case, the zero-order terms are the solution of the unperturbed system. The method of averaging and the method of multiple scales both give the same answer to the problem of finding a first approximation to the solution of LPE and NPE systems introduced in this thesis, although they obtain solutions by quite different reasoning. Beyond the first approximation, the method of averaging and the method of multiple scales do not always give the same results [34]. The averaging method performed in this thesis is verified by comparing the solutions with experimental results and numerical solutions. More details on these methods and error calculations can be found in [34, 35].

Perturbation methods and averaging methods are restricted by the existence of a generating solution (solutions without the problematic part) and a small parameter. To avoid this Chebyshev polynomial can be used to solve linear time-periodic systems. A novel approach using Chebyshev polynomials was developed by Sinha and Wu [36]. The theory of normal forms can also be used to solve nonlinear systems, which is not limited by small parameter requirements, unlike the method of averaging and multiple scales [33].

The method of averaging with a small parameter is used in this thesis for demonstrating the stability and responses of the LPE and NPE systems. The method of averaging presented in this thesis is based on the work explained in [6, 37]. The analytical derivations and simulation plots are performed using symbolic analysis, specifically Maple 2016 from Maplesoft[1].

2.1.2 Numerical methods

Nonlinear equations may be solved using iterative numerical schemes. The solution obtained from the numerical integration can be used to complement the analytical solution. For a nonlinear equation certain conditions must be met before a particular numerical technique can successfully produce a solution. For example, root finding methods require an initial guess that is close to the root. Nonlinear equations do not have unique solutions. Hence, the roots depend on the numerical method as well as the starting guess value [38].

---

[1] https://www.maplesoft.com

For solving nonlinear equations, several methods such as path-following methods, the Homotopy method, and continuation methods have been used in the literature to increase the chance of finding solutions that are very close to each other [39]. These methods work based on predicting the step-size to find the accurate solutions. For solving the nonlinear equation presented in Chapter 3 (Eq. (3.26)) and Chapter 4 (Eq.(4.7)), the ODEINT function in SciPy [40] is used. ODEINT solves the initial value problem for stiff or non-stiff systems. An ordinary differential equation problem is stiff if one of the solutions varies slowly, but there are nearby solutions that vary rapidly, so the numerical method must take small steps to obtain all solutions. This is particularly important if the nonlinear equation has two solutions in proximity.

2.2 Examples of parametric excitation in structural systems

In structural systems, parametric excitation occurs when stiffness, inertia or damping vary with time. For example, parametric excitation can be seen in marine risers, ships, ship-mounted cranes, planetary gear system, rotor systems, and cable-stayed bridges.

Marine risers are employed in a variety of applications in the marine industry, hence the behaviour of these structures has received significant attention [41, 42]. Figure 2.1a shows a marine riser in the free hanging mode. Marine risers undergo unwanted impacts as a result of their length and large motions. Marine riser incidents can occur due to collision, or due to nonlinear internal resonance caused by parametric loading from the vertical motion of the floater, which produces large motion and parametric resonance on risers [41, 43].

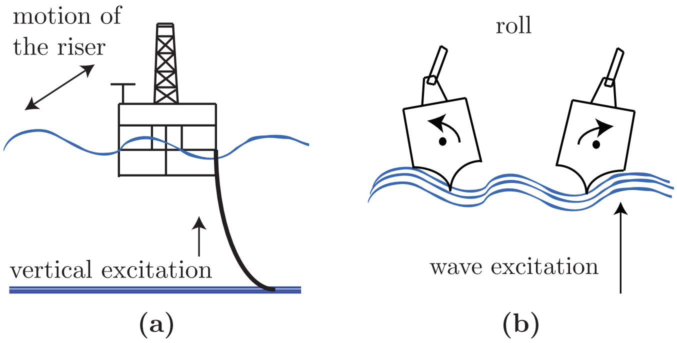

(a) (b)

Fig. 2.1. (a) An example architecture of a free hanging flexible riser. (b) Roll motion of a ship caused by wave excitation.

A ship can be seen as an auto-parametric system when it experiences parametric roll; a type of parametric resonance. Parametric roll consists of large oscillations about the roll axis, which results in disastrous consequences for the ship. Parametric roll occurs when the excitation frequency from the waves of water is twice the natural roll frequency of the ship. The first observation of parametric resonance of ships was recorded by Froude [44], and the resulting nonlinearity has also been recently studied [45].

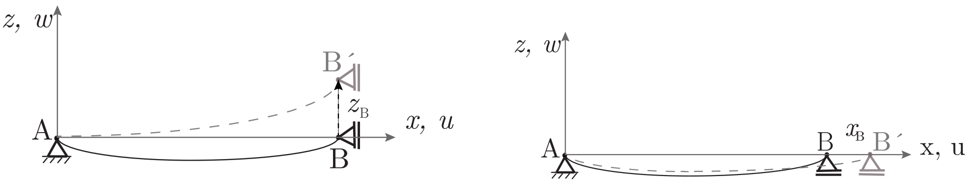

(a) **(b)**

Fig. 2.2. (a) Stay cable subjected to transverse motion at one anchorage causing point B to move to point B′. (b) Horizontal cable subjected to longitudinal harmonic motion at one anchorage causing point B to move to point B′. This figure is modified from [49].

Cargo from large ships is typically transferred directly to small ships using a ship-mounted crane when deep water ports are not accessible. The vertical sea-excited motion of the large crane ship can excite large motion on the cargo hanging on the crane, which may result in damage. To cause this, the sea-excited motion must either have a large amplitude, or must have a frequency close to twice the resonant frequency of the ship-crane system [46]. Parametric excitation in ship-mounted cranes is often modelled as a pendulum [46].

In planetary gears, fluctuating stiffness results from the changing contact conditions at the multiple tooth meshes, which produces parametric instability. The time-varying mesh stiffnesses parametrically excite the system. This parametric excitation causes instability, hence noise, increased load, and damage to the gear teeth and the bearings result [47, 48]. In rotating machinery parametric excitation can occur when the shaft has imperfect cross section and the stiffness is asymmetric.

The vibration of the deck and towers of cable-stayed bridges caused by the wind, traffic, and earthquakes produces an indirect excitation of the cable via the motion of their anchorages [49]. This excitation can be classified into two types, being external and parametric excitation. The external and parametric excitation have both been observed and measured in several bridges in the past [50–52]. Studying induced cable vibrations is important since they can oscillate with great amplitudes [53, 54].

The external excitation corresponds to a motion applied at anchorage perpendicular to the cable chord (Fig. 2.2a). The parametric excitation corresponds to oscillations in direction of the chord (Fig. 2.2b). The vibration of the deck introduces periodicity in the cable tension, hence parametric excitation results. The equation of motion of the stay cable under external excitation (Fig. 2.2a) can be presented as a linear or nonlinear second order differential equation.

To reduce the oscillation in such a bridge, different passive and active control methods have been applied, including the installation of hydraulic dampers between the stay and the girder [49]. To minimise in-plane vibrations from rain, wind, pylon motion and other sources, tuned mass-dampers, also known as TMDs, can be introduced [55, 56]. Understanding how neighbouring components of the stay cable system interact under parametric excitation is essential to design an appropriate damper.

Parametric excitation and large vibrations caused by excitation at certain multiples of the resonant frequency are important design factors in marine risers, ships, and bridges [49, 57]. Amplification of the system motion has been studied to determine the damping necessary to prevent the parametric system from large vibrations.

2.3 Exploiting parametric excitation in vibration amplification

Parametric amplification has been used to amplify external harmonic signals in electrical engineering applications for more than fifty years [58], considerably so in power and communication systems [59, 60]. Parametric amplification is used in mechanical systems, like resonant transducers in macro and nano scale systems such as bandpass filters [61]. Bandpass filters based on resonant micro-electromechanical systems, and mechanical vibration energy harvesters, both of which work commonly as single resonant systems, can benefit from parametric amplification [58].

Nonlinear Parametrically Excited (NPE) systems have several advantages compared to linear systems. Nonlinear tuning techniques are commonly used in the recent applications proposed for parametric resonance in single frequency bandpass filtering and vibration energy harvesting. Desired frequency response characteristics are achieved by introducing the linear and cubic nonlinear stiffness [10, 62]. Higher frequency bandwidth and controllable stop-band rejection can be achieved by controlling the nonlinearity in a NPE system. Rhoads et al. [63] introduced an electrostatically driven microelectromechanical systems (MEMS), which was used for designing a bandpass filter. By adding DC to an AC input signal (the signal which needs to be filtered), and by modifying the cubic nonlinearity, they designed a NPE filter. The main issue with this filter was overcoming the damping. Since damping can increase the instability threshold and prevent parametric amplification.

Various geometries have been chosen from micro to macro structures. These geometries include spring mass structures [64, 65], cantilever beam structure [66–68], tuning fork [69], and torsional spring oscillators [70]. The axially driven cantilever beam is extensively used due to its simple geometry, well known analytical model, and ease of fabrication. The axial load on the cantilever beam produces parametric excitation, which results in time-dependent coefficients in the governing differential equation of the system [66]. The stiffness of the beam is influenced by an axial force when the time-varying axial load generates a parametric excitation [71]. Parametric amplification [72] or suppression [73] has been observed in these systems as described in the next sections.

The effective nonlinearity in the axially driven cantilever beam due to curvature and inertia is studied in [74–77]. It has been shown that geometric nonlinearity produces a hardening effect, whereas inertial nonlinearity has a softening effect [76]. As such, depending on the strength of each term, the overall effect of the nonlinearities could be hardening or softening. For a beam, geometric and inertia nonlinearities are a function of the geometry of the beam, material properties, boundary conditions, curvature, and mode shapes. By altering one or a combination of these parameters, the effective nonlinearity of the beam can be changed, allowing the desired bend in the frequency response to be realized. The nonlinear geometric and inertia terms may have significant influence on the response of the system [76, 77]. Hence, these nonlinearities are exploited in the design of the PE systems [78, 79]. The effect of system parameters on these nonlinearities can be studied to increase the response amplitude in a wide range of frequency bandwidth.

As well as geometry variation, parametric amplification can be obtained by different method of actuation, such as piezoelectric [80], electrostatic [63], and electromagnetic [81]. A PE cantilever beam with an electromagnetic device has been introduced by Chen and Yeh [15, 16]. Further study on a linear PE cantilever beam with an electromagnetic system was carried out by Han et al. [82]. In this system, the amplitude and frequency of the parametric stiffness excitation were accurately controlled by the current flowing through the coil of the electromagnetic device. They showed that, by exciting the cantilever beam with a time-varying force, the nonlinearity induced by the geometric imperfection of the beam and the coupling effects between the excitation mechanism and the beam were effectively avoided [16]. Therefore, they showed the cantilever beam under electromagnetic parametric excitation can be a good choice for a linear PE system. However, the stiffness nonlinearities present in the electromagnetic system were not considered.

Electromagnetic micro-transducers have been utilized in a number of distinct applications in recent years [83, 84]. An example of this system with highly nonlinear parametric amplitude was presented by Rhoads et al. [85]. An electromagnetically actuated cantilever beam was implemented to understand the effect of fifth order nonlinearity on a PE system. Parametric studies based on the influence of different system parameters on the frequency response were qualitatively explained. Based on this study, they found careful parameter selection and microcantilever results in qualitatively distinct responses could be obtained [86].

Parametric amplifiers are divided into two types: degenerated [63, 87, 88] and non-degenerated [70]. The degenerated PE amplifiers employ parametric excitation or parametric amplitude (pumping) with a frequency twice the natural frequency of the system. Non-degenerated parametric amplifiers occur at any frequency due to interaction between modes [70]. The degenerated PE systems, corresponding to the larger tongue in the stability chart (see Chapter 3), are affected by the phase between the external excitation and parametric excitation (see Chapter 7).

Linear vibration energy harvesters are based on a vibrating mechanical structure with an additional seismic mass, with driving force applied parallel to the direction of the oscillation. Electrical dampers would reduce the amplitude of the seismic mass and store

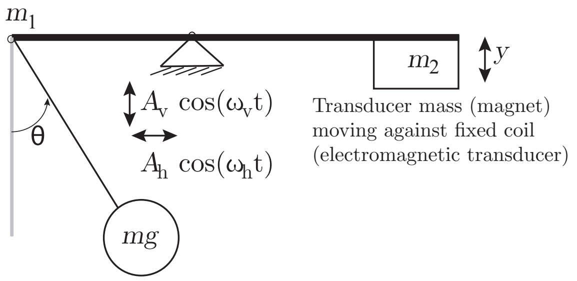

Fig. 2.3. PE vibration energy harvester presented by Jia et al. [12] with direct excitation from a horizontally driven pendulum ($A_\mathrm{h}\cos(\omega_\mathrm{h}t)$) and parametric excitation from a vertically driven pendulum ($A_\mathrm{v}\cos(\omega_\mathrm{v}t)$) (figure is modified). Direct excitation activates the ordinary resonance at the natural frequency and the parametric excitation activates the parametric resonance at twice the natural frequency. An electromagnetic transducer is placed on the right side of the lever to transform the energy from the pendulum displacement.

the energy by way of conservation. In linear SDOF systems, the maximum displacement of the seismic mass occurs when the excitation frequency is equal to the resonance frequency of the harvester. Unfortunately, the amount of energy harvested is sensitive to this excitation frequency, meaning that any change in the excitation frequency severely reduces the stored energy, making this design infeasible for use without modification. To counteract this, different methods to tune the harvester and reduce this sensitivity, known as broadening the bandwidth of the harvester, have been proposed [89–92]. In vibration energy harvesting, increasing the amplitude at parametric resonance as well as increasing the frequency bandwidth can be achieved by tuning the harvester to its parametric resonance [93].

2.3.1 Parametric amplification in vibration energy harvesting

Energy harvesting from directly-excited non-parametric systems has been studied extensively, but not much work has been done in exploiting parametric excitation in the context of vibration energy harvesting [72, 79, 94–96]. Jia et al. [12] demonstrated an experimental macro-sized electromagnetic harvester prototype under parametric resonance. The PE harvester had an order of magnitude higher peak power density, and a 50% increase in the half power band due to the amplification of the mechanical vibration at parametric resonance and nonlinear resonant peak, compared to the prototype directly driven at fundamental resonance.

The PE vibration energy harvester prototype consists of a pendulum and an electromagnetic harvester on both sides of the lever and is shown in Fig. 2.3. If the pendulum is excited horizontally ($A_\mathrm{h}\cos(\omega_\mathrm{h}t)$), the excitation is analogous to direct excitation, however if it is excited vertically ($A_\mathrm{v}\cos(\omega_\mathrm{v}t)$) the pendulum is PE and it has parametric resonance. Displacement generated by the pendulum motion moves the magnet in-between the fixed coils on the right side of the lever. The electromagnetic transducer transforms the me-

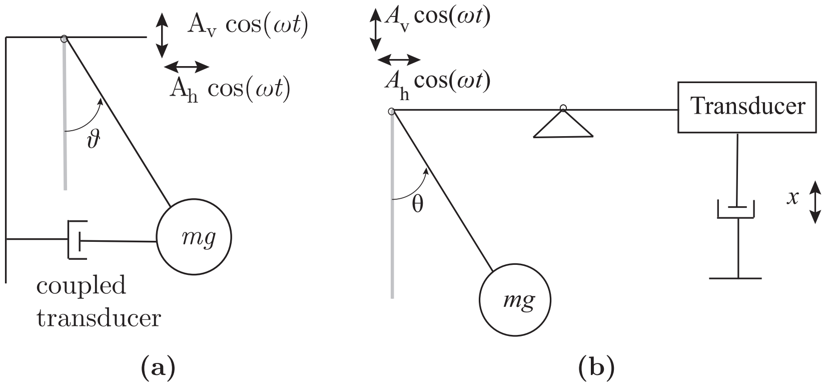

Fig. 2.4. PE systems introduced by Jia et al. [97] (a) A simple pendulum where the oscillatory angular displacement is directly damped by an electromagnetic transducer. (b) A pendulum coupled to a lever, which is electrically undamped on the left hand side.

chanical energy to electrical energy. In this study, Jia et al. [12] compared the peak power, frequency, volume, acceleration and normalised power density of the PE prototype with other existing publications to show that they have achieved higher peak power and normalised power density, however they need greater vertical excitation amplitude. This is due to an initiation threshold (instability threshold) for the system to have parametric amplification, which changes based on the damping in the system. Hence, Jia et al. [97] introduced two design routes to passively minimise the initiation threshold amplitude required for the system to obtain parametric amplification. Each design is compared with a simple PE system.

A simple pendulum where the oscillatory angular displacement is directly damped by the electromagnetic transducer (Fig. 2.4a) is compared with an electrically undamped parametric resonator; a pendulum which is coupled to an electrically damped lever beam by an electromagnetic transducer (Fig. 2.4b). Using an electrically undamped parametric resonator decreases the initiation threshold amplitude [12]. It has been observed experimentally that the initiation threshold for a passively undamped parametric resonator is reduced by an order of magnitude. Jia and Seshia [98] have deployed the second design to explore the maximum peak power from such a system, known as the auto-parametrically excited vibration energy harvester, both theoretically and experimentally. The design representation and the mechanical model of this design is shown in Figs 2.5a and 2.5b. From Fig. 2.5b, if the system is excited vertically from the base, the harvester moves laterally; this is a model of an auto-parametric system. However, if the harvester is excited horizontally it is under direct excitation. Only if the base is excited at its resonance perpendicular to the lateral direction, the initiation threshold can be reduced. Hence, the peak power can be increased for a lower input acceleration level.

Jia et al. [95] also used the second design to implement a MEMS harvester, which includes an electrostatic cantilever based harvester. This design has been modified to overcome the initiation threshold amplitude. They demonstrated that the vacuum pack-

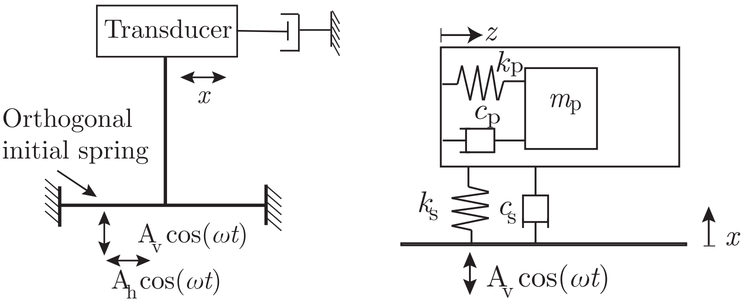

(a) (b)

Fig. 2.5. (a) A design representation [98] (figure is modified). (b) An auto-parametrically excited harvester model [98] (figure is modified).

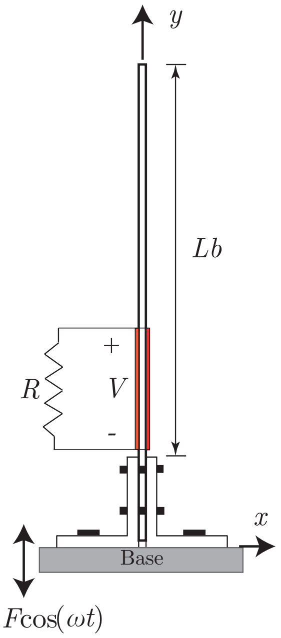

Fig. 2.6. The PE vibration energy harvester presented by Daqaq et al. [79] (figure is modified). The PE cantilever beam is excited vertically ($F\cos(\omega t)$) from the base.

aged MEMS electrostatic PE harvesters with an initial spring can be used to reduce the damping dependent initiation threshold for the parametric frequency (twice the natural frequency) and other orders [99]. This achievement has improved the peak power for different orders of parametric frequency, and has increased the frequency bandwidth.

Daqaq et al. [79] investigated the process of energy harvesting from an auto-parametric system. The auto-parametric system is a piezoelectric cantilever beam excited from the base perpendicular to the y direction as shown in Fig. 2.6. The aim of the study was to solve theoretically and experimentally the problem of estimating the output power and the effect of the design parameters on it. The effect of the coupling coefficient, the shunted load resistance parallel to the piezoelectric element, and the excitation level has been described. The lumped-parameter model presents the nonlinear single mode dynamics of the cantilever beam and the piezoelectric harvester. From the analytical model, the

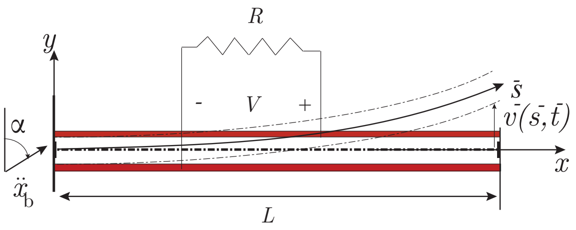

Fig. 2.7. A schematic of the piezoelectric cantilever bimorph [72] (figure is modified).

function that describes the amplitude and the phase of the beam displacement, the voltage across the resistive load, and the power were derived. Daqaq et al [100] determined from numerical simulations that the voltage across the resistive load is affected by the electromechanical coupling and the beam deflection amplitude. They showed there is an optimal value of the electromechanical coupling factor beyond which the harvester power decreases. As such, there is an optimal resistance amplitude at which the power is maximum. There are several papers that claim increasing the coupling factor can maximise the power. Daqaq presented that increasing the coupling factor increases the effective damping and as a result it raises the initiation threshold in instability curves. As explained by Jia et al. [97], there is a need for higher excitation to make the system vibrate at parametric resonance if the initiation threshold (instability threshold) is raised.

Daqaq et al. [79] derived the relation between the electromechanical coupling with small variation in parametric frequency, initiation threshold value and load resistance. They also observed the variation in natural frequency and voltage across the resistive load by changing the resistive load. Finally from the experiment, the optimal coupling factor and optimal resistive load was applied to find the maximum power. They successfully presented that, for an auto-parametric system, the coupling factor and load resistance affects the broadening of the harvester, as well as the peak power.

Daqaq and Bode [72] explored an approach to amplify the power at twice the natural frequency of a piezoelectric cantilever-typed bimorph harvester. This is achieved by tilting the axis of the beam through the proper angle with respect to the direction of excitation. Fig. 2.7 shows the piezoelectric cantilever-type bimorph harvester subjected to an external acceleration $\ddot{x}$. The external excitation can be direct ($\alpha = 0$) or PE ($\alpha \neq 0$). They proposed that with this method, there is an improvement in the maximum power relative to the direct excitation depending on the excitation parameters and mechanical damping ratio. The change in mechanical damping varies the optimal angle and the optimal harvested power. To achieve the maximum power, the mechanical damping should be controlled.

Employing the stiffness nonlinearity effect for a PE harvester has had little attention among researchers [101], although stiffness nonlinearity can be exploited to expand the frequency bandwidth of the harvester. In 2011, Abdelkefi et al. [94] considered a NPE harvester beam configuration. They included higher modes and nonlinear effects of the piezoelectric patch in their analysis. Their study was implemented to show that the nonlinear stress-strain piezoelectric coefficients significantly impact the behaviour of the harvester in terms of softening or hardening.

The limitation of the PE harvesters introduced in this section are as follows:

- The parametric amplification is limited by the vertical excitation amplitude. Only by increasing the parametric excitation to a sufficient value and overcoming the instability threshold, the parametric amplification can be achieved. In order to increase the efficiency of the PE harvesters, the instability threshold has to be reduced, hence less parametric amplitude is needed for parametric amplification.

- The frequency bandwidth of the harvester can be improved by introducing the cubic stiffness nonlinearity. The combination of PE and stiffness nonlinearities has not been studied.

- Analytical and experimental study on design consideration of nonlinear PE harvesters is not available in the literature. The design criteria of nonlinear PE harvesters can be achieved by parametric study with analytical and experimental investigations.

The NPE system introduced in this thesis can be employed to study a nonlinear PE harvester. Additionally, the NPE system can be employed for vibration suppression.

2.4 Exploiting parametric excitation in vibration suppression

A mechanical system that experiences large vibration amplitudes may be unwanted or even dangerous. Parametric excitation can be introduced to an engineering structure to affect the dynamic behaviour in a desired manner. For example, by tuning the self-excited or the PE system at specific parametric frequency, large response amplitudes can be damped.

Parametric resonances may be resonant or anti-resonant. Anti-resonant parametric resonances may occur at certain frequencies $\Omega_{n,m,j}^{PCR}$ (Eq. (2.3)). Anti-resonant parametric resonance does not cause vibration amplification. In 1978, for the first time, Tondl discovered that faster decay of vibration amplitudes may occur at these frequencies [102]. Tondl [103] also proved that it is possible to take advantage of parametric combination resonances referred to as parametric anti-resonance to stabilise large vibrations in self-excited systems. The unstable trivial solutions due to the self-excited mechanism can be mapped to an asymptotic stable one by parametric excitation at parametric anti-resonance [103]. This can be studied numerically with Floquet theory [32, 104]. Vibration suppression in rotor systems is demonstrated by Dohnal et al. [105–108] based on Tondl discovery. Vibration suppression applied by parametric excitation using electromagnets was presented by Dohnal [109]. Damping of beam structures with parametric anti-resonance and the design of a vibration absorber can be found in [73, 110]. Drive systems subject to parametric excitation can also benefit from vibration suppression [111, 112].

2.5 Summary

Parametric excitation in structural systems was briefly explained in this chapter. Solutions and stability of PE systems can be found analytically with Floquet theory, perturbation methods and the method of averaging. Several numerical methods were recommended to find the stable solutions and stability of the NPE systems. Some of these methods will be presented in the following chapter in detail.

The possibility of parametric amplification in PE vibration energy harvesters, filters and amplifiers were outlined. In contrast, parametric attenuation at anti-resonance, which was introduced to control the unwanted vibration was also explained. In the following chapters, several suggestions will be presented in order to improve the efficiency of PE vibration energy harvesters, filters and amplifiers. However, the effects of anti-resonances are not considered in this thesis.

Chapter 3

Free response of a nonlinear parametrically excited system

3.1 Introduction

Parametric excitation in linear time-varying systems and the stability of such systems has been studied in the literature [6, 113]. Different analytical methods, such as the method of averaging, harmonic balance, multiple scale, Floquet theory, and describing function have been employed to study the solution and stability of Linear Parametrically Excited (LPE) and Nonlinear Parametrically Excited (NPE) systems [9]. In this chapter, some of these methods are explained and compared, and the stability of LPE and NPE systems are investigated. The objective of this chapter is to provide an analytical model of a Parametrically Excited (PE) system in order to understand its behaviour.

Studying nonlinear systems is necessary due to their potential complex behaviour and instability. The structural dynamics which are made up of high flexible continuous elements, such as beams, and cables are examples of nonlinear systems [114]. One such nonlinearity, known as cubic stiffness nonlinearity, has been studied in both non-parametric and parametrically excited systems [114–116]. The nonlinear model presented in this work includes the cubic stiffness nonlinearity as well as time-varying cubic stiffness nonlinearity named “cubic parametric nonlinearity”, in a PE system. PE systems with cubic and cubic parametric nonlinearity have been investigated briefly for reducing or amplifying the response of the system in the field of electromechanical engineering [58, 87, 117]. Cubic and cubic parametric nonlinearities are observed in an electromagnetic system when the coils carry DC/AC current.

A general study on the effect of cubic parametric nonlinearity on the response amplitude is missing in the literature. The study of the cubic and cubic parametric nonlinearity in PE systems can be beneficial for decreasing or increasing the parametric amplitude of the system. Hence, in this chapter a parametric study on these nonlinearities is presented as a novel contribution. The system parameters considered in this chapter are chosen based on the experimental tests in Chapter 6.

In this chapter, first an analytical model of the LPE system is presented. Analytical solutions and stability of this system are described with the methods of averaging and harmonic balance. Several numerical simulations are carried out to present the behaviour of the LPE system. Secondly, an analytical model of the NPE system is demonstrated. Analytical solutions and stability are defined from the averaging methods. This chapter is concluded with novel contributions on parametric study for the NPE system with cubic parametric nonlinearity. The influence of cubic parametric nonlinearity to reduce the instability threshold is demonstrated.

3.2 Analytical modelling of a linear parametrically excited system

An example of a LPE system is a Single-degree-of-freedom (SDOF) system with a time-varying stiffness as shown in Fig. 3.1.

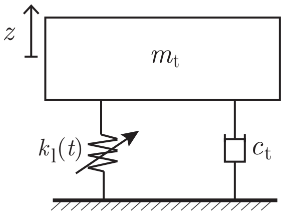

Fig. 3.1. A SDOF system with time-varying stiffness. An arrow on the stiffness symbol denotes time-varying stiffness.

The governing linear differential equation of this system is,

$$m_t\ddot{z} + \varepsilon c_t\dot{z} + k_l z = 0, \tag{3.1}$$

where the linear time-varying stiffness is $k_l(t) = k_1 + \varepsilon k_{p1}\cos(\Omega t)$, z is the displacement of the mass from its neutral position, m_t is the total mass, c_t is the total viscous damping coefficient, k_1 is the constant stiffness, and k_{p1} is the parametric stiffness (parametric amplitude) with the parametric frequency Ω. Normalising Eq. (3.1) by m_t yields

$$\ddot{z} + 2\varepsilon\zeta\omega_n\dot{z} + \omega_n^2\left(1 + \varepsilon\delta\cos\left(\Omega t\right)\right)z = 0, \tag{3.2}$$

where $\zeta = \frac{c_t}{2\omega_n m_t}$ is the damping ratio and $\delta = \frac{k_{p1}}{k_1}$ is the normalised parametric amplitude. To solve Eq. (3.1) all of the excitation and dissipation terms are assumed to be dependent on ε, which is the small parameter. Damping is assumed to be small and hence it is expressed as εc_t. Some analytical methods presented here are valid only for small values of ε, which is used as a scaling factor so that these methods can be compared.

Eq. (3.2) is similar to a damped Mathieu equation [25], which is a special form of a linear, second-order differential equation with a time-varying coefficient. The solution of the Eq. (3.2) can be found through different methods such as methods of averaging and harmonic balance [6]. These methods are compared in the next sections.

3.2.1 The method of averaging

The method of averaging is an approximation method, which is used as a compromise between exact analytic analysis and numerical approximations [118]. In order to explain the averaging method in this context, Eq. (3.2) is normalised by the time scaling $\tau = \Omega t$ and expressed with derivatives with respect to τ instead of t. The prime $(.)'$ is used to present a quantity differentiated with respect to τ. Normalisation in this way results in

$$z'' + \frac{2\varepsilon\zeta\omega_n}{\Omega} z' + \frac{\omega_n^2}{\Omega^2} \left(1 + \varepsilon\delta \cos\left(\tau\right)\right) z = 0. \tag{3.3}$$

The parametric frequency Ω is varied around a reference frequency Ω_0 thus[1]

$$\Omega = \Omega_0 \left(1 - \varepsilon\Delta\right), \tag{3.4}$$

where Δ is the detuning parameter [9]. If $\varepsilon = 0$, Eq. (3.3) becomes

$$z'' + \frac{\omega_n^2}{\Omega^2} z = 0. \tag{3.5}$$

The solution of Eq. (3.5) is a linear combination of $\cos(\tau)$ and $\sin(\tau)$. This linear combination can be written as

$$z\left(\tau\right) = a \cos\left(\kappa\tau + \varphi\right), \tag{3.6}$$

where a and φ are the constant amplitude and phase respectively, which can be determined from initial conditions. The frequency ratio

$$\kappa = \frac{\omega_n}{\Omega_0} \tag{3.7}$$

is used here for simplification.

When $\varepsilon \neq 0$, based on the method of Lagrange “variation of constant”, we can assume that the solution can still be written in the above form, but the amplitude a and phase φ, are now functions of time [32]. Hence, the complementary solution of the final simplified nonlinear equation (Eq. (3.3)) is a linear combination of $\cos\left(\Phi\left(\tau\right)\right)$ and $\sin\left(\Phi\left(\tau\right)\right)$, which can be written as

$$z\left(\tau\right) = a\left(\tau\right) \cos\left(\Phi\left(\tau\right)\right), \tag{3.8}$$

---

[1] This is an approximation method around the parametric frequency.

where $\Phi(\tau) = \kappa\tau + \varphi(\tau)$, and

$$z(\tau)' = a'(\tau)\cos(\Phi(\tau)) - a(\tau)(\kappa + \varphi'(\tau))\sin(\Phi(\tau)). \tag{3.9}$$

Substituting Eqs. (3.8) and (3.9) into Eq. (3.3) results in an equation which can be solved for $a'(\tau)$ and $\varphi'(\tau)$. $a'(\tau)$ and $\varphi'(\tau)$ are then averaged over one period $T = \frac{2\pi}{\Omega}$ under the assumption that $a(\tau)$ and $\varphi(\tau)$ are changing slowly. The resulting averaged equation can be integrated with respect to τ to find $a(\tau)$ and $\varphi(\tau)$ for a given κ, and reference frequency Ω_0.

The steady-state behaviour of the system can be recovered from the set of $a'(\tau)$ and $\varphi'(\tau)$ by setting $(a', \varphi') = (0, 0)$ and solving for steady-state values of a and φ. Thus, the resulting solution is an approximation of the original solution. This method has been studied for the solution of the damped Mathieu equation [6, 113]. For further details on LPE systems responses refer to Appendix A.

3.2.2 The method of harmonic balance

The method of harmonic balance assumes that the response to a sinusoidal excitation is a sinusoid at the same frequency [9]. This method is not used to find the solutions of a LPE system with free vibration, but it is appropriate for a forced system. The governing differential equation of a forced system with time-varying stiffness is

$$\ddot{z} + 2\varepsilon\zeta\omega_n\dot{z} + \omega_n^2(1 + \varepsilon\delta\cos(\Omega t))z = \omega_n^2\Gamma\cos(\omega t + \phi), \tag{3.10}$$

where $\Gamma = \frac{F}{k_1}$, F is the direct force amplitude, and ϕ is the relative phase term (introduced to account for the phase-dependent response). The solution of Eq. (3.10) can be defined as a Fourier series with the frequency of excitation (ω) and the combination frequency ($\omega \pm \Omega$). Substitution of the trial solution into Eq. (3.10), and the collection of trigonometric terms, leads to an infinite set of linear homogeneous equations for the Fourier series coefficients. This method is explained in Appendix C.1.4.

The method of harmonic balance is unable to solve the Mathieu equation without any external force (e.g. Eq. (3.2)) since the determinant defined by the coefficients of Eq. (3.2) and the Fourier series are non-zero. Hence, it is possible to find the solutions only if the Fourier coefficients are equal to zero [119]. Other similar techniques such as describing function have been used to find the solution of a PE system with an external excitation [120, 121]. A describing function assumes that the system response is a sinusoid at the natural frequency ω_n.

3.3 Stability of linear parametrically excited systems

The study of the stability of dynamic systems has been covered in different disciplines, such as stability of the solar system, stability in structures, and fluid dynamics [122–127]. Since the requirements of stability differ within different disciplines, there are many definitions of stability. Before considering the stability of PE systems, the definitions of stability used in this work are outlined here.

A system is usually defined at a stable equilibrium point when it has zero kinetic energy and minimum potential energy [123]. Lyapunov's theorem is used to obtain energy functions, which in turn allows the stability of a state to be identified without solving the governing equation of the system [122, 123]. Lyapunov's theorem is explained in several textbooks [122–127]. The general differential equation, which describes the motion of the system is of the form of

$$\dot{\mathbf{z}}(t) = \mathbf{f}(\mathbf{z}(t), t), \quad \mathbf{z}(t_0) = \mathbf{z}_0, \tag{3.11}$$

where $\mathbf{z} \in \mathbb{R}^n$ and $t \geq 0$. Eq. (3.11) is autonomous or time-invariant if $\mathbf{f}$ does not depend explicitly on t. It is linear if $\mathbf{f}(\mathbf{z}(t), t) = \mathbf{G}(t)\mathbf{z}$ for some $\mathbf{G}(.) : \mathbb{R}_{\geq 0} \mapsto \mathbb{R}^{n \times n}$ and nonlinear otherwise. $\mathbf{z}^*$ is an equilibrium point of Eq. (3.11), if $\mathbf{f}(\mathbf{z}^*, t) \equiv \mathbf{0}$ for all t. $\mathbf{z} = \mathbf{0}$ is also a stable point if trajectories of $\mathbf{z}(t)$ of Eq. (3.11) remain close to the origin when the initial condition $\mathbf{z}_0$ stays close to the origin. The following stability criteria are considered:

Stability in the sense of Lyapunov: An equilibrium point $\mathbf{z} = 0$ is stable if all solutions of Eq. (3.11) starting at nearby points stay nearby; otherwise the equilibrium point is unstable [122, 123].

Asymptotic stability (local): The equilibrium point is asymptotically stable if all solutions of Eq. (3.11) starting at nearby points tend to the equilibrium point as time tends to infinity [122, 123]. Other definitions such as, local uniform stability, local uniform asymptotic stability, global asymptotic stability, global uniform asymptotic stability, and exponential stability are explained in detail in [122, 123].

The stability of an equilibrium point can be characterised by the location of the eigenvalues of $\mathbf{G}$ from $\mathbf{f}(\mathbf{z}, t) = \mathbf{G}(t)\mathbf{z}$. The substitution of $\mathbf{z} = \mathbf{a}\mathrm{e}^{\lambda t}$ in $\mathbf{f}(\mathbf{z}, t) = \mathbf{G}(t)\mathbf{z}$ results in the characteristic equation

$$\det(\mathbf{G} - \lambda \mathbf{I}) = 0, \tag{3.12}$$

where $\lambda = \lambda_{1,2,\ldots,n}$ are the eigenvalues and $\mathbf{I}$ is the identity matrix. For the two-dimensional case ($\mathbf{z} \in \mathbb{R}^{2\times 1}$, $\mathbf{G} \in \mathbb{R}^{2\times 2}$), the eigenvalues classify the nature of the equilibrium point as follows:

- If $\lambda_{1,2} \in \mathbb{R}_+$, the equilibrium point is unstable.
- If $\lambda_{1,2} \in \mathbb{R}$, $\lambda_1 > 0$, and $\lambda_2 < 0$, the equilibrium point is a saddle.
- If $\lambda_{1,2} \in \mathbb{R}_-$, the equilibrium point is stable.

- If $\lambda_{1,2} \in \mathbb{C}$, $\Re(\lambda_{1,2}) = 0$, and $\lambda_1 = -\lambda_2$, the equilibrium point is a centre.
- If $\lambda_{1,2} \in \mathbb{C}$, and $\Re(\lambda_{1,2}) < 0$, the equilibrium point is a stable focus.
- If $\lambda_{1,2} \in \mathbb{C}$, and $\Re(\lambda_{1,2}) > 0$, the equilibrium point is an unstable focus.

The phase portrait (velocity versus displacement) plot can verify the above classifications. These plots can be found in [122, 123].

3.3.1 Floquet theory

There are many methods to determine the stability of single stationary points in the phase space [128]. One such method is to perturb the point and to identify whether or not the trajectory of the perturbed point converges to the stationary point; convergence results in a stable point being identified. However this simple approach does not extend well to limit cycles [129]. A limit cycle can be introduced by a periodic steady-state solution of the system (periodic trajectories). If a limit cycle is perturbed and the perturbed point returns close to the original trajectory, then the limit cycle is stable, otherwise it is unstable. Details about limit cycles can be found in [18, 129]. Floquet theory [28] is concerned with periodic ordinary differential equations, and deals with the stability of periodic trajectories in phase space [9, 130]. Floquet theory considers a looped trajectory as the solution of such equations, and analyses how a perturbed trajectory changes. If the perturbed trajectory tends to the original trajectory as time passes, the loop is considered stable. The stability can be determined by studying the trajectory change with respect to the perturbation [71, 128, 131].

Consider a set of periodic ordinary differential equations of motion of the form

$$\dot{\mathbf{z}}(t) = \mathbf{f}(\mathbf{z}(t), t) = \mathbf{G}(t)\mathbf{z}(t), \tag{3.13}$$

where $\mathbf{z}(t)$ is the state space column vector at time $t \in \mathbb{R}$, and $\mathbf{G}(t) = \mathbf{G}(t+T)$ is a periodic matrix with period T. The Floquet theory considers the solution

$$\mathbf{z}(t) = \mathbf{z}_0(t) + \Delta\mathbf{z}(t), \tag{3.14}$$

where the solution $\mathbf{z}(t)$ is comprised of periodic part $\mathbf{z}_0(t)$ and additional disturbance $\Delta\mathbf{z}(t)$. Floquet theory asserts that the solution is stable only if

$$\mathbf{z}(t+T) \leq \mathbf{z}(t). \tag{3.15}$$

This assertion is reasonable as it means that $\mathbf{z}$ will not increase over each trajectory, by satisfying the criteria of Lyapunov stability. $\mathbf{z}_0(t) = \mathbf{z}_0(t+T)$ as $\mathbf{z}_0$ is periodic, hence

$$\dot{(\Delta\mathbf{z})} = \dot{\mathbf{z}} - \dot{\mathbf{z}}_0 = \mathbf{G}\Delta\mathbf{z}. \tag{3.16}$$

A set of fundamental solutions $\Delta\boldsymbol{\Psi}$ of the additional disturbance $\Delta\mathbf{z}$ after a period of T of the periodic solution $\mathbf{z}_0$ are defined as

$$\Delta\boldsymbol{\Psi}(t+T) = \Delta\boldsymbol{\Psi}(t)\mathbf{R}. \tag{3.17}$$

$\mathbf{R}$ is known as a monodromy matrix [125, 132]. The Floquet theory determines the stability of a state without approximating the time-periodic system by evaluating the monodromy matrix. In order to adhere to the stability criteria presented in Eq. (3.15), it is required that

$$|\operatorname{eig}(\mathbf{R})| \leq 1, \tag{3.18}$$

so it is necessary to determine the eigenvalues of the monodromy matrix to identify whether or not the set of ordinary differential equations is stable. These eigenvalues are called characteristic multipliers or Floquet multipliers [9].

Based on the Floquet theory, the nature of equilibrium points can be found from the eigenvalues of the periodic system [9, 113]. When every eigenvalue has modulus less than one, Eq. (3.13) has stable solutions. If any one of the eigenvalues have modulus greater than one, unbounded solutions exist [37]. This method is relevant for linear differential equations, but it can also be applied to non-linear differential equations that have been linearised. However, the resulting monodromy matrix is difficult to obtain analytically, hence numerical methods are often used [133]. The accuracy of the eigenvalues of a monodromy matrix obtained in this way can be questionable; a relatively small time-step size is required, resulting in an expensive numerical computation [134].

3.3.2 Stability chart

In this thesis the stability of the LPE systems are defined as follows [18]:

- If the response of the LPE system (Eq. (3.2)) is damped (decayed exponentially in time) then the system is stable (S).
- The LPE system (Eq. (3.2)) is unstable (U) then the response grows exponentially.
- If the system is on the threshold of stability and instability (on the transition curve), its behaviour with time is dependent on external conditions. The limit cycle trajectories can be found on the transition curve (Fig. 3.2). The stability of limit cycles can be demonstrated by Floquet theory, and by computing the monodromy matrix (see section 3.3.1).

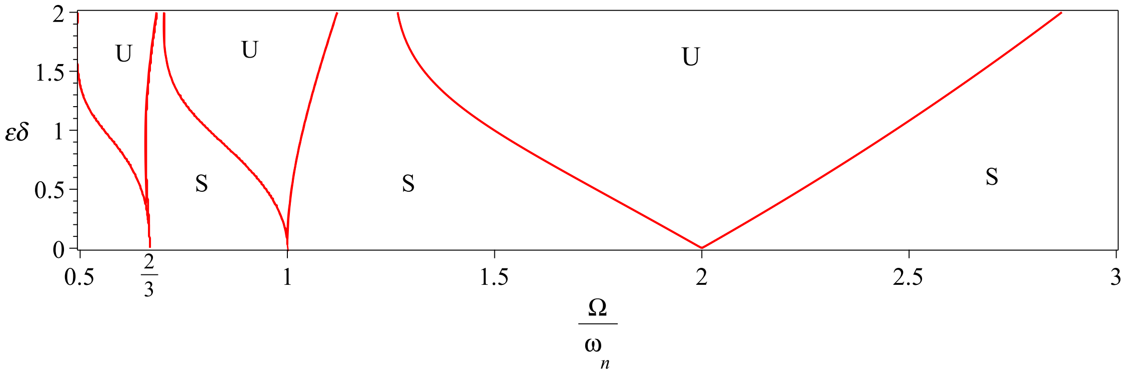

Fig. 3.2. Stability chart for Eq. (3.2) when $\zeta = 0$. The normalised parametric stiffness $\varepsilon\delta$ versus normalised frequency $\frac{\Omega}{\omega_n}$, where Ω is the parametric frequency and ω_n is the natural frequency. The stable (S) and unstable (U) regions are labeled. The red curves on the threshold of stability and instability are the transition curves.

There are bounded and unbounded solutions for Eq. (3.2) which depend on the normalised parametric stiffness $\varepsilon\delta$ and frequency ratio $\frac{\Omega}{\omega_n}$. If the solution is bounded then the corresponding point in the $\varepsilon\delta$ and $\frac{\Omega}{\omega_n}$ parameter plane is stable [9]. Fig. 3.2 shows the stability chart. The stability chart, the Strutt-Ince diagram, was first published by van der Pol and Strutt [135]. The stability chart shows the domains of stability and instability denoted by S and U and it is shown in parameter plane ($\varepsilon\delta$, $\frac{\Omega}{\omega_n}$). The unstable solutions occur when the parametric frequency satisfies $\Omega = \frac{2}{3}\omega_n$, $\Omega = \omega_n$, $\Omega = 2\omega_n$, or higher parametric frequency when the parametric amplitude is not zero. The instability regions are shown in Fig. 3.2, and are separated from stable regions by transition curves. The averaging and harmonic balance methods are used in the thesis to find the stability chart based on the aforementioned stability definitions, along with Fig. 3.2.

3.3.2.1 Stability chart obtained from the method of averaging

By employing the method of averaging, the transition curves in stability chart can be found from the eigenvalues of the system as explained in Appendix A.3. Here for simplicity the method of averaging for a LPE system is called LAVE. The eigenvalues are defined as

$$\lambda_{1,2} = -\kappa\varepsilon\zeta \pm \frac{1}{4}\kappa\varepsilon\left(-16\Delta^2 + \delta^2\right)^{\frac{1}{2}} + \mathcal{O}(\varepsilon^2). \tag{3.19}$$

The first instability region is obtained from Eq. (3.19) when the eigenvalues are real and positive ($\lambda_{1,2} \in \mathbb{R}_+$), and satisfy

$$\mid \Delta \mid < \sqrt{-\zeta^2 + \frac{\delta^2}{16}}. \tag{3.20}$$

When this condition is applied to the system, the instability for different parametric stiffnesses and parametric frequencies can be determined. Δ shows the relation between the parametric frequency and the natural frequency based on the approximation around the reference frequency ($1-\varepsilon\Delta = \frac{\Omega}{\Omega_0}$). Hence, Eq. (3.20) is accurate only if the reference frequency Ω_0 is close to twice the natural frequency. The method of averaging used in this thesis is a first order averaging method, which defines the solutions for $\Omega_0 = 2\omega_n$. The corresponding transition curves for $\lambda_{1,2} \in \mathbb{R}_+$ can be found from Eq. (3.20) as

$$\varepsilon\delta = \frac{2}{\omega_n}\sqrt{\Omega^2 - 4\Omega\omega_n + 4\varepsilon^2\zeta^2\omega_n + 4\omega_n^2}. \tag{3.21}$$

The approximation of the averaging method is limited by $\varepsilon\delta$ in Eq. (3.2). Indeed, for small values of $\varepsilon\delta$ when the magnitude of the time-parametric coefficient $\varepsilon\delta \ll 1$, the method of averaging can approximate the transition curve very close to the exact transition curve achieved by the method of harmonic balance. However, this method does not approximate the solution accurately for large $\varepsilon\delta$. This is shown by the comparison of different methods in Section 3.3.2.3.

3.3.2.2 Stability chart obtained from the method of harmonic balance

Based on the method of harmonic balance, there is a transition between stable and unstable solutions (in $\varepsilon\delta$ and $\frac{\Omega}{\omega_n}$ parameter plane), which is called transition curve. On the transition curves, the solution of Eq. (3.2) is periodic with period 2π and 4π. This solution can be written in the form of Fourier series with a period $T = \frac{2\pi}{\Omega}$

$$\begin{aligned} z(t) &= \sum_{m=0}^{M} A_m \cos\left(\frac{m\pi t}{T}\right) + B_m \sin\left(\frac{m\pi t}{T}\right) \\ &= \sum_{m=1}^{M} A_m \cos\left(\frac{m\Omega t}{2}\right) + B_m \sin\left(\frac{m\Omega t}{2}\right), \end{aligned} \tag{3.22}$$

where A_m and B_m are the Fourier series coefficients, and M is the number of terms. Substituting Eq. (3.22) into Eq. (3.2) allows terms in given sets of algebraic equations on the coefficients A_m and B_m to be collected. Setting the equations into a matrix form and finding the determinant for non-trivial solutions results in a set of equations which describes the line between stability and instability regions (Fig. 3.2). The accuracy of the method of harmonic balance depends on the number of terms M considered in the Fourier series Eq. (3.22). In order to minimise the error between the solution and the trial solution (Eq. (3.22)) for the large value of parametric stiffness, more terms M should be considered. The small parameter, ε, does not affect the accuracy of method of harmonic balance.

The method of harmonic balance with low number of terms $M = 1$ (here for simplicity it is called LHB1), assumes the solution of Eq. (3.2) to be

$$z(t) = A_1 \cos\left(\frac{\Omega t}{2}\right) + B_1 \sin\left(\frac{\Omega t}{2}\right). \tag{3.23}$$

The transition curve ($\varepsilon\delta$ versus $\frac{\Omega}{\omega_n}$) is based on the method of harmonic balance (LHB1) which can be found from Appendix C.1.1. The transition curve is presented as

$$\varepsilon\delta = \frac{1}{2\omega_n}\sqrt{\Omega^4 + 64\varepsilon^2\zeta^2\omega_n^2 - 8\Omega^2 + 16\omega_n^2}. \tag{3.24}$$

The only transition curve found from the low number of terms in harmonic balance method (LHB1) is the main instability region at twice the natural frequency ($\Omega = 2\omega_n$) (Fig. 3.2). Eq. (3.24) shows how the parametric frequency and damping ratio can change the instability region defined by the transition curve. It is expected that when the amplitude of excitation is reduced or the damping ratio is increased, the stability region is expanded.

Transition curve of the LPE system (Eq. (3.2)) based on the method of harmonic balance with high number of terms $M = 20$ (here for simplicity it is called LHB2) is described in Appendix C.1.2. The final solution is presented in Appendix C.1.3. The transition curves found from the high number of terms in harmonic balance is able to find all unstable tongues (transition curves) in the stability chart, as well as the main tongue at twice the natural frequency ($\Omega = 2\omega_n$).

3.3.2.3 Comparison between the methods of averaging and harmonic balance

The accuracy of the transition curves based on the method of averaging is limited by the $\varepsilon\delta$ value, while for the method of harmonic balance the accuracy is limited by the number of terms M. From the method of averaging, the tangents of exact stability curve can be determined correctly, but falsely suggest that periodic solutions exist on the averaged curve [34].

Fig. 3.3 shows the comparison between three methods: the method of averaging (LAVE), the methods of harmonic balance with low number of terms $M = 1$ (LHB1), and harmonic balance with high number of terms $M = 20$ (LHB2). The difference between the transition curves with harmonic balance with $M = 20$ and harmonic balance with $M = 30$ at $\varepsilon\delta = 0.5$ is off the order of $10^{-6}\frac{\Omega}{\omega_n}$. Hence, $M = 20$ is accurate enough to be chosen as exact solution. The stability curve achieved from LHB2 is in agreement with the results achieved from the Floquet multipliers [136]. The stability chart is plotted in Fig. 3.3 for the system parameters which are close to the experimental rig properties. $\zeta = 0.0316$, and $\omega_n = 31.62\,\mathrm{rad\,s^{-1}}$ are chosen for Fig. 3.3 based on the experimental set-up. These experiments are presented in Chapter 6. Figs 3.3a, 3.3b and 3.3c are also implemented for three different small parameter values of $\varepsilon = 0.01, 0.1$ and 1. From these figures, for the main transition curve at $\Omega = 2\omega_n$, the LHB1 and LAVE method are all in agreement

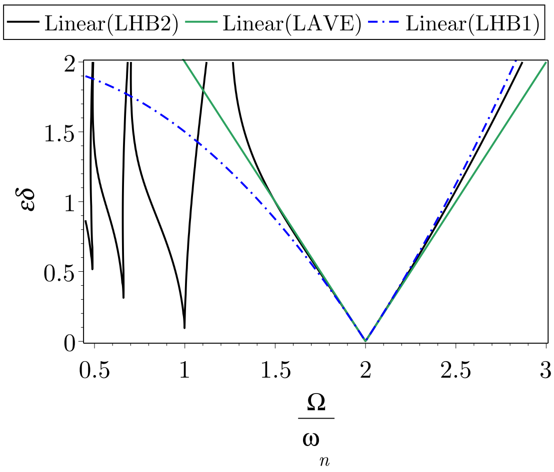

(a) $\varepsilon = 0.01$.

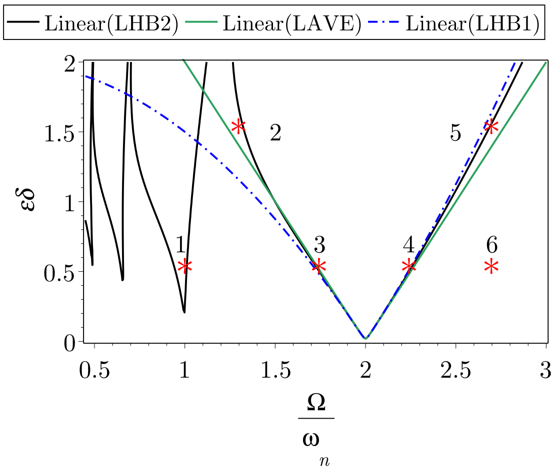

(b) $\varepsilon = 0.1$.

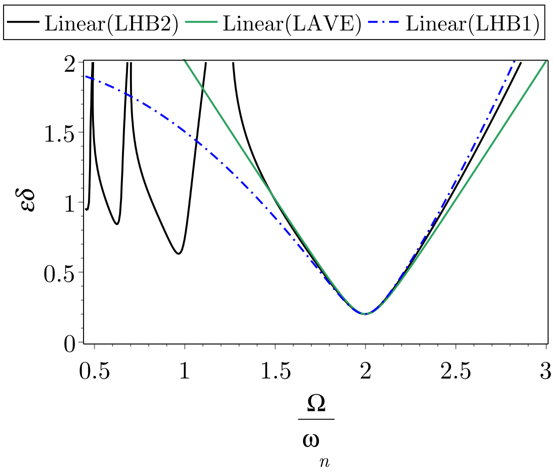

(c) $\varepsilon = 1$.

Fig. 3.3. Stability chart for Eq. (3.2). The methods of averaging (LAVE), harmonic balance with low number of terms $M = 1$ (LHB1) and harmonic balance with high number of terms $M = 20$ (LHB2) are implemented to show the transition curves. The response of the system for points shown in Fig 3.3b are computed numerically. The phase portrait for each point is demonstrated in Fig. 3.4.

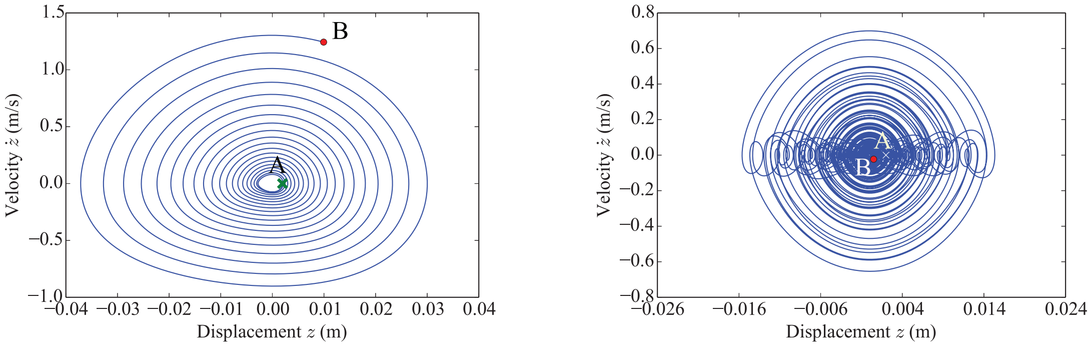

(a) Unstable point, point 1 in Fig 3.3b.

(b) Stable point, point 2 in Fig 3.3b.

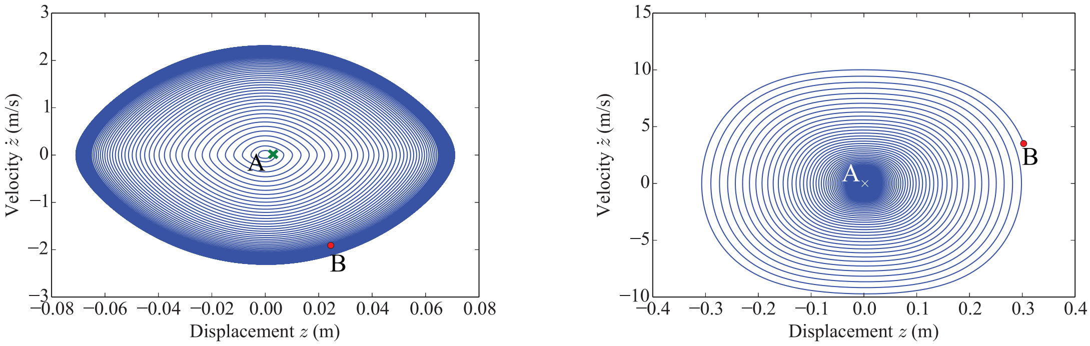

(c) Stable point, point 3 in Fig 3.3b.

(d) Unstable point, point 4 in Fig 3.3b.

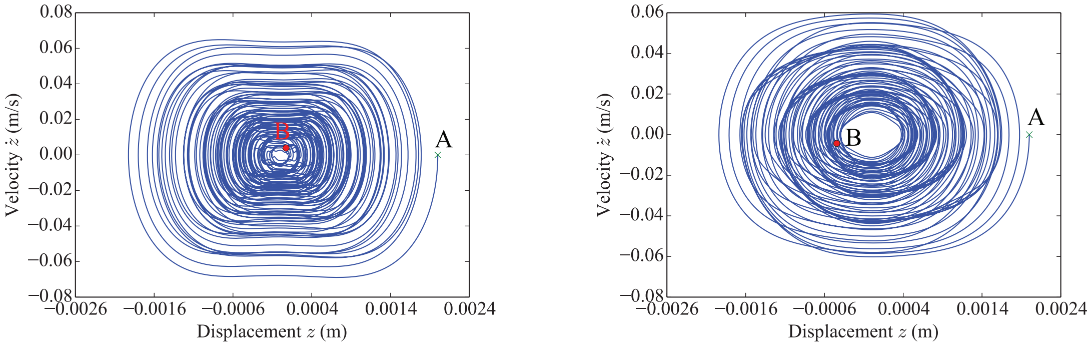

(e) Stable point, point 5 in Fig 3.3b.

(f) Stable point, point 6 in Fig 3.3b.

Fig. 3.4. Numerical phase portrait for Eq. (3.2) corresponds to points 1 to 6 in Fig. 3.3b. $\varepsilon = 0.1$, $\zeta = 0.0316$, and $\omega_n = 31.62 \mathrm{rad\,s}^{-1}$ are considered for all tests. The initial condition $z_0 = 0.002\mathrm{m}$ and $\dot{z}_0 = 0\mathrm{ms}^{-1}$ are considered for all six points. The green cross and label A is representative of the start point and the red circle and label B is the last point.

with LHB2 when $\varepsilon\delta \leq 0.5$. The difference between the LHB1 and LHB2 at $\varepsilon\delta = 0.5$ is of the order of $0.01\frac{\Omega}{\omega_n}$. The difference between the LHB1 and LAVE at $\varepsilon\delta = 0.5$ is $0.009\frac{\Omega}{\omega_n}$. This is the maximum difference between these two transition curves when $\varepsilon\delta \leq 0.5$.

Different points on transition curves in Fig. 3.3b are considered to check the behaviour of Eq. (3.2). Six points in different regions are selected, and for each point Eq. (3.2) is solved numerically. Python[2] has been used for numerical analysis. The initial condition was integrated using the ODEINT function in SciPy [40], which uses a Fortran routine from ODEPACK [40]. The displacement and velocity initial conditions, $z_0 = 0.002$m and $\dot{z}_0 = 0\text{ms}^{-1}$ were considered respectively for all six points. The initial conditions are chosen based on the experimental tests, which are explained in Chapter 6. Then the numerical phase portrait of each point is considered to check the stability of the response. Based on the stability definition, a damped system is stable if all trajectories of its solutions converge to a small value as time goes to infinity. The instability of the PE system (Eq. (3.2)) is explored from the numerical phase portrait. We consider if the trajectories converge to a small value the system to be stable. When the trajectories diverge and the response grows exponentially the system is unstable.

The six points (red asterisk) in Fig. 3.3b are selected such that

- Point 1 in Fig. 3.3b is inside the unstable region from LHB2 method. Fig. 3.4a shows that this point is unstable, since the trajectory is diverging. Point 1 is at $\varepsilon\delta = 0.5$ and $\frac{\Omega}{\omega_n} = 1$, Eq. (3.2) is solved for $t = 0$ to $20T$ when $T = \frac{2\pi}{\Omega}$. The time step used is $4T \times 10^{-5}$.

- Point 2 is inside the stable region from LHB2 method. However, from LHB1 and LAVE method, this point is found to be unstable. The numerical phase portrait shows this point is asymptotically stable, since the last point (point B) in the phase portrait in Fig. 3.4b is converging. Point 2 is at $\varepsilon\delta = 1.5$ and $\frac{\Omega}{\omega_n} = 1.3$, Eq. (3.2) is solved for $t = 0$ to $200T$ when $T = \frac{2\pi}{\Omega}$. The time step used is $4T \times 10^{-4}$.

- Point 3 is close to the transition curve from the LHB1 and LAVE methods, but is closer to the transition curve calculated from LHB2 method. The numerical result from the phase portrait clarifies that at this point the system is stable (Fig. 3.4c). The phase portrait shows limit cycle behaviour of this point, which can be stable or unstable as time approaches to infinity (Fig. 3.4c) [71]. Point 3 is at $\varepsilon\delta = 0.5$ and $\frac{\Omega}{\omega_n} = 1.7444$, Eq. (3.2) is solved for $t = 0$ to $200T$ when $T = \frac{2\pi}{\Omega}$. The time step used is $4T \times 10^{-4}$.

- Point 4 in Fig. 3.3b is inside the unstable region found from the LHB1, LHB2 and LAVE methods, and the phase portrait shows that the system is unstable at this point (Fig. 3.4d). The last point (point B) in Fig. 3.4d is diverging from the initial

---

[2] https://www.python.org

condition point (point A). Point 4 is at $\varepsilon\delta = 0.5$ and $\frac{\Omega}{\omega_n} = 2.24$, Eq. (3.2) is solved for $t = 0$ to $200T$ when $T = \frac{2\pi}{\Omega}$. The time step used is $4T \times 10^{-4}$.

- Point 5 in Fig. 3.3b is inside the stable region from the LHB1 and LHB2 methods. However, the LAVE method shows instability for this point. The phase portrait in Fig. 3.4e shows that the system is stable at this point. Point 5 is at $\delta = 1.5$ and $\frac{\Omega}{\omega_n} = 2.7$, Eq. (3.2) is solved for $t = 0$ to $200T$ when $T = \frac{2\pi}{\Omega}$. The time step used is $4T \times 10^{-4}$.

- Point 6 in Fig. 3.3b is inside the stable region from all methods, and the phase portrait also confirm this stability (Fig. 3.4f). Point 6 is at $\varepsilon\delta = 0.5$ and $\frac{\Omega}{\omega_n} = 2.7$, Eq. (3.2) is solved for $t = 0$ to $200T$ when $T = \frac{2\pi}{\Omega}$. The time step used is $4T \times 10^{-4}$.

By computing the phase portrait for different points on the stability chart, the transition curves obtained from LHB2 are closer to the numerical results for large values of parametric stiffness. For small values of the small parameter ($\varepsilon \ll 1$) and parametric stiffness ($\delta \leq 0.5$), the LHB1 and LAVE methods are in agreement with the numerical results. For different value of ε, the upwards and downwards shift of the transition curves is caused by the change in damping of the system. This shift of the transition curves for different ε is explained in Section 3.6.1.

3.4 Analytical modelling of a nonlinear parametrically excited system

In LPE systems, the unbounded responses can occur at the parametric frequency (Ω). However, unbounded responses do not occur in nonlinear systems due to the amplitude dependent behaviour. At resonance, the amplitude of the motion increases, and since the period of the system is amplitude dependent, the resonance detunes [37]. The free and forced responses of the NPE systems with cubic stiffness and cubic parametric stiffness nonlinearities have been explained in several publications [58, 87, 117]. However, few studies of the free response vibration of the NPE system with cubic parametric nonlinearity can be found in the literature [64].

The cubic stiffness nonlinear term is added to Eq. (3.1)

$$m_{\mathrm{t}}\ddot{z} + c_{\mathrm{t}}\dot{z} + \left(k_1 + k_{\mathrm{p1}}\cos\left(\Omega t\right)\right)z + k_3 z^3 = 0, \tag{3.25}$$

where z is the mass displacement, m_{t} is the total mass, c_{t} is the total viscous damping coefficient, ε is the small parameter, k_1 is the constant stiffness, k_{p1} is the parametric stiffness (parametric amplitude) with the parametric frequency Ω, and k_3 is the cubic stiffness. This equation represents a parametrically exited system with a cubic nonlinear term. Eq. (3.25) can be solved analytically with different methods, such as multiple scales and the method of averaging [6].

The NPE system considered in this chapter has cubic stiffness nonlinearity and cubic parametric stiffness nonlinearity. Both cubic and cubic parametric stiffnesses nonlinearity have been seen in real structures such as cable-stayed bridges and in electromechanical systems including electromechanical sensors [58, 87, 117]. The cubic parametric nonlinearity is considered in the experimental set-up (electromagnetic system) and is introduced in Chapter 6. Adding cubic parametric stiffness nonlinearity to Eq. (3.25) results in

$$m_{\mathrm{t}}\ddot{z} + c_{\mathrm{t}}\dot{z} + \left(k_1 + k_{\mathrm{p1}}\cos\left(\Omega t\right)\right)z + \left(k_3 + k_{\mathrm{p3}}\cos\left(\Omega t\right)\right)z^3 = 0, \tag{3.26}$$

where k_{p3} is the cubic parametric stiffness. The method of averaging is employed to solve Eq. (3.26), hence ε is added to limit some of the parameters to be small values. The method of averaging for a NPE system is abbreviated to NAVE.

Normalizing Eq. (3.26) with the total mass m_t yields

$$\ddot{z} + 2\varepsilon\zeta\omega_n\dot{z} + \omega_n^2\left(1 + \varepsilon\delta\cos\left(\Omega t\right)\right)z + \omega_n^2(\varepsilon\alpha + \varepsilon\gamma\cos\left(\Omega t\right))z^3 = 0, \tag{3.27}$$

where the normalised parametric amplitude is $\delta = \frac{k_{\mathrm{p1}}}{k_1}$, the normalised cubic stiffness nonlinearity is $\alpha = \frac{k_3}{k_1}$, and the normalised cubic parametric nonlinearity is $\gamma = \frac{k_{\mathrm{p3}}}{k_1}$. The steady-state solutions for the NPE system are presented in Appendix B.

3.5 Stability analysis of a nonlinear parametrically excited system

To study the stability of a nonlinear system, the nonlinear system can be linearised at the state of interest to obtain the Jacobian of the linearised system (where $\varepsilon\delta \neq 0$). The eigenvalues of the Jacobian matrix determine the stable and unstable solutions. However, the Jacobian of the NPE system and its eigenvalues are time-variant. The time-variant eigenvalues are not useful to find the stability of the solutions. In this section, the stability of the NPE system is investigated with the method of averaging. The NPE system defined by a set of time-periodic differential equation is averaged over one period of the vibration (see Appendix B). The time-constant set of equations are obtained after averaging. This set of equations are linearised and the Jacobian matrix is found from the time-constant set of equations.

The stability of the trivial and non-trivial solutions are investigated based on the eigenvalues of the Jacobian as illustrated in Appendix B.3. The non-trivial solutions are:

- $z_1\left(t\right) = a_1\cos\left(\frac{\Omega}{2}t + \varphi\right)$ when $\varphi > 0$ or $\varphi = 0$, this solution is stable.
- $z_2\left(t\right) = a_2\cos\left(\frac{\Omega}{2}t + \varphi\right)$ when $\varphi < 0$, this solution is unstable.

The averaged amplitude of the stable steady-state solution a_1 is found from Eq. (B.14) and the averaged amplitude of the unstable steady-state solution a_2 is presented by Eq. (B.15). φ is the averaged phase of the steady-state solutions and it is found from Eq. (B.18).

To find the stable and unstable solutions of the NPE system (Eq. (3.25)) the phase portrait is considered. The phase portrait for the NPE system with cubic parametric nonlinearity (Eq. (3.27)) with parameters $\zeta = 0$, $\delta = 0.25$, $\alpha = 150\text{m}^{-2}$ and $\gamma = 80\text{m}^{-2}$ is obtained analytically. To plot the phase portrait for this NPE system, the relation between the derivative of the averaged amplitude, and the phase with averaged amplitude and phase is examined. Dividing Eq. (B.7) by Eq. (B.8) yields an expression that can be integrated respect to the averaged amplitude and phase. The result is

$$\Delta a^2 + \frac{1}{2}\delta\cos(2\varphi)a^2 + \frac{3}{16}\alpha a^4 + \frac{1}{16}\gamma\cos(2\varphi)a^4 = C, \tag{3.28}$$

where C is a constant value. A and B are introduced to transform from polar coordinate system to Cartesian coordinate system. A and B represent

$$A = a\cos(\varphi), \quad \text{and,} \quad B = a\sin(\varphi). \tag{3.29}$$

Hence, Eq. (3.28) is changed to

$$(\Delta+\frac{1}{2}\delta)A^2+(\Delta-\frac{1}{2}\delta)B^2+\frac{3}{16}\alpha(A^2+B^2)^2+\frac{1}{16}\gamma(A^2+B^2)A^2-\frac{1}{16}\gamma(A^2+B^2)B^2 = C, \tag{3.30}$$

which is used to plot the phase portrait for different C values. The phase portraits are shown in the $B - A$ plane. The stability of the solutions of the NPE system are illustrated with the phase portrait. The phase portraits are shown for several points on the transition curve of the LPE system (Eq. (3.2)) without damping $\zeta = 0$ (see Fig. 3.5). The phase portrait of the point (a) on the transition curve at $\frac{\Omega}{\omega_n} = 2-\frac{\delta}{2} = 1.875$ is shown in Fig. 3.5a. This phase portrait describes that the steady-state solution of a single point $A = B = 0$ is a centre and therefore it is stable.

The phase portrait of the point (b), which is inside the transition curve shows that the steady-state solution of $A = B = 0$ is a saddle point and therefore is unstable (see Fig. 3.5b). However, the steady-state solutions of $a \neq 0$ along the A-axis correspond to two centres equilibrium points, which are stable. Hence, one unstable trivial solution and one stable non-trivial solution are expected at frequency $\frac{\Omega}{\omega_n} = 2$. Similarly, at $\frac{\Omega}{\omega_n} = 2 + \frac{\delta}{2} = 2.125$, for point (c) on the transition curve, the phase portrait is plotted in Fig. 3.5c. The steady-state solution of $A = B = 0$ is a saddle point, and the steady-state solutions of $a \neq 0$ along the A-axis correspond to two centres. This saddle point is unstable and these centres are stable. Outside the transition curve at $\frac{\Omega}{\omega_n} = 2 + 1.2\left(\frac{\delta}{2}\right) = 2.15$, for point (d), different stable and unstable points exist (see Fig. 3.5d). The phase portrait shows

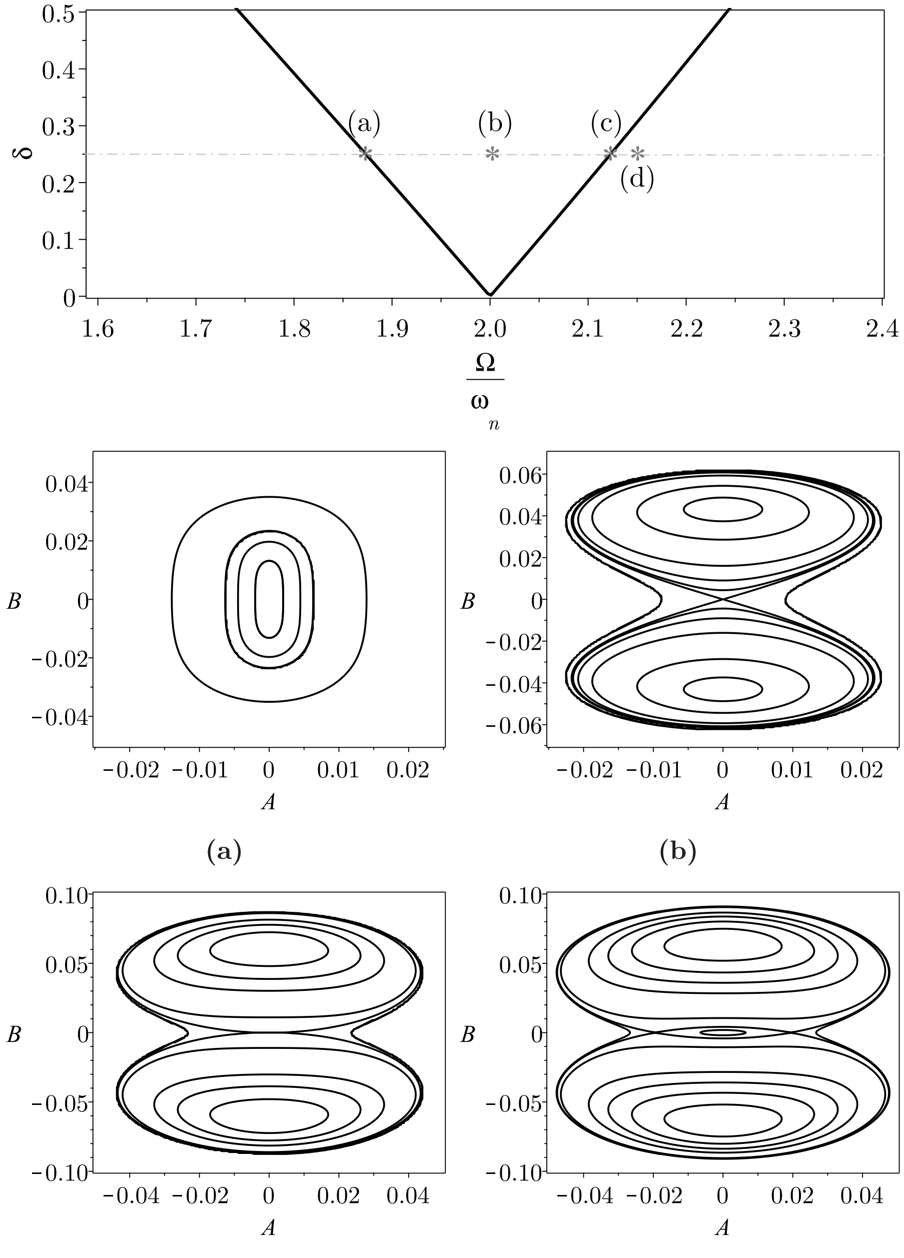

(a) **(b)**

(c) **(d)**

Fig. 3.5. The transition curve and the $B - A$ plane phase portraits for the NPE system (Eq. (3.27)) with $\varepsilon\zeta = 0$, $\varepsilon\delta = 0.25$, $\varepsilon\alpha = 150\text{m}^{-2}$ and $\varepsilon\gamma = 80\text{m}^{-2}$. The phase portraits correspond to different points on the transition curve. (a) The phase portrait for point a is at $\frac{\Omega}{\omega_n} = 1.875$. (b) The phase portrait for point b is at $\frac{\Omega}{\omega_n} = 2$. (c) The phase portrait for point c is at $\frac{\Omega}{\omega_n} = 2.125$. (d) The phase portrait for point d is at $\frac{\Omega}{\omega_n} = 2.15$.

a centre at $A = B = 0$, which is a stable point, and steady-state solutions when $a \neq 0$ along the B-axis are two saddles and unstable. Two centres and stable points exist along the A-axis . Outside the transition curve, unlike the behaviour of the LPE system, only one stable solution is expected. Two stable and one unstable solutions are found for the NPE system. On the right hand side of the transition curve for frequencies higher than parametric frequency, the two stable and one unstable solutions are found as a result of the positive cubic nonlinearity. The effects of cubic nonlinearity are presented in Section 3.6.2.

The transition curve and the phase portraits are presented for the NPE system only with cubic stiffness nonlinearity in the literature [37]. In this thesis, since the cubic parametric term is included, a transition curve for the NPE system is generated. This transition curve shows the relation between the normalized parametric stiffness δ, and the frequency ratio, $\frac{\Omega}{\omega_n}$ as a function of response amplitude a.

The relation between $\varepsilon\delta$ and the frequency ratio $\frac{\Omega}{\omega_n}$ as a function of response amplitude a can be found when the system has non-trivial solutions. This is achieved by finding the steady-state response of the NPE system from the method of averaging. Solving Eq. (B.13) for $\varepsilon\delta$ yields

$$\varepsilon\delta = -\varepsilon a^2\gamma + \frac{1}{2}\sqrt{9\varepsilon\alpha^2 a^4 - 48\varepsilon a^2\alpha\left(\frac{\Omega}{2\omega_n} - 1\right) + 64\left(\frac{\Omega}{2\omega_n} - 1\right)^2 + 16\varepsilon\zeta^2}, \tag{3.31}$$

which shows where the system has steady-state solutions. The corresponding transition curve can be found from Eq. (3.31) when $a \neq 0$. The transition curve is dependent on a. The transition curve for $a = 0.02$m is plotted as a dashed red curve in Fig. 3.6a. The transition curve for the NPE system is shifted to the right relative to the transition curve (black curve) for the LPE system as a result of the hardening nonlinearity. It is also shifted down by the cubic parametric nonlinearity. These shifts are explained in Section 3.6. At $\varepsilon\delta = 0.25$, the nonlinear system has a steady-state response for the frequency ratio $1.892 \leq \frac{\Omega}{\omega_n} \leq 2.107$. From the amplitude-frequency plot, both stable and unstable solutions can be found when $2.107 \leq \frac{\Omega}{\omega_n}$. Hence, there is an area in the transition curve for the NPE system in which the system has stable and unstable solutions. This area can also be found analytically based on the difference between the transition curves for the linear and nonlinear systems.

For the case $a = 0$, the transition curve from the harmonic balance method is plotted in Fig. 3.6a. The solid black curve in Fig. 3.6a shows the transition curve for the LPE system. For the LPE system, unbounded unstable solutions exist inside the transition curve, and bounded solutions exist outside. At $\varepsilon\delta = 0.25$ on the transition curve, the system is unstable when the frequency ratio is $1.892 \leq \frac{\Omega}{\omega_n} \leq 2.107$. From the amplitude-frequency relation in Fig. 3.6b, unstable trivial solutions exist when $a = 0$ and $1.892 \leq \frac{\Omega}{\omega_n} \leq 2.107$.

The amplitude-frequency relation is plotted in Fig. 3.6b from Eq. (B.14) and Eq. (B.15). This figure is the analytical amplitude-frequency relation of Eq. (3.27) when $\zeta = 0.0316$,

$\omega_n = 31.62 \mathrm{rad\,s^{-1}}$, $\varepsilon = 1$, $\alpha = 150 \mathrm{m^{-2}}$ and $\gamma = 80 \mathrm{m^{-2}}$. The stable trivial solutions ($a = 0$) and the stable non-trivial solutions (a_1 upper branch) are also found numerically using Python[3]. The initial condition was integrated using the ODEINT function in SciPy [40]. The numerical points were found by solving Eq. (3.27) from $\Omega = 1.6\omega_n$ up to $\Omega = 2.4\omega_n$. The initial conditions to solve Eq. (3.27) were chosen based on the amplitude of the previous steady-state solution. Hence, by increasing the frequency, the amplitude of the response is increased. The lower line (dashed line) in Fig. 3.6b shows the unstable solutions a_2 that could not be found numerically.

When $a = 0$, the effect of nonlinearity is zero since the nonlinear terms are amplitude dependent. In this case, the system can be treated as a linear time-varying system. The trivial solutions of the LPE system are zero. However, when $a = 0$, the system can be unstable as a result of any perturbation in the system.

The relation between the amplitude-frequency plot and the transition curve clarifies the difference between the transition curve for a LPE and a NPE system. Fig. 3.6b shows amplitude-frequency relation. This curve describes stationary values of the displacement amplitude a as a function of parametric frequency Ω normalised by the linear natural frequency ω_n. Some nonlinear features appeared for the NPE system:

- The NPE system with nonlinear restoring forces of hardening type ($\alpha > 0$) is considered. Hence, the response peak bends to the right.

- Multiple stationary solutions exist for certain parametric frequencies. This is as a result of the bent peak. In Fig. 3.6b on the left side of point I, outside the transition curve for the LPE system, the response is damped. Between points I and III there are two possible solutions: $a = 0$ (trivial unstable) and $a = a_1$ (trivial stable). The stable and unstable solutions are in agreement with the phase portrait results for point (b) in Fig. 3.5b. On the right side of point III, there are three possible solutions: $a = 0$ (trivial stable) and $a = a_1$ (trivial stable), and $a = a_2$ (trivial unstable). The phase portrait results for point (d) in Fig. 3.5d shows two stable points and one unstable point.

- There is one discontinuous jump in the response, which is from point III to point II. From high to low frequency, at point III the zero solution turns unstable. In Fig. 3.6b frequencies Ω_{I} and Ω_{III} are bifurcation values. Upon crossing any of these frequencies, sudden changes to possible response take place [137]. In Fig. 3.6b from low to high frequency, from above Ω_{I}, a stable limit cycle solution is born at Ω_{I} and the zero solution becomes unstable. This is Hopf bifurcation point. The Hopf bifurcation at Ω_{I} involves the transition of stable equilibrium to unstable equilibrium and stable limit cycle. This is a supercritical or soft Hopf bifurcation [137]. The term

---

[3] https://www.python.org

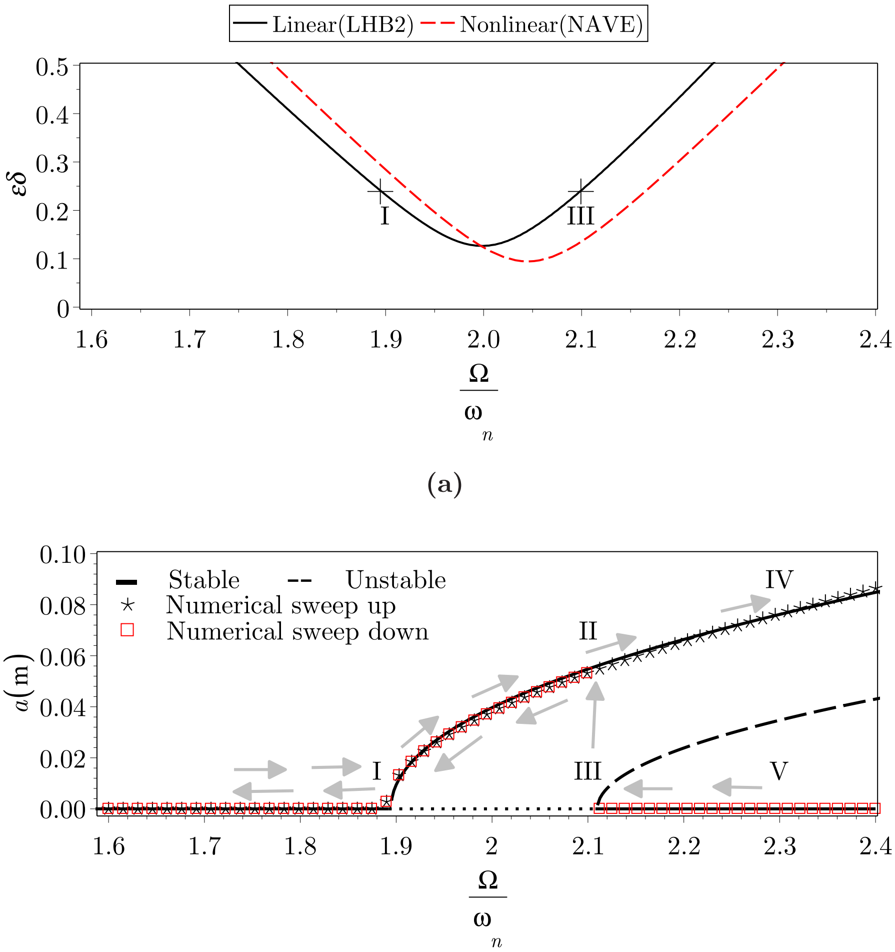

(a)

(b)

Fig. 3.6. (a) Analytical transition curve plots. The LPE transition curve (black solid line) and the NPE transition curve (dashed red line) is plotted based on Eq. (3.31) for $a = 0.02\text{m}$, $\varepsilon\zeta = 0.0316$, $\omega_n = 31.62\text{rad}\,\text{s}^{-1}$, $\varepsilon\alpha = 150\text{m}^{-2}$, and $\varepsilon\gamma = 80\text{m}^{-2}$. (b) The amplitude-frequency plot for the NPE system for $\varepsilon\delta = 0.25$. The steady-state solutions are found analytically as well as numerically. The upper stable branch (black solid line) has amplitude a_1 (Eq. (B.14)) and the unstable branch (black dashed line) has amplitude a_2 (Eq. (B.15)).

soft comes from the fact that across the bifurcation value drastic change in response has not happened. For the NPE system with strong cubic stiffness nonlinearity, the amplitude of response changes from a zero value to a small nonzero value. Hence, only a supercritical/soft bifurcation are expected.

In contrast at Ω_{III}, the bifurcation happens from an unstable equilibrium to a stable equilibrium and an unstable limit cycle. Ω_{III} is a Hopf bifurcation value, since a limit cycle is created from an equilibrium. This is a subcritical/hard Hopf bifurcation. For hard Hopf bifurcation it is possible that a finite disturbance to the stable equilibrium may throw the system beyond the unstable limit cycle.

3.5.1 Stability chart obtained by the methods of averaging and harmonic balance

The stability chart for Eq. (3.27) is plotted in Fig. 3.7 which shows the transition curves obtained from LHB2 and the transition curves for the NPE system. The LPE transition curves are shown as a reference to determine the changes resulting from nonlinearity. The transition curve from two nonlinear methods; the method of harmonic balance (NHB1) and the method of averaging (NAVE) are presented in Fig. 3.7. $\varepsilon = 0.01$ and $\varepsilon = 1$ are chosen to clarify the effect of the small parameter. Fig. 3.7a shows that as ε reduces the nonlinear system is closer to a linear system. When ε is large (Fig. 3.7b), the nonlinear effect on the transition curve is evident.

Transition curves of a NPE system (Eq. (3.27)) based on the method of harmonic balance with a low number of terms $M = 1$ (NHB1) is obtained from Appendix C.2. This method is similar to the method explained in Section 3.3.2.2 to find the transition curves for the LPE system. It is important to mention that with the method of harmonic balance the linearised model is not considered. The main transition curve found from Appendix C.2 is

$$\varepsilon\delta = -\varepsilon a^2\gamma + \frac{1}{2}\sqrt{\left(\frac{\Omega}{\omega_n}\right)^4 - 6\varepsilon\, a^2\alpha\left(\frac{\Omega}{\omega_n}\right)^2 + 64\varepsilon^2\zeta^2 - 8\left(\frac{\Omega}{\omega_n}\right)^2 + 24\varepsilon a^2\alpha + 16}. \quad (3.32)$$

Both the NAVE and the NHB1 methods can be employed to solve Eq. (3.27) when the parametric amplitude and nonlinear parameters are small. From Fig. 3.7 the transition curves from these two methods are largely separate when $\varepsilon\delta > 0.5$. From a series of numerical steady-state stable solutions, both the NAVE and the NHB1 methods are closer to the numerical results when $\varepsilon\delta \leq 0.25$. A zoom of Fig. 3.7b is provided in Fig. 3.8. For all points on Fig. 3.8, Eq. (3.27) is solved numerically from the numerical integration using the ODEINT function in SciPy [40], and the initial conditions $z_0 = 0.02$m and $\dot{z}_0 = 0$ are used to determine the phase portraits. The points on Fig. 3.8 are studied as follows:

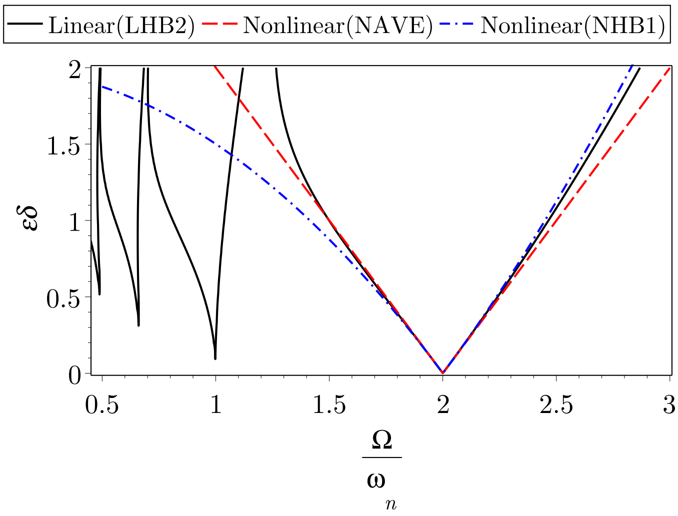

(a) $\varepsilon = 0.01$.

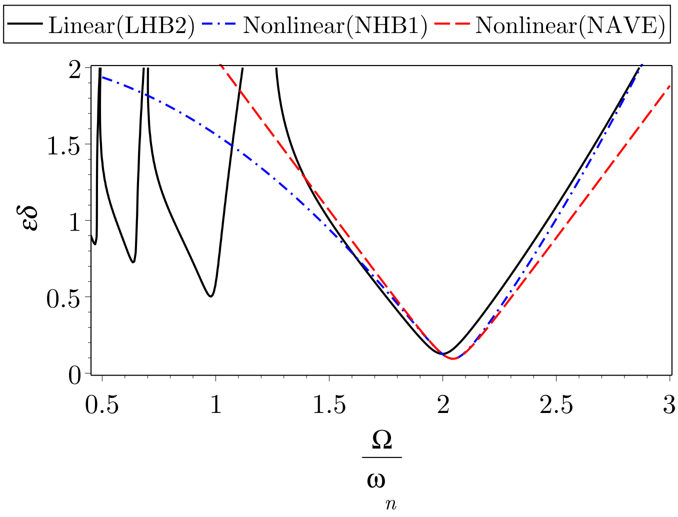

(b) $\varepsilon = 1$.

Fig. 3.7. The analytical transition curves with the method of harmonic balance with a high number of terms $M = 20$ (LHB2) for Eq. (3.2) is presented for comparison with the method of averaging (NAVE), and harmonic balance with low number of terms $M = 1$ (NHB1) for Eq. (3.27). $\varepsilon\zeta = 0.0316$, $\omega_n = 31.62\text{rad}\,\text{s}^{-1}$, $a = 0.02\text{m}$, $\varepsilon\alpha = 150\text{m}^{-2}$, $\varepsilon\gamma = 80\text{m}^{-2}$ are considered for the nonlinear system in Eq. (3.27). In the linear case, $\varepsilon\alpha = 0$ and $\varepsilon\gamma = 0$.

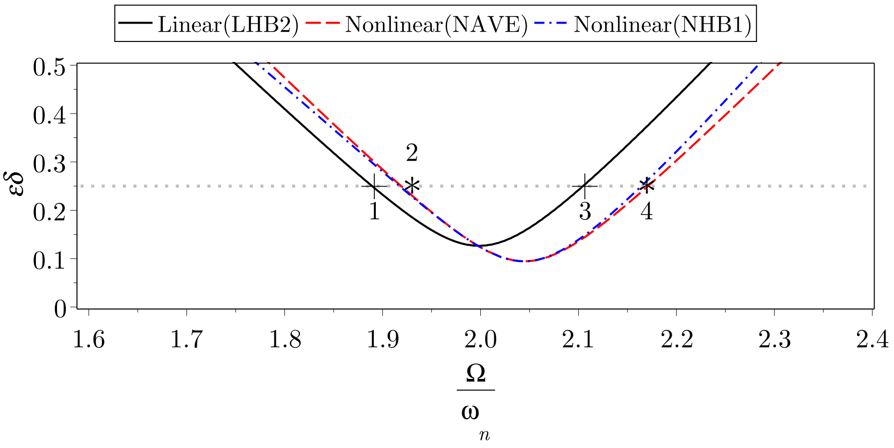

Fig. 3.8. A zoomed in version of Fig. 3.7b and similar case Fig. 3.6a. Labels 1,2,3, and 4 correspond to the phase portraits in Fig. 3.9. Points 1 and 3 are identical to point I and III in Fig. 3.6a.

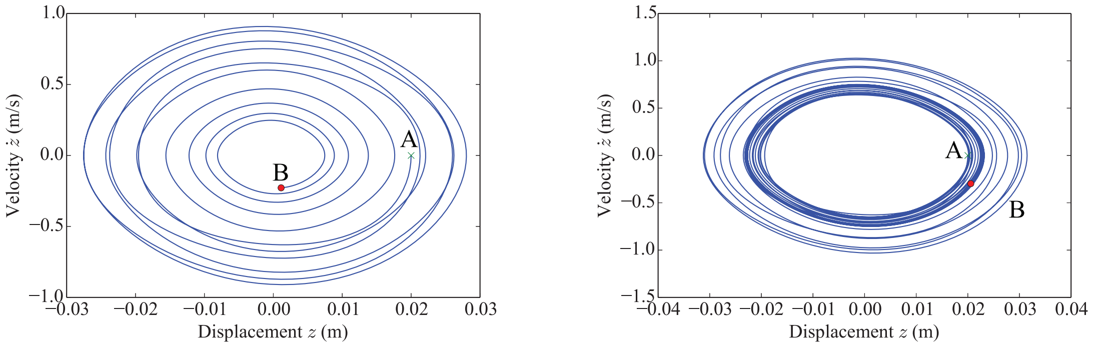

(a) Stable point (trivial stable solution), point 1 in Fig. 3.8.

(b) Stable point (non-trivial stable solution), point 2 in Fig. 3.8.

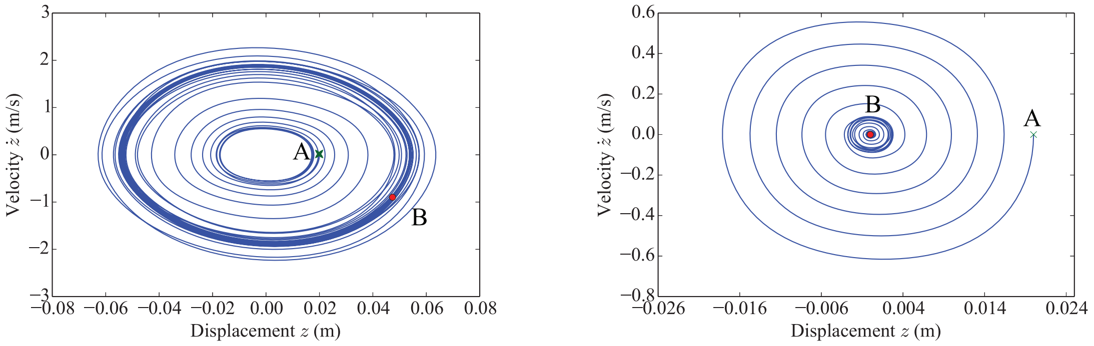

(c) Stable point (non-trivial stable solution), point 3 in Fig. 3.8.

(d) Stable point (trivial stable solution), point 4 in Fig. 3.8.

Fig. 3.9. Numerical phase portrait for Eq. (3.27) corresponding to points 1 to 4 in Fig. 3.8. $\varepsilon\zeta = 0.0316$, $\varepsilon\delta = 0.25$, $\varepsilon\alpha = 150\text{m}^{-2}$, $\varepsilon\gamma = 80\text{m}^{-2}$, and $\omega_n = 31.62\text{rad}\,\text{s}^{-1}$ are considered for all tests. Initial values $z_0 = 0.02\text{m}$ and $\dot{z}_0 = 0\text{ms}^{-1}$ are considered for all four points. The green cross and label A is representative of the start point and the red circle and label B is the last point.

- Point 1 is at $\varepsilon\delta = 0.25$ and $\frac{\Omega}{\omega_n} = 1.892$. This point is outside the NPE transition curves. From the numerical phase portrait Fig. 3.9a the solution at this point is stable. The phase portrait in Fig. 3.9a shows that the final point (point B) after 20 periods (20 T) converges to a small value. For point 1, Eq. (3.27) is solved for $t = 0$ to $20T$ when $T = \frac{2\pi}{\Omega}$. The time step used is $4\ T \times 10^{-5}$.

- Point 2 is at $\varepsilon\delta = 0.25$ and $\frac{\Omega}{\omega_n} = 1.93$. For point 2 Eq. (3.27) is solved for $t = 0$ to $500T$ when $T = \frac{2\pi}{\Omega}$. The time step used is $T \times 10^{-3}$. From the numerical phase portrait in Fig. 3.9b, point 2 is stable. At point 2, the NPE system has a non-trivial stable solution. Also point 2 is on a NPE transition curve (Fig. 3.8). The amplitude-frequency plot in Fig. 3.6b shows that the amplitude of the steady-state response a, is higher than the initial value z_0, $(a > z_0)$; this also can be seen in Fig. 3.9b. This means that the solution has jumped to an upper branch.

- Point 3 is at $\varepsilon\delta = 0.25$ and $\frac{\Omega}{\omega_n} = 2.107$. For point 3, Eq. (3.27) is solved for $t = 0$ to $500T$ when $T = \frac{2\pi}{\Omega}$. The time step used is $T \times 10^{-3}$.The numerical phase portrait in Fig. 3.9c presents the steady-state response at this point where the NPE system has a non-trivial stable solution. This point is inside the NPE transition curves. The amplitude-frequency plot in Fig. 3.6b and the phase portrait Fig. 3.9c show that the amplitude of the response is higher than the initial amplitude $(a > z_0)$.

- Point 4 is at $\varepsilon\delta = 0.25$ and $\frac{\Omega}{\omega_n} = 2.17$. For point 4, Eq. (3.27) is solved for $t = 0$ to $500T$ when $T = \frac{2\pi}{\Omega}$. The time step used is $T \times 10^{-3}$. This point is on the NAVE transition curve but it is outside the NHB1 transition curve. From the numerical phase portrait shown in Fig. 3.9d, this point is stable and point B has converged. The amplitude-frequency plot in Fig. 3.8 shows at this point the NPE system has stable and unstable non-trivial solutions, as well as a stable trivial solution. When the initial amplitude is not enough to make the amplitude of the response to jump to the higher branch, the solution jumps to the lower branch. Unstable non-trivial steady-state solutions cannot be found numerically. The numerical phase portrait Fig. 3.9d show the point 4 as a stable point. In order to see the unstable points (saddle nodes), the analytical phase portrait should be considered.

In conclusion, the unstable non-trivial solutions from the numerical phase portraits could not be obtained, hence we cannot conclude which methods among NAVE or NHB1 can detect the unstable non-trivial solutions accurately.

3.6 Effects of parametrically excited system parameters on the stability chart

In this section, the effects of PE system parameters such as linear damping, nonlinear cubic stiffness, and nonlinear cubic parametric stiffness on shifting the transition curves in the stability chart are considered. Shifting the transition curves results in a change in the response of the system for a given parametric amplitude and frequency, consequently increasing or decreasing the response amplitude.

3.6.1 Effect of damping

For a LPE system (for example Eq. (3.2)), corresponding to every instability region, there exists a threshold $\delta = \delta_{th}$, which must be exceeded before instability can occur (see Fig. 3.10). For a NPE system (for example Eq. (3.27)), there is a threshold before the steady-state response happens. As explained in previous section, the steady-state response can be stable or unstable.

For the LPE system, the analytical solutions show there is a threshold for instability at twice the natural frequency. When $\Omega = 2\omega_n$, the instability threshold δ_{th2} can be found by substituting $\Omega = 2\omega_n$ into Eq. (3.24)

$$\varepsilon\delta = \varepsilon\delta_{\mathrm{th2}} = 4\varepsilon\zeta, \tag{3.33}$$

$$\delta_{\mathrm{th2}} = 4\zeta, \tag{3.34}$$

which shows that the value of normalised parametric stiffness, which makes the system unstable, is a function of damping ratio. Fig. 3.10 shows the transition curves for two cases when $\varepsilon\zeta = 0.0316$ and 0.0031.

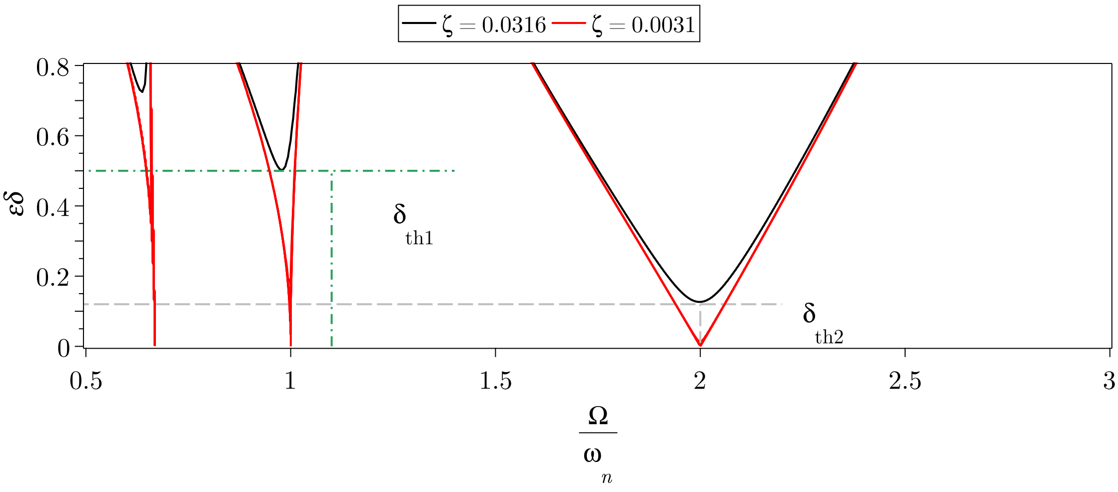

Fig. 3.10. Stability chart of Eq. (3.2). Damping ratios $\varepsilon\zeta = 0.0316$ and $\varepsilon\zeta = 0.0031$ are considered. $\omega_n = 31.62\mathrm{rad\,s^{-1}}$.

For the NPE system, the instability threshold δ_{th2} can be obtained by substituting $\Omega = 2\omega_n$ into Eq. (3.31). The $\delta_{\text{th2}} = 4\zeta$ is found, hence by increasing the damping in the system, NPE transition curve is shifted up. The instability threshold at other frequencies, for example δ_{th1} can be found by substituting $\Omega = \omega_n$ into the equation for the transition curve at that frequency obtained from Appendix C.1.2.

3.6.2 Effect of cubic nonlinearity

The effect of cubic nonlinearity for the NPE transition curve is discussed here. The effect of cubic parametric nonlinearity γ is not considered in this section. Transition curves as a result of cubic nonlinearity α in Eq. (3.27) shift to the right or left. This shift is because of the change in the natural frequency of the NPE system. The natural frequency of the linearised NPE system ω_{N} (as opposed to the natural frequency of the LPE system, ω_{n}) is derived from Eq. (C.34) as follows

$$\omega_{\text{N}} = \sqrt{\frac{(1+\frac{3}{4}\varepsilon k_3 a^2)k_1}{m_{\text{t}}}}. \tag{3.35}$$

For the normalised Eq. (3.27), $\alpha = \frac{k_3}{k_1}$, hence

$$\omega_{\text{N}} = \omega_n \sqrt{1 + \frac{3}{4}\varepsilon\alpha a^2}. \tag{3.36}$$

The change in the nonlinear natural frequency can be seen in the transition curve for the NPE system. Fig. 3.11 shows the transition curves for three cases when $\varepsilon\alpha = 150\text{m}^{-2}$, $\varepsilon\alpha = -150\text{m}^{-2}$ and $\varepsilon\alpha = 0$. The transition curves for both the LPE and NPE systems are presented in Fig. 3.11. The positive cubic nonlinearity has shifted the transition curve to the right (Fig. 3.11b). The transition curve is shifted to the left as a result of negative cubic nonlinearity (Fig. 3.11a). The frequency shift $\frac{2|\omega_N - \omega_n|}{\omega_n}$ is shown in Fig. 3.11 and is calculated from Eq. (3.36).

From Fig. 3.11 for the NPE system at $\Omega = 2\omega_N$, the instability threshold is same as the LPE systems threshold at $\Omega = 2\omega_n$. Substituting Eq. (3.36) into Eq. (3.32) or Eq. (3.31) when $\Omega = 2\omega_{\text{N}}$ yields the same instability threshold found in Eq. (3.34).
The instability thresholds for the LPE and NPE systems are shown in Fig. 3.11.

3.6.3 Effect of cubic parametric nonlinearity

When the only nonlinearity in the NPE system, Eq. (3.27), is the cubic parametric nonlinearity ($\varepsilon\alpha = 0$ and $\varepsilon\gamma \neq 0$), the transition curve at twice the natural frequency shifts up and down. These shifts depend on the sign of the cubic parametric nonlinearity. Shifting down is caused by an increase in the parametric amplitude when the cubic parametric nonlinearity is positive. This reduces the instability threshold. Negative cubic paramet-

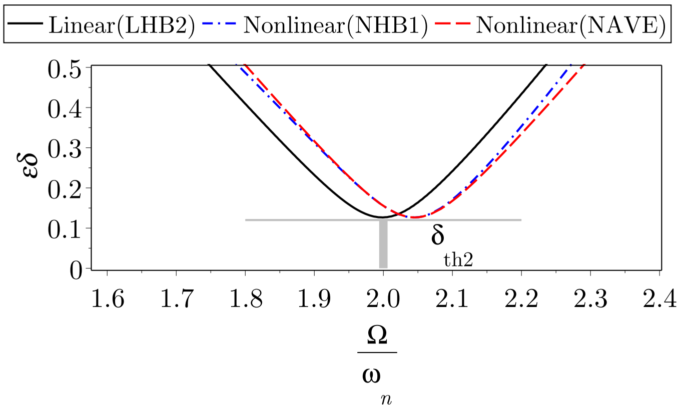

(a)

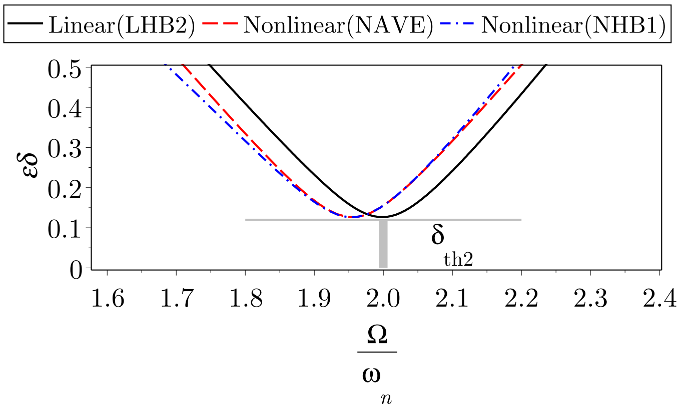

(b)

Fig. 3.11. Effects of varying the cubic stiffness nonlinearity on transition curve for the NPE system (Eq. (3.27)). (a) $\varepsilon\alpha = 150\text{m}^{-2}$, $\omega_N = 1.022\omega_n$, and $\delta_{\text{th2}} = 0.126$. (b) $\varepsilon\alpha = -150\text{m}^{-2}$, $\omega_N = 0.969\omega_n$, and $\delta_{\text{th2}} = 0.126$. Transition curve plots for a linear system when $\varepsilon\zeta = 0.0316$, $\omega_n = 31.62\text{rad}\,\text{s}^{-1}$, $\varepsilon\alpha = \varepsilon\gamma = 0$ with harmonic balance method with higher orders (LHB2) is shown as a reference (black lines). For the NPE system $a = 0.02\text{m}$, $\varepsilon\zeta = 0.0316$, $\omega_n = 31.62\text{rad}\,\text{s}^{-1}$ and $\varepsilon\gamma = 0$. The transition curves are found using the harmonic balance method with one order (NHB1) and the nonlinear averaging method (NAVE).

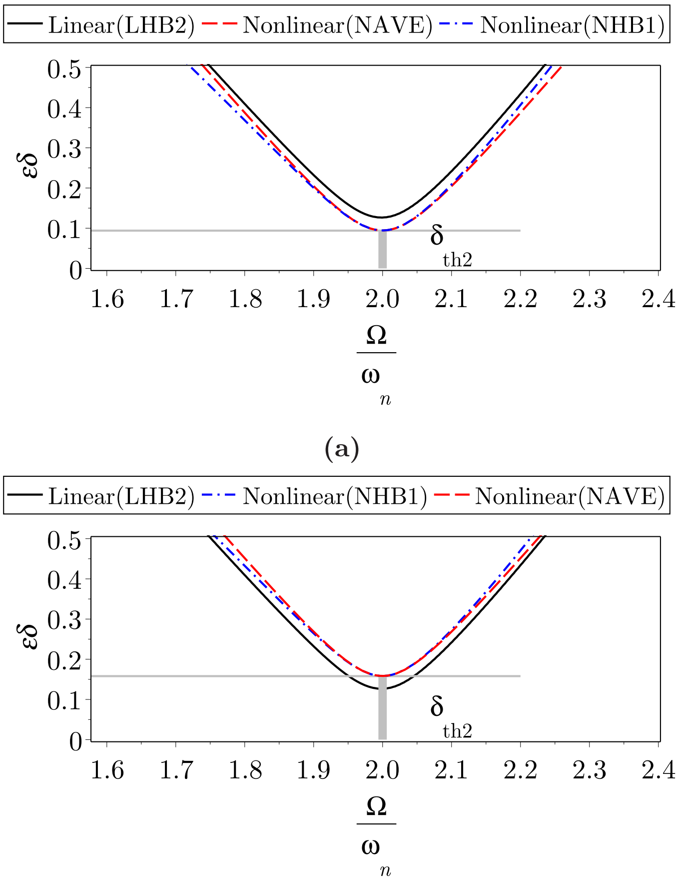

(a)

(b)

Fig. 3.12. Effects of varying the cubic parametric nonlinearity on transition curve for the NPE system (Eq. (3.27)). (a) $\delta_{\text{th2}} = 0.094$, when $\varepsilon\zeta = 0.0316$, $\omega_n = 31.62\text{rad}\,\text{s}^{-1}$, $\varepsilon\alpha = 0$, and $\varepsilon\gamma = 80\text{m}^{-2}$ are chosen. (b) $\delta_{\text{th2}} = 0.158$, when $\varepsilon\zeta = 0.0316$, $\omega_n = 31.62\text{rad}\,\text{s}^{-1}$, $\varepsilon\alpha = 0$, and $\varepsilon\gamma = -80\text{m}^{-2}$. Transition curve plots for a linear system $\varepsilon\zeta = 0.0316$, $\omega_n = 31.62\text{rad}\,\text{s}^{-1}$ with harmonic balance method with higher orders (LHB2) is shown as a reference (black lines). For a NPE system with the amplitude of $a = 0.02\text{m}$ the transition curve is found using the method of harmonic balance with one order (NHB1) and the nonlinear averaging method (NAVE).

ric nonlinearity decreases the effect of parametric amplitude, increasing the instability threshold.

The natural frequency of the linearised NPE system ω_{N} is found from Eq. (C.34) as [9]

$$\omega_{\mathrm{N}} = \sqrt{\frac{(1 + \frac{1}{2}\varepsilon k_{\mathrm{p3}} a^2) k_1}{m_{\mathrm{t}}}}. \tag{3.37}$$

For the normalised Eq. (3.27), $\gamma = \frac{k_{\mathrm{p3}}}{k_1}$, hence

$$\omega_{\mathrm{N}} = \omega_n \sqrt{1 + \frac{1}{2}\varepsilon\gamma a^2}. \tag{3.38}$$

This natural frequency is very close to the natural frequency of the linear system when the amplitude is small. So the natural frequency of the nonlinear systems is considered close to the natural frequency of the linear system (when $\Omega = 2\omega_{\mathrm{N}} \approx 2\omega_{\mathrm{n}}$). Substituting $\Omega = 2\omega_{\mathrm{N}} \approx 2\omega_{\mathrm{n}}$ into Eq. (3.32) or Eq. (3.31), yields the instability threshold as

$$\varepsilon\delta = \varepsilon\delta_{\mathrm{th2}} = -\varepsilon\gamma a^2 + 4\varepsilon\zeta, \tag{3.39}$$

$$\delta_{\mathrm{th2}} = -\gamma a^2 + 4\zeta. \tag{3.40}$$

Fig. 3.12 shows the transition curves for the LPE and NPE system for three cases when $\varepsilon\gamma = 0$, $80\mathrm{m}^{-2}$ and $-80\mathrm{m}^{-2}$. The instability threshold for the LPE system's transition curve when $\varepsilon\gamma = 0$ is $\delta_{\mathrm{th2}} = 0.126$. However, this instability threshold is decreased to $\delta_{\mathrm{th2}} = 0.094$ when $\varepsilon\gamma = 80\mathrm{m}^{-2}$ (Fig. 3.12a) and increased to $\delta_{\mathrm{th2}} = 0.158$ when $\varepsilon\gamma = -80\mathrm{m}^{-2}$ (Fig. 3.12b).

When both cubic and cubic parametric nonlinearities are considered in Eq. (3.27), the natural frequency of the nonlinear system, based on the linearisation of Eq. (3.27) with harmonic balance (Appendix C.34) is

$$\omega_{\mathrm{N}} = \sqrt{\frac{k_1 + \frac{3}{4}\varepsilon k_3 a^2 + \frac{1}{2}\varepsilon k_{\mathrm{p3}} a^2}{m_{\mathrm{t}}}}. \tag{3.41}$$

For the normalised Eq. (3.27), $\alpha = \frac{k_3}{k_1}$ and $\gamma = \frac{k_{\mathrm{p3}}}{k_1}$, hence

$$\omega_{\mathrm{N}} = \omega_n \sqrt{1 + \frac{3}{4}\varepsilon\alpha a^2 + \frac{1}{2}\varepsilon\gamma a^2}. \tag{3.42}$$

When the cubic parametric nonlinearity is small and $\alpha \gg \gamma$, Eq. (3.42) is simplified to

$$\omega_{\mathrm{N}} \approx \omega_n \sqrt{1 + \frac{3}{4}\varepsilon\alpha a^2}. \tag{3.43}$$

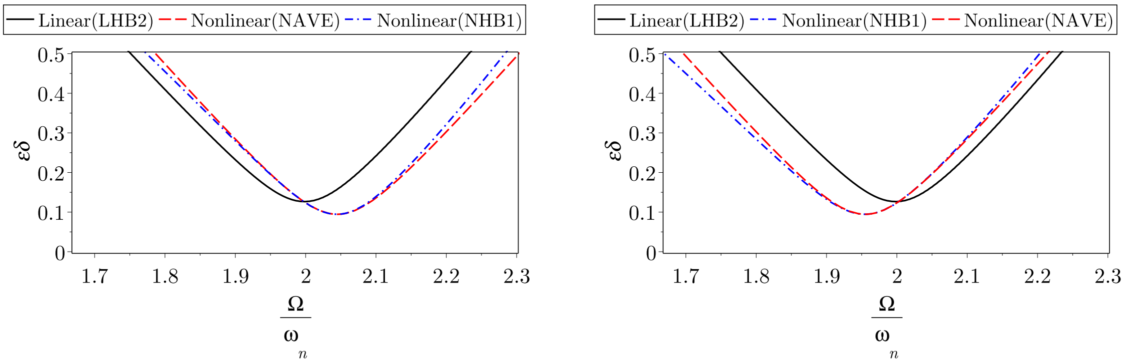

(a) $\varepsilon\alpha = 150\text{m}^{-2}$ and $\varepsilon\gamma = 80\text{m}^{-2}$.

(b) $\varepsilon\alpha = -150\text{m}^{-2}$ and $\varepsilon\gamma = 80\text{m}^{-2}$.

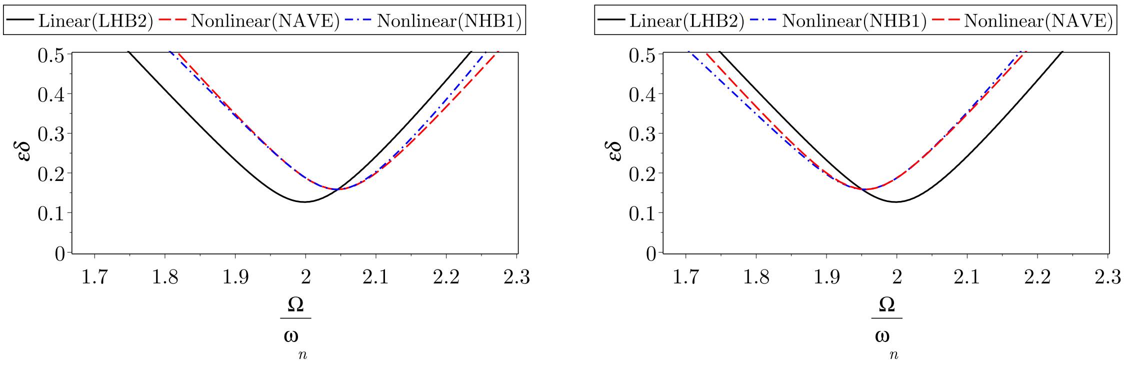

(c) $\varepsilon\alpha = 150\text{m}^{-2}$ and $\varepsilon\gamma = -80\text{m}^{-2}$.

(d) $\varepsilon\alpha = -150\text{m}^{-2}$ and $\varepsilon\gamma = -80\text{m}^{-2}$.

Fig. 3.13. Effects of varying the cubic stiffness and cubic parametric stiffness on transition curve for the NPE system (Eq. (3.27)). $\varepsilon\alpha$ and $\varepsilon\gamma$ have been changed in the different plots to show their effect on shifting the transition curve. The transition curve plots for a linear system with $\varepsilon\zeta = 0.0316$, $\omega_n = 31.62\text{rad}\,\text{s}^{-1}$ were plotted using the harmonic balance method with higher orders (LHB2) as a reference. For a nonlinear system with the amplitude of $a = 0.02$m using the harmonic balance method with one order (NHB1) and the nonlinear averaging method (NAVE).

Substituting $\Omega = \omega_n$ into Eq. (3.32) or Eq. (3.31), yields the instability threshold as

$$\delta_{\text{th2}} = -\gamma a^2 + 4\zeta. \tag{3.44}$$

Fig. 3.13 shows the transition curves for four cases when $\varepsilon\gamma = 80\text{m}^{-2}$, $\varepsilon\gamma = -80\text{m}^{-2}$, $\varepsilon\alpha = 150\text{m}^{-2}$, and -150m^{-2}. Fig. 3.13a and Fig. 3.13c present the effect of hardening cubic nonlinearity with positive and negative cubic parametric nonlinearity. Hence, the transition curves for the NPE systems are shifted both to the right and vertically compared to the transition curve for the LPE system. The effect of softening nonlinearity, and positive and negative cubic parametric nonlinearity is shown in Figs. 3.13b and 3.13d. The shift of the transition curves for the nonlinear system to the right and vertically is also presented in comparison with the transition curve for the LPE system.

Amplitude-frequency plots for three given cubic parametric nonlinearities $\varepsilon\gamma = -80\text{m}^{-2}$, $\varepsilon\gamma = 0\text{m}^{-2}$ and $\varepsilon\gamma = 80\text{m}^{-2}$ when $\varepsilon\delta = 0.25$, $\varepsilon\zeta = 0.0316$, $\varepsilon = 1$ and $\varepsilon\alpha = 150\text{m}^{-2}$ are shown in Fig. 3.14. For a NPE system when the only nonlinearity is a cubic nonlinearity, two branches are expected from the analytical solutions as explained in this chapter (see Fig. 3.6). The upper branch is the stable branch and the lower branch is the unstable branch. When the system has a positive cubic parametric nonlinearity, for example $\varepsilon\gamma = 80\text{m}^{-2}$, the upper branch (the stable solutions) is higher than the system with no cubic parametric nonlinearity. This means the system response is also higher when $\varepsilon\gamma = 80\text{m}^{-2}$. Also with positive cubic nonlinearity ($\varepsilon\gamma = 80\text{m}^{-2}$), the stable and unstable branches do not meet at high frequency, which can be beneficial for expanding the frequency of the response. However, preventing the jump between the upper branch to the lower branches is important.

When the cubic parametric nonlinearity is negative the system response is lower as shown in Fig. 3.14. As mentioned before the negative cubic parametric nonlinearity shifts the transition curve up, so the region in which the system has three solutions becomes smaller than the system with positive cubic nonlinearity (see section 3.5).

The frequency bandwidth ($2w$) shown in Fig. 3.14 is the range of frequency in which the NPE system has only two solutions. The steady-state non-trivial stable solution and the unstable trivial solution. The frequency bandwidth w is the normalised frequency starting from the point where the system has a steady-state solution to the point where $\frac{\Omega}{\omega_n} = 2$. The bandwidth w can be calculated from Eq. (3.20)

$$w = 2\sqrt{-\varepsilon^2\zeta^2 + \frac{\varepsilon^2\delta^2}{16}}. \tag{3.45}$$

The frequency bandwidth ($2w$) can be increased by reducing damping or increasing the parametric amplitude. Altering this bandwidth is beneficial for applications where increasing the response amplitude over wide range of frequency is desirable. For designing

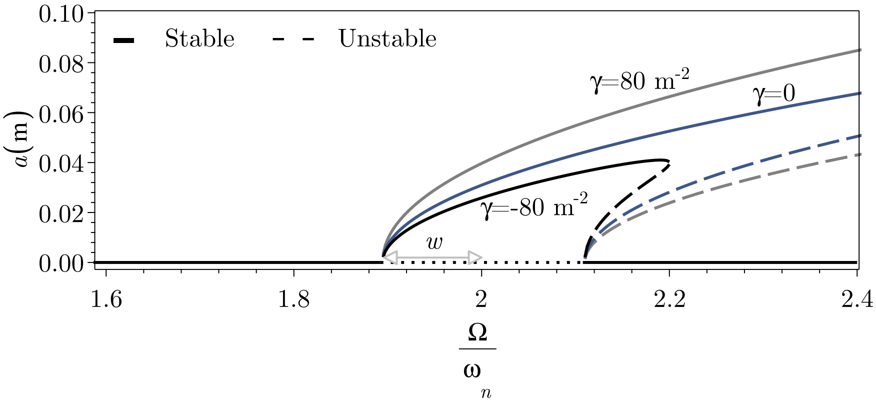

Fig. 3.14. Analytical amplitude-frequency plot with the method of averaging (NAVE) for the NPE system (Eq. (3.27)) when $\varepsilon\delta = 0.25$, $\varepsilon\zeta = 0.0316$, $\varepsilon\alpha = 150\text{m}^{-2}$ and the cubic parametric nonlinearities are $\varepsilon\gamma = -80\text{m}^{-2}$, 0 and 80m^{-2}.

vibration energy harvesters, amplifiers and filters, an increase of the parametric amplitude results in an amplitude increase. Expanding the frequency bandwidth can be done by introducing the cubic stiffness nonlinearity or by increasing the damping.

3.7 Concluding remarks

This chapter investigates the dynamics of PE systems for both linear and nonlinear models. The LPE model represents the behaviour of the systems with time-varying coefficients. The nonlinear model was constructed and solved with cubic and cubic parametric nonlinearity. The method of averaging was used to find the solutions to the linear and nonlinear systems. The stability of these systems were evaluated using the methods of averaging and harmonic balance. Stability for the LPE system with damping can be found using three criteria. If the response decays the solution is stable, otherwise it is unstable. Also, there is a transition between the stable and unstable solutions. The stability of the solutions on the transition curves is defined by their behaviour as time goes to infinity. The stability of the LPE system was defined based on the eigenvalues with the method of averaging, however this method is used for systems with small parametric amplitude. The comparison between the method of averaging and the method of harmonic balance with low and high number of terms was conducted and also verified with the numerical phase portrait for some points in stability chart plots. These comparisons verified the accuracy of the above methods with the numerical results. The method of harmonic balance was chosen for the stability analysis, since solutions with multiple frequencies can be determined by considering higher order terms.

The stability of the NPE system is defined differently from the stability of the LPE system. The NPE system can have multiple steady-state solutions; these solutions can be stable or unstable. The stability of the steady-state solutions were defined based on the eigenvalues of the linearised model. Mostly these nonlinear systems have been linearised for simplicity. The amplitude dependency of the solutions and the existence of multiple solutions differed from the transition curve for the linear system. The transition curves of the NPE system present the regions where non-trivial steady-state solutions exist, however they do not show regions where the unstable solutions can be found. The transition curves were plotted along with the amplitude-frequency plot. The amplitude-frequency relation shows the amplitude of the steady-state solution at different parametric frequencies for a given parametric amplitude. The transition curve was plotted for a given amplitude and could demonstrate the relation between the parametric amplitude and parametric frequency. For the nonlinear model, the method of averaging was used for its simplicity and accuracy. The analytical and numerical phase portraits were presented for four points in the stability chart, to show the response of the system in vicinity of the transition curve. The analytical methods of averaging and harmonic balance were introduced in the literature, however the analytical derivation for the NPE system with cubic parametric nonlinearity was developed in this chapter and is the novel contribution of this work.

Chapter 4

Dynamic response of a nonlinear parametrically excited system subject to harmonic base excitations

4.1 Introduction

A real example of a base excited system is where the cable is moving due to the vibration of the deck in a cable-stayed bridge. Parametrically excited oscillators have been introduced recently to amplify [1], suppress [13] and control [66] the response amplitude. For example, Nonlinear Parametrically Excited (NPE) oscillators have been used to design low-noise signal amplifiers. Rhoads et al. [58] demonstrated the potential of parametric amplification in a macro-scale mechanical amplifier. They used a cantilever beam under longitudinal and transverse base excitation as an example of a parametric amplifier. They found parametric amplification achieved a gain increase of a factor between 1.4 and 1.6 in practice. Gain is defined as the ratio between the amplitude of response without parametric excitation and when parametric amplification is applied [58, 87]. Careful selection of phase can also reduce the response, which can be used in vibration absorbers. Parametric amplification in the model presented by Rhoads et al. [58] occurred as a result of exciting the cantilever beam at twice its natural frequency at an angle with its motion in the vertical direction. This model only could be used to check the effect of parametric amplification on the gain. However, the nonlinearities in the system could not be controlled, and their effects were not examined separately.

Rhoads et al. [87] have shown analytical results on the effect of hardening nonlinearity on a classical degenerate parametric amplifier (where the parametric frequency is locked at twice the frequency of the direct excitation). They evaluated the change in the gain of the amplifier due to the effect of hardening nonlinearity for different parametric amplitudes and phases between the direct excitation and parametric excitation. They also demonstrated that the phase difference between the base excitation and the parametric excitation that maximise the response amplitude is $\frac{3\pi}{4}$ for the LPE system and close to $\frac{\pi}{2}$ for the NPE system with cubic nonlinearity. The gain was found only under the linear instability threshold and at parametric resonance. A similar LPE system is considered in this chapter, however the effect of phase is investigated over and under the linear instability threshold, at parametric resonance and at other frequencies. Furthermore, the effect of phase on upper and lower stable branches is investigated for the NPE system. Rhoads et al [87] only considered the effect of phase difference on the upper stable branch at parametric resonance.

In this chapter, the dynamic response of a NPE system subject to harmonic base excitations is studied. The degenerate NPE system is considered for the purpose of parametric amplification. The degenerate NPE system is tuned at twice the natural frequency of that system. The effect of parametric amplitude and parametric nonlinearities on the steady-state response is investigated analytically and numerically. In Section 4.2 analytical solutions and stability of the NPE system is obtained with the method of averaging. Several numerical simulations are carried out to present the behaviour of the NPE system subject to base excitation. The effects of parametric excitation for linear and nonlinear base excited systems is studied in Section 4.4. Several cases are considered to show the effect of parametric amplification, cubic stiffness nonlinearity and cubic parametric nonlinearity on the response. The influence of the phase difference between the base excitation and the parametric excitation is investigated for the linear and nonlinear parametrically excited system and is presented in Section 4.5. This chapter is concluded with a short summary. The novel contributions of this chapter are as follows:

- The responses and the stability of a NPE system subject to harmonic base excitations is presented analytically with the method of averaging. The stability of the response is determined from Jacobian eigenvalues.
- The maximum response amplitude for the LPE system with large damping is shown to occur when the parametric frequency is twice the base excitation frequency.
- The phase difference for each stable and unstable branches of solutions are examined. It is found that the phase difference variation is found to affect the response amplitude.

4.2 Methodology

A SDOF system with harmonic base excitation is considered. The base excitation is in the form of translation in the transverse direction. Rotational motion is neglected in this study. The SDOF system represents the clamped-free cantilever beam used for the experiments.

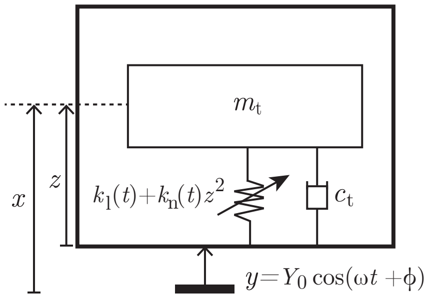

Fig. 4.1. A SDOF system with time-varying and nonlinear stiffness under harmonic base excitation.

The governing differential equation of motion for the SDOF system is

$$m_t\ddot{x} + c_t(\dot{x} - \dot{y}) + k_l(t)(x - y) + k_n(t)(x - y)^3 = 0, \tag{4.1}$$

where x is the displacement of moving mass m_t, y is the base excitation, c_t is the total damping coefficient, and $k_l(t)$ and $k_n(t)$ are the linear and nonlinear stiffness respectively. The linear stiffness is the combination of the static stiffness k_1 and the time varying stiffness k_{p1} such that

$$k_l(t) = k_1 + k_{p1}\cos(\Omega t). \tag{4.2}$$

The nonlinear stiffness consists of the cubic stiffness k_3 and the cubic parametric stiffness k_{p3} such that

$$k_n(t) = k_3 + k_{p3}\cos(\Omega t). \tag{4.3}$$

The parametric stiffness $k_{p1}\cos(\Omega t)$ and cubic parametric stiffness $k_{p3}\cos(\Omega t)$ are changing periodically in time with parametric frequency Ω. Substituting Eq. (4.2) and Eq. (4.3) into Eq. (4.1) results in

$$m_t\ddot{x}+c_t(\dot{x}-\dot{y})+k_1(x-y)+k_{p1}\cos(\Omega t)(x-y)+k_3(x-y)^3+k_{p3}\cos(\Omega t)(x-y)^3 = 0, \tag{4.4}$$

where m_t, c_t, and k_1 are the physical parameters. Rearranging Eq. (4.4) in terms of the relative displacement of the mass $z = x - y$ yields

$$m_t\ddot{z} + c_t\dot{z} + k_1 z + k_{p1}\cos(\Omega t)z + k_3 z^3 + k_{p3}\cos(\Omega t)z^3 = -m_t\ddot{y}. \tag{4.5}$$

The base excitation is $y = Y_0\cos(\omega t + \phi)$. Y_0 is the amplitude of harmonic base displacement at frequency ω and phase ϕ. Eq. (4.5) is rearranged so that

$$m_{\mathrm{t}}\ddot{z}+c_{\mathrm{t}}\dot{z}+k_1 z+k_{\mathrm{p}1}\cos(\Omega t)z+k_3 z^3+k_{\mathrm{p}3}\cos(\Omega t)z^3=m_{\mathrm{t}}\omega^2 Y_0\cos(\omega t+\phi). \tag{4.6}$$

Eq. (4.6) is normalised by the mass m_{t} resulting in

$$\ddot{z}+2\varepsilon\omega_n\zeta\dot{z}+\omega_n^2\left(1+\varepsilon\delta\cos(\Omega t)\right)z+\omega_n^2\left(\varepsilon\alpha+\varepsilon\gamma\cos(\Omega t)\right)z^3=\frac{1}{4}\Omega^2 Y_0\cos\left(\frac{\Omega}{2}t+\phi\right), \tag{4.7}$$

where $\omega_n=\sqrt{\frac{k_1}{m_{\mathrm{t}}}}$ is the linear resonance frequency, and ζ is the damping ratio. The normalised parametric amplitude $\delta=\frac{k_{\mathrm{p}1}}{k_1}$, the normalised cubic stiffness nonlinearity $\alpha=\frac{k_3}{k_1}$, the normalised cubic parametric nonlinearity $\gamma=\frac{k_{\mathrm{p}3}}{k_1}$, and ϕ is the phase between the parametric stiffness and base excitation. ε is the small parameter for keeping the system parameters small to solve Eq. (4.7) with the method of averaging. When $\varepsilon=1$, the magnitude of the system parameters is small compared to the linear term and hence the method of averaging can be applied to solve Eq. (4.7).

Based on the method of averaging the periodic solutions of Eq. (4.7) at resonance for the degenerate parametric amplifier are given by

$$z(t)=a\cos\left(\frac{\Omega}{2}t-\varphi\right), \tag{4.8}$$

where the amplitude a and the phase φ of the steady-state solutions are

$$a=\frac{\Omega^2 Y_0\sqrt{\left(-p_1\sin(2\phi)+\zeta\right)^2+\left(p_2-p_3\cos(2\phi)\right)^2}}{8\omega_n^2\left(p_1^2(1-\cos(2\phi)^2)+p_3^2\cos(2\phi)^2-p_2^2-\zeta^2\right)},\ \text{and} \tag{4.9}$$

$$\varphi=\frac{1}{2}\arctan\left(\frac{p_3\left(\zeta-\frac{1}{2a}Y_0\sin(\varphi+\phi)\right)}{p_1\left(p_2-\frac{1}{2a}Y_0\cos(\varphi+\phi)\right)}\right). \tag{4.10}$$

These quantities are derived in Appendix D. In Eq. (4.9) and Eq. (4.10), a represents the steady-state amplitude of non-trivial solutions, $p_1=\frac{1}{4}\left(\delta+\frac{1}{2}\gamma a^2\right)$, $p_2=\frac{3}{8}\alpha a^2-\frac{\Omega}{2\omega_n}+1$, and $p_3=\frac{1}{4}\left(\delta+\gamma a^2\right)$. Eq. (4.7) has at least five stable and unstable non-trivial solutions when the system parameters are non-zero (δ, α, $\gamma\neq 0$).

4.3 Varying base excitation frequency and parametric excitation frequency for the LPE system

The dependency of the response amplitude with base excitation frequency and parametric frequency is investigated for the LPE system. The steady-state amplitude is found for different base excitation and parametric excitation frequencies. The maximum response amplitude a is found from the harmonic balance method. The harmonic balance method

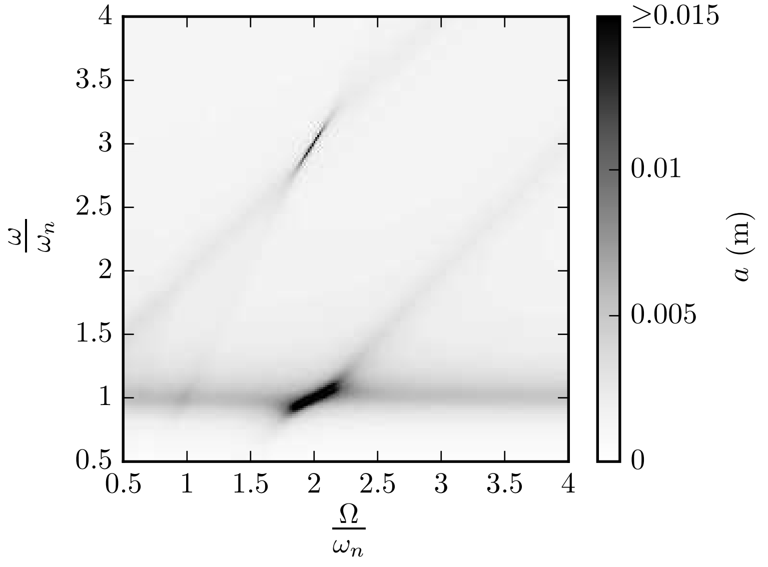

Fig. 4.2. Maximum steady-state response amplitude a at different frequencies. $\delta = 0.4$, $\zeta = 0.1$, and $Y_0 = 0.001$m.

is used because of the simplicity with which it finds the response of the LPE system at different excitation frequencies.

For the LPE system, when k_3 and $k_{\mathrm{p}3} = 0$, Eq. (4.6) simplifies to

$$m_{\mathrm{t}}\ddot{z} + c_{\mathrm{t}}\dot{z} + k_1 z + k_{\mathrm{p}1}\cos(\Omega t)z = m_{\mathrm{t}}\omega^2 Y_0 \cos(\omega t + \phi). \tag{4.11}$$

By assuming that the response to a sinusoidal excitation is a sinusoid at the same frequency [9], the solution is

$$\begin{aligned} z(t) = A_0\cos(\omega t) + B_0\sin(\omega t) + \sum_{m=1}^{M} A_m\cos((\omega + m\Omega)t) + B_m\cos((\omega - m\Omega)t) \\ + C_m\sin((\omega + m\Omega)t) + D_m\sin((\omega - m\Omega)t). \end{aligned} \tag{4.12}$$

When $\omega = \omega_n$, the LPE system does not only respond at the resonance frequency ω_n, but also at its combined resonances $\omega_n \pm N\Omega, N \in \mathbb{Z}$. Hence, for the trial solution other harmonics are considered. By substituting Eq. (4.12) into Eq. (4.11), the Fourier series coefficients A_m, and B_m can be found. The coefficients of sine and cosine of all harmonics are partitioned. For example, the number of terms $M = 6$ can be considered to account for the combined harmonics up to $\omega + 6\Omega$. The steady-state response of the LPE system with the harmonic balance method is derived in Appendix C.

Fig. 4.2 shows that there are areas in which the LPE system has higher steady-state amplitude:

- At $\Omega = 2\omega$ and $\Omega = \frac{2\omega}{3}$ close to parametric resonance $\Omega \approx 2\omega_n$, where the parametric frequency Ω varies with the excitation frequency ω.

- At $\Omega = 2\omega_n$ when the parametric frequency matches with twice the resonance frequency, the system response is amplified. When $\omega = \omega_n$ the LPE system has higher amplitude.

For the studies carried out in this chapter, the parametric frequency is considered to be twice the base excitation frequency, which results in maximum amplification. Dependency of the response amplitude on frequency detuning for the NPE system has been demonstrated by Neumeyer et al. [138]. They investigated the effect of frequency detuning of parametric and direct excitation on near resonant nonlinear systems. They showed frequency detuning can increase the steady-state response in some frequency ranges. This work is relevant to studies where frequency detuning can be expected between the parametric and direct excitation, or between the parametric and direct excitation and the system's natural frequency during system operation. Also, as well as the parametric frequency tuning, the choice of stiffness nonlinearity and parametric amplitude is important in order to increase or decrease the response amplitude.

4.4 The effects of magnitude and frequency of parametric excitation

The effects of parametric excitation on linear and nonlinear base excited systems is studied here. Several cases are introduced in Table 4.1. A linear base excited system, case A, is shown as a reference. A LPE system, case B, shows the parametric amplification caused by the parametric excitation. A system with cubic stiffness nonlinearity is shown in case C. For case D parametric amplification under the instability threshold for a NPE system is considered in. For cases E, F, and G parametric amplification over the instability threshold is considered. Different phase differences ϕ are considered in each case. The effect of the phase difference is explained in Sections 4.5 and 4.6.

For each case the system response is found analytically and numerically. The analytical solutions are based on the method of averaging. The numerical integration is carried out by using the ODEINT function in SciPy [40]. The displacement and velocity initial conditions, $z_0 = 0\text{m}$ and $\dot{z_0} = 0\text{ms}^{-1}$ are used for all cases. For cases C to G the parametric frequency Ω and the base excitation frequency $\omega = \frac{\Omega}{2}$ are stepped up and down gradually. The frequency spacing is kept constant equal to $0.05\omega_n$. For each sweep test the previous steady-state amplitude is chosen for the initial condition of the next point. The simulation is run for sufficient time to ensure that the steady-state response is reached. The sufficient time is calculated based on the peak amplitude difference in each cycle.

The transition curve for each case is obtained along with the amplitude-frequency curve (in Fig. 4.3). The effect of positive and negative cubic parametric nonlinearity for a system with hardening nonlinearity is investigated in cases E and F.

4.4.1 Case A: A linear system

For case A a linear SDOF is considered, hence $\delta = \alpha = \gamma = \phi = 0$ are substituted into Eq. (4.7). Parameters for case A are defined in Table 4.1. In this case the maximum amplitude is expected when base excitation frequency is equal to the natural frequency ω_n. The response amplitude can be found from Eq. (4.9) when $\delta = \alpha = \gamma = \phi = 0$. The response phase φ in Eq. (4.8) is

$$\varphi = \arctan\left(\frac{\zeta}{1-\frac{\Omega}{2\omega_n}}\right). \tag{4.13}$$

The response phase is $\varphi = \frac{\pi}{2}$ at resonance. Figure 4.4a shows the amplitude frequency plot. Figure 4.4b shows the phase of the response φ, at a different base excitation frequency $\frac{\Omega}{2}$, normalised by the natural frequency ω_n.

4.4.2 Case B: A LPE system

For case B a linear parametrically excited system is considered. Parameters for case B (the LPE system) are defined in Table 4.1. For this case, the steady-state amplitude of non-trivial solutions of the LPE system from Eq. (4.9) are simplified to:

$$a = \frac{\Omega^2 Y_0 \sqrt{\left(-\frac{1}{4}\delta\sin(2\phi)+\zeta\right)^2 + \left(1-\frac{\Omega}{2\omega_n}-\frac{1}{4}\delta\cos(2\phi)\right)^2}}{\omega_n^2\left(2\frac{\Omega^2}{{\omega_n}^2}-\frac{1}{2}\delta^2+8\zeta^2-8\frac{\Omega}{\omega_n}+8\right)}, \tag{4.14}$$

and the phase (φ) of the steady-state solutions is

$$\varphi = \arctan\left(\frac{\zeta}{1-\frac{\Omega}{2\omega_n}}\right) - \phi. \tag{4.15}$$

The steady-state solutions and the response phase are only found in the vicinity of parametric resonance outside the tongue in the transition curve (see e.g. Fig. 4.3).

The transition curves define the regions where the amplitude of the response is increased as a result of parametric excitation (inside the tongues) without the base excitation effect ($Y_0 = 0$). When parametric amplification exists in linear systems, exponentially growing responses are expected inside the tongues [18]. Note that the denominator of Eq. (4.14) is zero when $\frac{\Omega}{\omega_n} = 2 \pm \frac{1}{2}\sqrt{\delta^2 - 16\zeta^2}$. Hence, unbounded solutions exist when

$$2 - \frac{1}{2}\sqrt{\delta^2-16\zeta^2} < \frac{\Omega}{\omega_n} < 2 + \frac{1}{2}\sqrt{\delta^2-16\zeta^2}, \tag{4.16}$$

Table 4.1: Linear and nonlinear system parameters are presented. The small parameter ε is equal to 1.

	δ	α (m^{-2})	γ (m^{-2})	ζ	Y_0 (m)	ϕ (rad)
Case A: Linear system	0	0	0	0.001	0.001	0
Case B: LPE system	0.1	0	0	0.001	0.001	0
Case C: Nonlinear system	0	1000	0	0.001	0.001	0
Case D: NPE system	0.001	1000	0	0.001	0.001	$\frac{\pi}{2}$
Case E: NPE system	0.1	1000	0	0.001	0.001	$\frac{\pi}{2}$
Case F: NPE system	0.1	1000	300	0.001	0.001	$\frac{\pi}{2}$
Case G: NPE system	0.1	1000	-300	0.001	0.001	$\frac{\pi}{2}$

which is the region inside the transition curve, and shows the width of the tongue at specific parametric amplitude δ. The width of the tongue is also affected by damping. Increasing the damping ratio ζ reduces the width of the tongue.

The amplitude frequency relation plot is presented analytically and numerically in Fig. 4.4c. Figure 4.4c shows that the steady-state amplitude increases close to parametric resonance, and the exponentially growing solutions are calculated numerically for $1.95 < \frac{\Omega}{\omega_n} < 2.05$. In Fig. 4.3 the region inside the instability tongue can be found for $\delta = 0.1$. This region is between $1.95 < \frac{\Omega}{\omega_n} < 2.05$, which matches with the unbounded solutions in Fig. 4.4c.

For case B the phase difference between the base excitation and the parametric excitation ϕ is set equal to 0. This relative phase can change the response amplitude before and after parametric resonance for the LPE system. For example, when the phase difference $\phi = 0$, the response amplitude at frequencies greater than the parametric resonance is higher than the response amplitude at frequencies lower than the parametric resonance. In Fig. 4.4c the response amplitude at frequencies greater than $\frac{\Omega}{\omega_n} = 2$ is higher than the response amplitude at frequencies lower than $\frac{\Omega}{\omega_n} = 2$.

The response phase φ at frequencies lower and higher than the parametric resonance are shown at 0 and π rad. The response phase φ is shown analytically and numerically for the region where steady-state solutions are found (see Fig. 4.4d). The response phase is not calculated for the unstable region $1.95 < \frac{\Omega}{\omega_n} < 2.05$.

4.4.3 Case C: A nonlinear system with positive cubic stiffness nonlinearity

A harmonically excited Duffing oscillator has been studied in the literature [139]. The effect of hardening ($\alpha > 0$) and softening ($\alpha < 0$) nonlinearities have also been studied [139]. Case C in Table 4.1 is a base excited Duffing oscillator when $\delta = \gamma = \phi = 0$ is substituted in Eq. (4.7). Figure 4.5c shows the frequency response plot for case C, where three branches of solutions are present. These solutions can be found from Eq. (4.9). Solid lines represent the stable branches, and dashed lines represent the unstable branches.

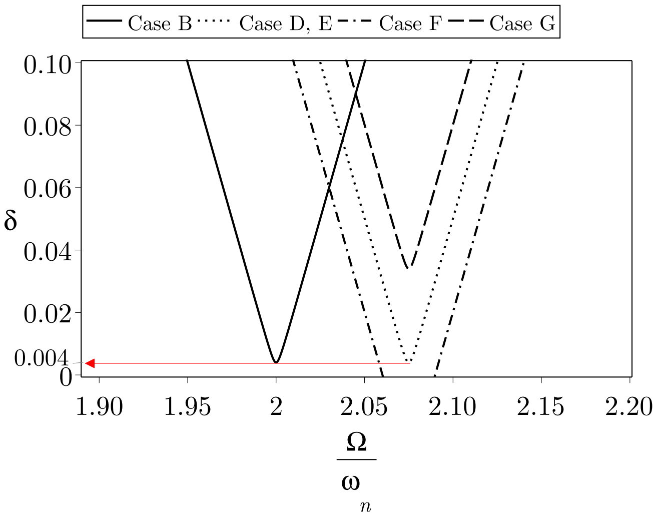

Fig. 4.3. Transition curve corresponding to case B, D, E, F, and G for a given parametric amplitude δ. Since the transition curves for NPE systems are dependent on the amplitude of the steady-state response, the amplitude $a = 0.01$m is kept constant. These cases are presented in Table 4.1.

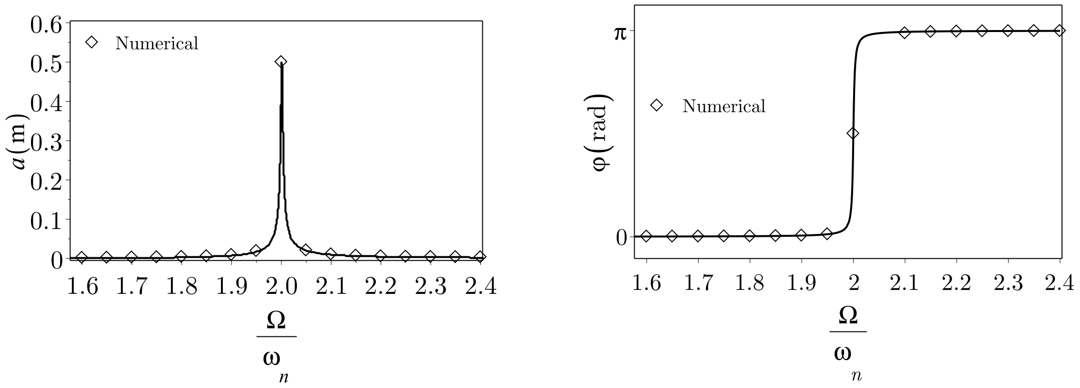

(a) Case A **(b)** Case A

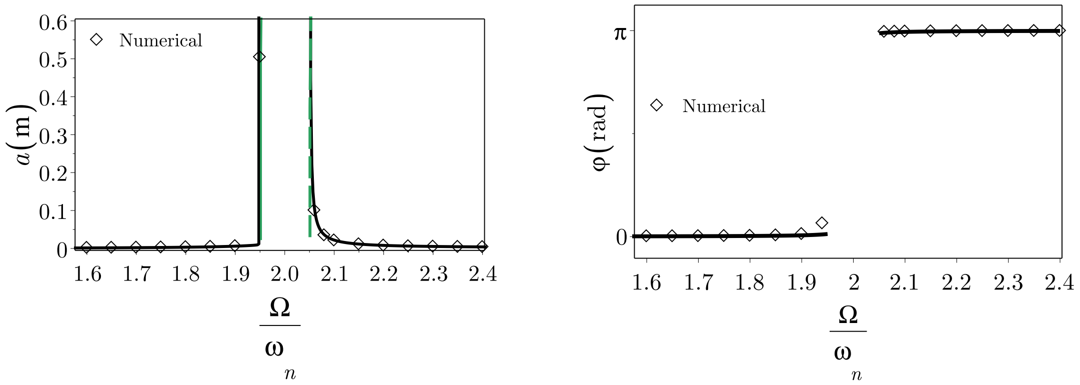

(c) Case B **(d)** Case B

Fig. 4.4. Amplitude a and phase φ of the system responses versus $\frac{\Omega}{\omega_n}$ for cases A and B in Table 4.1. These systems are solved analytically using the averaging method, and direct numerical integration. The analytical solutions are denoted by lines. The green line and dashed line represent solutions only affected by parametric excitation.

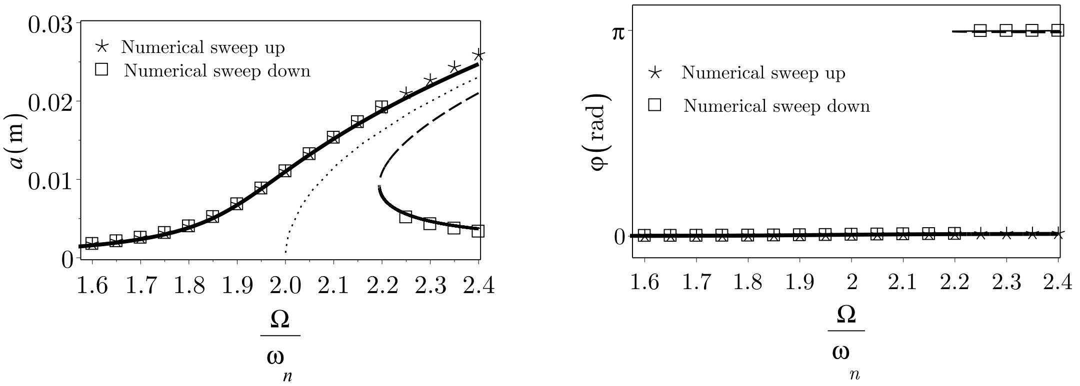

(a) Case C **(b)** Case C

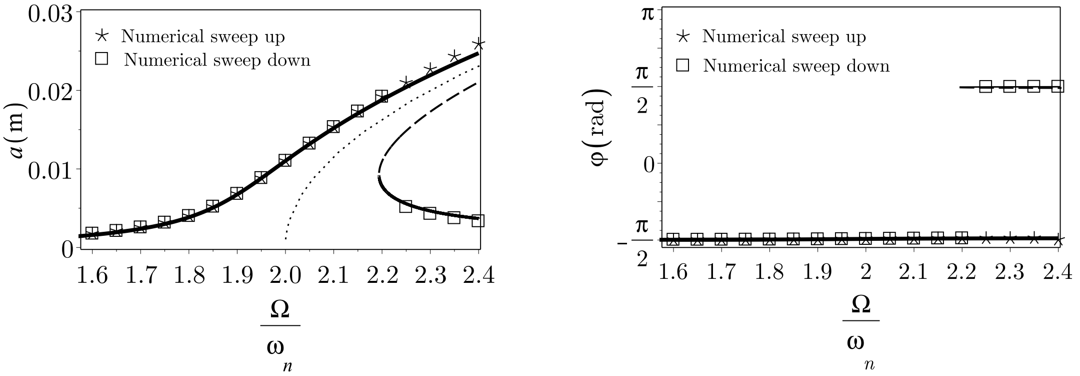

(c) Case D **(d)** Case D

Fig. 4.5. Amplitude a and phase φ of the system responses versus $\frac{\Omega}{\omega_n}$ for cases C and D in Table 4.1. These systems are solved analytically using the averaging method, and direct numerical integration. The analytical solutions are denoted by lines. Black lines represent solutions produced by base and parametric excitation. Solid lines denote stable branches, and dashed lines denote unstable branches. The dotted line in (a) and (c) is the *backbone curve*. The *backbone curve* is obtained from Eq. (D.18).

The phase-response curve for case C is shown in Fig. 4.5b. The variation of the phase with respect to the base excitation frequency normalised by the natural frequency is shown for each branch. The phase response for the upper stable branch is shown equal to 0. The phase response for the unstable branch and the lower stable branch is shown at π rad. In Fig. 4.5b the phase for the unstable and the stable branch is shown with dashed and solid black lines at π rad.

The phase-response curve is dependent on damping. For case C, damping is very small ($\zeta = 0.001$). Hence, the turning point from the stable upper branch to the unstable branch does not happen in the amplitude-frequency curve (see Fig. 4.5b). Consequently the phase-response curve shows that the stable upper branch and the unstable branch do not meet (see Fig. 4.5b). The effect of damping on the phase response for a forced Duffing oscillator with hardening nonlinearity is presented in [139]. For a forced Duffing oscillator with large damping, the turning point from the unstable branch to the upper stable branch is expected.

4.4.4 Case D: A NPE system with parametric amplitude under the instability threshold

Case D in Table 4.1 investigates the effect of adding parametric amplitude below its parametric instability ($\delta < 4\zeta$) with hardening nonlinearity. Since the parametric amplitude is below the instability threshold, the response amplitude is not amplified and in comparison with case C, the response amplitude is not varied. Figure 4.5c shows the frequency response plot for case D, where three branches of solutions are present from Eq. (4.9). For case D, only branches which are affected by base excitation and cubic nonlinearity are present.

The phase-response curve for case D is shown numerically and analytically in Fig. 4.5d. The phase response for the upper stable branch is shown equal to $-\frac{\pi}{2}$ rad. The phase response for the unstable branch and the lower stable branch is shown at $\frac{\pi}{2}$ rad. The phase for the unstable and the stable branch is shown with dashed and solid black lines at $\frac{\pi}{2}$ rad. The shift in phase compared to the case C results from the non-zero base excitation phase. For case D the relative phase ϕ is considered equal to $\frac{\pi}{2}$. When $\phi = \frac{\pi}{2}$ the upper stable branch has high amplitude and the lower stable branch has low amplitude. The effect of relative phase ϕ on the response amplitude is explained in Section 4.6.

The stability of stationary solutions is determined by Jacobian eigenvalues (see Appendix D.1). A solution a is unstable if at least one eigenvalue has a positive real part, otherwise it is stable. In Fig. 4.6a the region in which the eigenvalues are real and positive is shown in gray. A contour plot is used to fill the region where the solutions are unstable. The unstable solutions exist in this region, and are shown with dashed lines. Also, the Jacobian eigenvalues are determined for the NPE system with parametric amplitude under the instability threshold (see Appendix D.1). In Fig. 4.6b the region in which the

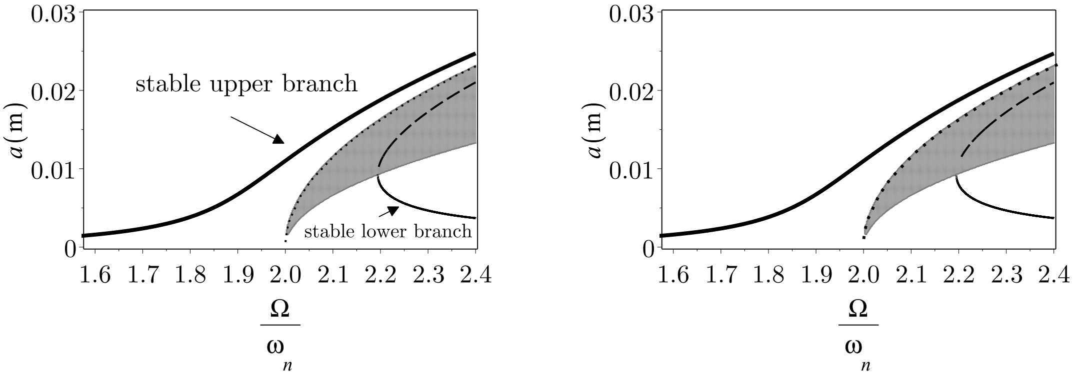

(a) Case C **(b)** Case D

Fig. 4.6. Amplitude frequency relation a versus $\frac{\Omega}{\omega_n}$ for cases C and D. The region in gray shows the unstable region where positive real eigenvalues are found. These systems are solved analytically using the averaging method. The analytical solutions are denoted by lines. Black lines represent solutions produced by base and parametric excitation. Solid lines denote stable branches, and dashed lines denote unstable branches. The dotted line is the *backbone curve*, obtained from Eq. (D.18).

eigenvalues are real and positive is shown by a gray area. The unstable solutions exist in this region and are shown with dashed lines.

4.4.5 Case E: A NPE system with parametric amplitude above the instability threshold

For case E the NPE system is driven near parametric resonance above the parametric instability, where $\delta > 4\zeta$ (see Table 4.1). Case E features five distinct response branches. The two additional branches present compared to cases D and C arise from the coexistence of two resonances within the nonlinear parametric system. One resonance is induced by a combination of base and parametric excitation, and the other is caused only by parametric excitation. In this chapter, we refer to stable and unstable branches caused only by parametric excitation as “additional branches”. In Fig. 4.7a, the additional branches are shown in green and the other branches are presented in black. In Fig. 4.7a the solid lines are the stable branches and the dashed lines are the unstable branches. The stability of the additional branches is found based on the eigenvalues when the base excitation amplitude is equal to zero. The stability of the additional branches is found in Appendix B.3. The two additional branches are comparable in amplitude and phase to the other stable/unstable branch pair. The stable/unstable branches are affected by parametric and base excitation amplitude and the phase between them. However, the additional branches only alter when the parametric amplitude is varied.

The NPE transition curves are independent of the base excitation amplitude and are dependent on the amplitude of the response. Figure 4.3 shows the transition curves for case E when a = 0.01m. The transition curves for the NPE systems define the regions

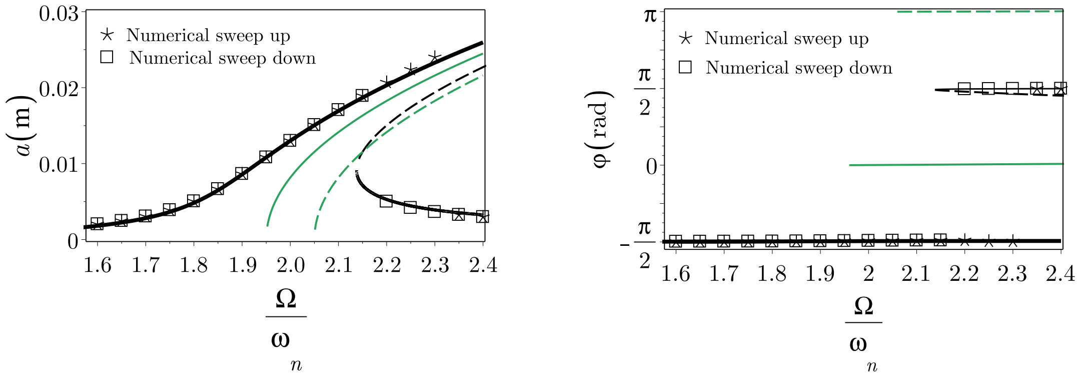

(a) Case E **(b)** Case E

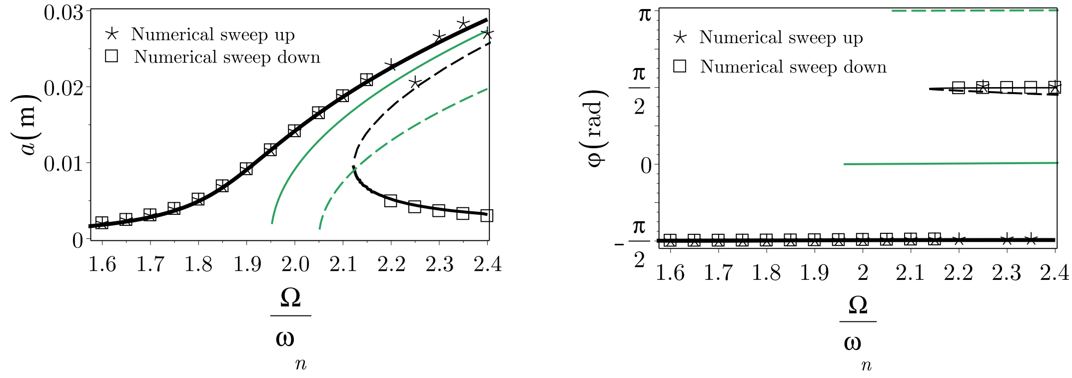

(c) Case F **(d)** Case F

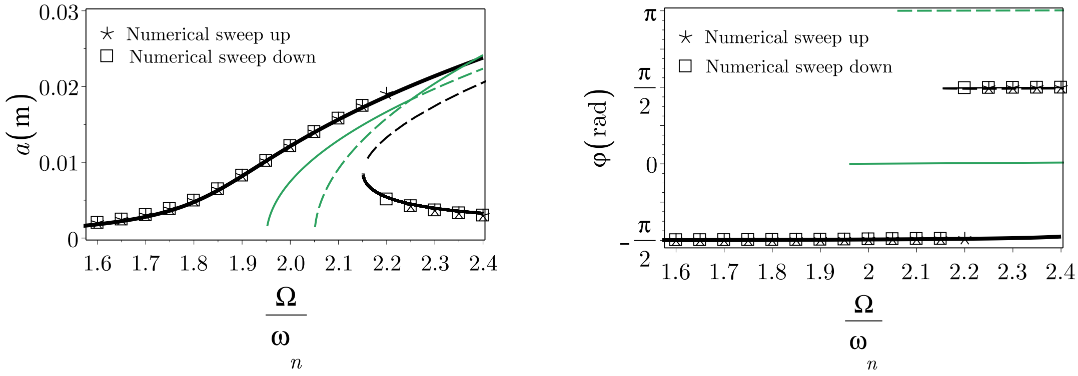

(e) Case G **(f)** Case G

Fig. 4.7. Amplitude a and phase φ of the systems responses versus $\frac{\Omega}{\omega_n}$ for cases E, F, and G in Table 4.1. These systems are solved analytically using the averaging method, and direct numerical integration. The analytical solutions are denoted by lines. Black lines represent solutions produced by base and parametric excitation, and the green lines represent solutions affected only by parametric excitation. Solid lines denote stable branches, and dashed lines denote unstable branches. Green lines denote additional branches.

where for a given amplitude of response, additional stable and unstable solution branches exist. The transition curves for the NPE system are also shifted to the right as a result of positive cubic nonlinearity.

4.4.6 Case F: A NPE system with positive cubic parametric nonlinearity

The effect of positive cubic parametric nonlinearity on a NPE system driven near parametric resonance above the parametric instability is considered (case F in Table 4.1). Cubic parametric nonlinearity increases the amplitude of the steady-state response. Both upper stable branches in Fig. 4.7c have been increased as a result of positive cubic parametric nonlinearity, compared to Fig. 4.7a when cubic parametric nonlinearity was equal to zero. Additional stable and unstable branches separate from each other at higher amplitude and frequency. Since the transition curve for a given system is expanded. Figure 4.3 shows the transition curve for case F when the response amplitude $a = 0.01$m. At $\delta = 0.1$ the transition curve for case F is larger than the transition curve for case E, which shows that the stable and unstable additional branches for case F have larger separation compared to the stable and unstable additional branches for case E. However, if negative cubic parametric nonlinearity is applied (case G), the amplitude of the steady-state response will be decreased.

4.4.7 Case G: A NPE system with negative cubic parametric nonlinearity

Figure 4.7e shows the effect of negative cubic parametric nonlinearity on upper stable branches. This also can be seen in the transition curve plot, Fig. 4.3 for case G, where the transition curve is shifted up compared to the transition curves for cases D and E, where higher cubic parametric nonlinearity is applied. At $\delta = 0.1$ the transition curve for case G has the smallest region compared to cases E and F. This is in agreement with Fig. 4.7e, when the additional stable and unstable branches are closer together when compared to cases E and F in Figs. 4.7a and 4.7c.

The phase-response curves for cases E, F and G are shown numerically and analytically in Figs. 4.7b, 4.7d, and 4.7f. The phase response for the upper stable branch is shown to equal $-\frac{\pi}{2}$ rad. The phase response for the unstable branch and the lower stable branch is shown at $\frac{\pi}{2}$ rad. The phase for the unstable and the stable branch is shown with dashed and solid black line at $\frac{\pi}{2}$ rad.

4.5 The effects of phase difference for the LPE system

The response amplitude of the LPE system subject to base excitation is affected by the relative phase between the base and parametric excitation ϕ. It is possible to increase or

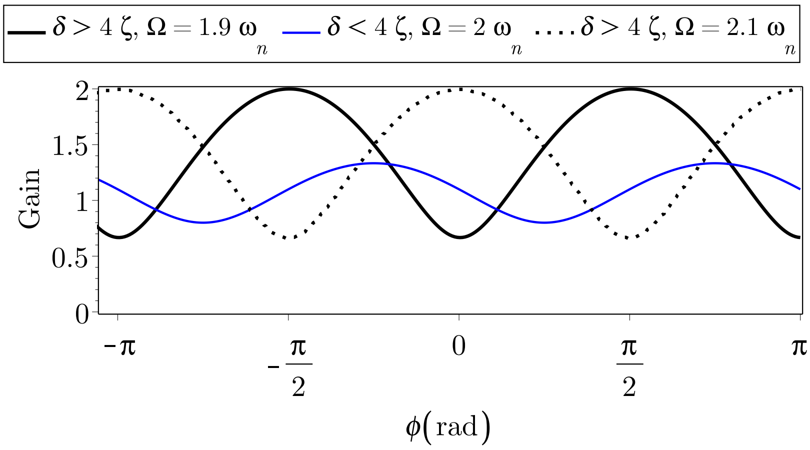

Fig. 4.8. Gain versus phase ϕ for a LPE system.

decrease the response amplitude of the LPE system by controlling the phase difference. In this section the response amplitude of the LPE system is compared with the response amplitude of the linear system at different relative phase. The gain associated with the LPE system is

$$\text{Gain} = \frac{a\mid_{\delta\neq 0}}{a\mid_{\delta,\alpha,\gamma=0}}. \tag{4.17}$$

This gain is calculated analytically from the amplitude of the steady-state response. This amplitude is the averaged amplitude obtained from the averaging method. The gain is calculated for the averaged amplitude when $\alpha = \gamma = 0$ and $\delta \neq 0$ over the amplitude of the response for a linear system ($\delta = \alpha = \gamma = 0$). This metric shows the value of parametric amplitude δ or relative phase ϕ for which the LPE system has a higher or lower response amplitude compared to the linear system.

The gain depends on relative phase ϕ. Figure 4.8 presents the effect of varying relative phase on gain. Three different cases are considered:

1. Parametric amplitude above the instability threshold ($\delta > 4\zeta$) with parametric frequency less than parametric resonance ($\Omega < 2\omega_n$).

2. Parametric amplitude under the instability threshold ($\delta < 4\zeta$) with parametric frequency at parametric resonance ($\Omega = 2\omega_n$).

3. Parametric amplitude above the instability threshold ($\delta > 4\zeta$) with parametric frequency higher than parametric resonance ($\Omega > 2\omega_n$).

Figure 4.8 shows the gain for the three above cases: (1) The maximum gain is found when $\phi = \frac{\pi}{2}$ rad with the parametric amplitude above its parametric instability and for frequencies less than parametric resonance. (2) The maximum gain is achieved at $\phi = \frac{3\pi}{4}$ rad at parametric resonance when the parametric amplitude is chosen under the parametric instability. (3) The maximum gain is found when $\phi = 0$ and the minimum gain is found when $\phi = \frac{\pi}{2}$ rad for the LPE system with the parametric amplitude above its parametric instability at frequencies higher than parametric resonance. The phase relationship is repeated in π rad intervals. Parametric amplitude $\delta = 0.1$ and $\delta = 0.001$ are considered for above and below the instability threshold respectively. Damping ratio is equal to $\zeta = 0.001$.

When the LPE system is excited with parametric amplitude above its parametric instability at $\frac{\Omega}{\omega_n} = 2$, the gain grows exponentially since the response is unbounded (see Fig. 4.4c). Hence, gain is calculated at $\frac{\Omega}{\omega_n} = 1.9$ when the steady-state response is bounded. When the LPE system is excited with parametric amplitude below its parametric instability, it is possible to excite the system at $\frac{\Omega}{\omega_n} = 2$ since solutions are bounded. From Fig. 4.4c, it is evident that for a LPE system excited above its parametric instability, at $\frac{\Omega}{\omega_n} = 1.9$ and $\frac{\Omega}{\omega_n} = 2.1$ the amplitude of the response (a) is different. The response amplitude is higher at $\frac{\Omega}{\omega_n} = 2.1$. Fig. 4.4c shows the response amplitude for the LPE system when $\phi = 0$. This is also in agreement with the gain calculated at $\frac{\Omega}{\omega_n} = 2.1$, which is higher when $\phi = 0$.

The response amplitude of the LPE system can be controlled by varying the relative phase ϕ between the base and the parametric excitation. The parametric amplification or attenuation depends on the parametric amplitude and parametric frequency when the relative phase is varied. For the NPE system it is also possible to control the response amplitude based on the relative phase. The effect of relative phase at different parametric frequencies is investigated.

4.6 The effects of phase difference for the NPE system

The response amplitude of the NPE system subject to base excitation is affected by the relative phase between the base and parametric excitation, ϕ. The aim is to show the effect of relative phase on the amplitude of the lower stable branch in order to control the jump between stable branches. The NPE system with hardening nonlinearity $\alpha = 1000\text{m}^{-2}$, and parametric amplitude $\delta = 0.1$ is considered above the instability threshold. Figure 4.7a shows the amplitude frequency response of the NPE system with hardening nonlinearity when $\phi = \frac{\pi}{2}$ rad.

At four different parametric frequencies, $\Omega = 1.9\omega_n$, $2\omega_n$, $2.1\omega_n$, and $2.3\omega_n$, the response amplitude of the NPE system is compared with the non-parametric system through calculation of the gain. The gain associated with the NPE system is

$$\text{Gain} = \frac{a\,|_{\delta,\alpha \neq 0}}{a\,|_{\delta,\alpha,\gamma=0}}. \tag{4.18}$$

This gain is calculated analytically from the amplitude of the stable steady-state response when $\gamma = 0$ and $\delta = \alpha \neq 0$ over the amplitude of the response for a linear system

($\delta = \alpha = \gamma = 0$). The stable upper branch and lower branch amplitudes are considered for the gain calculation. For example for the NPE system's response shown in Fig. 4.7a, at $\Omega = 1.9\omega_n$ only the amplitude of the upper stable branch is considered. However, at $\Omega = 2.3\omega_n$ the amplitude of the upper stable branch and lower stable branch is obtained for calculating the gain. The additional stable branch response amplitude is not included in calculating the gain. The additional branches are not affected by base excitation, hence they are independent of the phase between the base excitation and the parametric excitation.

Figure 4.9 shows the gain calculated from the NPE response based on the amplitude of the upper stable branch for parametric frequencies $\Omega = 1.9\omega_n$, $2\omega_n$, $2.1\omega_n$, and $2.3\omega_n$. For all four cases the maximum gain is found when $\phi = \frac{\pi}{2}$ rad and the minimum gain is found when $\phi = 0$. The gain is very low at parametric resonance $\Omega = 2\omega_n$ as a result of the strong cubic nonlinearity in the NPE system (see Fig. 4.9b). However, the gain is increased at higher parametric frequencies when $\Omega = 2.1\omega_n$ and $\Omega = 2.3\omega_n$. Since the response amplitude of the NPE system with hardening nonlinearity is increased at higher parametric frequencies.

At $\Omega = 2.3\omega_n$ the gain is calculated based on the amplitude of the lower stable branch (see Fig. 4.10). This gain is smaller than the gain for the upper stable branch, however the main difference is that for the lower stable branch the maximum gain is found when $\phi = 0$ and the minimum gain is found when $\phi = \frac{\pi}{2}$.

The response of the NPE system is affected by the relative phase between the base excitation and parametric excitation. Stable branches can be varied by the relative phase. The lower stable branch is higher when the relative phase is $\phi = 0$. It is possible to change the relative phase when the jump to the lower stable branch occurs. Increasing the lower branch amplitude as result of the relative phase provide enough initial condition for a jump to the upper stable branch. Modifying the relative phase in this way can help to increase the frequency bandwidth and gain of filters and amplifiers.

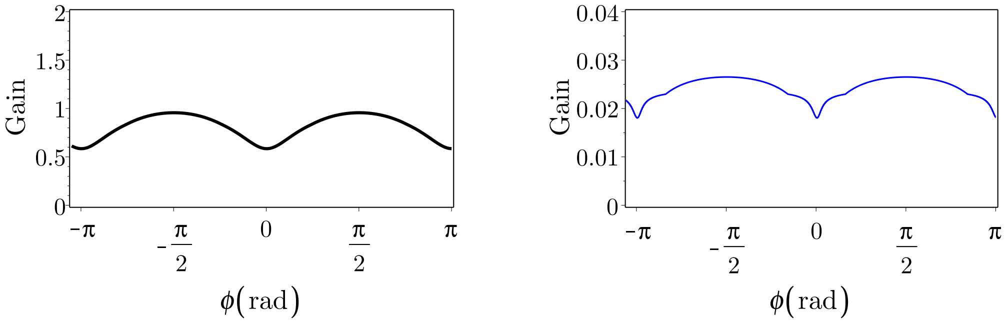

(a) $\Omega = 1.9\omega_n$ **(b)** $\Omega = 2\omega_n$

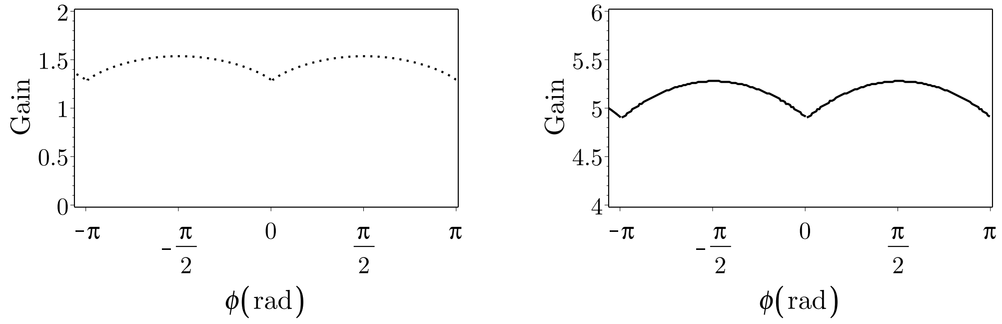

(c) $\Omega = 2.1\omega_n$ **(d)** $\Omega = 2.3\omega_n$

Fig. 4.9. Gain versus phase ϕ for the NPE system with cubic hardening nonlinearity $\alpha = 1000\text{m}^{-2}$, parametric amplitude $\delta = 0.1$, and damping ratio $\zeta = 0.001$. Gain is obtained based on the amplitude of the upper stable branch.

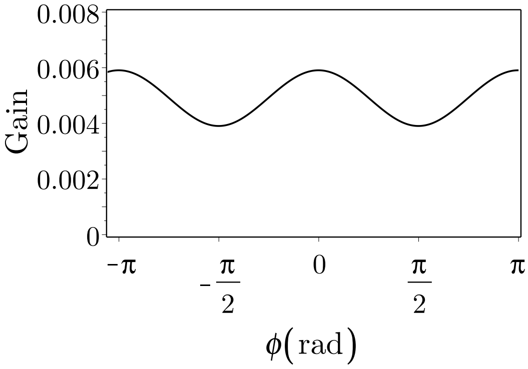

Fig. 4.10. Gain versus phase ϕ for the NPE system with cubic hardening nonlinearity $\alpha = 1000\text{m}^{-2}$, parametric amplitude $\delta = 0.1$, and damping ratio $\zeta = 0.001$. Gain is obtained based on the amplitude of the lower stable branch at $\frac{\Omega}{\omega_n} = 2.3$.

4.7 Concluding remarks

The work in this chapter demonstrated the effect of nonlinearities on the near-resonant and parametric resonant response of a base excited SDOF system. The SDOF system was excited by both a parametric excitation and a base excitation. The amplitude and the phase of the response for the linear and nonlinear parametrically excited systems were derived analytically for various system parameters using the averaging method. These results were in agreement with the numerical integration. However, the numerical integration is not obtained for the unstable solutions. For a LPE system it was shown that the system has parametric amplification above its parametric instability, however adding hardening nonlinearity reduces the response amplitude at resonance. For the NPE system with parametric excitation above the instability threshold the response is amplified. The parametric amplification has increased the amplitude of the stable branches as well as the additional branches.

The novel achievement of this work is in determining the effect of relative phase on the different branches of solutions. It is possible to decrease or increase the amplitude of each stable branches by varying the relative phase. Consequently it is possible to decrease or increase the frequency bandwidth of the response by controlling the jump between the lower and upper stable branch. Additional stable branches were generated only because of the parametric amplification and they are not affected by the base excitation. Hence, they are not affected by the relative phase. Controlling the frequency bandwidth and the response amplitude is beneficial for designing amplifiers, which can operate at different frequencies. For example a vibration energy harvester with high efficiency at frequencies different from its resonance frequency can benefit from this configuration.

The following chapters present the experimental model and results used for verification of the theoretical results, and investigates the system with different parameters to determine their impact on the response amplitude.

Chapter 5

Design consideration of an electromagnetic system

5.1 Introduction

In this Chapter, applying time-varying and nonlinear stiffness with an electromagnetic system to a fixed-free cantilever beam is investigated. Time-varying stiffness is the parametric amplitude for the parametrically excited system introduced in Chapters 3 and 4. Nonlinear stiffnesses such as cubic and cubic parametric stiffness are considered from the electromagnetic system. The effects of cubic and cubic parametric stiffness on the response of the NPE system is demonstrated analytically in Chapters 3 and 4.

To observe time-varying and nonlinear stiffness either a vertically excited cantilever beam or a cantilever beam with an electromagnetic system can be used. The advantages of using an electromagnetic system compared to a vertically excited cantilever beam are: (1) the electromagnetic excitation force is non-contact; (2) the excitation force acts on the beam in the transverse direction; and the direct and parametric excitation can be applied independently; (3) the accurately controlled frequency and amplitude of the excitation force by a DC/AC power source; (4) with the electromagnetic system, cubic and cubic parametric stiffness nonlinearities can be controlled and their effect on parametric amplification is demonstrated independently. The parametrically excited cantilever beam with an electromagnetic system has strong hardening nonlinearity, which can be controlled with an electronic circuit. The parametric amplification in an axially driven cantilever beam is only influenced by the vertical excitation, however in a parametrically excited cantilever beam with an electromagnetic system, the parametric amplification can be controlled by AC current generated in the coils.

This chapter introduces a model that could predict forces applied to the cantilever beam as a result of coils carrying DC/AC current. The main interest is in finding the time-varying and nonlinear stiffness from the applied electromagnetic forces theoretically and experimentally. The effect of electromotive force (e.m.f) generated when the cantilever beam is moving and consequently generating AC current in coils is stated in the theoretical model.

The electromagnetic system consists of two coil and magnet pairs. Two configurations have been considered for the electromagnetic system: coils connected in parallel and and in series in opposing connection. These configurations are described further in Appendix E.2. Only the coils connected in series are presented in this chapter. For both configurations the electrical damping is investigated theoretically and experimentally. The series connection is selected which applies less electrical damping. Since reducing the electrical damping applied from the electromagnetic system results in reducing the instability threshold for the PE system.

This chapter is arranged as follows: The electromagnetic system is described based on the mutual electromagnetic forces acting between the coils and magnets. The physical and mathematical explanation of the electromagnetic system is presented in Appendix E. The system configuration and experimental set-up is explained in Section 5.2. The induced current generated from the moving magnet between two coils in series opposing connection is calculated analytically and is measured experimentally, and the results are presented in Section 5.3. The linear and nonlinear stiffnesses generated by DC current in the coils connected in series are presented in Sections 5.4. The effects of DC current on changing the damping ratio and natural frequencies are demonstrated for coils connected in series in Sections 5.4.1. The effect of AC current on time-varying stiffness is described in Section 5.4.2. The mathematical model of the NPE system with an electromagnetic system is presented in Section 5.4.2. The induced e.m.f force as a result of moving magnet attached to the cantilever beam is investigated as part of the NPE system.

5.2 Electromagnetic system

An electromagnetic system is used to produce the time-varying stiffness desired in the experimental model. The electromagnetic device consists of a pair of identical magnets and a pair of identical coils. Controlling DC/AC input current carried by the coils gives the possibility of changing system's parameters such as the damping coefficient, linear and nonlinear stiffness, time-varying stiffness and consequently natural frequencies and amplitude of the response.

Figure 5.1 shows the fixed-free cantilever beam and an electromagnetic system. The cantilever beam is at equilibrium when the two coils carry the same DC current, and the magnets are positioned at the same distance h from the centre of coils.

The coils exhibit electromagnetism when current flows through them. The mutual electromagnetic forces acting between the coils and magnets cause the electromagnetic device to act as a spring. If the magnets and coils are repulsive, the attached beam returns to its equilibrium position when the beam is perturbed. In this case, the stiffness produced

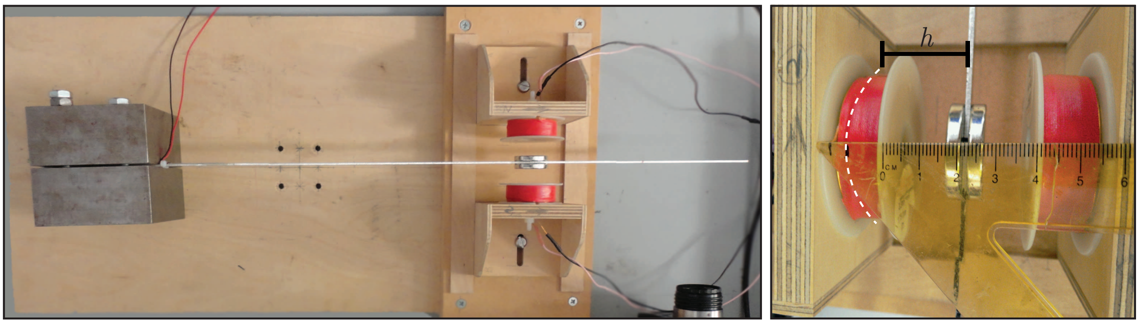

(a) (b)

Fig. 5.1. (a) A fixed-free cantilever beam and an electromagnetic system. (b) A pair of coils and magnets.

by the electromagnetic device is positive. If the magnets are reversed, an attractive force is generated and negative stiffness is obtained. The negative stiffness comes from the fact that the attractive force pushes the magnet away from the equilibrium position. In this thesis only repulsive forces and consequently positive stiffness is considered.

Figure 5.2 shows the experimental set-up used to generate the periodic electromagnetic stiffness on a cantilever beam. The pair of coils are from mundorf (type L71-3,30) and made of copper. Note that maximum ampere for the coil L71-3,30, based on the mundorf manual is 2.84 A. This means that above this range the temperature of the coils increases and consequently the internal resistance of the coil changes. The pair of coils are fixed to a wooden support. Neodymium (N42) disc magnets type F359 from first4magnets are attached to the cantilever beam. The LAMBDA ZUP is a programmable DC power supply and is used to generate DC/AC current from an input DC/AC voltage. Circuit diagram for generating DC and AC current through the coils is explained in Appendix E. A support was used to clamp the cantilever beam in a fixed orientation and location. To decrease the vertical movement, the beam has to be precisely located between the axis of the two coils. This position is adjusted entering the attractive mode of the magnets, and returning to the repulsion mode once the centred state is reached.

The experimental tests are compared with the results from the SDOF parametrically excited system introduced in previous chapters. Hence, the position $l_1 = 0.34\,\mathrm{m}$ in Fig. 5.2 was identified for the electromagnetic subsystem that best approximated the SDOF system model. When the electromagnetic system is placed in this position, the first and second modes of the cantilever beam are at a reasonable distance from each other to consider the model as a SDOF system. The parameters for the electromagnetic system and the beam are provided in Table 5.1.

In order to model the cantilever beam with an electromagnetic system several design requirements are considered including:

- Induced current generated as a result of moving magnet between the coils must be considered in the model. The induced current can change the damping and stiffness

Table 5.1: Mechanical properties and dimensions

Property	Value	Units
Material of the cantilever beam	Aluminium	
Young's Modulus of the beam (E)	70	GPa
Area moment of inertia (I_{m})	6.6×10^{-12}	m^4
Mass of the beam (m_{b})	0.034	kg
Length of the beam (l_{b})	0.54	m
Width of the beam (b_{b})	0.01	m
Thickness of the beam (t_{b})	0.002	m
Masses of the magnets (m_{m})	0.07	kg
Outer radius of the magnets (r_{m2})	0.015	m
Inner radius of the magnets (r_{m1})	0	m
Thickness of the magnets (t_{m})	0.005	m
Mounting position of the magnets (l_1)	0.405	m
Residual magnetic flux density of the permanent magnet (B_r)	1.1	T
Magnetic dipole moment (μ)	3.08	Am^2
Magnetic flux density field of magnet (B)	0.16	T
Permeability of free space (μ_0)	$4\pi 10^{-7}$	$\mathrm{N\,A}^{-2}$
Inner radius of the coils (r_1)	0.0085	m
Outer radius of the coils (r_2)	0.0225	m
Mean radius of the coils (r_c)	0.0155	m
Number of turns of in coil (N)	485	-
Length of wire in one rotation (l_{w})	0.078	m
Diameter of the coils (D_{w})	0.00071	m
Height of the coils with shield (h_{coil})	0.02	m
Coordinate for coils (z_1)	0.007	m
Coordinate for coils (z_2)	-0.007	m
Electrical resistance of the coil L71-3,30 from mundorf manual	1.77	Ohm
Measured electrical resistance of the coil and extra wiring (R_{coil})	1.91	Ohm
Amperage of the coil (Max ampere based on mundorf manual)	2.84	A
Electrical resistance of the load resistor (R_3)	0.1	Ohm
Inductance of the coil from mundorf manual	3.3	mH
Measured inductance of the coil (L_{coil})	3.31	mH
Total physical mass (m_{t})	0.104	kg
Measured static stiffness of the beam with no coils attached (k_{b})	32.84	Nm^{-1}
Measured first natural frequency of the beam with no coils attached (ω_{n})	17.4	$\mathrm{rad\,s}^{-1}$
Measured second natural frequency of the beam with no coils attached (ω_{n2})	210	$\mathrm{rad\,s}^{-1}$
Measured mechanical damping coefficient of the beam (c_{m})	0.104	Nsm^{-1}

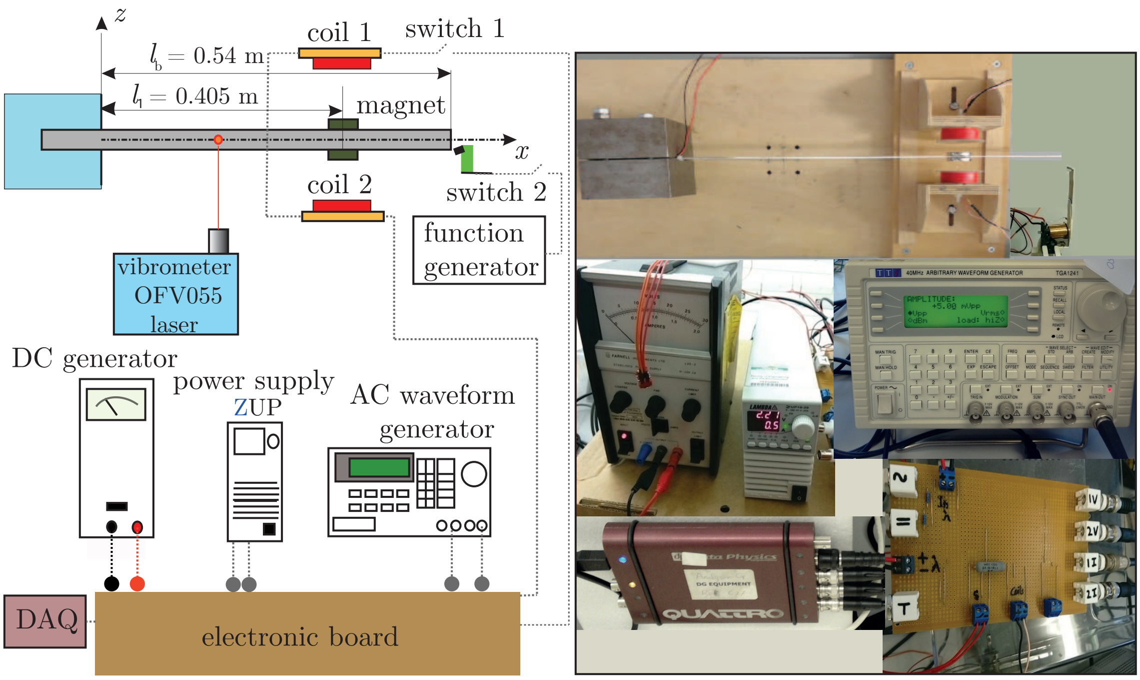

Fig. 5.2. Experimental set-up and schematic diagram to show each component of the set-up. The electronic board set-up is explained in Appendix E.1.

nonlinearities of the cantilever beam.

- Electrical damping ratio of the cantilever beam with the electromagnetic system with coils connected in series in opposing connection must be included in the model.
- The change in linear natural frequency of the cantilever beam as a result of coils carrying DC current is considered. Since the parametric amplification can happen at twice the natural frequency, identifying the system's natural characteristic is important.
- The feasibility of modelling the system as a SDOF system is investigated by looking at the separation between the first and second resonance frequencies of the cantilever beam.
- Linear and nonlinear stiffnesses of the cantilever beam with the electromagnetic system are measured and calculated theoretically. The dependency of the linear and nonlinear stiffnesses on electromagnetic system parameters such as DC/AC current, coil and magnet's geometry, and induced current is included in the study.

5.3 Induced current generated by harmonic magnet motion

This section describes the induced current generated by a moving magnet. Electromagnetic induction results from relative motion between a conductor (the coil) and a magnetic field (produced by the disc magnet). From this phenomenon, mechanical motion can be converted to and from electrical energy. Electromagnetic induction has been used to convert ambient motion to electricity, the set up of such harvesters consist of a permanent magnet and a coil. The relative motion of the magnet and coil produces induced current in the coils. This induced current can change the electrical damping applied from the electromagnetic system and consequently alter the parametric amplification. Hence, in order to show the dependency of response amplitude for the NPE system on damping it is necessary to evaluate the induced current.

Based on Faraday law of induction any change of magnetic flux through a conductive loop of wire will cause a voltage to be induced in that wire loop [140]. The magnetic field generated by a magnet and one pair of coil is demonstrated in [141]. A short summary of the method is presented in Appendix E.6. The magnetic field generated by a moving magnet between two coils is achieved based on the concept explained in [141].

The induced voltage across the coils can be expressed as

$$V = \dot{z} k_{\mathrm{t}}, \tag{5.1}$$

where $\dot{z}$ is the velocity of the moving magnet, the quantity k_{t} is the nonlinear electromechanical coupling for two coils and magnets with configuration shown in Fig. 5.3. A disk magnet is between a pair of coils connected in series opposing connection. The disk magnet has motion in z direction. Eq. (5.1) is derived from Eq. (E.35). The nonlinear electromechanical coupling is a function of magnet movement z and this displacement varies in with time. From Appendix E.6 the electromechanical coupling is

$$k_{\mathrm{t}}(z) = \frac{\varsigma q_1}{(r_2 - r_1)(z_2 - z_1)} \left(\sum_{n,m=1}^{2} (-1)^{n+m} \left(\ln(r_n + z'_{nm}) - \frac{r_n}{z'_{nm}} - \ln(r_n + z''_{nm}) + \frac{r_n}{z''_{nm}} \right) \right), \tag{5.2a}$$

$$z'_{nm} = \sqrt{r_n^2 + (z_m - (z + h))^2}, \tag{5.2b}$$

$$z''_{nm} = \sqrt{r_n^2 + (z_m - (-z + h))^2}, \tag{5.2c}$$

where ς is the fill factor [142]

$$\varsigma = \frac{D_{\mathrm{w}}^2 l_{\mathrm{w}} N}{4(r_2^2 - r_1^2) h_{\mathrm{coil}}}, \tag{5.3}$$

where D_{w} is the diameter of the coils, l_{w} is the length of the wire in one rotation, N number of turns in one coil, h_{coil} is the height of the coil, and r_2 and r_1 are the inner and outer radius of the coil respectively.

In Eq. (5.2) z_1 and z_2 refer to the height of the coil. Also, q_1 is the conveniently defined parameter

$$q_1 = \frac{3}{2} V_{\mathrm{m}} B_{\mathrm{r}}, \tag{5.4}$$

where V_{m} is the volume of the magnet and B_{r} is the residual magnetic flux density.

Note that assumptions for the nonlinear coupling coefficient may not be valid for all coil configurations, and careful consideration is needed when the electromagnetic system geometry is varied [141].

The mechanical domain (input force and relative velocity of the mass) and the electromagnetic domain (e.m.f and induced current) are related via the electromechanical coupling k_{t}. For a closed circuit condition the e.m.f voltage will cause a current to flow. This current creates a magnetic field, which opposes the cause according to Lenz' law [140]. The feedback electromechanical force is

$$F_{\mathrm{emf}} = k_{\mathrm{t}}(z) i_{\mathrm{es}} \tag{5.5}$$

where i_{es} is the current in coils in series opposing connection. From Eq. (5.1) and Ohm's law,

$$F_{\mathrm{emf}} = \frac{(k_{\mathrm{t}}(z))^2}{Z_{\mathrm{coil}}} \dot{z}, \tag{5.6}$$

and at high frequency the total impedance is

$$Z_{\mathrm{coil}} = \sqrt{4R_{\mathrm{coil}}^2 + 4L_{\mathrm{coil}}^2 \omega^2}, \tag{5.7}$$

where R_{coil} is the internal resistance of the coil, L_{coil} is the inductance of the coil and ω is the frequency of the moving magnet. In this work, since the frequency of the moving magnet is in the order of Hertz and the coil's inductance contributions at this range is small, the effect of inductance is neglected. The coil's impedance is $Z_{\mathrm{coil}} \approx 2R_{\mathrm{coil}}$. The induced current in coils i_{es} can be calculated from

$$i_{\mathrm{es}} = \frac{k_{\mathrm{t}}(z)}{Z_{\mathrm{coil}}} \dot{z}. \tag{5.8}$$

The dissipative feedback force due to the electromagnetic system can be calculated from Eq. (5.6) using a velocity proportional viscous damping element with the electrical damping coefficient as

$$c_{\mathrm{es}} = \frac{(k_{\mathrm{t}}(z))^2}{Z_{\mathrm{coil}}}. \tag{5.9}$$

Since the electromechanical coupling k_{t} is nonlinear the electrical damping is also nonlinear. This nonlinearity can only be observed for large displacements z. The nonlinearity in electrical damping is examined in Section 5.4.1. The electrical damping is also affected by the internal resistance of the coil. Optimum internal resistance can be found by changing the electrical damping [143].

Figure 5.4 shows a plot of electromechanical coupling k_{t} for electromagnetic configuration shown in Fig. 5.3. The theoretical electromechanical coupling is found based on Eq. (5.2). The experimental electromechanical coupling is found by substituting the

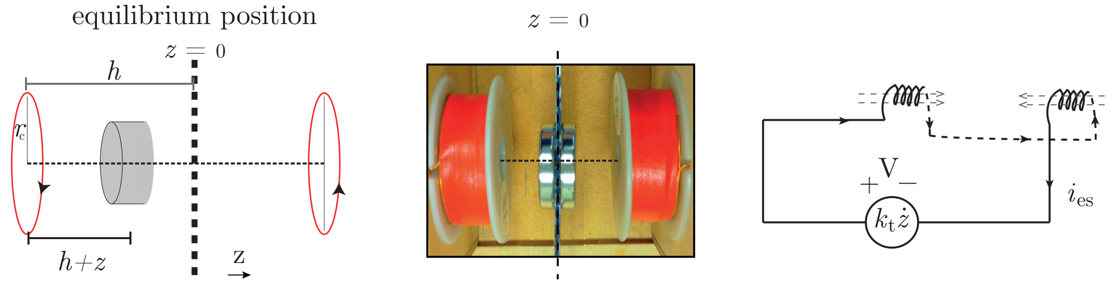

(a) (b) (c)

Fig. 5.3. (a) Diagram showing a pair of coils along with moving magnet. (b) A pair of coils along with pair of magnets at the centre. (c) Schematic of the circuit consisting of two coils in series opposing connection. The circuit is powered by electromagnetic induction.

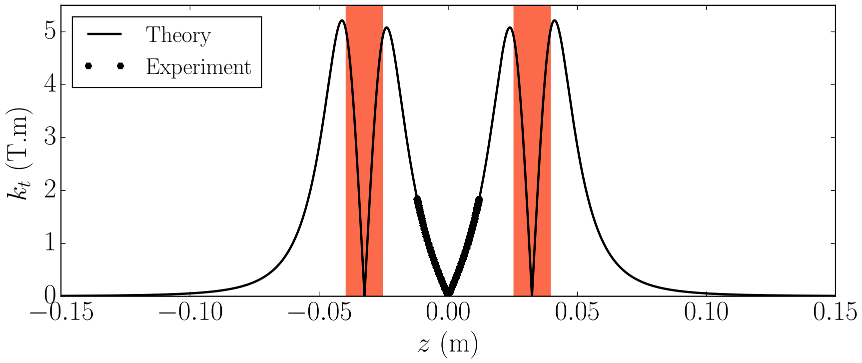

Fig. 5.4. Theoretical and experimental electromechanical coupling, k_{t} at different positions of the magnet as demonstrated in Fig. 5.3. The red regions show the position of the coils. At the centre of each coils the electromechanical coupling is zero.

measured velocity and voltage in to Eq. (5.1). The magnet displacement $z(t)$ is selected to be between -0.15 and 0.15. The distance between the equilibrium point and the centre of the coil is $h = 0.0325$m. The other parameters in Eq. (5.2) are presented in Table 5.1.

Figure 5.4 shows that between the coils (red regions), there are three positions where the electromechanical coupling is zero. Also, there are four peaks within $-0.15 \leq z \leq 0.15$ distance. The zero electromechanical coupling happens when the magnet motion is zero (at equilibrium) and in the centre of the coils (centre of the red regions in Fig. 5.4). However, this might not be achieved experimentally as the coils are not perfectly identical. As the magnets move further from the coils the electromagnetic coupling reduces. The maximum electromechanical coupling occurs when the magnet is moved very close to the coils where the greatest magnetic field is generated.

The experimental results in Fig. 5.4 are achieved by moving the magnet and beam with a shaker attached to the cantilever beam 0.08m away from the support (see Fig. 5.5). A horizontal force is applied by the shaker to the cantilever beam at frequency 3Hz. A vibrometer is used to measure the velocity of the cantilever beam and it is positioned at

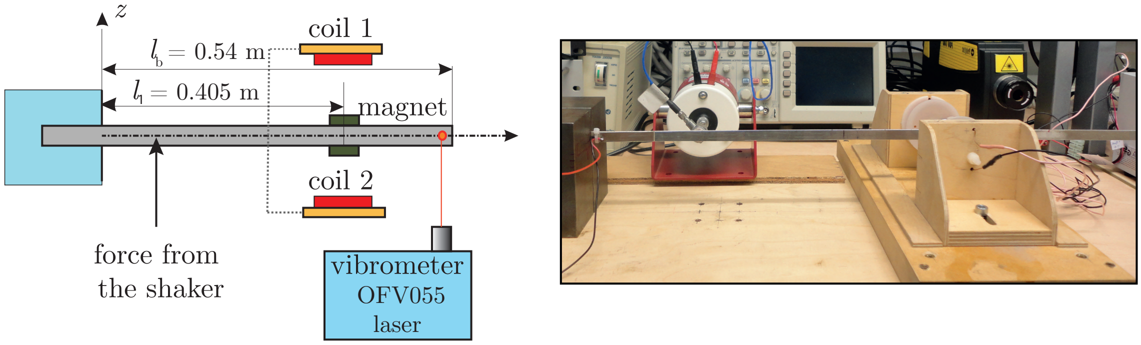

Fig. 5.5. Experimental set-up and schematic diagram. This set-up is used for measuring the induced current generated by the moving magnet on the fixed-free cantilever beam.

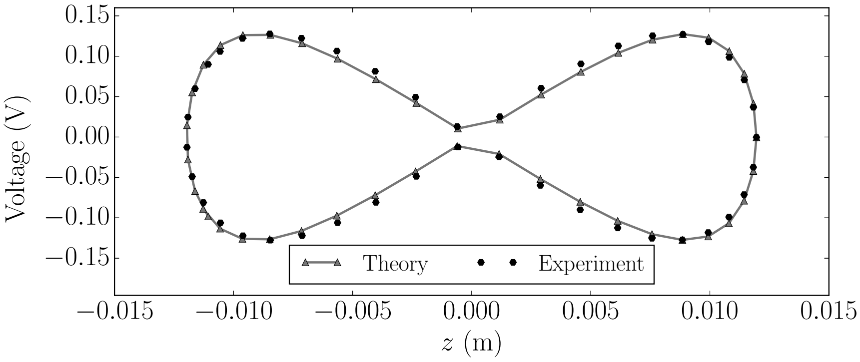

(a)

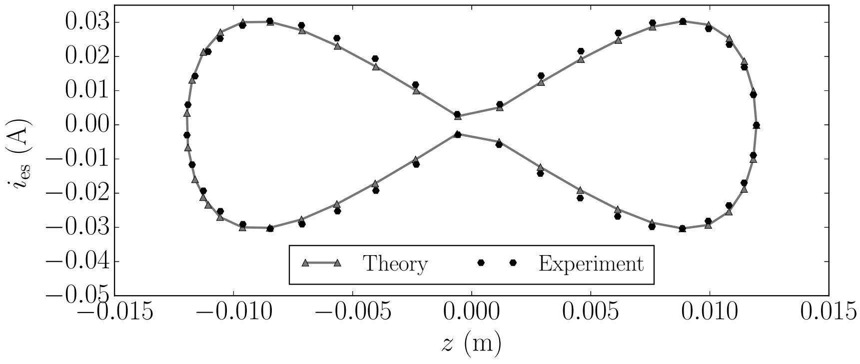

(b)

Fig. 5.6. (a) Theoretical and experimental voltage across the coils. (b) Theoretical and experimental induced current in the coils. The coils are connected in the series opposing connection. This voltage/current is generated as a result of moving magnet between the coils in direction z as shown in Fig. 5.3.

0.01 from the cantilever beam end. The recorded velocity is integrated numerically to find the magnet displacement. The measured displacement $z(t)$ is then substituted into Eq. (5.1) to obtain the electromechanical coupling k_{t}. The experimental result show that the electromechanical coupling is zero at the equilibrium position and it is increased as the displacement is increased and the magnet is getting closer to the coil.

Figure 5.6a shows the voltage across the coils in the series opposing connection for the electromagnetic configuration shown in Fig. 5.3. Voltage across the coils is calculated analytically from Eq. (5.1). The measured displacement is substituted to Eq. (5.1) in order to find the analytical voltage. The voltage across the coils is recorded when the magnet is moved between the coils. From Fig. 5.6a it can be seen that the voltage is increased as the magnet motion z is increased and at the equilibrium position the voltage is close to zero. Note that when the magnet motion has frequency f, several harmonics can appear in the generated voltage as Nf where $N \in \mathbb{N}_+$ [141]. For the coil configuration with series connection the second harmonic $2f$ has greater magnitude compared to the first harmonics f. Hence, here the magnitude of the second harmonic is considered.

Figure 5.6b shows the current i_{es} in the coils in the series opposing connection for the electromagnetic configuration shown in Fig. 5.3. The current in the coils is calculated analytically from Eq. (5.8). The measured voltage is substituted to $i_{\mathrm{es}} = \frac{V}{2R_{\mathrm{coil}}+R_3}$ in order to find the measured current. R_3 is the additional resistance in series with the coils. R_3 is defined in Table 5.1. The load resistance is chosen equal to 0.1 Ohm. The load resistance is not an optimised resistor for reducing the damping. This resistor is a silicone coated power resistor and the coating and marking are resistant to heat. It can happen that when coils are hot their internal resistance changes and measuring the coils current based on the voltage across the coils in this case is not accurate. Hence, the load resistance R_3, is added as a reference to find the current in coils when coils are found to get hot.

In this section generating the induced current with a moving magnet on the cantilever beam is demonstrated. In the next section, the effect of input DC/AC current which is supplied in the coils from an external source is presented. For a full model of the electromagnetic system the combination of the input current and the induced current in the coils are considered.

5.4 The effects of DC and AC current flow in coils connected in series

In order to obtain the insights necessary for a general understanding, a canonical model consisting of a mechanical system coupled to an electric circuit through an electromechanical coupling mechanism is considered. As shown in Fig. 5.7 the electric circuit of the electromagnetic system with the coils connected in the series in opposing connection is considered. The coils are identical and each coil is considered as a resistance and inductance in series connection. The current I_c, supplied to the coils is shown in Fig. 5.7 is

$$I_c = I_{DC} + I_{AC}\cos(\Omega t), \tag{5.10}$$

where I_{DC} is the DC current and Ω is the frequency of the AC current, I_{AC}.

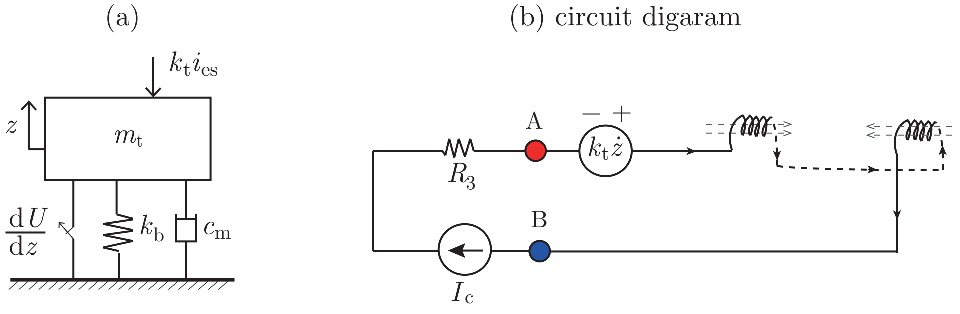
(a)

(b) circuit digaram

Fig. 5.7. Schematic of the NPE oscillator with an electromagnetic system with coils connected in series.

The equations governing the motion of the mechanical system can be written in the following general form:

$$m_t\ddot{z} + c_m\dot{z} + k_b z + \frac{dU(z)}{dz} + k_t i_{es} = 0, \tag{5.11a}$$

$$2L_{coil}\dot{i}_{es} + (R_3 + 2R_{coil})\, i_{es} = k_t\dot{z}, \tag{5.11b}$$

where the overdot represents a derivative with respect to time, t. The variable z represents the displacement of the system mass m_t, c_m is the linear viscous damping coefficient, k_b is the static stiffness of the cantilever beam, k_t is the electromechanical coupling coefficient, and i_{es} is the electric quantity representing the induced current in the electromagnetic system. The system parameters are presented in Table 5.1.

The function $U(z)$ is the potential energy of the electromechanical system, and $\frac{dU(z)}{dz}$ is the force applied by the electromagnetic system with coils connected in series:

$$\frac{dU(z)}{dz} = H_1 (I_c + i_{es})\, z + H_2 (I_c + i_{es})\, z^3. \tag{5.12}$$

where H_1 and H_2 are obtained from Eqs. (E.24) and (E.25). H_1 and H_2 are function of the distance between the coils h, the number of turns in the coil N, the magnetic dipole μ, the permeability of free space μ_0, and the mean radius of the coil r_c (see Table 5.1, and Appendix E.5 for more details).

When the DC current is generated and $I_{AC} = 0$, the force applied by the electromagnetic system is calculated as

$$\frac{dU(z)}{dz} = H_1 I_{DC} z + H_2 I_{DC} z^3. \tag{5.13}$$

The total linear stiffness of the cantilever beam k_1, is

$$k_1 = k_b + k_{\mathrm{ext}}, \tag{5.14}$$

where k_{ext} is the linear external stiffness due to the electromagnetic force defined by

$$k_{\mathrm{ext}} = H_1 I_{\mathrm{DC}}. \tag{5.15}$$

Furthermore, the natural frequency of the cantilever beam with the existence of the electromagnetic force, when $I_{\mathrm{c}} = I_{\mathrm{DC}}$, can be found. The first natural frequency of the cantilever beam ω_n, with the electromagnetic system can be found using the Rayleigh Energy Method as shown in Appendix F. The result is presented here for convenience

$$\omega_n = \sqrt{\frac{61.4 E I_{\mathrm{m}} + k_{\mathrm{ext}} D_1}{0.42 m_{\mathrm{b}} + m_{\mathrm{m}} D_1}}, \text{ where} \tag{5.16}$$

$$D_1 = 0.5 \left(-1.36 \cos\left(\frac{2\pi l_1}{\lambda_b}\right) + 1.36 \cosh\left(\frac{2\pi l_1}{\lambda_b}\right) + \sin\left(\frac{2\pi l_1}{\lambda_b}\right) - \sinh\left(\frac{2\pi l_1}{\lambda_b}\right)\right)^2, \tag{5.17}$$

and E is the Young's modulus, I_{m} is the area moment of inertia, l_1 is the distance between the magnets and the coils with respect to the fixed end of the cantilever beam, and λ_b is the wavelength. The relationship between the electromagnetic stiffness and the current flow in the coils is found analytically and is implemented here from the relation between the natural frequency and the electromagnetic stiffness k_{ext}.

First the effects of the DC current and the induced current in the coils is considered. Normalizing Eq. (5.11) with the total mass m_t yields,

$$\ddot{z} + 2\zeta\omega_n \dot{z} + \omega_n^2 z + \omega_n^2 \alpha z^3 = 0, \tag{5.18}$$

where ζ is the damping ratio, and it is the combination of mechanical and electrical damping ratios ($\zeta = \zeta_{\mathrm{m}} + \zeta_{\mathrm{es}}$). The mechanical damping ratio is

$$\zeta_{\mathrm{m}} = \frac{c_{\mathrm{m}}}{2 m_{\mathrm{t}} \omega_n}, \tag{5.19}$$

and ζ_{es} is the electrical damping applied from the electromagnetic system with coils connected in series in opposing connection. The electrical damping ζ_{es}, as a result of magnetic flux density is calculated analytically from Eq. (5.9), and it is presented here as

$$\zeta_{\mathrm{es}} = \frac{(k_{\mathrm{t}}(z))^2}{2 m_{\mathrm{t}} \omega_n \left(2 R_{\mathrm{coil}} + R_3\right)}, \tag{5.20}$$

when the effect of inductance at low frequencies is neglected.

In Eq. (5.18) the nonlinear term added to the system as a result of the coils carrying a

DC current is the normalised cubic stiffness nonlinearity. The cubic stiffness nonlinearity, α is

$$\alpha = \frac{H_2 I_{\mathrm{DC}}}{k_1}. \tag{5.21}$$

The cubic stiffness nonlinearity is strongly affected by the DC current and the electromagnetic system parameters, such the distance between coils, the number of turns in the coil, and the mean radius of the coil.

For generating electromagnetic force two electromagnetic configurations can be considered, coils connected in series and parallel in opposing connection. Coils in series can have two main benefits, increasing the internal resistance since the total coil resistance is $2R_{\mathrm{coil}}$, and for half of the current of the coils in parallel, the same electromagnetic force is applied. It is shown in the previous section that increasing the internal resistance reduces the electrical damping. Reducing the total damping, affects the transition curves. The instability threshold can be reduced and for smaller parametric amplitude parametric amplification can occur. Strong electrical damping from the coils in the parallel opposing connection increases the instability threshold for LPE and NPE systems. Strong damping effect in the coils connected in parallel opposing is as a result of the circulating current in this configuration. More detail of circulation current in the coils in the parallel opposing connection is presented in Appendix E.2. The measured damping and natural frequencies for the coils in parallel opposing connection show that high damping can be seen upon connecting the coils. Several experiments are carried and the results are presented in Appendix E.8.

5.4.1 Electrical and mechanical damping

In this section the electrical and mechanical damping in the coils in the series opposing connection are measured and calculated analytically. There are several methods to find the damping of a linear SDOF system such as the peak-amplitude method [144] (So called half-power point method [145]), the logarithmic decrement approach and the circle-fit method [144]. From the mobility, one can say the first and second modes are separated from each other, hence, it can be assumed that all responses can be attributed to the first mode and the effect of the second mode is ignored.

In general the peak-amplitude method is applied for systems with well separated modes so that the SDOF approximation is valid. Also, when the modes are not so lightly damped, accurate measurement is not possible because the bandwidth converges [144]. The measurements were carried out having clear peaks at resonances. Also, the electromagnetic system can apply nonlinearity to the cantilever beam during impact tests when the beam displacement is large. Hence, strong impact forces were avoided to reduce the beam displacement during the impact tests.

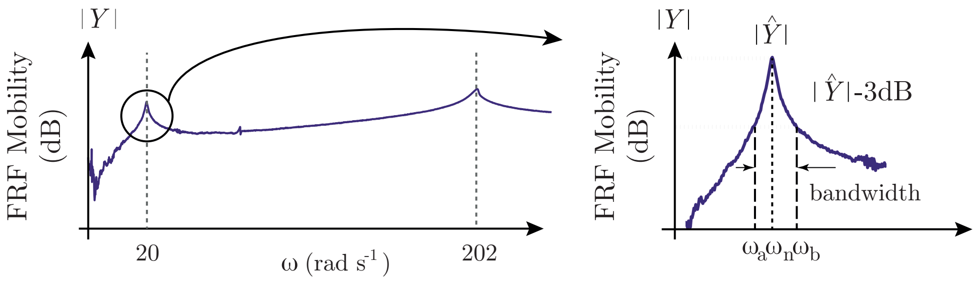

Fig. 5.8. The peak-amplitude method of Mobility FRF from an experimental test.

From the Mobility Frequency Response Function (FRF) of a cantilever beam with an electromagnetic system, the first peak, which corresponds to the maximum response of the first mode at natural frequency ω_n is obtained. Fig. 5.8 illustrates the method used to obtain the damping ratio [144]. The value of Mobility FRF $\mid \hat{Y} \mid$ at resonance ω_n subtracted by -3dB can define the frequency bandwidth. The upper and lower frequencies correspond to frequencies which $\mid \hat{Y} \mid - 3$dB exist are called ω_a and ω_b. Damping ratio at the first resonance is,

$$\zeta = \frac{\omega_\mathrm{b} - \omega_\mathrm{a}}{2\omega_\mathrm{n}}. \tag{5.22}$$

The limitations of the peak-amplitude method are:

- The accuracy of this method depends on the accuracy of the measurements and defining the maximum FRF peak at resonance, ω_n.
- When high damping is observed, in the case of coils in parallel connection, the FRF peak at resonance, ω_n, is not recognised hence the peak-amplitude method cannot be implemented.
- This method only finds the linear damping.

Hilbert damping analysis can be used to recognise and calculate the nonlinear damping [146]. Obtaining damping from a transient response, whether for linear or nonlinear damping, is based on the decay envelope. The amplitude of the transient response varies slowly with time, and the shape of slow time variation is called the decaying envelope [147, 148]. Determining damping based on the nature of the transient decay envelope, unlike other methods such as the peak-amplitude method, the logarithmic decrement method and moving block analysis, does not require a limiting assumption of viscous damping [147]. Calculating damping from the Hilbert transform is explained in Appendix G. Hilbert damping analysis is implemented to find the nonlinear damping. The limitations of the Hilbert damping analysis are:

- The signal-to-noise ratio of the transient signal affects on the quality of the envelope and therefore appropriate filtering is required.

Table 5.2: Measured damping ratios from the peak-amplitude method and the Hilbert transform

Tests Methods	ζ peak-amplitude	ζ Hilbert transform	ζ_{m} peak-amplitude	ω_{n} $(\mathrm{rad\,s^{-1}})$	I_{DC} (A)
Case 1	0.003	0.003	0.003	16.70	open circuit
Case 2	0.003	0.0026	0.003	18.46	0
Case 3	0.001	0.0007	0.003	37.11	0.5
Case 4	0.001	0.0005	0.003	49.24	1

- For the case of coils in parallel connection, the transient response is highly damped, and the envelope cannot be found accurately.

Impact tests with an instrumented hammer are conducted [144]. The impact is applied at 0.08 m away from the support end, with an instrumented hammer type (208C01 ICP force sensor from **PCB** PIEZOTRONICS). The laser vibrometer, OFV056 POLYTECH is used to measure the beam velocity at 0.52 m away from the support end. DAQ system, QUATTRO from Data Physics is used to collect the data from the instrumented hammer and the vibrometer. The FRF of the cantilever beam is obtained from the time domain data. The following acquisition parameters for FRF modal testing were selected as: acquisition time, 40 s, frequency resolution (Δf), 0.0025 Hz, time step (ΔT), 0.0096 s, sampling frequency, 102.39 Hz, the window type was chosen to be rectangular, and 10 FRF averaging. The first and second natural frequencies were identified from the Mobility Frequency Response Function (FRF).

Eq. (5.9) shows that the electrical damping is nonlinear for the coils in series in the opposing connection. Hence, the effect of linear and nonlinear damping from the coils in series is verified experimentally. In order to check the effect of nonlinear damping for the range $I_{\mathrm{DC}} = 0\,\mathrm{to}\,1A$, a study based on the Hilbert transform is carried out. Since the DC current for the NPE system in this thesis is considered in this DC range. Four cases are presented. Case 1 is when the coils are in series and in an open circuit. The coils are not connected to the resistive load R_3. Coils from point A and B are in an open circuit. This can be achieved by disconnecting the coils 1 and 2 from point A and B in Fig. 5.7. Case 2 is when the coils are in series and are connected to the resistive load R_3, and no current is generated by the LAMBDA ZUP. Cases 3 and 4 are when the coils are in series and are connected to the resistive load R_3, and currents I_{DC} of 0.5A and 1 A are generated by the LAMBDA ZUP. For these cases, the half distance between coils, h is chosen to be equal to 0.03m.

An instrumented hammer with a soft tip is used to excite the cantilever beam, and the velocity of the beam is measured with the vibrometer. Both time domain and frequency domain responses are recorded. Mobility FRF, which is the ratio between the velocity response and the harmonic force from the hammer, is measured to estimate natural frequencies and damping factors for cases 1 to 4 (see Figs. 5.9a, 5.10a, 5.11a, and 5.12a). From Mobility plots a resonance peak at the first natural frequency is observed and the second natural frequency is occurred between $202 - 211 \mathrm{rad\,s^{-1}}$. This shows the first and the second natural frequencies are well separated.

First, the damping ratio for each case in Table 5.2 is found from the peak-amplitude method based on the Mobility FRF plots. Second, the Hilbert transform is applied. The velocity response recorded from impact tests is a decaying transient signal. The velocity response is filtered with a Butterworth bandpass filter to limit the velocity signal to its natural frequency ω_n. Lower and upper cutoff frequencies are chosen to be $\omega_\mathrm{n} - 6.28 \mathrm{rad\,s^{-1}}$ and $\omega_\mathrm{n} + 31.4 \mathrm{rad\,s^{-1}}$. This bandwidth is chosen to consider the velocity response only at its first resonance. The order of Butterworth bandpass filter is chosen to be equal to 5. The velocity signals and the signals with the Butterworth bandpass filter for cases 1 to 4 are presented in Figs. 5.9b, 5.10b, 5.11b, and 5.12b. The Butterworth bandpass filter increases the signal-to-noise ratio without greatly distorting the envelope signal [149]. This filter works based on the method of least square [150].

The envelope of the filtered velocity is found based on the Hilbert transform. The envelopes of velocity signals for cases 1 to 4 are shown in Figs. 5.9c, 5.10c, 5.11c, and 5.12c. The damping ratio ζ is determined by the shape of the envelope of the velocity signal, where the envelope is introduced as $e^{-\zeta \omega_\mathrm{n} t}$ (see Appendix G). The envelope can be shown on a logarithmic amplitude scale where the exponential envelope curve determined by a decaying rate $\zeta \omega_\mathrm{n}$, can be seen as a linear decay. Higher order interpolation is employed to match with the ζt plots (see Figs. 5.9d, 5.9d, 5.9d, and 5.9d), and a linear interpolation agrees with each plot perfectly. Thus, the damping factor for a system when the coils are connected in series can be assumed as a linear damping.

The mechanical damping is measured from both the peak-amplitude and the Hilbert transform and it is equal to 0.003. This is the damping of the cantilever beam when coils are not around the cantilever beam and when the electrical damping is zero ($\zeta = \zeta_\mathrm{m}$). Both the peak-amplitude and the Hilbert transform method show that for case 1, the total damping ratio is 0.003 (see Table 5.2). Thus, the nonlinear electrical damping for small displacement is considered equal to zero.

When the coils are in series and are connected with a resistive load R_3, and the LAMBDA ZUP generates DC current, which is equal to 0.5 and 1 A, a small difference between the coils or the small change in distance between the magnets and the coils can cause a movement for the cantilever beam. The reason for this movement is the repulsion force applied from the electromagnetic system when the coils carry a DC current.

The first natural frequency ω_n, and the stiffness of the beam k_1, when the coils are carrying a DC current and are connected in series are calculated and measured. The first natural frequency ω_n is calculated from Eq. (5.16) and the beam stiffness is found from Eq. (5.14). The experimental tests were repeated for different DC currents between the

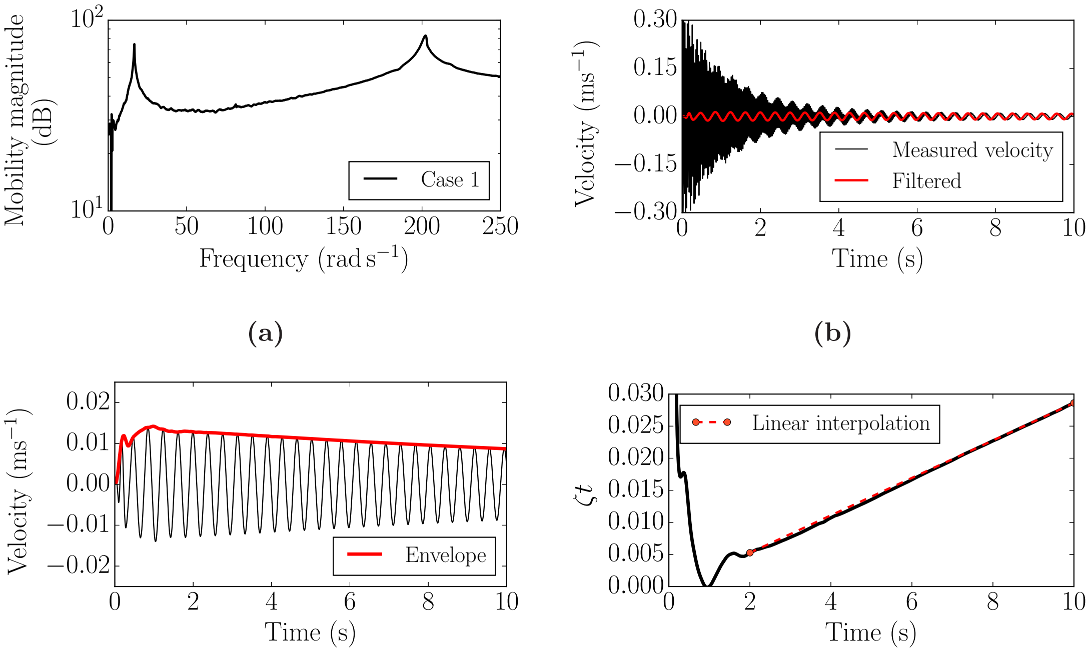

(a) **(b)** **(c)** **(d)**

Fig. 5.9. Tests corresponding to case 1 in Table 5.2. (a) Measured FRF of a cantilever beam with open circuit coils in series connection. (b) Measured velocity and a filtered velocity with a bandpass filter. (c) The envelope for the filtered velocity with a bandpass filter. (d) Variation of damping ratio with time t found from the envelope.

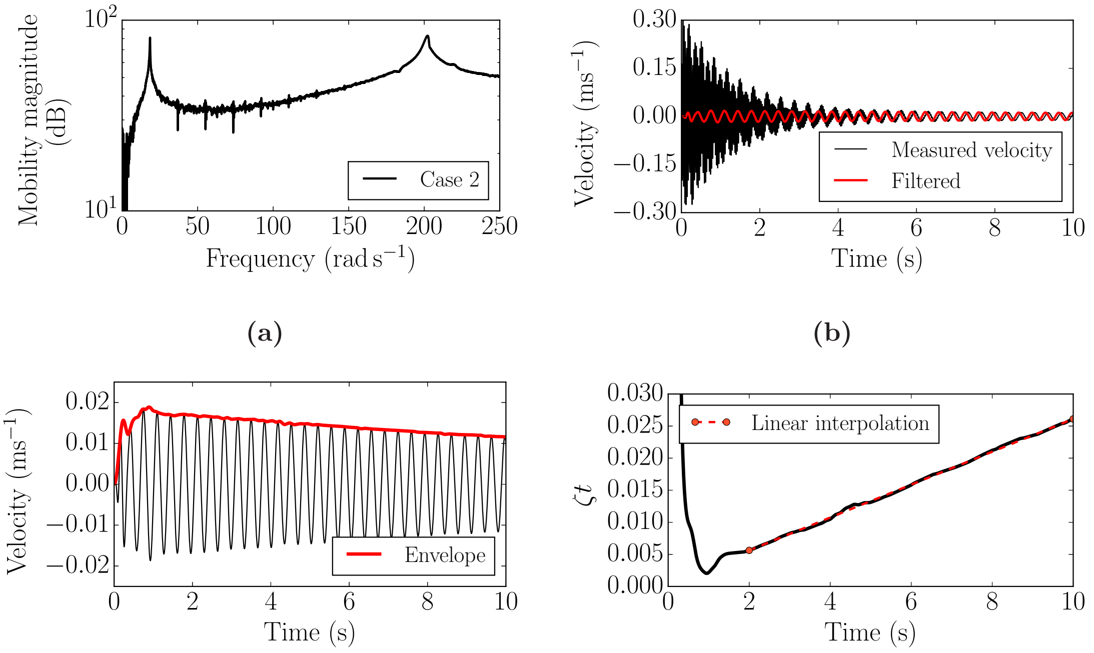

(a) **(b)**

(c) **(d)**

Fig. 5.10. Tests corresponding to case 2 in Table 5.2. (a) Measured FRF of a cantilever beam with the coils in series connected to the resistive load R_3 and the electronic board. (b) Measured velocity and filtered velocity with a bandpass filter. (c) The envelope for the filtered velocity with a bandpass filter. (d) Variation of damping ratio with time t found from the envelope.

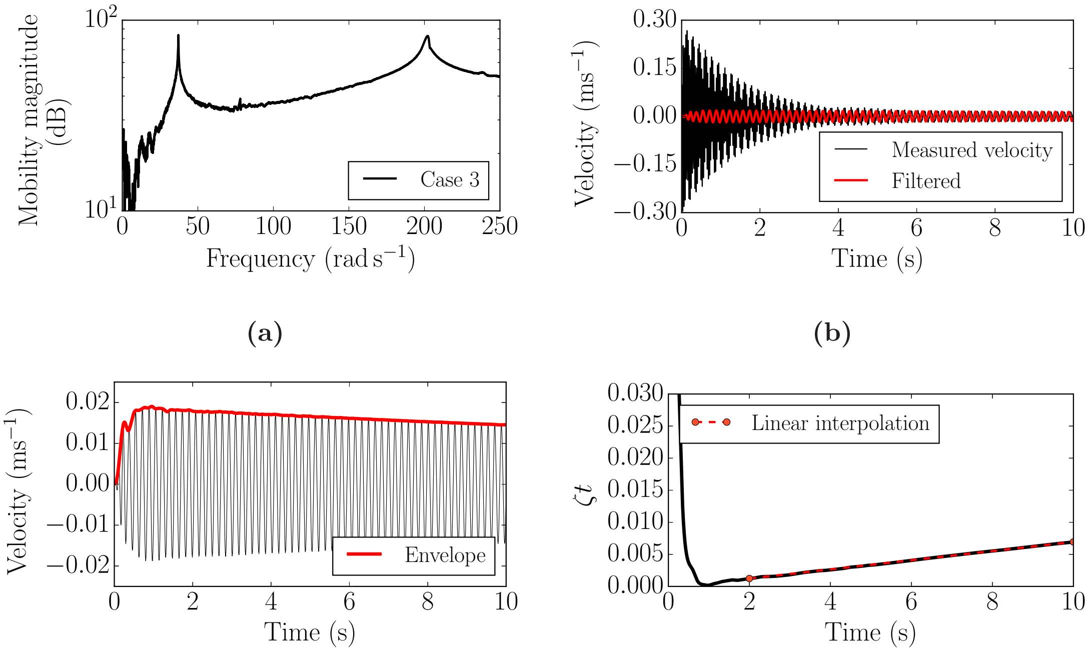

(a) **(b)**

(c) **(d)**

Fig. 5.11. Tests corresponding to case 3 in Table 5.2. (a) Measured FRF of a cantilever beam with coils in series connected to the resistive load R_3 with a 0.5 A DC current generated by the LAMBDA ZUP. (b) Measured velocity and filtered velocity with a bandpass filter. (c) The envelope for the filtered velocity with a bandpass filter. (d) Variation of damping ratio with time t found from the envelope.

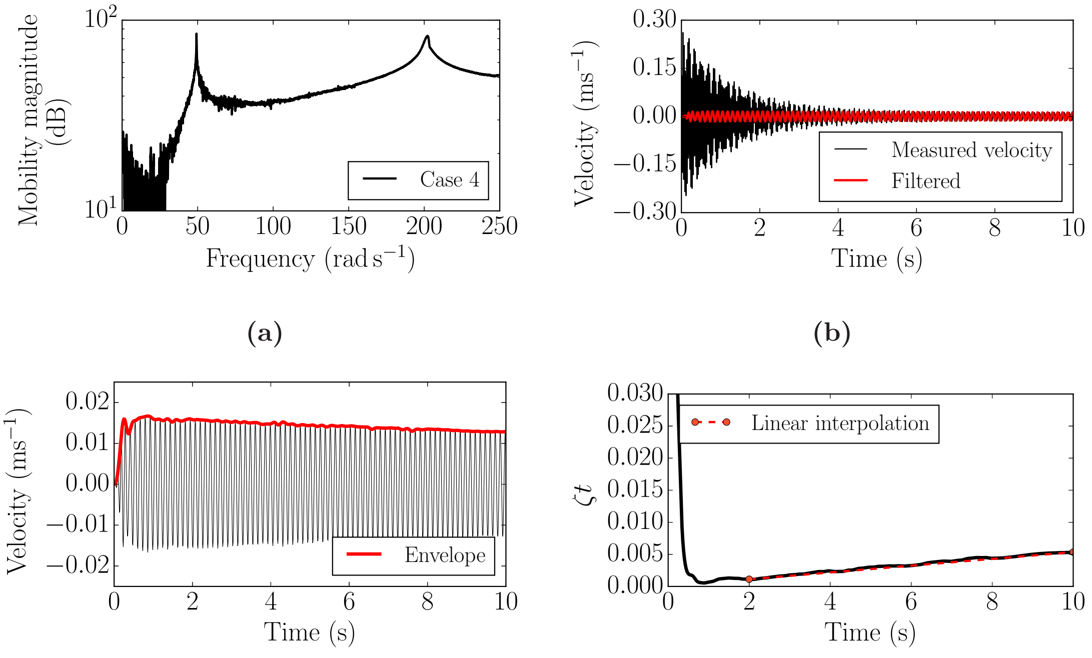

(a) **(b)**

(c) **(d)**

Fig. 5.12. Tests corresponding to case 4 in Table 5.2. (a) Measured FRF of a cantilever beam with coils in series connected to the resistive load R_3 with a 1 A DC current generated by the LAMBDA ZUP. (b) Measured velocity and a filtered velocity with a bandpass filter. (c) The envelope for the filtered velocity with a bandpass filter. (d) Variation of damping ratio with time t found from the envelope.

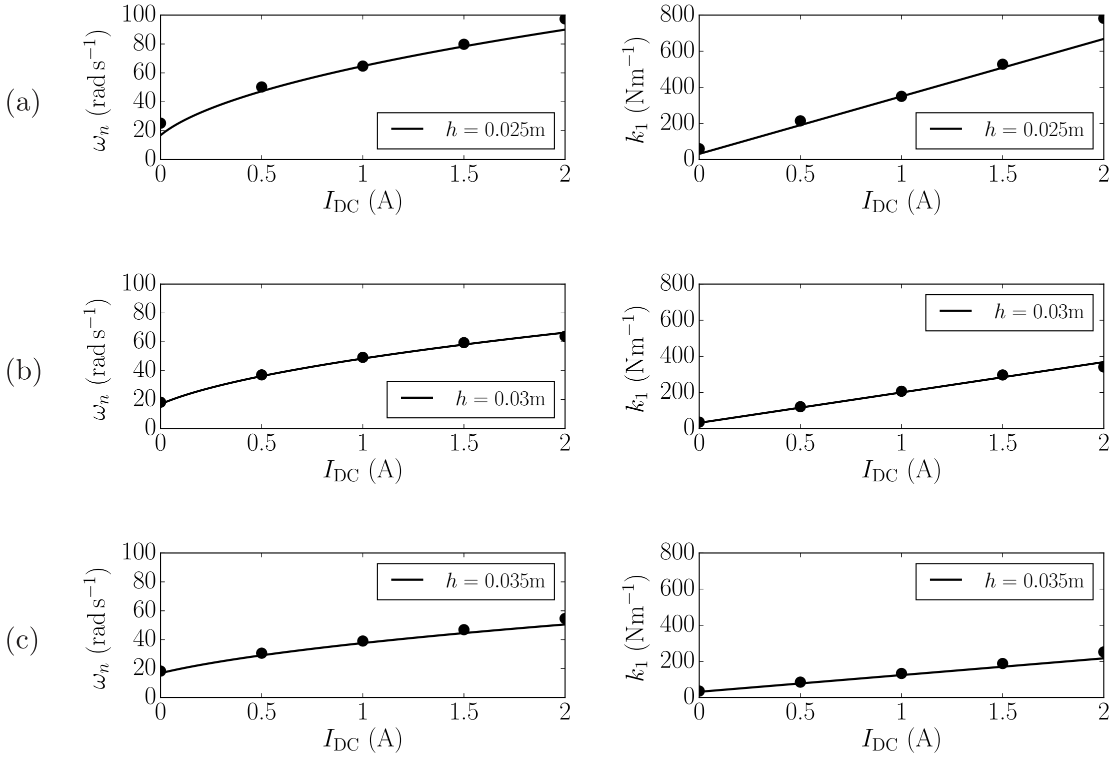

Fig. 5.13. Experimental and analytical linear first natural frequency and stiffness of the cantilever beam when the coils carry DC current and for different positions between coils h. These results are obtained when the coils are in series and they are attached to the resistive load R_3 and the LAMBDA ZUP. (a) $h = 0.025$m, (b) $h = 0.03$m, (c) $h = 0.035$m.

range 0 to 4 (A). From the experimental natural frequency found from FRF tests, the experimental electromagnetic stiffness k_{ext} is identified. The theoretical natural frequency is achieved by substituting the theoretical electromagnetic stiffness k_{ext} from Eq. (5.15) into Eq. (5.16). The experimental and theoretical first natural frequencies and beam stiffness $k_1 = k_b + k_{\text{ext}}$ when the coils are carrying DC current are shown in Fig. 5.13. The position between the coils is varied during the measurements. Linear natural frequencies are obtained from these analyses.

In summary:

- The peak-amplitude method is used to find the linear damping and the Hilbert transform method is implemented to find the nonlinear damping. The result of these methods have been in agreement with experimental results. When the coils are connected in series the nonlinear damping for small displacements is investigated. The damping ratio found by the Hilbert transform shows that the nonlinear damping is negligible.

- The analytical and experimental results for the linear natural frequency are in agreement so the analytical model is used through out this thesis.

- In this section, the effect of DC current on the first natural frequency is discussed. Increasing the DC current increases the first natural frequency.

- It is confirmed that since the first and second modes are far from each other, a SDOF model can be used as a model of the cantilever beam.

5.4.2 Linear time-varying and nonlinear stiffnesses

When DC and AC currents are generated in coils the electromagnetic force applied to the cantilever beam varies in time. The force applied to the cantilever beam is presented in Eq. (5.12).

The cantilever beam is excited by the electromagnetic force, and as a result of this excitation the moving magnet can generate magnetic field. A change in the magnetic field through two pairs of coils, induces an e.m.f in the coils, which causes current to flow. The induced current is only generated if the magnets or coils are moving relative to each other. When the cantilever beam is moving towards the coils (see Fig. 5.3), the e.m.f current flows in the coils together with the input current.

In Section 5.4.1 it was demonstrated that the cantilever beam natural frequencies are well separated hence the cantilever beam can be modeled as a SDOF system. A SDOF model when the AC current is generated in the coils is considered. Normalizing Eq. (5.11), with the total mass m_{t} yields,

$$\ddot{z} + 2\varepsilon\omega_n(\zeta_{\mathrm{m}} + \zeta_{\mathrm{es}})\dot{z} + \omega_n^2\left(1 + \varepsilon\delta\cos(\Omega t)\right)z + \omega_n^2\left(\varepsilon\alpha + \varepsilon\gamma\cos(\Omega t)\right)z^3 + \varepsilon\omega_n^2\delta_{\mathrm{es}}z + \varepsilon\omega_n^2\gamma_{\mathrm{es}}z^3 = 0, \quad (5.23)$$

where ε is the small parameter, δ is the normalised parametric stiffness (parametric amplitude, or pump), and it can be found from

$$\delta = \frac{H_1 I_{\mathrm{AC}}}{k_1}, \quad (5.24)$$

the cubic nonlinearity α, is defined similar to Eq. (5.21). The static stiffness k_1 is presented in Eq. (5.14). The normalised cubic parametric nonlinearity γ, is added to the system as a result of nonlinearity from the electromagnetic system when the coils carry an AC current. Normalised cubic parametric nonlinearity γ, is

$$\gamma = \frac{H_2 I_{\mathrm{AC}}}{k_1}. \quad (5.25)$$

H_1 and H_2 are obtained from Eqs. (E.24) and (E.25). For simplicity, expressions involving the quantities δ, α and γ will not explicitly state their dependency on current.

The nonlinear parameters δ_{es} and γ_{es} are generated as a result of including the induced current in electromagnetic system:

$$\delta_{\mathrm{es}} = \frac{H_1 i_{\mathrm{es}}}{k_1}, \quad (5.26)$$

$$\gamma_{\mathrm{es}} = \frac{H_2 i_{\mathrm{es}}}{k_1}. \quad (5.27)$$

where the induced current i_{es} is obtained from Eq. (5.8). The induced current i_{es}, is a function of z and $\dot{z}$.

The electrical damping ζ_{es} is included in the model. The electrical damping is presented from Eq. (5.20). Since the electromechanical coupling k_t is a function of z then from Eq. (5.20) the dependency of electrical damping on displacement z can be seen. Hence, for large displacements the parameters introduced above should be considered in the model.

5.5 Concluding remarks

The experimental set-up, which is designed in this chapter is employed to represent the NPE system introduced in Chapters 3 and 4. This chapter investigated a PE cantilever beam. An experimental model of the PE system was proposed, which used electromagnetic coils and magnets to emulate time-varying and nonlinear stiffness. The electromagnetic system and magnetic force was explained analytically. The induced current generated in the coils was calculated analytically and is included in the model of the NPE system.

When the coils were connected in series the stiffness of the cantilever beam was expressed as a function of current passing through the coils of the electromagnet. Nonlinear terms as a result of the electromagnetic forces were explained. Cubic and cubic parametric nonlinearity in the electromagnetic system were defined analytically as a function of current. The maximum stiffness was found for different distances between the coils. The first natural frequency of the LPE system was then related to the linear stiffness, which in turn created a relationship between natural frequency and current. The analytical results were validated using experiments.

In this contribution, the induced current and the electrical damping was found analytically and experimentally for coils connected in series. In order to reduce the effect of damping on LPE and NPE system with an electromagnetic subsystem the series configuration was recommended. In the next chapter the induced current and the electrical damping is included in the model of the NPE system with the electromagnetic system.

Chapter 6

Experimental investigations of a nonlinear parametrically excited system for free oscillations

6.1 Introduction

In this chapter an experimental study of a Nonlinear Parametrically Excited (NPE) system is carried out. The parametrically excited model can be used for instance in designing electromagnetic filters, resonators and amplifiers. These systems can benefit from a large amplitude of oscillation in a wide frequency bandwidth. Hence, parametric amplification is exploited to increase the amplitude of oscillation whereas stiffness nonlinearities are employed to increase the frequency bandwidth at which the large amplitudes are experienced [62, 151].

In this chapter, the degenerated parametrically excited oscillator is considered. The linear natural frequency of the system is tuned to be half of the frequency of the input signal. In order to design a filter the input AC signal is the signal which needs to be amplified or filtered. The change in the natural frequency of the system can be achieved by applying DC current in the electromagnetic system.

The response of the NPE system is measured experimentally. The experimental results and processing of the data give credence to the purely theoretical analysis presented in this chapter and Chapter 3. A theoretical model for an electromagnetic system is proposed and its robustness is examined by the repeatability of experimental data from several rigorous tests. The theoretical model addressed here, models the strong nonlinearities observed in the electromagnetic system. Based on the literature, the accuracy of analytical approaches such as the multiple scale method, the harmonic balance, and the averaging methods is limited to weak nonlinearities and small damping [152]. The analytical method, which is the method of averaging, is tested with strong nonlinearity and large damping and is compared with the experimental results. In this chapter the small parameter ε is considered to be equal to 1.

This chapter is arranged as follows: a parametric study is carried out and the behaviour of the response is illustrated. The experimental results and the analytical responses based on the averaging method are presented in Section 6.2. In addition, the effect of damping, parametric amplitude, and nonlinearities on response of the NPE system are carried out experimentally and analytically. By increasing the AC current the parametric amplitude and cubic parametric nonlinearity apply higher parametric amplification. The increase in amplitude of the response is investigated and the experimental and analytical results are presented in Section 6.3. The cubic nonlinearity in the NPE system is examined when the parametric amplitude is fixed and the position between the coils is varied. The experimental and analytical results are presented in Section 6.4.

This chapter is concluded with a short summary. The novel contributions of this chapter are as follows:

- A simple model of a NPE system with an electromagnetic system is introduced. The induced current generated by the coils is included in the model of the NPE system.

- An electromagnetic configuration with coils connected in series to reduce the damping is presented. Reduction in damping has significant contribution on parametric amplification [64].

- The effects of parametric amplitude and cubic nonlinearity for the NPE system are demonstrated independently. The parametric amplitude can amplify the response amplitude. The cubic nonlinearity reduces the response amplitude but increases the frequency bandwidth.

6.2 Measured responses of the nonlinear parametrically excited system

In Chapter 3 the analytical responses of the linear and nonlinear parametrically excited systems are presented. For linear systems the amplitudes and frequencies of oscillations are independent quantities. However, the responses of the nonlinear systems is dependent on both. Solutions of nonlinear systems may be stable or unstable. The stable solutions are observed experimentally. In the physical test, the oscillations of the cantilever beam can either be in a stable state or on the way to one when the bifurcation happens [137].

In this section the free responses of a nonlinear parametrically excited system, the cantilever beam with an electromagnetic system, is measured in order to find the states of the periodic solutions. For the nonlinear parametrically excited system, if the parametric frequency Ω is close to twice the natural frequency ω_{n}, there are two stable and one unstable solutions. The stable solution with amplitude $a = 0$ is the trivial solution, and

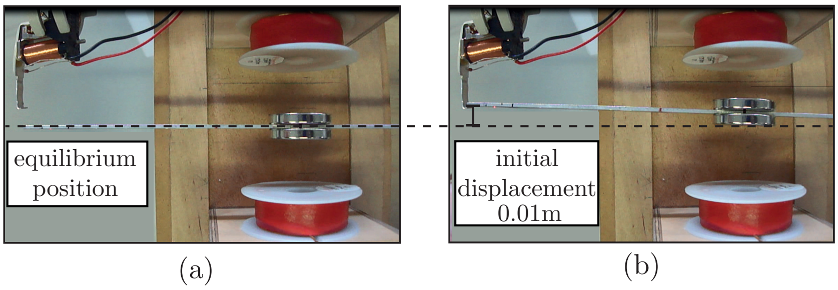

Fig. 6.1. (a) Cantilever beam at equilibrium position. (b) Cantilever beam with initial displacement applied by a relay switch from the tip.

the periodic stable solution is the nontrivial solution when the averaged amplitude is constant and $a \neq 0$. Free vibration is considered and the initial conditions are

$$z(0) = z_0, \text{ and } \dot{z}(0) = 0, \tag{6.1}$$

where the initial displacement z_0 is assumed to be 0.01m for all experimental tests. Figure 6.1 shows the relay switch, which holds the cantilever beam tip 0.01m away from the equilibrium position. The relay switch once triggered, releases the cantilever beam and starts the current flow in the coils at the same time.

The free responses of the nonlinear parametrically excited system are examined to show the stability and amplitude of the periodic solutions. The stability and amplitude of the periodic solutions depend on parametric amplification, parametric frequency, and nonlinearities. In Chapter 3 it is demonstrated that if the parametric amplitude satisfies the instability threshold, the amplitude of the response can increase. Here, the electromagnetic set-up is modified in order to reduce the electrical damping by connecting coils in series opposing connection. By reducing the damping the instability threshold is reduced. Setting up coils in series has the advantage of reducing the damping even if the distance between the coils is varied. Consequently, periodic solutions are observed even for a small parametric amplitude at parametric resonance or close to the parametric resonance. The instability threshold near the parametric resonance from Eq. (3.40) in Chapter 3 is

$$\delta_{\text{th2}} = 4\zeta - \gamma a^2, \tag{6.2}$$

where the instability threshold can be found from the total damping ζ (here the combination of electrical and mechanical damping), cubic parametric nonlinear term γ, and a is the amplitude of the response[1]. The parametric amplitude is then set to be higher than the instability threshold ($\delta > \delta_{\text{th2}}$). The instability threshold can be modified by increasing the positive cubic parametric nonlinear term γ, which is a function of AC current, the number of turns in the coil, and the distance between the coil and the magnet. It is also

---

[1] From the averaging method the solution of the nonlinear system is considered to have only one frequency component at $\frac{\Omega}{2}$. Hence, the measured response amplitude a is only considered at this frequency.

possible to optimise the nonlinear system for strong cubic parametric nonlinearity (see Section 6.4).

Since the elastic force acting on the magnets attached to the cantilever beam is created through magnetic repulsion, the relation between the displacement $z(t)$, and the resulting elastic restoring force is nonlinear. The nonlinearity generated by the electromagnetic system is calculated in the previous chapter and can be determined experimentally. To identify the relationship between the applied force and the resulting displacement, several techniques have been introduced in the literature [69, 153–155]. To estimate the nonlinear parameters of the system, a curve-fitting method used by Krauss and Nayfeh [153] has been recently modified and used in the literature. The nonlinear parameters can be estimated by curve-fitting the experimental amplitude frequency data. This method is sensitive to and dependent on the initial guesses [156]. One typical method is to use a digital force gauge attached to the magnets to measure the force applied by the electromagnetic system. Measuring the cantilever beam displacement and plotting the experimental force and displacement gives an illustration for the force applied for a given displacement. A polynomial interpolation through the experimental points can give an analytical expression. This method is limited to the force gauge accuracy and its physical connection.

In order to identify the nonlinearity in the electromagnetic system proposed in this chapter, the electromagnetic forces are calculated (see Appendix E.5). By changing the DC/AC current in the coils, the stiffness nonlinearities can be varied.

One of the objectives of this section is to illustrate that parametric amplitude and cubic parametric nonlinearity can increase the amplitude of the bounded solutions and the frequency bandwidth. The stiffness cubic nonlinearity reduces the amplitude of the bounded solutions and increases the frequency bandwidth. The effect of stiffness cubic nonlinearity for the NPE system is demonstrated in Section 6.4.

Fig. 6.2a shows the amplitude-frequency plot for the cantilever beam excited with linear time-varying and nonlinear forces from the electromagnetic system. The curve describes values of the cantilever beam displacement a as a function of parametric frequency Ω normalised by the linear natural frequency ω_{n}, and trivial responses $a = 0$ (see Section E.7). Stable branches are indicated by solid lines, and unstable branches by dashed lines, according to the result of Section E.7.

The distance between coils $h = 0.03$m is considered. Hence, the maximum displacement of the beam is limited by this distance. The maximum displacement of the beam when the magnets are close to hit the coils from the equilibrium position is 0.021m. In Fig. 6.2a this physical limit is shown with a gray line.

The DC current considered for the test in Fig. 6.2a is $I_{\mathrm{DC}} = 0.48$A, and the input AC current $I_{\mathrm{AC}} = 0.06$A with the parametric frequency Ω. The DC current is selected to generate a strong cubic nonlinearity. The AC current is chosen large enough to generate parametric amplification. The induced current is then added when magnets are moving.

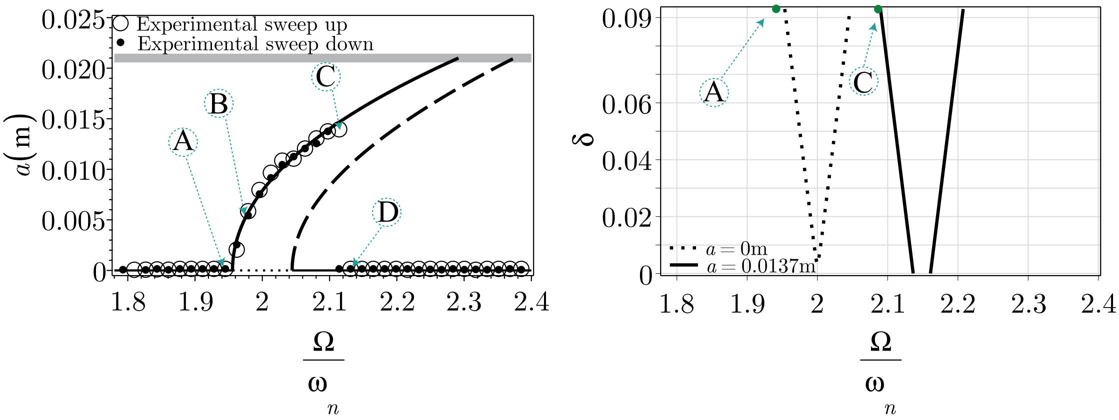

(a) **(b)**

Fig. 6.2. (a) Experimental and analytical amplitude-frequency plot for a NPE system; a cantilever beam with an electromagnetic system. System parameters are: the half distance between coils $h = 0.03$m, the measured damping ratio at point A $\zeta = 0.001$, the linear natural frequency $\omega_n = 37.11\text{rad}\,\text{s}^{-1}$, and the input current in coils in series connection when $I_\text{c} = 0.48 + 0.06\cos(\Omega t)$. The initial conditions for the experimental results are $z(0) = 0.01$m and $\dot{z}(0) = 0\text{ms}^{-1}$. (b) The transition curves for two constant amplitudes $a = 0$m and $a = 0.0137$m.

For each sweep up and sweep down test, when the response is decaying, only the input current is considered, and the induced current is neglected. The linear natural frequency $\omega_n = 37.11\text{rad}\,\text{s}^{-1}$, and the damping ratio $\zeta = 0.001$, are measured when $I_\text{DC} = 0.48$A is generated in coils. For point A in Fig. 6.2a the system parameters are calculated without considering the effect of induced current, and they are: $\delta = 0.093$, $\alpha = 1055.86\text{m}^{-2}$, and $\gamma = 131.98\text{m}^{-2}$ (see Section 5.4.2 for the relation between δ, α, and γ with DC and AC current).

There are three distinct characteristics for the amplitude-frequency curve of the NPE system (Fig. 6.2a):

1. The response peak bends over to the right. This features the characteristics of nonlinearity with restoring forces of hardening type. Hardening and softening nonlinearities are explained in Chapter 3. Fig. 6.2a exemplifies some characteristics of a nonlinear parametrically excited system. At point C in Fig. 6.2a there is a difference between the analytical and experimental responses. At point C the electrical damping generated by the electromagnetic system is higher than at point A, since a higher induced current is generated when the velocity of moving magnets increases. When the magnets are getting close to the coil, the analytical model cannot evaluate the electromagnetic behaviour accurately. Since the amplitude at the peak of the amplitude-frequency plot depends on the damping value [9], it is possible that there are other nonlinear damping sources which affect the peak. The nonlinear damping model with a quadratic damping term proposed by P. Malatkar [156] can be im-

plemented to predict the analytical results close to experimental data points. Also, Anderson et al. [157] found that the addition of quadratic damping to the nonlinear cantilever beam model can improve the agreement between the experimental and theoretical results.

2. For certain values of parametric frequency Ω, there are multiple solutions. Depending on the initial conditions, one of the two stable branches of solutions is observed experimentally. This shows the dependence of nonlinear systems on initial conditions. For example point A in Fig. 6.2a is a trivial solution. Figure 6.3c shows the beam displacement at the tip with initial conditions of $z(0) = 0.01$m and $\dot{z}(0) = 0\text{ms}^{-1}$. The beam displacement is found from measuring the velocity with the vibrometer at position 0.14m away from the support end. The velocity signal is filtered with a high-pass filter with a cutoff frequency of 0.1Hz. The beam displacement is found from integrating the velocity numerically. For calculating the displacement at the tip, the beam curvature for the first mode is considered [158]. At the start of the test the cantilever beam has shown rotational motion as well as horizontal motion. The rotational motion is small and its effect is neglected here. The total current in coils I, is plotted in Fig. 6.3a. The current frequency, the parametric frequency Ω, is set to be $72.85\text{rad}\,\text{s}^{-1}$. Also, the Power Spectrum Density (PSD) of the current shows a peak at $\Omega = 72.85\text{rad}\,\text{s}^{-1}$.

   Fig. 6.2b shows the analytical transition curve when $a = 0$. Point A is outside the transition curve when the parametric amplitude is $\delta = 0.093$. Hence, this point is not amplified as a result of the parametric amplification. From the PSD of the displacement Fig 6.3d several peaks can be identified. Peaks at Ω and 2Ω occur as a result of the electromagnetic force generated by the electromagnetic system. The maximum peak of the displacement PSD happens close to the linear natural frequency ω_n.

   The phase portrait and the Poincaré map of this test shows that the response decays in time. The phase portrait is found from the velocity versus the displacement from the start of the tests, where the relay switch is released at $t = 139\,\text{sec}$. During first few seconds, the response is influenced by the initial condition, and the phase portrait shows that the large amplitude of the response decays rapidly. The Poincaré map is plotted based on the velocity and displacement at each period $T = \frac{2\pi}{\Omega}$. The first point on the Poincaré map is placed at $t = 139\,\text{sec}$, and then for each cycle, a point is placed on the Poincaré map. All points on Poincaré map converge to zero velocity and zero displacement where the cantilever beam is at rest. The Poincaré map shows that the response is decaying.

   If the initial conditions $z(0) = 0.01$m and $\dot{z}(0) = 0\text{ms}^{-1}$ are applied when the system is on/inside the transition curve, periodic solutions are observed. From the measured

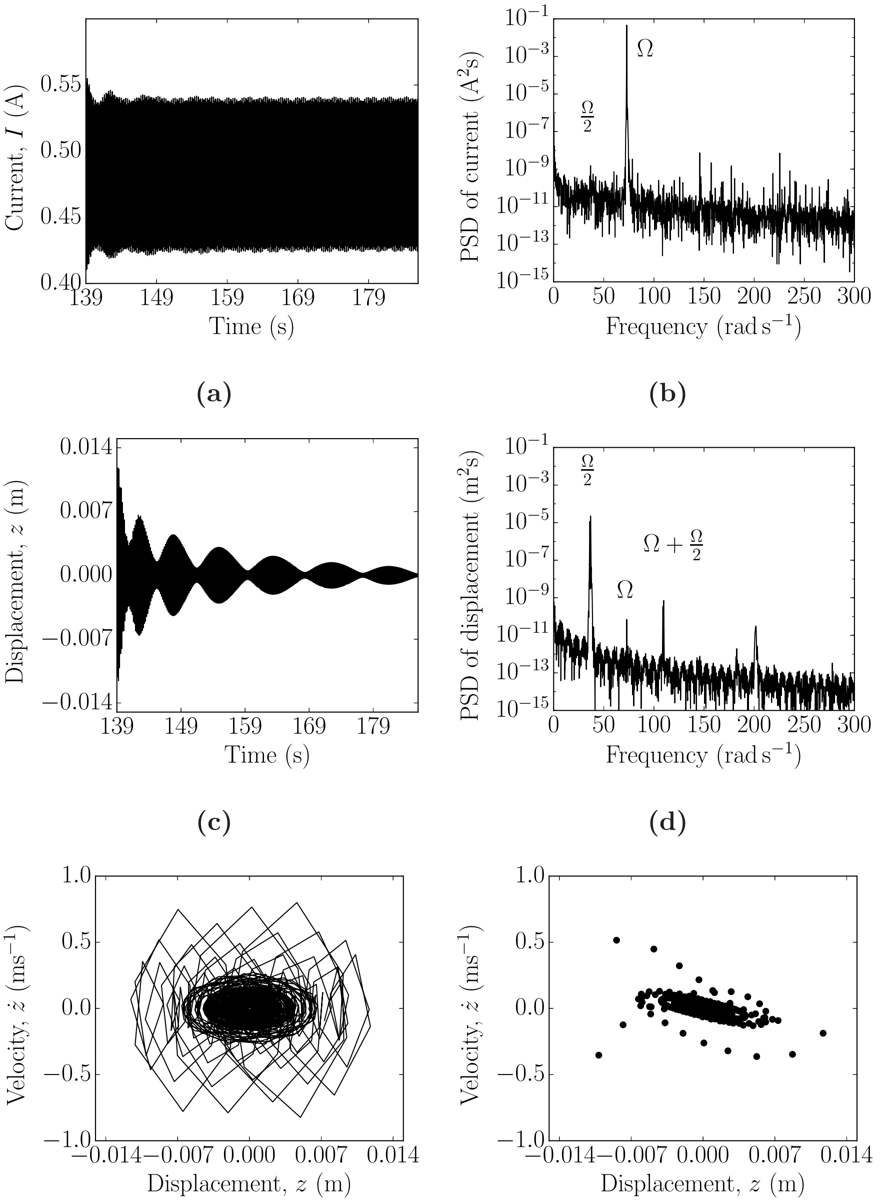

(a) (b)

(c) (d)

(e) (f)

Fig. 6.3. Experimental results for point A in Fig. 6.2a. (a) Current measured across the coils in series connection. (b) Power spectrum density of the current. (c) Measured displacement at the cantilever beam tip. (d) Power spectrum density of the displacement signal. (e) Phase portrait plot. (f) Poincaré map.

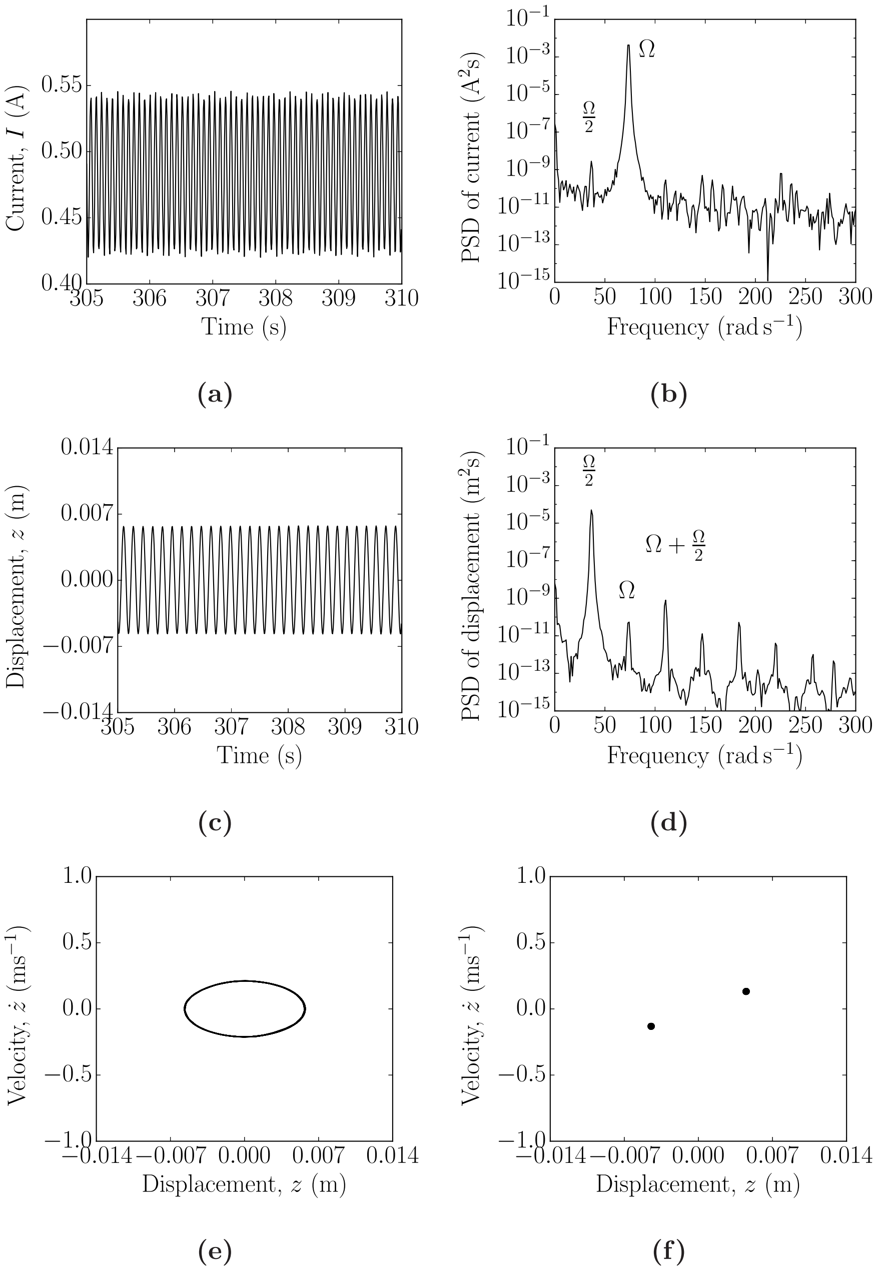

(a) **(b)**

(c) **(d)**

(e) **(f)**

Fig. 6.4. Experimental results for point B in Fig. 6.2a. (a) Current measured across the coils in series connection. (b) Power spectrum density of the current. (c) Measured displacement at the cantilever beam tip. (d) Power spectrum density of the displacement signal. (e) Phase portrait plot. (f) Poincaré map.

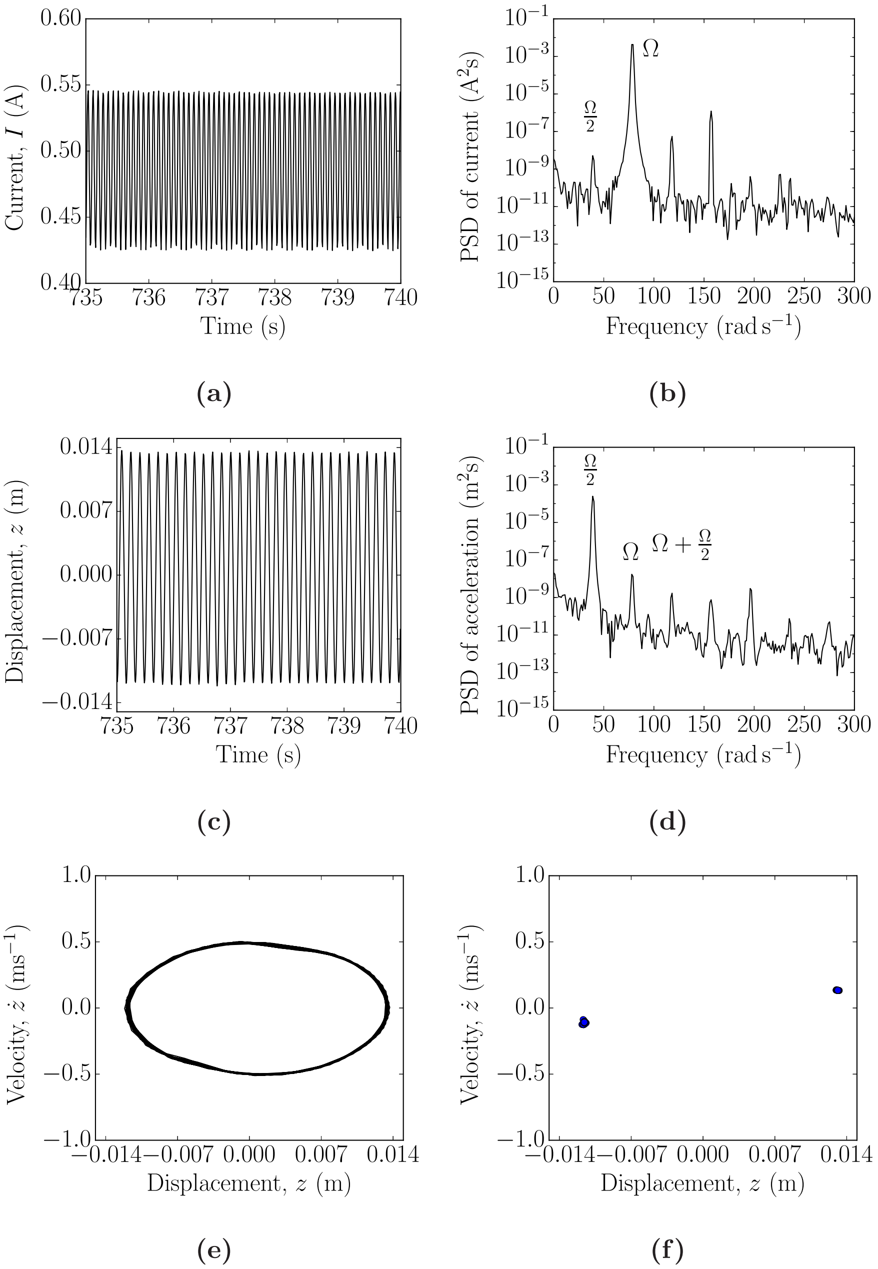

(a) **(b)**

(c) **(d)**

(e) **(f)**

Fig. 6.5. Experimental results for point C in Fig. 6.2a. (a) Current measured across the coils in series connection. (b) Power spectrum density of the current. (c) Measured displacement at the cantilever beam tip. (d) Power spectrum density of the displacement signal. (e) Phase portrait plot. (f) Poincaré map.

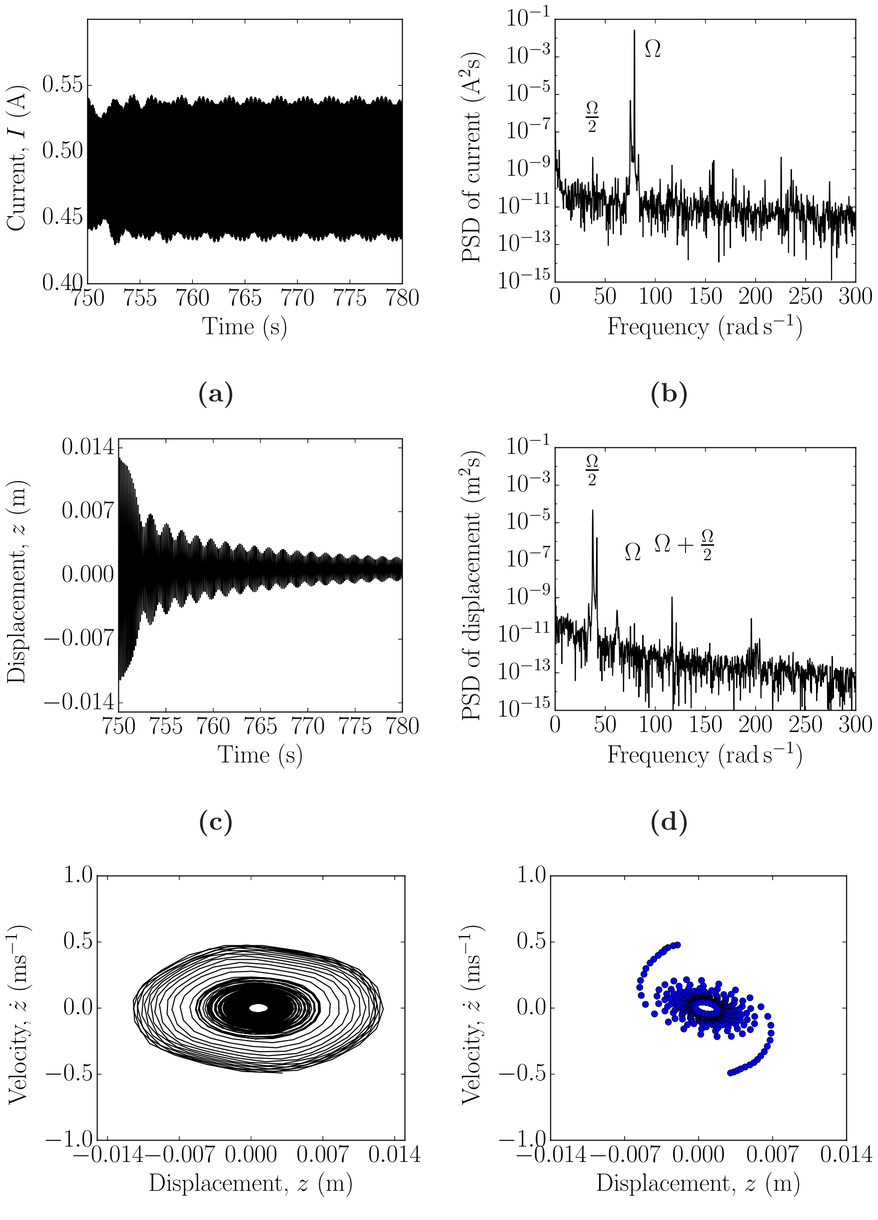

(a) **(b)**

(c) **(d)**

(e) **(f)**

Fig. 6.6. Experimental results for point D in Fig. 6.2a. (a) Current measured across the coils in series connection. (b) Power spectrum density of the current. (c) Measured displacement at the cantilever beam tip. (d) Power spectrum density of the displacement signal. (e) Phase portrait plot. (f) Poincaré map.

displacement after the decay of the transient response (approximately 40 seconds), and when the periodic solutions are settled, then the parametric frequency is altered. The parametric frequency Ω, is increased for sweep up tests, then decreased slowly to allow periodic responses to settle. In this experiment, the parametric frequency is increased or decreased in increments of 0.1Hz. For the sweep up test, after point A in Fig. 6.2a, point B is considered at parametric frequency $\Omega = 73.47\text{rad}\,\text{s}^{-1}$. Point B is inside the transition curve, hence the periodic response is expected. 80 seconds after the initial condition, both the total current in the coils and the beam displacement are recorded and shown in Figs. 6.4a and 6.4c. In these figures the maximum amplitude of the beam displacement does not change significantly since the transient response is decayed.

Frequencies Ω, $\frac{\Omega}{2}$, $\frac{3\Omega}{2}$, and 2Ω can be seen in PSD of the displacement signal (see Fig. 6.4d). The phase portrait plot Fig. 6.4e shows that point B is a periodic solution. The Poincaré map in Fig. 6.4f shows the two points, which represent two frequencies in the solution with the ratio of one half. These two points show the displacement and velocity signal contains frequencies of $\frac{\Omega}{2}$ and Ω. The Poincaré map is plotted based on the measured velocity and displacement signals, and their values at each period $T = \frac{2\pi}{\Omega}$ is shown. The phase portrait and the Poincaré map are plotted for 5 seconds of measurement. The displacement of the beam and the current in the coils for this duration are shown in Figs. 6.4c and 6.4a.

3. There are discontinuous jumps in the response, as a consequence of the bent peak in the presence of hardening or softening nonlinearity. The analytical stable branch in Fig. 6.2a does not show that the stable nontrivial solutions will reduce or stop at high frequencies. There are several reasons for this:

   - The damping of the system is not sufficient to reduce the amplitude of the parametrically excited system.
   - As long as parametric amplitude can overcome the instability threshold the amplitude of the periodic response increases.

   However, in a physical system it is challenging to maintain all the above criteria to keep the solution on the higher stable branch up to high frequencies. A jump can happen from the upper stable branch to the lower stable branch.

   By increasing the parametric frequency Ω, the amplitude of the response increases. This increase in amplitude can also be identified from the transition curve. Although the transition curves are used for linear parametrically excited systems, here for a constant amplitude, they are implemented to identify the parametric amplification and the frequencies where jumps occur. Fig. 6.2b shows the analytical transition curve for point C in Fig. 6.2a when the amplitude of the response is $a = 0.0137$m.

This point is on the transition curve for the given amplitude and is a periodic response (see Fig. 6.5e).

The displacement signal and the total current in the coils in series are plotted in Figs. 6.5c and 6.5a. The displacement of the cantilever beam is not symmetric to the equilibrium position; this happens when the magnets on the cantilever beam move slightly from their original position or the beam is not exactly in the centre between the coils. During the experiments several preparation and measurements are carried out to keep the beam motion symmetric. The PSD of the displacement signal shows that the parametric amplification has happened and hence, the peak at $\frac{\Omega}{2}$ is dominant (see Fig. 6.5d). The phase portrait and the Poincaré map also shows the periodic response (see Figs. 6.5e and 6.5f).

After point C in Fig. 6.2a the amplitude of the response is increased smoothly until it jumps to the lower stable branch (trivial solution $a = 0$), and stays at rest. The transition curve for a maximum amplitude of $\delta = 0.093$ shows where this jump can happen. If the previous amplitude is not large enough to keep the response inside the transition curve, the response jumps to the lower branch. Point D in Fig. 6.2a indicates where the jump happens. Also the displacement of this point, Fig. 6.6c, shows a decaying response after the jump. In this case, vertical and rotational motions can be seen during the experiment in addition to the horizontal motion. As a result of this the PSD of the current and displacement signals shows other frequencies with a high magnitude as well as at Ω and $\frac{\Omega}{2}$. The phase portrait and Poincaré map (Figs. 6.6e and 6.6f) show that the response decays over time.

By reducing the parametric frequency Ω the amplitude of the response is approximately zero, and the beam response decays until the zero solution turns unstable and jumps to the higher branch. This jump is observed experimentally. This jump shows that the system is affected by nonlinearity. The jump of free responses of a nonlinear parametrically system depends on the parametric amplitude and damping as well as nonlinearities.

6.3 Parametric amplification with parametric amplitude and cubic parametric nonlinearity

In order to increase the parametric amplification, the parametric amplitude and cubic parametric amplitude can be increased as explained in Chapter 3. In this section three positions of the coils $h = 0.035\text{m}, 0.03\text{m}$ and 0.025m are considered. Since the coils are connected in series the damping ratios for these three positions are equal to $\zeta = 0.001$. A fixed damping ratio makes the comparison easier since the effect of damping is not included. The measured damping ratio and natural frequency for each test are presented

Table 6.1: System parameters for tests when the coils are connected in series. The AC current and the half position between coils h are varied.

Tests	h (m)	I_{DC} (A)	I_{AC} (A)	ζ	ω_{n} ($\mathrm{rad\,s^{-1}}$)	α ($\mathrm{m^{-2}}$)	δ	γ ($\mathrm{m^{-2}}$)
Low amplitude, Fig. 6.7	0.035	0.98	0.06	0.001	39.81	954.05	0.047	59.62
High amplitude, Fig. 6.7	0.035	0.98	0.155	0.001	40.12	956.4	0.122	152.8
Low amplitude, Fig. 6.8	0.03	0.97	0.035	0.001	49.23	1214.5	0.03	43.37
High amplitude, Fig. 6.8	0.03	0.97	0.08	0.001	49.23	1214.5	0.07	99.14
Low amplitude, Fig. 6.9	0.025	0.55	0.055	0.01	50.3	1262.17	0.093	138.83
High amplitude, Fig. 6.9	0.025	0.55	0.095	0.001	50.3	1279.46	0.149	221

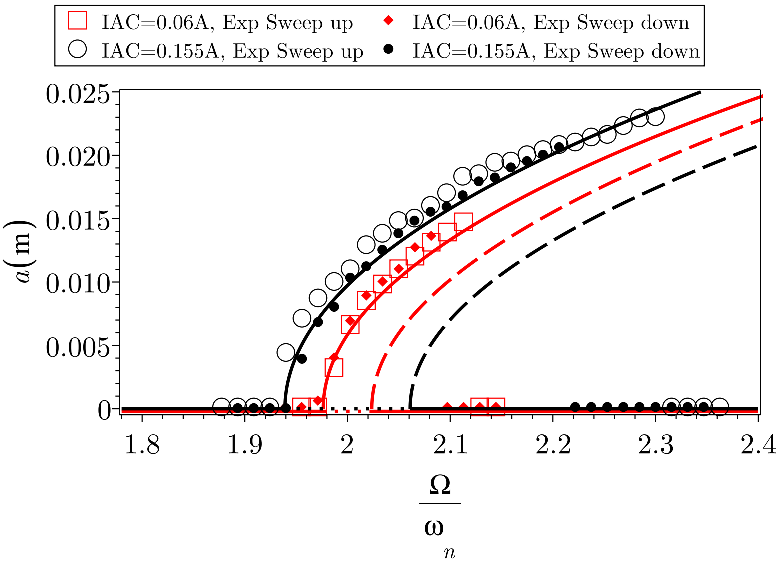

Fig. 6.7. Experimental and analytical amplitude-frequency plot when the coils are in position $h = 0.035$m. The results in red and black correspond to low and high AC currents. The system parameters are shown in Table 6.1. Stable branches are indicated by solid lines, and unstable branches by dashed lines, according to the result of Section E.7. The unstable trivial solutions are shown by dotted lines.

in Table 6.1.

The DC current is kept constant to keep the cubic nonlinearity approximately equal. Comparison between each position is based on the effect of parametric amplitude and for simplicity the cubic nonlinearity is kept constant for each position. Then, the increase in AC current and its effect on the amplitude-frequency curve is illustrated. The DC currents for positions $h = 0.035\text{m}, 0.03\text{m}$ and 0.025m are $0.98A$, $0.97A$, and $0.55A$ respectively. The DC and AC current for these tests are chosen to keep the cantilever beam motion in a range in which the magnets do not hit the coils and at the same time the amplitude-frequency plots can be compared for each cases. In Table 6.1 the DC/AC current, the damping ratio ζ, and the linear natural frequency ω_n are the measured values and the cubic nonlinearity α, parametric amplitude δ, and cubic parametric nonlinearity γ are calculated based on the DC/AC current (see Section 5.4.2).

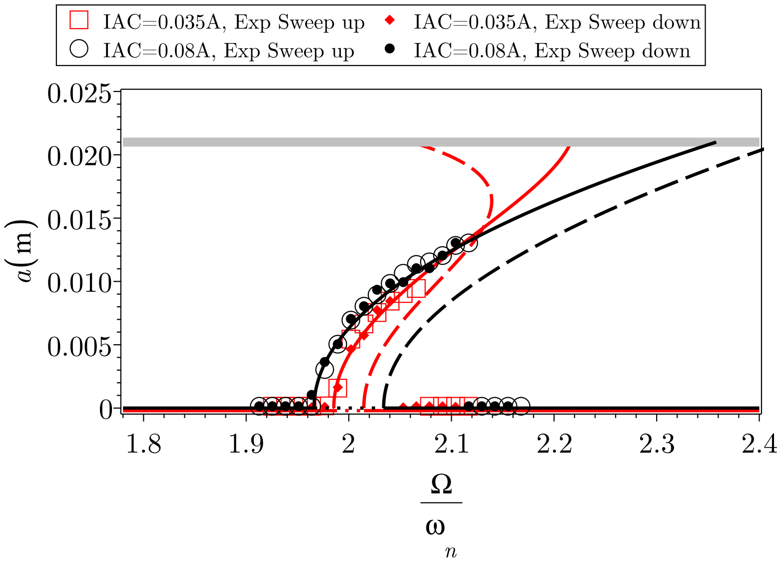

Fig. 6.8. Experimental and analytical amplitude-frequency plot when the coils are in position $h = 0.03$m. The results in red and black correspond to low and high AC currents. The system parameters are shown in Table 6.1. Stable branches are indicated by solid lines, and unstable branches by dashed lines. The unstable trivial solutions are shown by dotted lines.

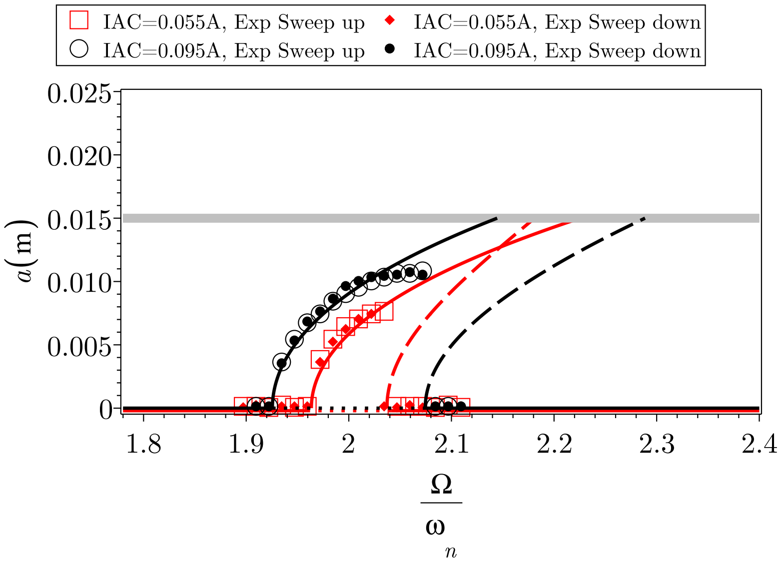

Fig. 6.9. Experimental and analytical amplitude-frequency plot when the coils are in position $h = 0.025$m. The results in red and black correspond to low and high AC currents. The system parameters are shown in Table 6.1. Stable branches are indicated by solid lines, and unstable branches by dashed lines. The unstable trivial solutions are shown by dotted lines.

For position $h = 0.035$m two different AC currents are applied, such as 0.06A and 0.0155A. It is expected that the system with higher AC current generates higher parametric amplitude δ, and cubic parametric nonlinearity γ. The amplitude-frequency plot is shown in Fig. 6.7. Fig. 6.7 shows both experimental and analytical results. The increase in parametric amplitude increases the amplitude of the response and expands the frequency bandwidth. The positive cubic parametric nonlinearity can also increase the magnitude of the response. In these tests, the parametric amplitude and cubic parametric nonlinearity are linked since they both change with the AC current. Hence, considering one independent of the other is not possible. In Fig. 6.7, it is shown that increasing the AC current increases the parametric amplitude and frequency bandwidth. This is beneficial for the applications where increasing the AC current is possible.

For position $h = 0.03$m two different AC currents are applied, such as 0.035A and 0.08A. Similar to the previous case, it is expected that the system with higher AC current generates higher parametric amplitude δ, and cubic parametric nonlinearity γ. The amplitude-frequency plot is shown in Fig. 6.8. From Table 6.1 the parametric amplitude δ, for each case can be compared. The parametric amplitude δ, is higher when AC current is 0.08A.

For position $h = 0.025$m again two different AC currents are applied, such as 0.055A and 0.095A. The amplitude-frequency plot is shown in Fig. 6.9. Since the coils are close to the cantilever beam the analytical model is not able to predict the experimental results at a frequency higher than the parametric frequency. The increase in the AC current has an effect on increasing the amplitude of the response and frequency bandwidth. Strong cubic nonlinearity is expected in this case (see Table 6.1).

From the tests explained in this section, the effect of increasing the AC current on parametric amplitude is illustrated. The increase in AC current and consequently the increase in induced current as well as the parametric amplitude and positive cubic parametric nonlinearity has a direct effect on increasing the amplitude of the response. Increasing damping or cubic nonlinearity can reduce the effect of parametric amplification. As the amplitude of the response increases and as the magnets get closer to the coils, the damping increases which results in the bend in the amplitude-frequency curve. However, in contrast the induced current is increased which increases the parametric amplitude. From the experimental results it can be seen that at position $h = 0.025$m the effect of damping is stronger than the effect of induced current and hence the curve is bent down. The experimental results for this case, $h = 0.025$m is different from the analytical expression, but at positions $h = 0.035$m and $h = 0.03$m, the effect of damping and induced current are calculated accurately.

6.4 The effects of cubic stiffness nonlinearity

The cubic stiffness nonlinearity in the NPE system reduces the amplitude of the response compared to the amplitude of the LPE system at parametric resonance. However, it can extend the frequency bandwidth. At different positions between the coils and magnets, the strong cubic nonlinearity can reduce jump-down frequencies and the amplitudes of displacement at these frequencies. These concepts are shown analytically and experimentally in this section.

The cubic nonlinearity generated by the electromagnetic system increases when the DC current in coils in series is increased. Also, from the physical derivation, Eq. (5.21), it can be seen that the cubic nonlinearity α, is a function of half of the distance between the coils, the radius of the coil, number of turns in the coil and the magnetic dipole. Here, the half distance between the coils is altered to investigate the changes in the cubic stiffness nonlinearity. The maximum cubic stiffness can be found by differentiating α with respect to h. The maximum $\frac{\alpha}{\delta}$ ratio can be seen in Fig. 6.10 for a given DC current based on the analytical expressions. Close to position $h = 0.025$m, the highest cubic nonlinearity is expected, and for positions smaller than 0.025m the effect of cubic nonlinearity is not considered here. When coils are very close to the magnets the magnets hit the coils and change the initial conditions, hence, positions smaller than 0.025m are not considered. At positions lower than 0.025m the damping effect is more dominant than the cubic nonlinearity and the analytical model has not predicted the behaviour of the system accurately.

Note that, the main aim of this section is to investigate the effect of cubic nonlinearity at different positions on response amplitude, while the AC input current is fixed. However, from the measured current, a slight difference is observed, although the aim is to keep the current constant. This difference can be due to measurements over different days and the discrepancy of the LAMBDA ZUP to generate the current from the input voltage. Hence, for each position under study, the accurately measured current is considered. The input current, I_{c}, is slightly different for positions $h = 0.035$m, 0.03m, and 0.025m, however their effect on the parametric amplitude and the cubic parametric amplitude is neglected.

Fig. 6.10 shows the $\frac{\alpha}{\delta}$ ratio, for two input DC/AC currents in the coils I_{c}. In each graph, two experimental cases are shown by the label ⊗ for two positions h, where the $\frac{\alpha}{\delta}$ ratio is varied. Table 6.2 presents the system parameters for cases marked in Fig. 6.10. Similar to the previous section, the damping ratio ζ, and the linear natural frequency ω_{n}, are the measured values and the cubic nonlinearity α, parametric amplitude δ, and cubic parametric nonlinearity γ are calculated based on the DC/AC current.

The analytical amplitude-frequency plot for the four points specified in Fig. 6.10d are plotted to show the effect of cubic nonlinearity (see Fig. 6.11). The analytical amplitude-frequency is plotted based on the limitation of each position for reaching highest amplitude

Table 6.2: System parameters for tests when the coils are connected in series. The half position between the coils h is varied.

Tests	h (m)	I_{DC} (A)	I_{AC} (A)	ζ	ω_{n} (rad s^{-1})	α (m^{-2})	δ	γ (m^{-2})
Fig. 6.12a	0.03	0.92	0.14	0.001	48.6	1203.19	0.129	183.1
Fig. 6.12b	0.035	0.97	0.155	0.001	40.12	956.4	0.122	152.82
Fig. 6.13a	0.03	0.56	0.15	0.001	37.99	1059.95	0.206	293.55
Fig. 6.13b	0.035	0.57	0.15	0.001	32.15	820.4	0.172	215.89
Fig. 6.14a	0.025	0.5	0.055	0.01	50.3	1262.17	0.093	138.83
Fig. 6.14b	0.03	0.48	0.06	0.001	37.11	1055.86	0.092	131.98
Fig. 6.15a	0.03	0.98	0.08	0.001	49.23	1214.5	0.069	99.14
Fig. 6.15b	0.035	0.96	0.06	0.001	39.81	954.05	0.047	59.62

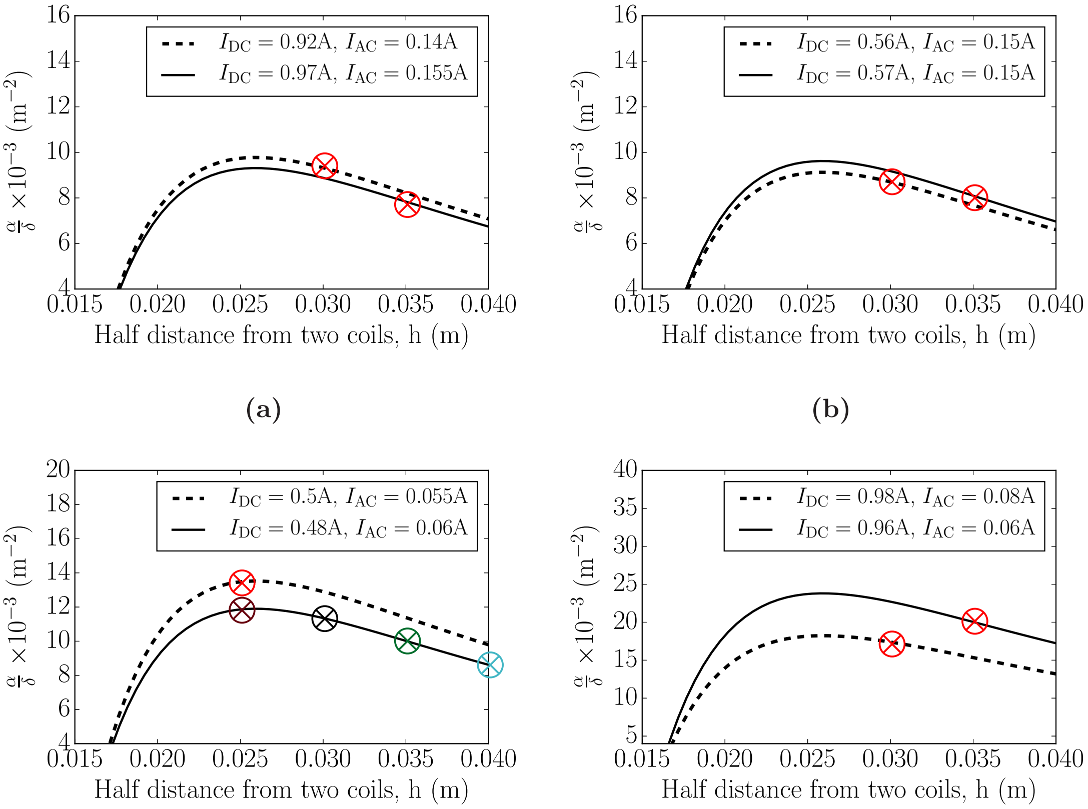

(a) (b)

(c) (d)

Fig. 6.10. The ratio between the cubic nonlinearity α, and parametric amplitude δ for different positions and input current. The $\otimes$ labels show positions, which are chosen to compare two cases in each individual graph with the current specified. The comparison is based on the amplitude-frequency plot shown in Figs. 6.12, 6.13, 6.14, and 6.15.

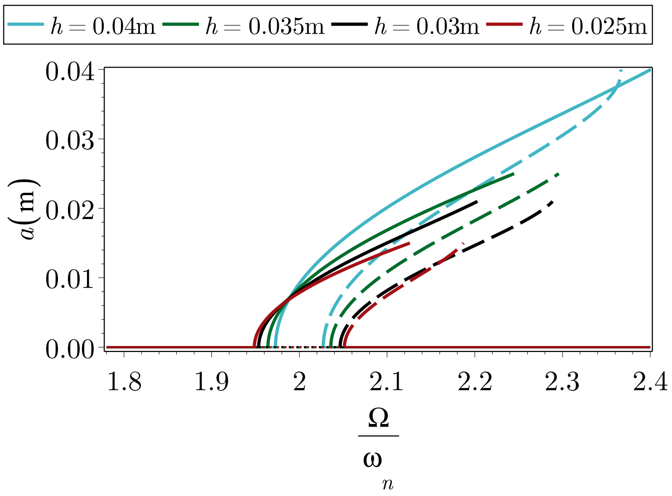

Fig. 6.11. Analytical amplitude-frequency plot based on the points in Fig. 6.10c.

before the magnets hit the coils. From the points specified in Fig. 6.10d, we can see that at $h = 0.025$m the highest $\frac{\alpha}{\delta}$ is found and for the positions higher than 0.025 the $\frac{\alpha}{\delta}$ is reduced. The effect of cubic stiffness nonlinearity vanishes as the coils separated. Consequently, the response amplitude is increased. Also, the frequency bandwidth is increased as the cubic nonlinearity is reduced.

Based on the result shown in Fig. 6.10a, the $\frac{\alpha}{\delta}$ ratio at position $h = 0.03$m is larger than position $h = 0.035$m. The amplitude-frequency plot for the two points marked in Fig. 6.10a shows that where the $\frac{\alpha}{\delta}$ is lower, the amplitude of the upper stable branch is higher. The amplitude-frequency plot is shown in Fig. 6.12a for position $h = 0.03$m and in Fig. 6.12b for position $h = 0.035$m. By comparing these two graphs, it can be seen that from both experimental and analytical results the case with the higher cubic nonlinearity (Fig. 6.12a) has the lower amplitude. Also, the jump-frequency is lower for the case with high cubic nonlinearity.

Reducing the DC current, compared to the previous test, eliminates the effect of cubic nonlinearity. The amplitude-frequency of the two marked points in Fig. 6.10b shows that the case at lower h has been affected by the highest cubic nonlinearity. The amplitude-frequency curve for the case with high cubic nonlinearity is plotted in Fig. 6.13a and the case at position $h = 0.035$m with lower nonlinearity is shown in Fig. 6.13b. Comparing these experimental and analytical results with the previous case (Fig. 6.12) shows the highest amplitude of the response is achieved for lower DC current.

The cubic nonlinearity is at its maximum at position $h = 0.025$m (see Fig. 6.10c). The amplitude-frequency curve at this point (see Fig. 6.14a) is compared with the amplitude-frequency at point $h = 0.03$m (Fig. 6.14b). At a given frequency the response amplitude for the case, Fig. 6.14a with higher cubic nonlinearity, is smaller than the case with weak cubic nonlinearity (see Fig. 6.14b). Also, at small distances between the coils, the effect of nonlinear damping should be included which is not considered in the analytical model.

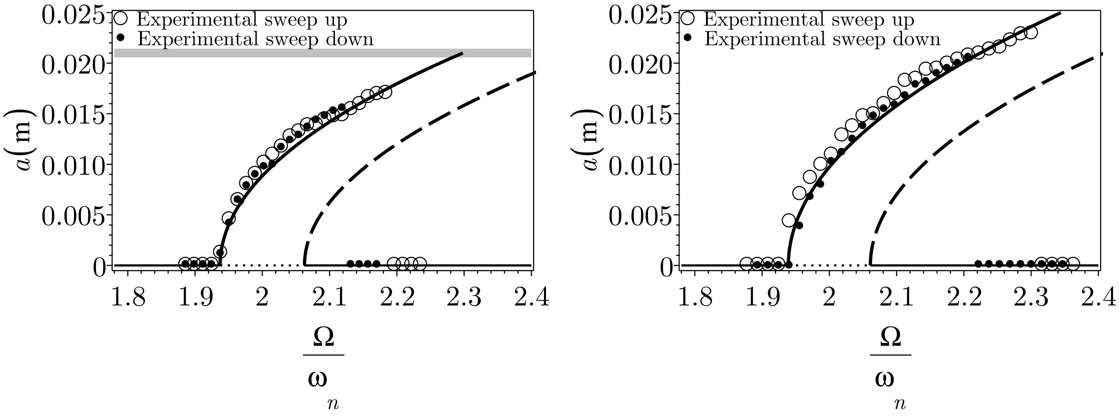

(a) **(b)**

Fig. 6.12. Experimental and analytical amplitude-frequency plot. (a) $h = 0.03$m, $I_{\rm DC} = 0.92A$ and $I_{\rm AC} = 0.14A$. (b) $h = 0.035$m, $I_{\rm DC} = 0.97A$ and $I_{\rm AC} = 0.155A$. The system parameters are shown in Table 6.2. Stable branches are indicated by solid lines, and unstable branches by dashed lines. The unstable trivial solutions are shown by dotted lines.

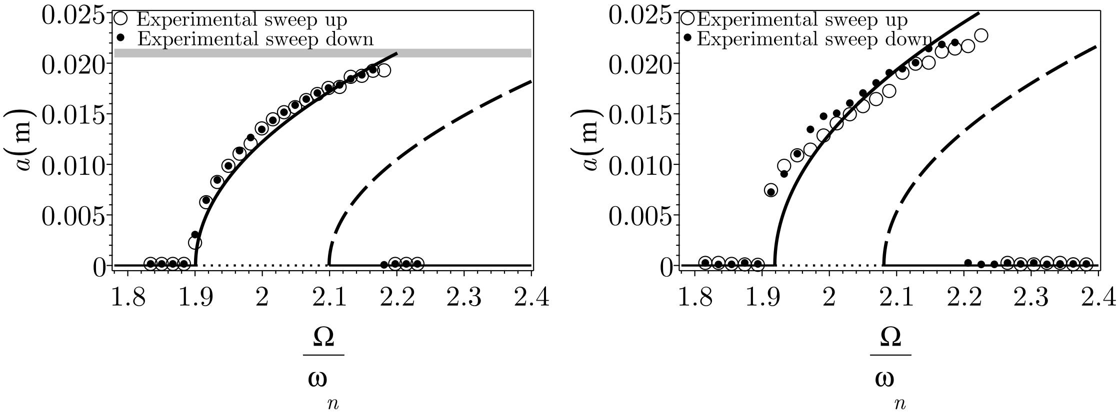

(a) **(b)**

Fig. 6.13. Experimental and analytical amplitude-frequency plot. (a) $h = 0.03$m, $I_{\rm DC} = 0.56A$ and $I_{\rm AC} = 0.15A$. (b) $h = 0.035$m, $I_{\rm DC} = 0.57A$ and $I_{\rm AC} = 0.15A$. The system parameters are shown in Table 6.2. Stable branches are indicated by solid lines, and unstable branches by dashed lines. The unstable trivial solutions are shown by dotted lines.

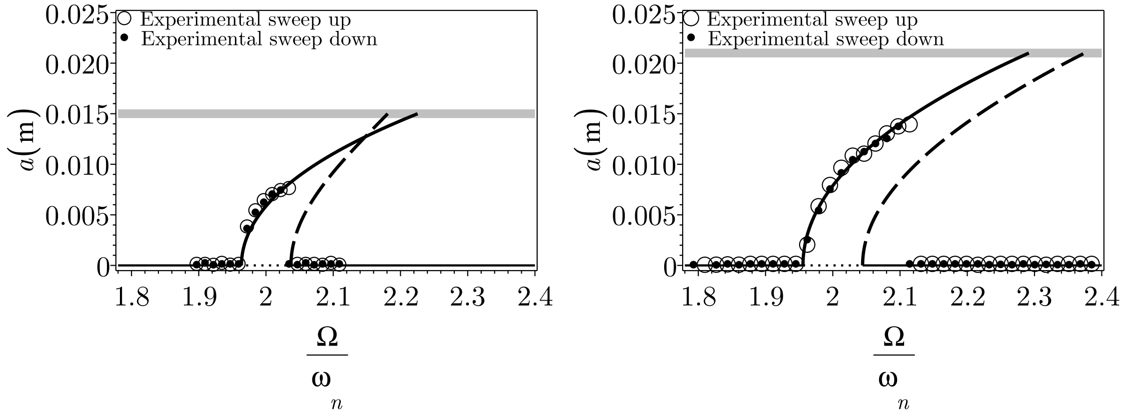

(a) (b)

Fig. 6.14. Experimental and analytical amplitude-frequency plot. (a) $h = 0.025$m, $I_{\mathrm{DC}} = 0.5A$ and $I_{\mathrm{AC}} = 0.055A$. (b) $h = 0.035$m, $I_{\mathrm{DC}} = 0.48A$ and $I_{\mathrm{AC}} = 0.06A$. The system parameters are shown in Table 6.2. Stable branches are indicated by solid lines, and unstable branches by dashed lines. The unstable trivial solutions are shown by dotted lines.

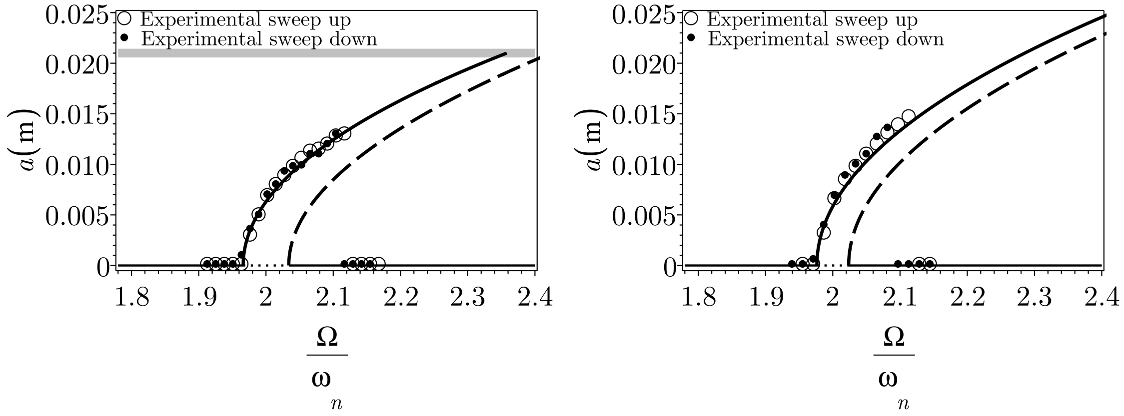

(a) (b)

Fig. 6.15. Experimental and analytical amplitude-frequency plot. (a) $h = 0.03$m, $I_{\mathrm{DC}} = 0.98A$ and $I_{\mathrm{AC}} = 0.08A$. (b) $h = 0.035$m, $I_{\mathrm{DC}} = 0.96A$ and $I_{\mathrm{AC}} = 0.06A$. The system parameters are shown in Table 6.2. Stable branches are indicated by solid lines, and unstable branches by dashed lines. The unstable trivial solutions are shown by dotted lines.

The DC and AC currents are altered for position $h = 0.03$m and $h = 0.035$m in Fig. 6.10d to have slightly higher $\frac{\alpha}{\delta}$ ratio at position $h = 0.035$m. However, this difference is not enough to affect the amplitude-frequency curves. Comparing the amplitude-frequency (Figs. 6.15a and 6.15b) for these two positions marked in Fig. 6.10d shows that the amplitude of the response at a given frequency is slightly higher when position $h = 0.035$m, although it has a slightly higher $\frac{\alpha}{\delta}$ ratio. From this comparison we can conclude that the difference between the $\frac{\alpha}{\delta}$ ratio at higher positions has to be significantly larger than small positions to change amplitude of the response.

6.5 Concluding remarks

The averaging method was used as an analytical approach in this chapter to find the response of the cantilever beam with an electromagnetic system with strong nonlinearity. The electromagnetic forces from both the input current in the coils, and the induced current generated by the back e.m.f were implemented in the analytical model. Experimental results presented in this chapter agree with the analytical model. The time-varying stiffness generated by the electromagnetic system was found to amplify the response amplitude near parametric resonance. Using a series configuration of coils reduces the electrical damping, consequently increasing the response amplitude. Also, the cubic stiffness nonlinearity was increased by changing the coil-to-coil distance.

To conclude, the parametric study presented in this chapter shows that a signal can be amplified, and its frequency bandwidth can be broadened using the proposed NPE system. This design can be implemented experimentally and theoretically for electromagnetic actuators, high pass filters, and amplifiers. The validated analytical model also enables designers to optimise design parameters.

Chapter 7

Experimental investigations of a nonlinear parametrically excited system subject to harmonic base excitations

7.1 Introduction

A Nonlinear Parametrically Excited (NPE) system subjected to a harmonic base excitation is investigated experimentally. This chapter demonstrates the effect of cubic stiffness nonlinearity and cubic parametric nonlinearity on the response of the system. These nonlinearities are generated by the electromagnetic system described in Chapter 5. The effect of the phase difference between the base excitation with the parametric excitation is also investigated. A careful selection of system parameters, such as relative phase and cubic parametric nonlinearity, can result in significant parametric amplification, and can prevent the jump from upper to lower stable branches.

PE systems can be exploited for amplification and attenuation which vary strongly with parametric excitation and the base excitation amplitudes. The response amplification of PE systems has been an attractive topic for designing vibration energy harvesters. Energy harvesting from LPE systems has been investigated in [72, 79, 94, 96–98]. Jia et al. demonstrated an experimental macro-sized electromagnetic harvester prototype driven into parametric resonance [12]. They presented that the parametrically excited harvester has an order of magnitude higher peak power density and a 50% increase in the half power band due to the amplification of the mechanical vibration at parametric resonance and nonlinear resonant peak, compared to the prototype directly driven at fundamental resonance. However, they have mentioned that overcoming the instability threshold has been one of the main reasons to reduce parametric amplification. The instability threshold can be reduced when the damping in the system is reduced.

Vijay Kumar et al. demonstrated the phase dependence of a NPE oscillator for response amplification and suppression purposes [159]. They considered a cantilever beam simultaneously actuated by longitudinal and transverse base excitations to provide parametric and direct excitation. They studied the effect of hardening nonlinearity and phase difference on parametric amplification and attenuation. Their experimental study is limited to the response amplitude only at parametric resonance. The results shown in this chapter are in agreement with the work done by Vijay Kumar et al. [159]. However, in this chapter the effect of phase difference is studied at different parametric frequencies for the response amplitude of the upper and the lower stable branches. Several parametric studies are carried out in this chapter to show the phase dependence of parametric amplification when strong cubic stiffness nonlinearity is observed.

The NPE system investigated experimentally in this chapter can be employed in principle for designing a vibration energy harvester. For the proposed NPE harvester the instability threshold is overcome by designing an electromagnetic system with coils connected in series. The reduction of damping in this way is demonstrated in Appendix E.2. In comparison with the study by Jia et al. [12, 95, 97–99, 101], the electromagnetic nonlinearities and the optimised phase difference are included in the design of the energy harvester. It is shown in this chapter that by introducing the electromagnetic nonlinearities and by optimising the phase difference the frequency bandwidth and the response amplitude can be increased.

The experimental set-up for the cantilever beam on a shaker is explained in Chapter 5. The mechanism used to vary the phase difference between the base excitation and current generated in coils is investigated in Section 7.2.1. A brief analysis of the nonlinear response is presented in Section 7.3 using the equation of motion. The effect of system parameters such as cubic nonlinearity, parametric amplitude, phase difference and base excitation amplitude are studied both experimentally and analytically in Sections 7.4.1, 7.4.2 and 7.4.5, respectively. This chapter is concluded with a short summary.

The novel contributions of this chapter are as follows:

- The effect of the induced current and the electrical damping is included in the model of the NPE system. The induced current in the coils is generated as result of the moving magnet between the coils. For a harmonically excited cantilever beam with a moving magnet the effect of induced current is not negligible.

- The analytical model predicts the response of the NPE system subject to harmonic base excitations. This is shown from the agreement between the experimental and analytical results for different system parameters.

- The effects of the base excitation amplitude and the parametric amplitude on parametric amplification is shown independently. In previous studies for a vertically excited cantilever beam, the parametric excitation is dependent on base excitation.

- An experimental set-up is introduced to alter the phase difference between the base excitation and the parametric excitation independently.

- The effects of parametric amplitude are demonstrated experimentally and analytically. The parametric amplitude can pump the response amplitude when the phase difference between the base excitation and the parametric amplitude is $\phi = \frac{\pi}{2} \pm n\pi$ for the upper stable branch and $\phi = \pm n\pi$ for the lower stable branch. The phase control allows us to increase the response amplitude and frequency bandwidth. By adjusting the phase it is possible to control the jumps between the upper stable branch and the lower stable branch.

7.2 Experimental set-up

A clamped-free cantilever beam is fixed to a shaker plate (Fig. 7.1). The cantilever beam with an electromagnetic system is excited in the transverse direction. The mechanical properties and dimensions of the cantilever beam and the electromagnetic system are shown in Table 5.1. In this chapter, half of the distance between the coils, h, is equal to 0.03m and the maximum beam displacement is 0.022m as the magnets hit the coils at a greater displacement than this value.

A LDS-Dactron shaker control system from Brüel and Kjær is used. The shaker control system consists of a controller, an amplifier, and a shaker to convert the signal that describes the desired test into vibratory motion. The accelerometer attached to the shaker plate sends an electronic signal to the control system to be measured (see Fig. 7.1). The controller uses this information to control the oscillation frequency of the shaker plate while maintaining a constant peak displacement.

An Arduino Due[1] is used to regulate the voltage passed to the current generator. The current generator is a LAMBDA ZUP, which generates current for the coils in the electromagnetic system. Figure 7.2 shows the experimental set-up used to generate the periodic electromagnetic stiffness on a cantilever beam.

7.2.1 Phase difference between the base and parametric excitation

The relative phase difference between the base and parametric excitation is controlled by adjusting the phase between the shaker acceleration and current supplied to the coils. To generate a current with various phase differences with the acceleration of the shaker, an Arduino Due as described in Section 7.2 was programmed. While the Arduino generates a cosine voltage signal when initialised, it cannot consistently be coordinated with the

---

[1] The Arduino Due is a 32-bit ARM core microcontroller.

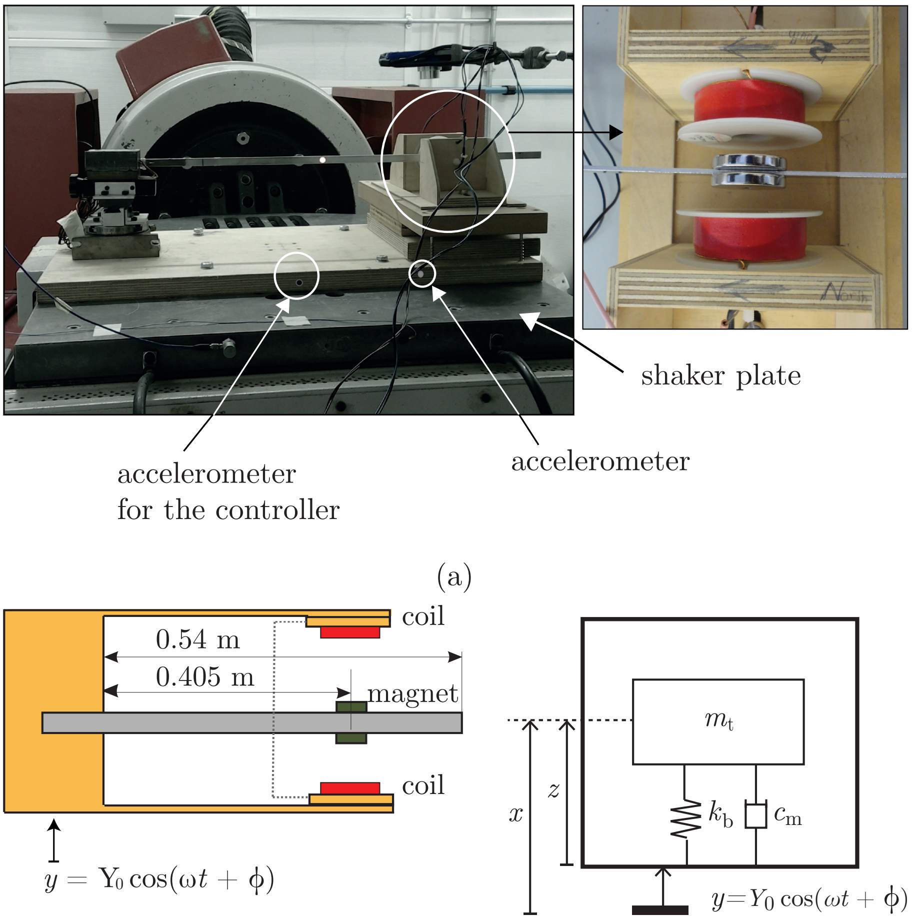

(a)

(b)

(c)

Fig. 7.1. (a) Experimental set-up consisting of a cantilever beam on a shaker and an electromagnetic system. (b) Schematic model of a cantilever beam under transverse base excitation. (c) A SDOF system with linear stiffness and damping subject to harmonic base excitation represents the clamped-free cantilever beam.

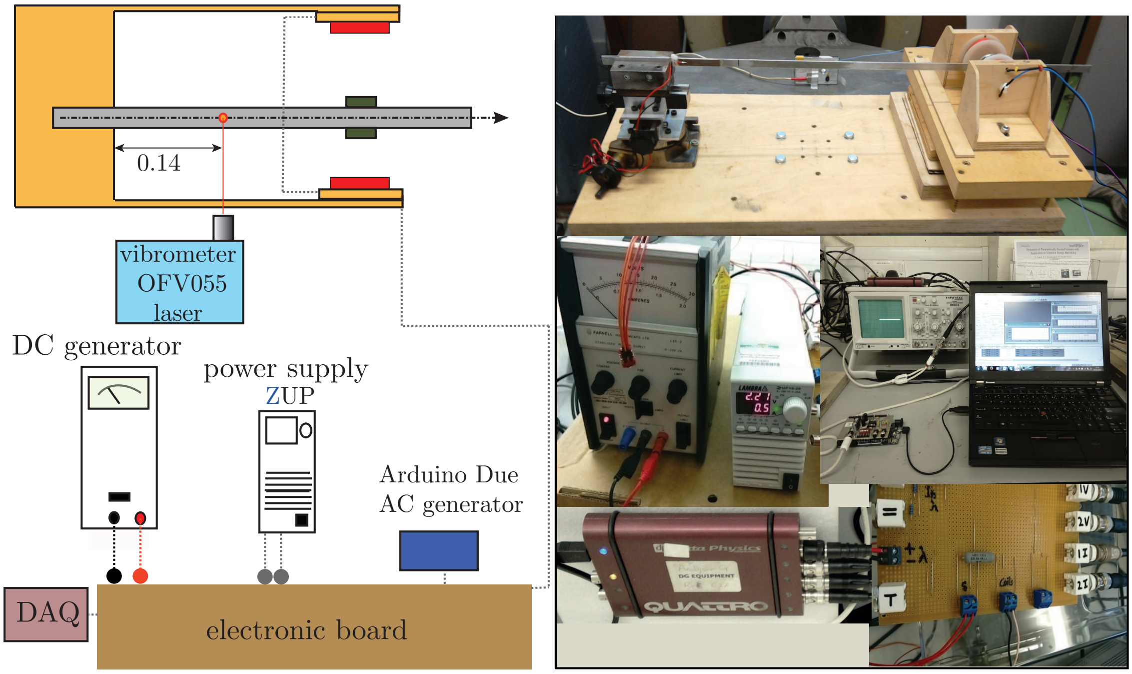

Fig. 7.2. Experimental set-up and schematic diagram to show each component.

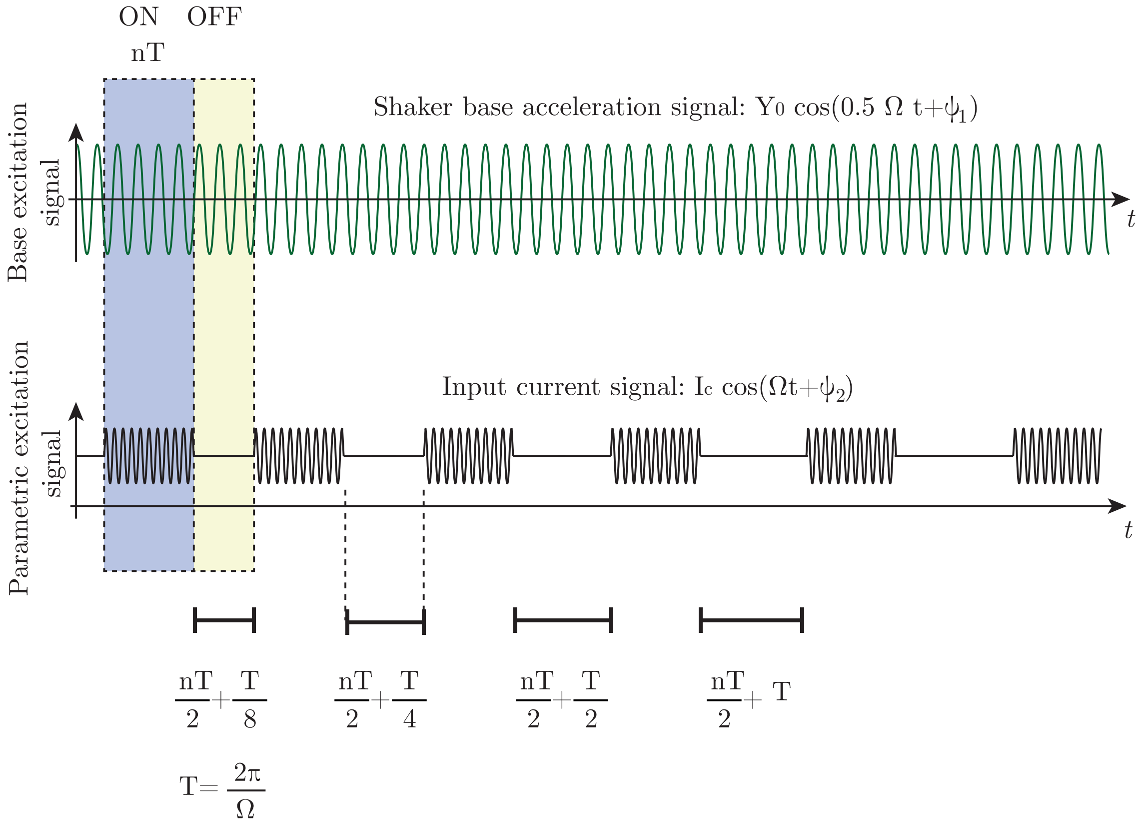

Fig. 7.3. The method for changing the phase between the shaker plate acceleration and the current in coils.

oscillation of the shaker. This means that the initial phase difference between the shaker and the current cannot be applied consistently.

To change the phase difference between the shaker and the current, the Arduino zeroes its output voltage after many “on” cycles, then it resets its cosine output voltage phase after a non-integer number of shaker oscillations (“off” cycles). This results in a change in the phase difference between the shaker and the current, and can be repeated for different numbers of off cycles in a single experimental run to change the phase difference multiple times. This method is shown in Fig. 7.3, which also shows the off times used in the experiments.

While the shaker vibrates the cantilever beam, the AC current through the coils is on for nT seconds, where $n \in \mathbb{N}$ is the number of cycles, $T = \frac{2\pi}{\Omega}$ is the duration of a cycle, and Ω is the input current frequency. This AC current is then turned off for $\frac{nT}{2} + \frac{T}{8}$ seconds while the DC current is still applied, as shown in Fig. 7.3.

During this off time, the shaker is still vibrating the cantilever beam with the same frequency. After this duration, the AC current is turned on for nT seconds again, and the process repeats for different off times. This results in a variety of phase differences with controlled spacing between $-\frac{\pi}{2}$ and $\frac{\pi}{2}$ rad. The number of cycles $n \geq 2 \times 10^8$ is chosen large enough to allow the cantilever motion to reach a steady-state motion in both the on and off cases. This means that the cantilever beam motion at a given AC current phase is not affected by the displacement caused by the previous phase.

The phase difference between the acceleration signal and the current generated in the coils is calculated based on Fourier analysis. The phase calculation is explained in Appendix H. Based on the Fourier analysis, any periodic motion can be presented by a series of sines and cosines that are harmonically related [145]. The acceleration (acceleration of the shaker plate) signal and the current signal (input current in coils) and is presented as series of sine and cosine signals.

7.3 Methodology

A SDOF model is presented to analyse the cantilever beam motion as shown in Fig. 7.4, where x is the displacement of moving mass m_t, and Y_0 is the amplitude of harmonic base displacement at frequency ω and phase ϕ. The relative displacement z is the displacement between the mass and the base. The overall damping coefficient $c_\mathrm{t} = c_\mathrm{m} + c_\mathrm{e}$, where c_m and c_e are components due to mechanical and electrical damping, respectively. The electrical damping c_e represents an electrical load from the electromagnetic system.

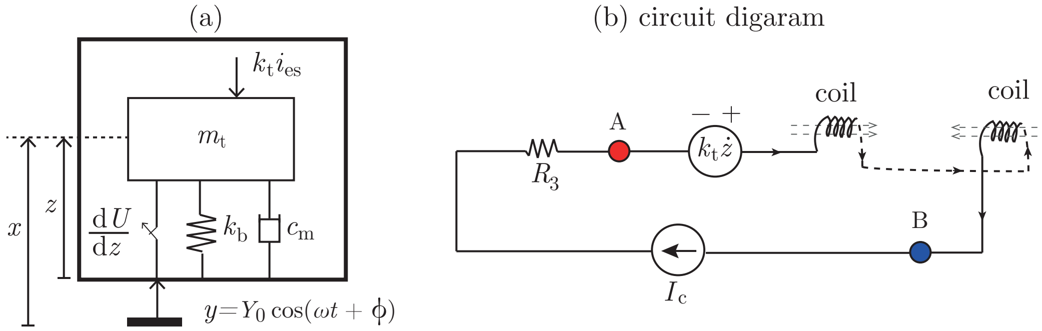

Fig. 7.4. Schematic of the base excited NPE system with an electromagnetic system with coils connected in series.

The equations governing the motion of the mechanical system are

$$m_t \ddot{z} + c_m \dot{z} + k_b z + \frac{dU(z)}{dz} + k_t i_{es} = m_t \omega^2 Y_0 \cos(\omega t + \phi), \tag{7.1a}$$

$$2L_{coil} \dot{i}_{es} + (R_3 + 2R_{coil})\, i_{es} = k_t \dot{z}, \tag{7.1b}$$

where the overdot represents a derivative with respect to time t. k_b is the static stiffness of the cantilever beam; k_t is the electromechanical coupling coefficient (see Eq. (5.2)); L_{coil} is the inductance of the identical coils; R_3 is the load resistance connected in series with the coils; R_{coil} is the electrical resistance of the coils; and i_{es} is the induced current in the electromagnetic system (see Eq. (5.8)).

The function $U(z)$ is the potential energy of the electromechanical system, and $\frac{dU(z)}{dz}$ is the force applied by the electromagnetic system with coils connected in series:

$$\frac{dU(z)}{dz} = H_1 I z + H_2 I z^3, \tag{7.2}$$

where I is the total current in coils

$$I = I_c + i_{es}, \tag{7.3}$$

where the AC/DC input current in the coils is

$$I_c = I_{DC} + I_{AC} \cos(\Omega t). \tag{7.4}$$

In Eq. (7.2) H_1 and H_2 are obtained from Eqs. (E.24) and (E.25). H_1 and H_2 are functions of the distance between coils h; the number of turns in the coil N; the magnetic dipole μ; the permeability of free space μ_0, and the mean radius of the coil r_c (see Table 5.1, and Appendix E.5 for more details). The force applied from the two magnets on the cantilever beam is not included here (see assumptions for the electromagnetic system in Appendix E.2).

Substituting the total current into Eq. (7.1) and normalising with respect to the total mass m_t yields,

$$\ddot{z} + 2\varepsilon\omega_n(\zeta_\mathrm{m} + \zeta_\mathrm{es})\dot{z} + \omega_n^2\left(1 + \varepsilon\delta\cos(\Omega t)\right)z + \omega_n^2\left(\varepsilon\alpha + \varepsilon\gamma\cos(\Omega t)\right)z^3 + \varepsilon\omega_n^2\delta_\mathrm{es}z + \varepsilon\omega_n^2\gamma_\mathrm{es}z^3 = \frac{1}{4}\Omega^2 Y_0\cos\left(\frac{\Omega}{2}t + \phi\right). \quad (7.5)$$

The cubic stiffness nonlinearity α, parametric amplitude δ, and cubic parameteric nonilinearity, γ, in Eq. (7.5) are defined in Eqs. (5.21), (5.24), and (5.25). ε is the small parameter and it is considered to be equal to 1. The parameters related to the induced current, δ_es and γ_es, are obtained from Eqs. (5.26) and (5.27) respectively. δ_es and γ_es are only negligible for small velocity and displacement. However, for large responses the effect of induced current and consequently δ_es and γ_es cannot be neglected. Especially for the case where the relative phase between the base and the parametric excitation is varied and the response is increased. The amplification as result of the induced current can be found independently from the effect of the phase difference. In Eq. (7.5) ζ_m is the mechanical damping ratio, and the electrical damping ratio ζ_es is obtained from Eq. (5.20).

Based on the method of averaging the periodic solutions of Eq. (7.5) at resonance are given by

$$z(t) = a\cos\left(\frac{\Omega}{2}t - \varphi\right), \quad (7.6)$$

where φ is the phase of the steady-state response, and a is the amplitude defined in Eq. (D.17), which has five stable and unstable solutions when the system parameters are non-zero (α, δ, $\gamma \neq 0$).

The effect of system parameters, such as cubic stiffness nonlinearity, α, parametric amplitude, δ, and the cubic parametric nonlinearity, γ, on response amplitude is investigated.

7.4 The effects of stiffness nonlinearities and parametric excitation

In the following sections these questions are aimed to be addressed:

- Does the measured response amplitude for the cases where the cantilever beam is only affected by hardening nonlinearity match with the analytical solutions? How does the nonlinearity change the response amplitude at different base excitation frequencies? (see Section 7.4.1).

- Does the relative phase between the base and the parametric excitation change the measured response amplitude for the NPE system? Does the relative phase effect change with increasing parametric amplitude? (see Sections 7.4.2 and 7.4.4).

Table 7.1: Nonlinear and NPE system parameters

	δ	α (m^{-2})	γ (m^{-2})	ζ	Y_0 (m)	ϕ(rad)
Nonlinear system (Fig. 7.5)	0	937.58	0	0.001	0.001	0
NPE system (Fig. 7.6a)	0.167	1031	238.12	0.001	0.001	$\frac{\pi}{2}$
NPE system (Fig. 7.6b)	0.167	1031	238.12	0.001	0.001	0

- Does the maximum and minimum response amplitude as a result of altering the relative phase change by increasing the base excitation amplitude? How does the relative phase effect the upper stable branch and the lower stable branch? Do the experimental results match with the theory? (see Section 7.4.5).

7.4.1 Nonlinear system with positive cubic stiffness nonlinearity

In this section the effect of hardening nonlinearity is investigated experimentally and is compared to analytical predictions. An experiment is designed so that cubic parametric nonlinearities are negligible, so that the effect of the hardening nonlinearity is studied independently. The cantilever beam is placed on the shaker and excited with the displacement amplitude $Y_0 = 0.001$m. A small displacement amplitude is considered to prevent the magnets hitting the coils and changing the initial conditions during the test.

Figure 7.5 shows the experimental and analytical amplitude frequency relation for the nonlinear system under harmonic base excitation. The nonlinear system parameters are presented in Table 7.1. For this test, the cantilever beam is excited with frequency ω. The half distance between the coils h is chosen to be equal to 0.03m. In Fig. 7.5 the base excitation frequency is $\frac{\Omega}{2}$, where $\omega = \frac{\Omega}{2}$. The DC current in the coils in series is set to $I_c = 0.38A$. The AC input current is set to zero so parametric amplitude $\delta = 0$ and cubic parametric amplitude $\gamma = 0$ as required by the design of the experiment. The linear natural frequency and the linear damping ratio is measured from impact tests as $\omega_n = 32.59\,\text{rad}\,\text{s}^{-1}$ and $\zeta = 0.001$. From Eq. (5.21), the normalised cubic nonlinearity is $\alpha = 937.58\text{m}^{-2}$. Since this nonlinearity is positive, it is a hardening nonlinearity.

Sweep up and down tests are carried out by increasing and decreasing the base excitation (shaker) frequency. For sweep up tests the shaker is set up to accelerate from 5 to 8Hz in 0.0025Hz/sec linear steps, with constant displacement amplitude $Y_0 = 0.001$m at all frequencies. The sweep down tests are done from 8 to 5Hz in the same way. The shaker displacement at frequencies lower than 5Hz is not considered since this is the lowest frequency the shaker can excite. Each sweep up/down test takes 1240sec in total. In Fig. 7.6 each experimental point corresponds to the amplitude of the steady-state response (the amplitude of the relative displacement $z(t)$) at some selected frequencies. The beam displacement $x(t)$ is subtracted by the base displacement $y(t)$ to find the relative displacement $z(t) = x(t) - y(t)$. The cantilever beam velocity is measured by the vibrometer, and is integrated numerically with respect to time to find the beam displacement. The

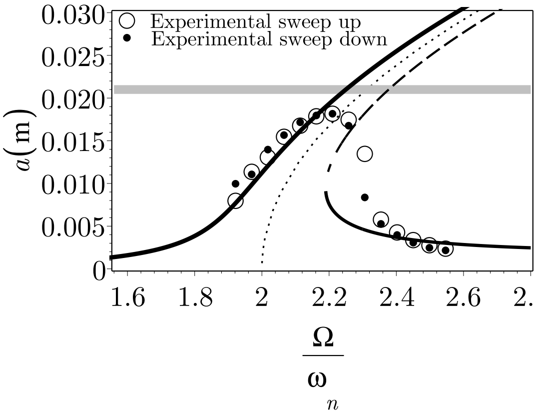

Fig. 7.5. Experimental and analytical amplitude frequency relation, a versus $\frac{\Omega}{\omega_n}$. The nonlinear system parameters are shown in Table 7.1. The dotted line is the *backbone curve*. The solid lines are the stable branches, and the dashed line is the unstable branch. The gray line shows the limit for the beam transverse vibration above which the magnets hit the coils.

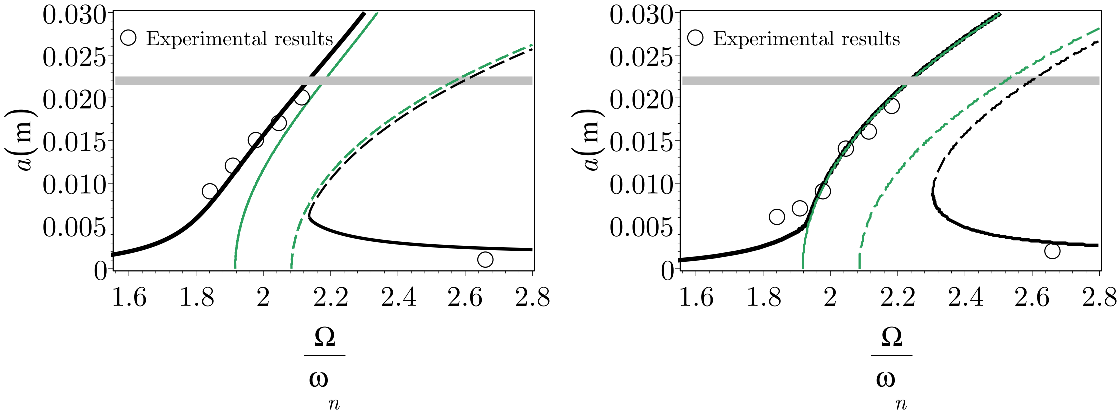

(a) $\phi = \frac{\pi}{2}$ rad.

(b) $\phi = 0$ rad.

Fig. 7.6. Experimental and analytical amplitude frequency relation, a versus $\frac{\Omega}{\omega_n}$ for experimental tests with parameters in Table 7.1. Analytical results are found using the averaging method. Black lines represent solutions produced by base and parametric excitation, and the green lines represent solutions affected only by parametric excitation. Solid lines denote stable branches, and dashed lines denote unstable branches. The gray line denotes the limit before magnets hit the coils.

acceleration of the shaker is recorded by an accelerometer attached to the shaker plate, which is integrated with respect to time twice to find the displacement of the shaker $y(t)$. The velocity response and the acceleration signal are filtered with a Butterworth high pass filter. The cut of frequency is chosen equal to 1 Hz. The order of the Butterworth high pass filter is chosen equal to 4.

From the averaging method, the solution of the nonlinear system is considered to have only one frequency component $\frac{\Omega}{2}$. Hence the measured relative displacement is only considered at harmonics with frequency $\omega = \frac{\Omega}{2}$. Fourier analysis finds the relative displacement with ω harmonics (see Appendix H). The experimental point results in Fig. 7.6 are found from the steady-state amplitude of the signal after Fourier decomposition.

From the experimental tests the presence of a hardening nonlinearity shifts the maximum peak amplitude to a higher frequency. When the response amplitude is large and the magnets are close to the coils, there are discrepancies between the experimental and analytical results. For example between $\frac{\Omega}{\omega_\mathrm{n}} = 2.2$ and $\frac{\Omega}{\omega_\mathrm{n}} = 2.3$, there are experimental points close to the unstable branch. In this frequency region the stable steady-state solutions from the analytical stable branch do not match with the steady-state solutions from experiment. This is due to the effect of damping and the electromagnetic force near the coils, which is not considered in the analytical model. In other frequency regions where the magnets are not close to the coils, the experimental and analytical results are in good agreement.

7.4.2 NPE system with cubic and cubic parametric nonlinearity

In this section the effect of parametric amplitude is investigated experimentally and is compared with the analytical predictions. The model used in the previous section is considered here, but with non-zero AC current amplitude. This results in a non-zero parametric amplitude, allowing its effects to be studied. In Chapter 4, the analytical and numerical analyses demonstrate that the parametric amplitude δ increases the response amplitude near the parametric frequency Ω if the base excitation frequency is half of the parametric frequency ($\omega = \frac{\Omega}{2}$), and if $\delta > \delta_{\mathrm{th2}}$ exceeds the instability threshold. Also, the phase difference between the parametric frequency and the base excitation ϕ must be $\frac{\pi}{2} \pm n\pi$, $n \in \mathbb{Z}$ to maximise the increase in the response amplitude. Due to this, we expect the non-zero parametric amplitude to increase the response amplitude in this experiment, which satisfies the aforementioned conditions.

Owing to the difficulty in controlling the phase difference between the current and the base excitation as described in Section 7.2.1, the frequency sweep method used in Section 7.4.1 is not used here. Instead, each frequency is considered independently, and the phase is varied using the method described in Section 7.2.1. The NPE system parameters for this test are presented in Table 7.1.

The amplitude frequency relation for the NPE system is plotted experimentally and analytically in Fig. 7.6 when the phase difference $\phi = \frac{\pi}{2}$ and 0 rad. As predicted analytically, the steady-state amplitude of the response is higher compared to the response of the nonlinear system shown in Fig. 7.5 when the phase ϕ is equal to $\frac{\pi}{2}$ rad. No experimental data was gathered in $2.15 \leq \frac{\Omega}{\omega_n} \leq 2.62$ because the response amplitude caused the magnets to hit the coils.

Five distinct response branches are shown in Fig. 7.6. The two analytical additional branches compared to Fig. 7.5 arise from the additional resonance frequencies in the nonlinear parametric system. One resonance frequency is induced by a combination of base and parametric excitation, and the other is caused by the parametric excitation.

7.4.3 Parametric amplification at parametric resonance

The effects of the phase difference on parametric amplification at parametric resonance is investigated. Therefore, the NPE system response at $\Omega = 2\omega_n$ when the phase difference is $\phi = \frac{\pi}{2}$ and 0 rad is compared experimentally (see Figs. 7.7 and 7.8). The base displacement amplitude for both cases when $\phi = \frac{\pi}{2}$ and 0 rad is chosen to be 0.001m throughout the tests (see Figs. 7.7c and 7.8c). The base excitation frequency is $\frac{\Omega}{2}$ (see Figs. 7.7d and 7.8d). In Figs. 7.7d and 7.8d other frequencies such as Ω and $\frac{3\Omega}{2}$ are appeared as result of the nonlinearity in the system and its influence on shaker base acceleration. The shaker did not operate accurately at low amplitude to remove the effect of nonlinearity.

The relative displacement, $z(t)$, when the phase difference is $\phi = \frac{\pi}{2}$ rad is higher than the case with the phase difference 0 rad. This can be seen by comparing Figs. 7.7e and 7.8e. Figs. 7.7f and 7.8f show the Power Spectrum Density (PSD) of the relative displacement signals. The maximum peak of the relative displacement PSD happens at $\frac{\Omega}{2}$.

Increasing the relative velocity when the phase difference is $\phi = \frac{\pi}{2}$ rad results in increasing the current in the coils since the induced current is increased. Fig. 7.7a shows the current in the coils when the phase difference is $\phi = \frac{\pi}{2}$ rad and Fig. 7.8a shows the current in coils when the phase difference is $\phi = 0$ rad. The maximum peak of the current PSD happens at Ω, which is the frequency of the input AC current in coils, I_c (see Figs. 7.7b and 7.8b). $\frac{\Omega}{2}$ in the current PSD appears as a result of the induced current i_{es}.

The phase portrait and the Poincaré map show that the response is steady-state. The phase portrait is found from the velocity versus displacement from the last 5sec of the tests. During first few seconds, the response is influenced by the initial condition. The Poincaré map is plotted based on the velocity and the displacement at each period $T = \frac{2\pi}{\Omega}$. The first point on the Poincaré map is placed at the start of the steady-state solution and then for each cycle, a point is placed on the Poincaré map. The phase portrait and the Poincaré map also show the periodic response for both cases with different phase difference (see Figs. 7.7g, 7.7h, 7.8g, and 7.8h).

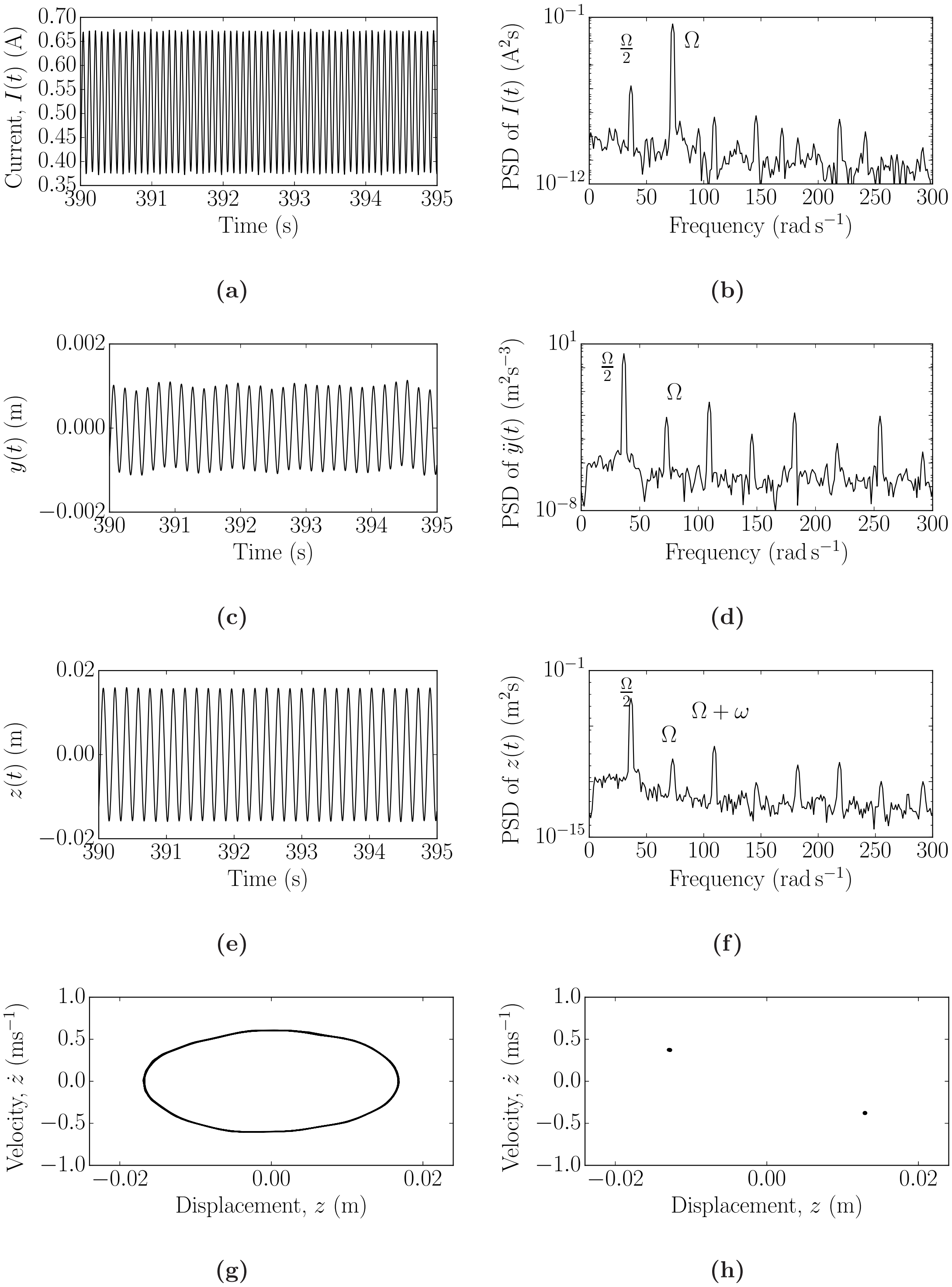

(a) **(b)**

(c) **(d)**

(e) **(f)**

(g) **(h)**

Fig. 7.7. Experimental results for $\Omega = 2\omega_n$ in Fig. 7.6a when $\phi = \frac{\pi}{2}$rad. (a) Current measured across the coils in series connection. (b) Power spectrum density of the current. (c) Measured displacement of the base excitation $y(t)$. (d) Power spectrum density of the base displacement signal. (e) Measured relative displacement $z(t)$. (f) Power spectrum density of the relative displacement signal. (g) Phase portrait plot. (h) Poincaré map.

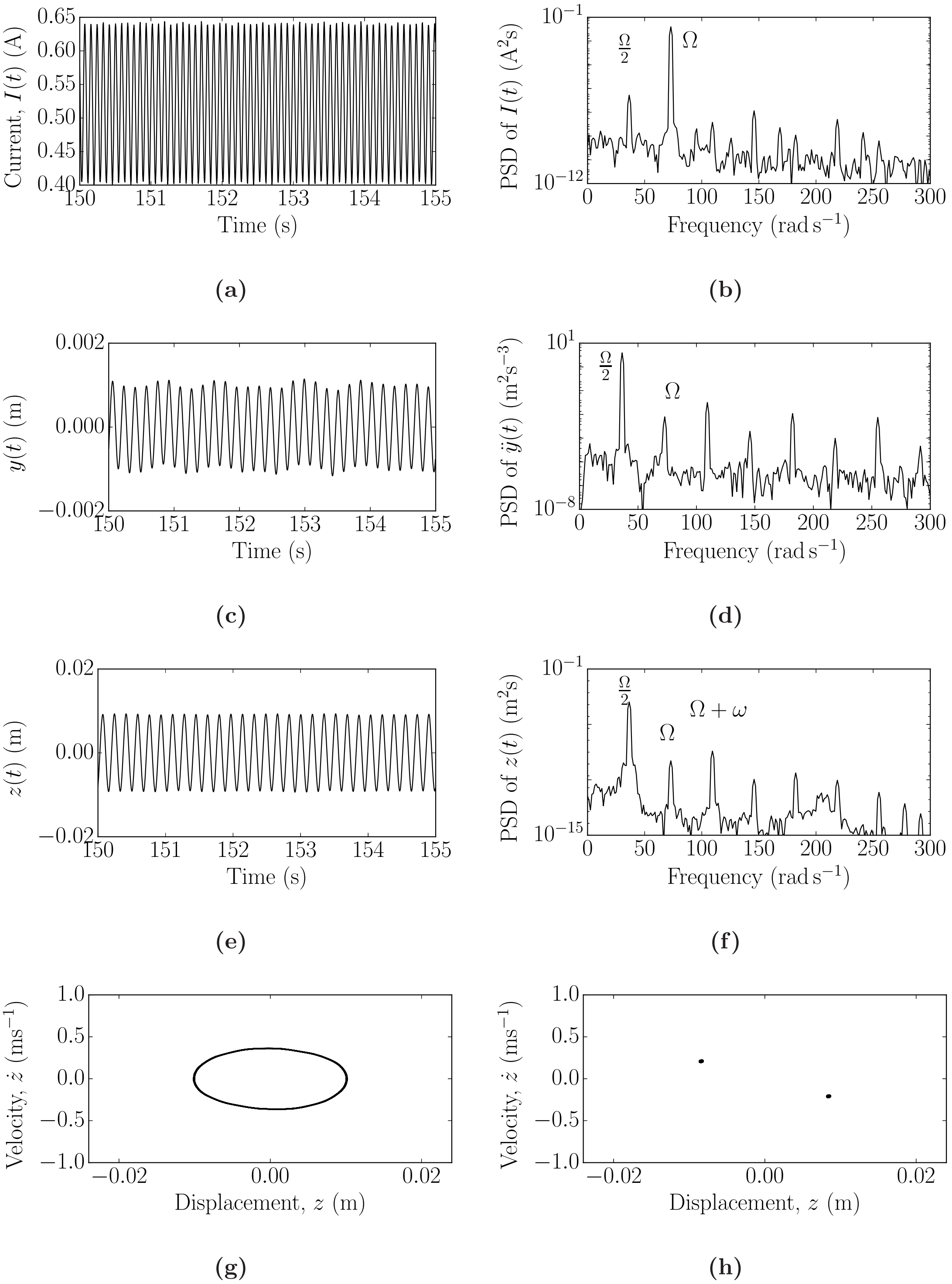

Fig. 7.8. Experimental results for $\Omega = 2\omega_n$ in Fig. 7.6b when $\phi = 0\,\mathrm{rad}$. (a) Current measured across the coils in series connection. (b) Power spectrum density of the current. (c) Measured displacement of the base excitation $y(t)$. (d) Power spectrum density of the base displacement signal. (e) Measured relative displacement $z(t)$. (f) Power spectrum density of the relative displacement signal. (g) Phase portrait plot. (h) Poincaré map.

Table 7.2: System parameters derived from non-zero AC current.

	I_{DC}	I_{AC}	δ	α (m^{-2})	γ (m^{-2})	ζ	Ω(rad s^{-1})	Y_0 (m)
Fig. 7.9a	0.54	0.002	0.0027	1042.4	3.86	0.001	74.72	0.001
Fig. 7.9b	0.54	0.025	0.034	1042.4	48.25	0.001	74.72	0.001
Fig. 7.9c	0.54	0.05	0.068	1042.4	96.52	0.001	74.72	0.001
Fig. 7.9d	0.54	0.16	0.218	1042.4	308.86	0.001	74.72	0.001

7.4.4 The effects of increasing the parametric amplitude

To demonstrate that increasing parametric amplitude increases the response amplitude, another experiment is conducted where the parametric amplitude varies under and above the instability threshold. The phase difference is also varied in the same way as the previous study. The system parameters are shown in Table 7.2.

Figure 7.9 shows the analytical stable and unstable branches versus phase ϕ. The parametric amplitude, δ, and cubic parametric nonlinearity, γ, are increased from Figs. 7.9a to 7.9d. Analytical results demonstrate that increasing the parametric amplitude at different phase ϕ has increased the response amplitude of both the stable and the unstable branches, and the stable and the unstable additional branches. In Fig. 7.9a when the parametric amplitude is under the instability threshold ($\delta < \delta_{\mathrm{th2}}$) at low response amplitude only stable and unstable branches are appeared. The additional stable and unstable branch only appears for the parametric amplitude above the instability threshold ($\delta > \delta_{\mathrm{th2}}$). The additional stable and unstable branches (green lines and green dashed lines) are appeared in Figs. 7.9b, 7.9c and 7.9d.

The experimental points in Fig. 7.9 correspond to the amplitude of the steady-state response. The experimental points are observed only on the stable branch because the stable branch and the stable additional branch have a similar amplitude. The experimental and analytical results in Fig. 7.9 show that the minimum and maximum response amplitudes occurs when $\phi = 0\,\mathrm{rad}$ and $\phi = \pm\frac{\pi}{2}\mathrm{rad}$ respectively. The phase relationship is repeated every $\pi\,\mathrm{rad}$.

7.4.5 The effects of increasing the base excitation amplitude with phase difference

In this section, the effect of the amplitude of the base excitation on the response amplitude is determined experimentally and analytically. The model used in the previous section is considered here with different base excitation amplitudes. Displacement amplitudes $Y_0 = 0.00075,\ 0.001,\ 0.00125\mathrm{m}$ are considered, and the resulting system parameters are shown in Table 7.3. The parameters of the experiment are chosen to minimise the differences between parametric amplitude, cubic nonlinearity, cubic parametric nonlinearity, damping ratio, and linear natural frequency for each Y_0.

The amplitude frequency relations are plotted analytically in Fig. 7.10 when the phase

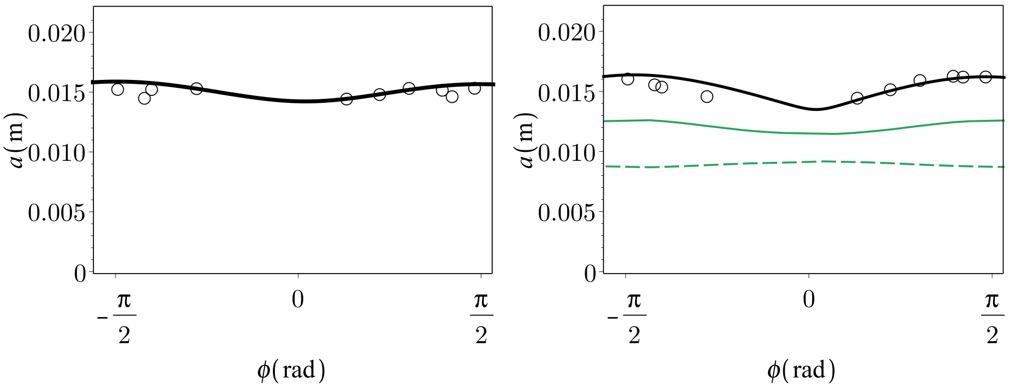

(a) Under the instability threshold **(b)** Above the instability threshold

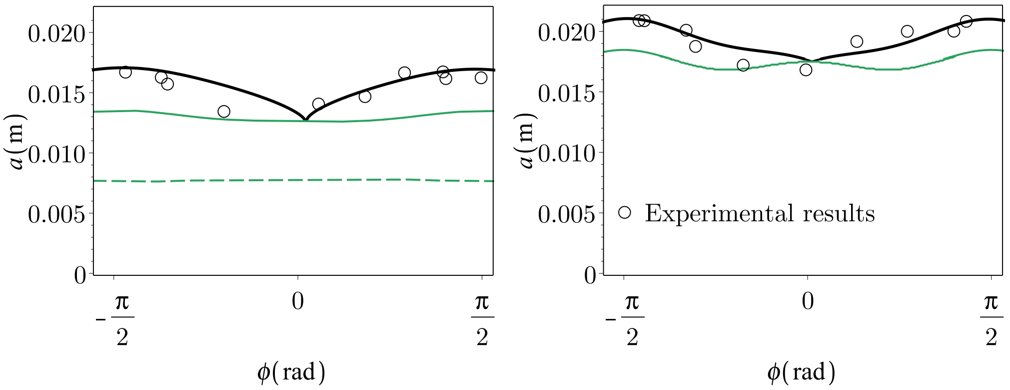

(c) Above the instability threshold **(d)** Above the instability threshold

Fig. 7.9. Amplitude of the steady-state response versus phase ϕ for the NPE system with four different parametric amplitudes δ and cubic parametric amplitudes γ. δ and γ are increased from Figs. (a) to (d). (a) $\delta = 0.0027$, (b) $\delta = 0.034$, (c) $\delta = 0.068$, and (d) $\delta = 0.218$. The system parameters are presented in Table 7.2. These systems are solved analytically using the averaging method, and these solutions are denoted by lines. Black lines represent solutions produced by the base and the parametric excitation, and the green lines represent solutions affected only by parametric excitation. Solid lines denote stable branches, and dashed lines denote unstable branches. Green lines denote additional branches.

Table 7.3: NPE system parameters at three displacement amplitudes

	Y_0 (m)	δ	α (m^{-2})	γ (m^{-2})	ζ	ω_n ($\mathrm{rad\,s^{-1}}$)
Fig. 7.11	0.00075	0.16	1047	228.5	0.001	37.63
Fig. 7.12	0.001	0.167	1031	238.12	0.001	36.8
Fig. 7.13	0.00125	0.19	1037	273.97	0.001	37.08

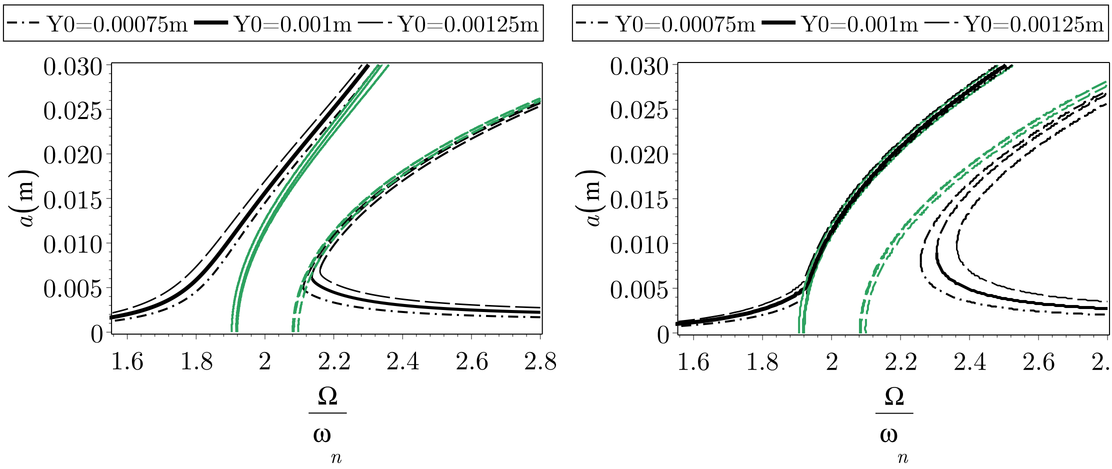

(a) $\phi = \frac{\pi}{2}$rad.

(b) $\phi = 0\,\mathrm{rad}$.

Fig. 7.10. Analytical amplitude frequency relation, a versus $\frac{\Omega}{\omega_n}$ for the experiments in Table 7.3. Increasing Y_0 increases the amplitude of the stable branches.

difference $\phi = \frac{\pi}{2}$, $0\,\mathrm{rad}$. The analytical response amplitudes are based on the experimental system parameters in Table 7.3. The amplitude frequency relations show that an increase in the base excitation amplitude Y_0 increases the response amplitude. This effect is greatest on stable branches, and is negligible on additional branches when the response amplitude is low, since additional branches are affected only by the parametric amplitude. When the response amplitude is large, the induced current increases, which consequently increases the amplitude of the additional branch. The difference in the additional branches at low response amplitudes arises from the different parametric amplitudes between experiments.

When the phase difference $\phi = 0$, this effect is reduced on the higher stable branch, but is increased on the lower stable branch compared to the $\phi = \frac{\pi}{2}$ case. Furthermore, the amplitude of the additional stable branch is decreased in the $\phi = 0$ case because the induced current is reduced.

Similar amplitude frequency plots are shown in Figs. 7.11, 7.12, and 7.13 for $Y_0 = 0.00075$, 0.001, 0.00125m respectively. In Figs. 7.11g, 7.12g, and 7.13g the points indicated by alphabetic letters are demonstrated experimentally to show the effect of phase difference on response amplitude. For each point on the amplitude frequency curve the phase difference between the base excitation and the parametric excitation is varied.

The experimental results are in agreement with the analytical results, apart from when the amplitude is close to the maximum possible amplitude experimentally. This occurs because the response amplitude is unable to increase to the stable branch, which is beyond the spacing of the coils. An example of this is in Fig. 7.11e, where the experimental data shows that the response amplitude is close to the unstable branch because it cannot increase beyond this physical limitation.

Observing the solution at both upper and lower stable branches at a specific parametric frequency has been unsuccessful. For example, from Fig. 7.11e it can be seen that the solution is on the upper stable branch when the phase ϕ is close to zero and the solution on the lower stable branch is not achieved. Several experimental tests were carried out to change the base excitation amplitude slowly to observe the lower stable branch and the jump to the higher stable branch. However, the jump to the upper stable is happened immediately. This jump happens since the coils are not perfectly identical and in order to get results on lower branch identical forces have to be applied to the cantilever beam otherwise the differences act as small excitation and the jump will occur. This can be exploited for designing energy harvesters and filters when the jump from higher branch to the lower branch is not ideal. In this case it is hard to predict when the jump occurs during experiment in order to calculate the frequency bandwidth extended from this configuration.

The experimental results also demonstrate that the amplitude of the response is minimised on the upper stable branch when $\phi = 0$, and is maximised when $\phi = \frac{\pi}{2}$. This is exemplified by Figs. 7.11a. The opposite is true for the lower stable branch, as shown in Fig. 7.11f. This agrees with the analysis presented in Chapter 4.

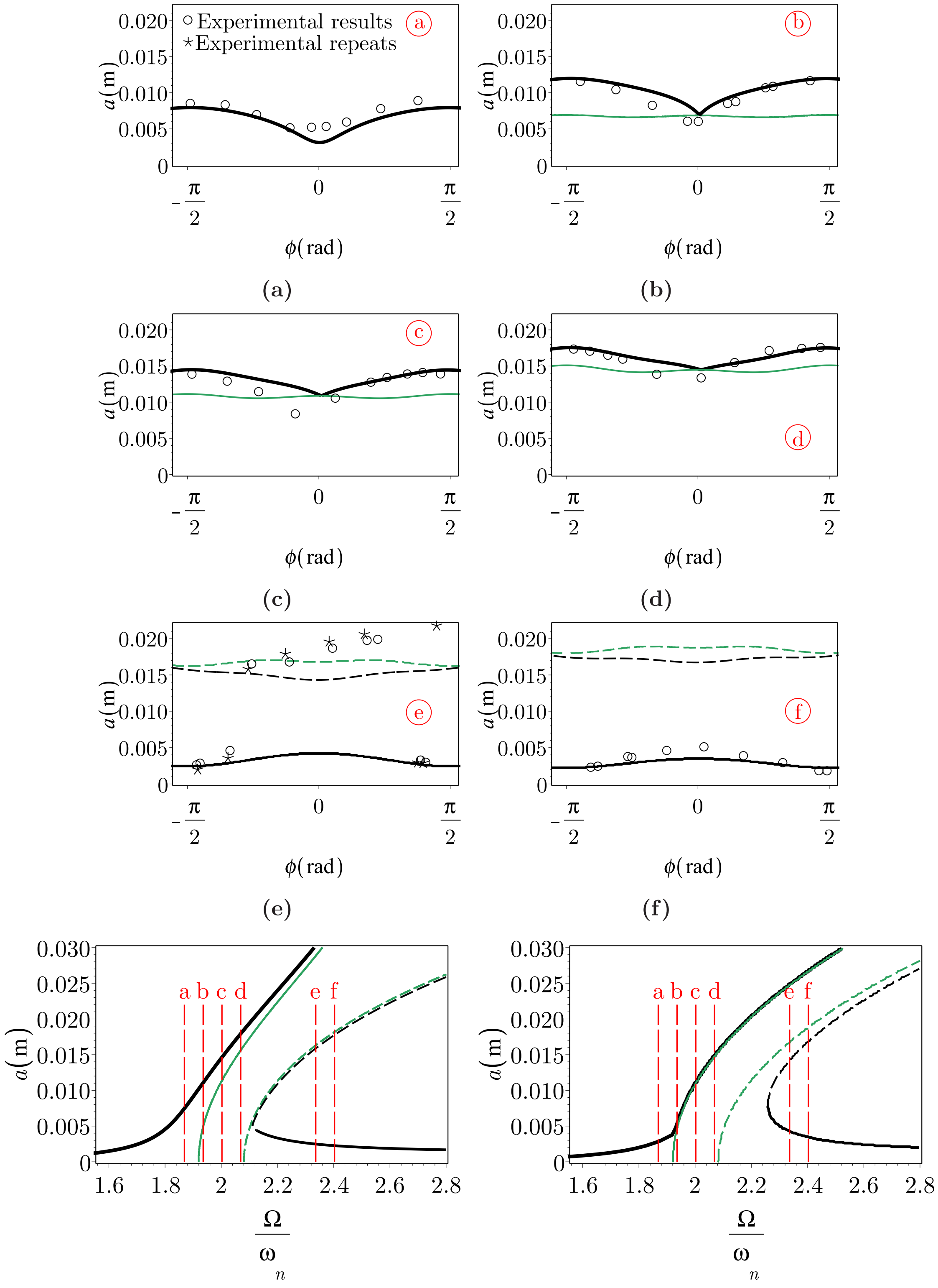

(a) **(b)** **(c)** **(d)** **(e)** **(f)**

(g) $\phi = \frac{\pi}{2}$rad. **(h)** $\phi = 0$ rad.

Fig. 7.11. Analytical (averaging method) and experimental results for base displacement amplitude $Y_0 = 0.00075$m. Labels (a)-(f) denote different normalised parametric frequencies $\frac{\Omega}{\omega_n}$. An experiment, as described in Section 7.4.2, is conducted at each frequency denoted by a label. The values of these experiments at $\phi = \frac{\pi}{2}$ and $\phi = 0$ are mapped onto the amplitude frequency relation plots (g) and (h) respectively.

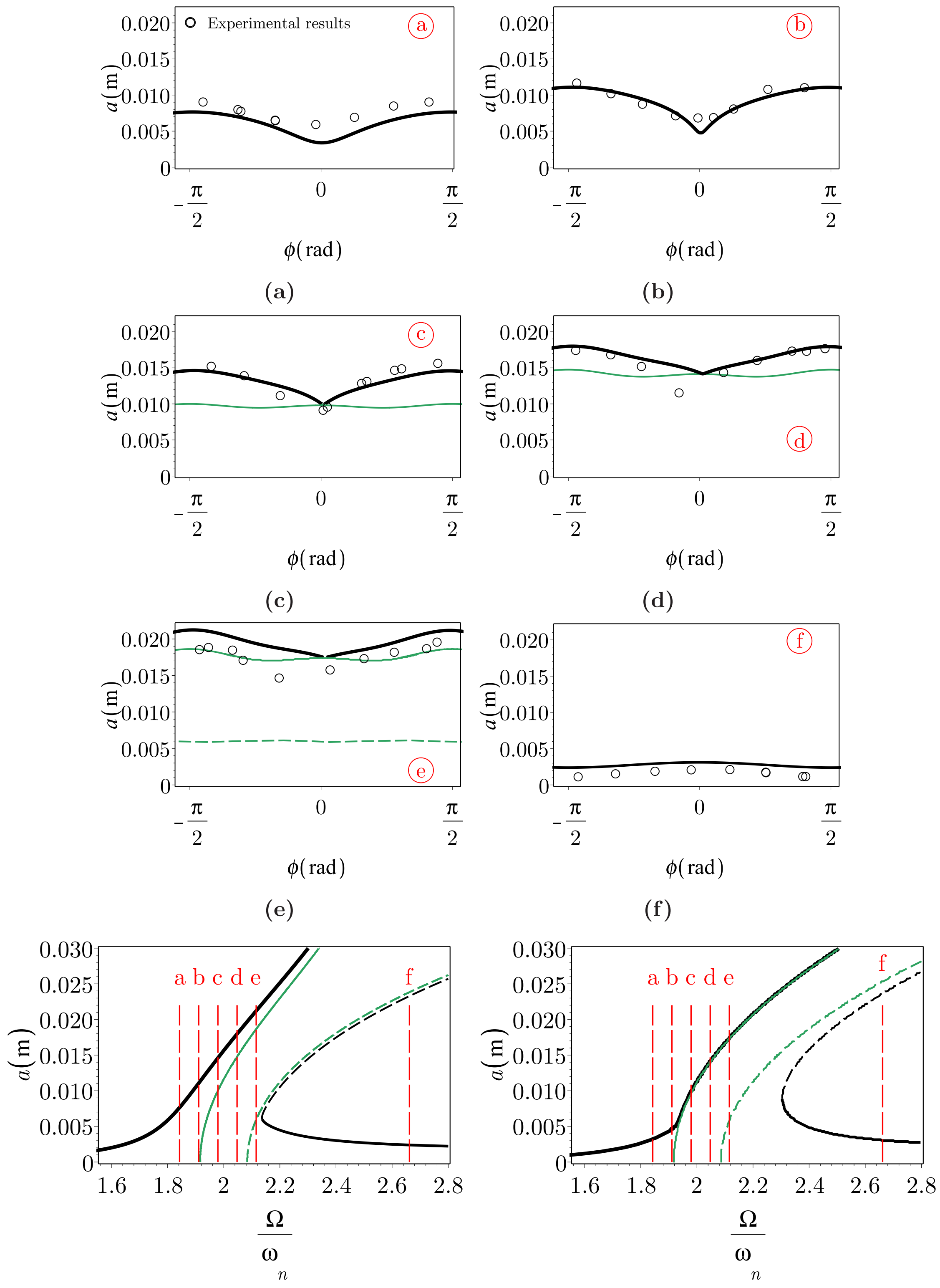

(a) **(b)** **(c)** **(d)** **(e)** **(f)**

(g) $\phi = \frac{\pi}{2}$rad. **(h)** $\phi = 0$ rad.

Fig. 7.12. Analytical (averaging method) and experimental results for base displacement amplitude $Y_0 = 0.001$m. Labels (a)-(f) denote different normalised parametric frequencies $\frac{\Omega}{\omega_n}$. An experiment, as described in Section 7.4.2, is conducted at each frequency denoted by a label. The values of these experiments at $\phi = \frac{\pi}{2}$ and $\phi = 0$ are mapped onto the amplitude frequency relation plots (g) and (h) respectively.

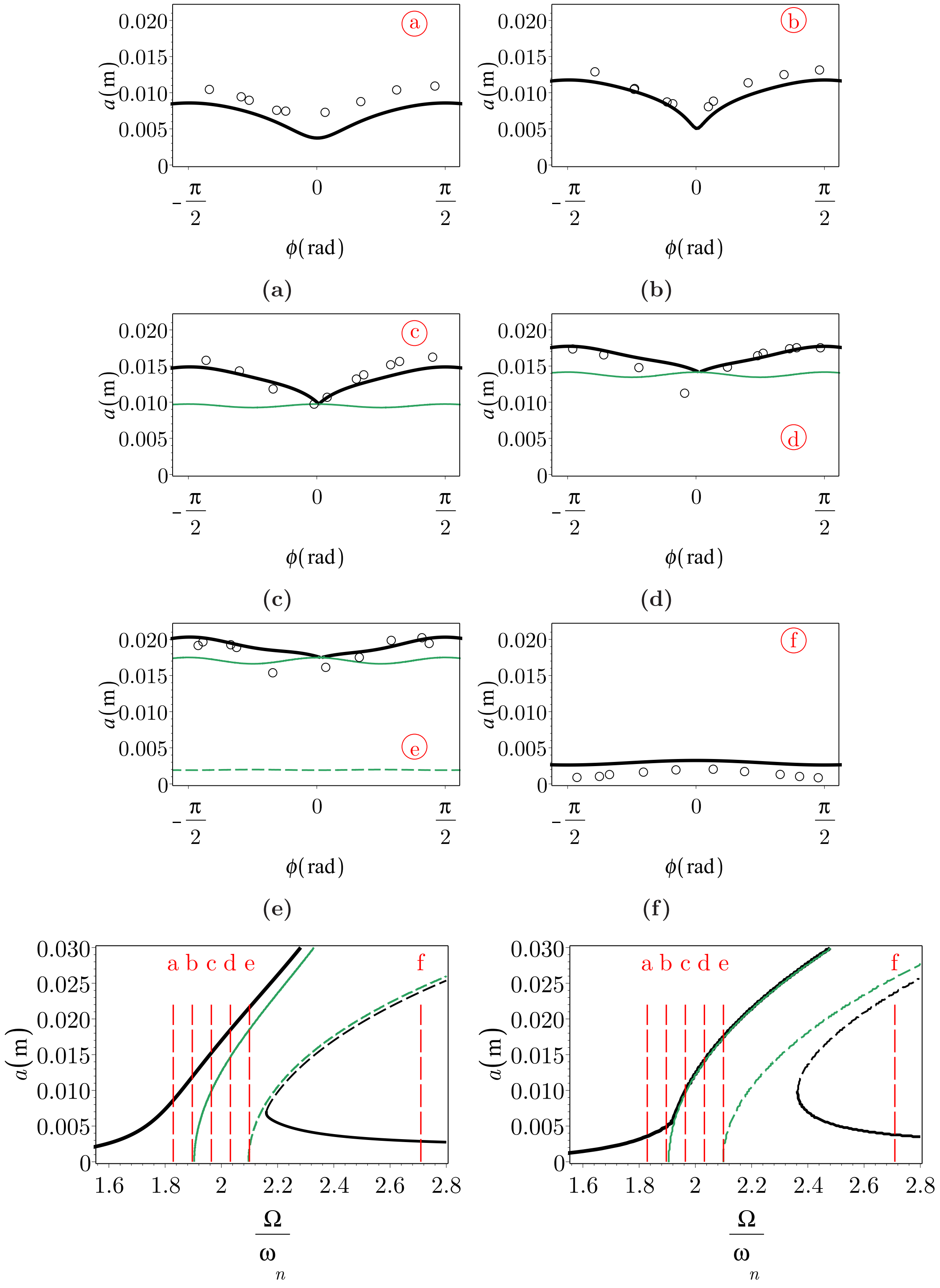

(a) **(b)** **(c)** **(d)** **(e)** **(f)**

(g) $\phi = \frac{\pi}{2}$rad. **(h)** $\phi = 0\,$rad.

Fig. 7.13. Analytical (averaging method) and experimental results for base displacement amplitude $Y_0 = 0.00125$m. Labels (a)-(f) denote different normalised parametric frequencies $\frac{\Omega}{\omega_n}$. An experiment, as described in Section 7.4.2, is conducted at each frequency denoted by a label. The values of these experiments at $\phi = \frac{\pi}{2}$ and $\phi = 0$ are mapped onto the amplitude frequency relation plots (g) and (h) respectively.

7.5 Concluding Remarks

In this chapter experiments were carried out to augment the analytical model presented in Chapter 4. The experimental model was in agreement with the analytical model in all cases with different parametric amplitudes and relative phases, except for when the response amplitude is great enough that the magnet on the cantilever beam approaches or impacts the coil. This experimental model has also been used to confirm expected behaviour changes predicted by the analytical model. These are summarised as follows:

- An increase in hardening nonlinearity causes the frequency of the peak response amplitude to increase. This was investigated independently of parametric amplitude and parametric nonlinearity by disabling the alternating component of the current in the electromagnetic system.
- An increase in the parametric amplitude increases the amplitude of the response, which is significant when the phase difference between the current and the base excitation is $\phi = \frac{\pi}{2}\,\mathrm{rad}$ for the upper stable branch. For the lower stable branch, this increase is significant when $\phi = 0\,\mathrm{rad}$.
- An increase in the amplitude of the base excitation increases the response amplitude. This increase is lessened on additional branches.
- The system explored in this study can be used to design an energy harvester when increasing the frequency bandwidth and the response amplitude is essential.

Chapter 8

Conclusions and future work

To conclude, a model of a simplified nonlinear parametrically excited system was presented and then was augmented with base excitation effects. An experimental approach was conducted to explore and validate both of these models. Time-varying stiffness and cubic and cubic parametric nonlinearities were applied using an electromagnetic system on a clamped-free cantilever beam. The electromagnetic forces were calculated analytically, and comprehensive independent studies of behaviour with different system parameters were conducted. The model of the electromagnetic system and the cantilever beam was introduced in Chapters 3 and 4 as a Single Degree of Freedom (SDOF) system. This model was improved in response to the experimental set-up in Chapters 6 and 7 by considering the effect of electrical damping and induced current in the equation of motion. The experimental results showed good agreement with the analytical results.

8.1 Research findings

This study aimed to answer these research questions:

- **In SDOF linear and nonlinear parametrically excited systems, which parameters can cause parametric amplification? In contrast, how the response can be attenuated?**

  In Chapter 3 examples of linear and nonlinear parametrically excited systems were presented. It was demonstrated that upon overcoming an instability threshold, the response of a PE system can be amplified in the vicinity of parametric resonance. The instability threshold varies with the damping in the system, hence overcoming this threshold has been a challenge in previous studies. To fill this void in the open literature, the effect of different parameters on the instability threshold was illustrated. Specifically, a positive cubic parametric nonlinearity increased the response, and a negative cubic parametric nonlinearity attenuated the response. The positive cubic parametric nonlinearity was observed in the electromagnetic system, and its contribution was illustrated in Chapters 6 and 7. Although the parametric amplitude and cubic parametric amplitude are both dependent on the AC current, they can be optimised for different electromagnetic system configurations. Due to the presence of positive cubic parametric amplitude in the electromagnetic system, the instability threshold could be minimised for designing electromagnetic actuators and filters.

- **Can experimental tests validate the theory of SDOF nonlinear parametrically excited systems? Which design criteria should be considered for the best predictions?**

  In Chapter 6 the free response of the Nonlinear Parametrically Excited (NPE) system was presented both analytically and experimentally. The response amplitude was investigated under varying system parameters, and good agreement between the analytical and experimental results was demonstrated. In Chapter 5, a SDOF model was shown to represent the cantilever beam with an electromagnetic system, since the first and the second modes were well separated. The parametric stiffness and stiffness nonlinearity applied from the electromagnetic system was found analytically from the electromagnetic forces, hence the effects of current flow through the coils on parametric stiffness, stiffness nonlinearities, resonance frequencies and damping were investigated. Furthermore when a large velocity of the cantilever beam was observed, both electrical damping and induced current contribute significantly to the response amplitude, hence their inclusion in the model.

- **What assumptions in the theory are not valid in the experiments for the stability and responses of the NPE system?**

  The method of averaging is an approximation method that was used to solve the NPE system (see Chapters 3 and 4). This method is limited to approximate systems with small damping, parametric amplitude, cubic nonlinearity and cubic parametric nonlinearity parameters. For the experimental parameters chosen in this thesis, the method of averaging converges. Consequently, for small scale applications such as amplifiers, filters, and vibration energy harvesters, the system parameters are not assumed to be large and the methods presented in this thesis fit very well for these applications. The first order averaging method was implemented in order to find the stability and the response of the system around the parametric resonance Ω. The first order averaging method was limited to the transition curve at $\Omega = 2\omega_n$, and in order to find the transition curves at lower parametric resonance, higher order ε terms in the averaging method must be considered.

- **In SDOF linear and nonlinear parametrically excited systems subject to harmonic base excitation, which parameters can cause parametric amplification or suppression?**

  In Chapters 4 and 7 linear and nonlinear parametrically excited systems subject to harmonic base excitation were considered. The effect of parametric amplitude and stiffness nonlinearity close to parametric resonance was examined analytically and experimentally. Both experimental and analytical results both showed that an increase in parametric amplitude and cubic parametric amplitude amplifies the response. Similar to the free response case for the NPE systems, the cubic stiffness nonlinearity can increase the frequency bandwidth, but reduces the response amplitude at parametric resonance. Furthermore, the effect of phase difference between the base excitation and parametric excitation was considered. For this contribution the increase of the response amplitude is significant when the phase difference between the current and the base excitation is $\phi = \frac{\pi}{2}$rad for the upper stable branch. For the lower stable branch, this increase is significant when $\phi = 0$rad. The response can be attenuated when the phase difference between the current and the base excitation is $\phi = 0$rad for the upper stable branch and $\phi = \frac{\pi}{2}$rad for the lower branch. This difference between the lower and upper stable branch can be exploited to avoid jumps from the higher branch to the lower branch, or to manipulate the system to have jumps from the lower branch to the upper branch. As well as the upper and lower stable branches, there are additional branches. For the first time in the literature, the dependency of these branches on the phase difference and base excitation amplitude was shown in this work. The additional branches change with the induced current, which changes when the base excitation amplitude and the phase difference is varied.

- **What are the benefits and limitations of a cantilever beam with an electromagnetic system in comparison with a vertically excited cantilever beam? Also, which nonlinearities are observed from an electromagnetic system and how can they be included in SDOF model of the PE system?**

  The cantilever beam with an electromagnetic system was introduced in Chapter 5, which concluded that the electromagnetic system is a useful tool to apply time-periodic and nonlinear stiffness. The advantages of using an electromagnetic system compared to a vertically excited cantilever beam are:

  - the non-contact electromagnetic excitation force;
  - the direct and parametric excitation can be applied independently;

  - the frequency and amplitude of the excitation force can be accurately controlled by a DC/AC power source;
  - the cubic and cubic parametric stiffness nonlinearities can also be controlled independently of the response amplitude; and
  - the hardening nonlinearity can be controlled with an electronic circuit.

  The electromagnetic system is configured to generate a small electrical damping by connecting the coils in series opposing connection. Hence, reducing the distance between the coils does not increase the electrical damping considerably. This configuration demonstrates the effect of cubic nonlinearity from the electromagnetic system without the dominant effect of electrical damping. In contrast, when coils are connected in the parallel opposing configuration, the circulating current causes the electrical damping to increase, which dominates other dynamics of the cantilever beam. Hence, the system response is highly affected by the electrical damping as well as cubic nonlinearity. When the magnets are very close to the coils, the model of the electrical damping fails. The electromagnetic system can be configured for different applications by varying the properties of the system to obtain desired characteristics. This thesis presents how the time-periodic stiffness, cubic stiffness nonlinearity, and other characteristics can be calculated from the geometry of the system and the type of current passed through the coils.

- **What are the benefits of using an electromagnetic system for parametric excitation in designing filters, amplifiers and vibration energy harvesters?**

  The NPE system presented in this thesis can be used for vibration amplification or suppression. Chapters 4 and 7 demonstrated that controlling the phase difference between the parametric excitation and the base excitation for a base excited NPE system can increase or decrease the response amplitude. Furthermore, through experimental and analytical analyses, this work determined that stable branches can be controlled in this way. This is particularly relevant for designing filters and vibration energy harvesters where the jump from the higher amplitude branch to a lower amplitude branch is not ideal.

8.2 Research impact

Cable-stayed bridges, free hanging marine flexible risers, ships, planetary gear systems and other engineering structures are often subject to parametric excitation. Due to the high amplitude of responses as a result of parametric amplification, parametric excitation can be disastrous if not accounted for. Understanding the instability of the parametrically excited systems can help to design vibration absorbers. However, the parametric excitation can be exploited for different applications in different disciplines, from fruit pickers [160] to electronic filter or vibration energy harvester design [12, 63, 115].

The results shown in Chapters 3 and 4 are general, and can be applied to any system which can be modeled as described in Section 6 or Section 7.3. For example, several Micromechanical Systems (MEMS) are modelled in the literature as a SDOF system with parametric amplification [63, 115]. This research could influence further understanding and applications in MEMS, which would benefit from the parametric study carried out in this thesis.

The NPE system introduced in this thesis can be used to design macro/micro scale vibration energy harvesters. With the set-up introduced in this thesis the efficiency of the harvester is poor when the energy required to generate current for the coils is considered. In applications where the current is already generated, such as in electromagnetic rotors, the efficiency is respectable. This should be considered if the system described in this work is to be used for energy harvesting.

8.3 Study limitations

The study has proposed methodologies for the design of a NPE system. As a consequence of these methodologies and experimental study, this investigation has the following limitations:

- The parametric amplification and attenuation is only considered in the vicinity of the parametric resonance at twice the natural frequency. In order to study the stability of the linear and nonlinear parametrically excited systems at higher parametric frequency, a higher order averaging method should be considered.

- In order to show the effect of phase difference on measured response amplitude of the NPE system subject to harmonic base excitation, the amplitude frequency plots were presented (see 7.4.5). In general, the amplitude frequency plots show the response amplitude at each frequency with the influence of the amplitude and velocity of the previous motion. However, in this study the effect of sweep up and down in frequencies was not included. This is due to the difficulty with fixing the phase difference between the base excitation and the parametric excitation at different frequencies during the sweep tests.

- Several assumptions were made to model the electromagnetic forces from the electromagnetic system. For example, the effect of nonlinear electrical damping is neglected for small vibration of the cantilever beam with DC current flow in the coils. However, if the cantilever beam with the electromagnetic system is subjected to a harmonic base excitation (similar to the examples presented in Section 7.4) the nonlinear electrical damping is not negligible. Hence, further study is needed to investigate the nonlinear damping for large vibrations when magnets are close to the coils.

- This study does not consider the dynamics of the cantilever beam in cases when the magnets strike the coils. An extension of this study is to consider the effect of this impact, and how it can be exploited when the excitation has a high frequency.

8.4 Recommendations for future work

The ultimate goal of this research study is to evaluate the dynamics of the nonlinear parametrically excited systems. To achieve this goal, future work is needed to fill the gap presented by the limitations of this study. Investigation of the following areas as future research strategies can achieve this goal:

- Throughout this thesis several suggestions have been presented in order to increase the efficiency of the electrical filters, amplifiers and vibration energy harvesters. The suggestions made in this thesis can be extended to design nonlinear parametrically excited filters and amplifiers.

- The NPE system subject to a harmonic base excitation was illustrated in Chapter 4. The parametric frequency was tuned at twice the base excitation frequency when the base excitation frequency was varied in vicinity of the linear natural frequency. With the experimental set-up introduced in Chapter 7 it is possible to tune the parametric frequency and the base excitation frequency independently. It would be beneficial to investigate the change in parametric frequency and the base excitation frequency and their effect on response amplitude. For example, for designing a vibration energy harvester with the proposed NPE system the base excitation can be assumed to be the motion from the environment with a wide range of frequencies. Hence, as part of the future work relevant to design of the energy harvester the study on excitation frequencies can be recommended.

- In Chapter 6 the parametric frequency was tuned at twice the first natural frequency. Hence the response amplitude of the NPE system was only demonstrated at low frequencies (less than 10Hz). With the experimental set-up introduced in Chapter 5 it is possible to generate parametric amplitude at very high frequency: far beyond the highest underdamped natural frequency of the system. The effect of high-frequency excitation in NPE systems has been studied in the literature [161, 162]. Some of their effects, such as the change in the system stiffening [163], natural frequency, stability, and equilibrium [164, 165] can be illustrated experimentally with the set-up designed in this thesis.

Appendix A

The method of averaging to study a linear parametrically excited system

The Linear Parametrically Excited (LPE) system introduced in Section 3.2.1 is explained in detail here. From Section 3.2.1 substituting Eq. (3.4) into Eq. (3.3) leads to

$$z'' + \frac{2\varepsilon\zeta\omega_n\left(1+\varepsilon\Delta\right)}{\Omega_0}z' + \frac{\omega_n^2\left(1+2\varepsilon\Delta\right)}{\Omega_0^2}\left(1+\varepsilon\delta\cos\left(\tau\right)\right)z(\tau) + \mathcal{O}(\varepsilon^2) = 0. \tag{A.1}$$

using the Taylor expansion $\left(1-\varepsilon\Delta\right)^{-1} = 1+\varepsilon\Delta+\mathcal{O}\left(\varepsilon^2\right)$ and $\left(1-\varepsilon\Delta\right)^{-2} = 1+2\varepsilon\Delta+\mathcal{O}\left(\varepsilon^2\right)$, and ignoring high order terms, Eq. (A.1) can be simplified to

$$z'' + \frac{2\varepsilon\zeta\omega_n\left(1+\varepsilon\Delta\right)}{\Omega_0}z' + \frac{\omega_n^2}{\Omega_0^2}\left(1+2\varepsilon\Delta+\varepsilon\delta\cos\left(\tau\right)\right)z(\tau) + \mathcal{O}(\varepsilon^2) = 0. \tag{A.2}$$

Changing the frequency ratio to $\frac{\omega_n}{\Omega_0} = \kappa$ results in,

$$z'' + \kappa^2 z\left(\tau\right) = -2\kappa\varepsilon\zeta\left(1+\varepsilon\Delta\right)z' - \kappa^2\left(2\varepsilon\Delta+\varepsilon\delta\cos\left(\tau\right)\right)z(\tau) + \mathcal{O}(\varepsilon^2). \tag{A.3}$$

The complementary solution of Eq. (A.3) is a linear combination of $\sin\left(\tau\right)$ and $\cos\left(\tau\right)$, which can be written as

$$z(\tau) = a\cos\left(\Phi\left(\tau\right)\right), \tag{A.4}$$

where $\Phi\left(\tau\right) = \kappa\tau+\varphi$, and

$$z(\tau)' = -a\kappa\sin\left(\Phi\left(\tau\right)\right), \tag{A.5}$$

The amplitude a, and the phase φ are constant and are determined from the initial values. To study the behaviour of the system for these solutions, the constant parameters vary as a function of τ. Hence Eqs. (A.4) and (A.5) become,

$$z\left(\tau\right)=a\left(\tau\right)\cos\left(\Phi\left(\tau\right)\right), \tag{A.6}$$

where $\Phi\left(\tau\right)=\kappa\tau+\varphi\left(\tau\right)$ and,

$$z\left(\tau\right)'=-a\left(\tau\right)\kappa\sin\left(\Phi\left(\tau\right)\right). \tag{A.7}$$

Differentiating equation Eq. (A.6) yields

$$z\left(\tau\right)'=a'\left(\tau\right)\cos\left(\Phi\left(\tau\right)\right)-a\left(\tau\right)\left(\kappa+\varphi'\left(\tau\right)\right)\sin\left(\Phi\left(\tau\right)\right). \tag{A.8}$$

Comparing with Eq. (A.7) yields the relation between $a'\left(\tau\right)$ and $\varphi'\left(\tau\right)$

$$a'\left(\tau\right)=\frac{a\left(\tau\right)\sin\left(\Phi\left(\tau\right)\right)}{\cos\left(\Phi\left(\tau\right)\right)}\varphi'\left(\tau\right). \tag{A.9}$$

Substituting Eq. (A.6) and derivative of Eq. (A.7) into Eq. (A.3) yields,

$$\begin{aligned}a'\left(\tau\right)\sin\left(\varphi\left(\tau\right)\right)+a\left(\tau\right)\varphi'\left(\tau\right)\cos\left(\Phi\left(\tau\right)\right)=-2a\left(\tau\right)\kappa\varepsilon\zeta\sin\left(\Phi\left(\tau\right)\right)\\+2\kappa a\left(\tau\right)\varepsilon\Delta\cos\left(\Phi\left(\tau\right)\right)+a\left(\tau\right)\kappa\varepsilon\delta\cos\left(\tau\right)\cos\left(\Phi\left(\tau\right)\right)+\mathcal{O}(\varepsilon^2).\end{aligned} \tag{A.10}$$

Substituting Eq. (A.9) into Eq. (A.10), the new equation can be solved for $a'(\tau)$ and $\varphi'(\tau)$ where a and φ are considered to be constant.

$$a'\left(\tau\right)=\frac{-1}{4}a\kappa\varepsilon\delta\sin\left(\left(2\kappa-1\right)\tau+2\varphi\right)-a\kappa\varepsilon\zeta+\mathcal{O}(\varepsilon^2), \tag{A.11}$$

$$\varphi'\left(\tau\right)=\frac{-1}{4}\kappa\varepsilon\delta\cos\left(\left(2\kappa-1\right)\tau+2\varphi\right)+\kappa\varepsilon\Delta+\mathcal{O}(\varepsilon^2). \tag{A.12}$$

The averaging of $a'\left(\tau\right)$ and $\varphi'\left(\tau\right)$ can be found by integrating Eqs. (A.11) and (A.12) over one period $T=\frac{2\pi}{\Omega}$.

$$a'\left(\tau\right)=\frac{\Omega}{2\pi}\int_0^{\frac{2\pi}{\Omega}}a'\left(\tau\right)\mathrm{d}\tau, \tag{A.13}$$

$$\varphi'\left(\tau\right)=\frac{\Omega}{2\pi}\int_0^{\frac{2\pi}{\Omega}}\varphi'\left(\tau\right)\mathrm{d}\tau. \tag{A.14}$$

The solution of the Eq. (3.3) can be found at different values of κ. Two conditions are considered here, when $\kappa\neq\frac{1}{2}$ $(\Omega_0\neq2\omega_n)$ and when $\kappa=\frac{1}{2}$ $(\Omega_0=2\omega_n)$.

A.1 First condition: $\kappa \neq \frac{1}{2}$ $(\Omega_0 \neq 2\omega_n)$, decaying solutions

For the first condition when $\kappa \neq \frac{1}{2}$, the averaged $a'(\tau)$ and $\varphi'(\tau)$ in Eqs. (A.11) and (A.12) are

$$a'(\tau) = -a\kappa\varepsilon\zeta + \mathcal{O}(\varepsilon^2), \tag{A.15}$$

and

$$\varphi'(\tau) = \kappa\varepsilon\Delta + \mathcal{O}(\varepsilon^2). \tag{A.16}$$

Integrating both $a'(\tau)$ and $\varphi'(\tau)$ respect to τ

$$a(\tau) = a\mathrm{e}^{-\kappa\varepsilon\zeta\tau} + \mathcal{O}(\varepsilon^2), \tag{A.17}$$

and

$$\varphi(\tau) = \kappa\varepsilon\Delta\tau + \mathcal{O}(\varepsilon^2). \tag{A.18}$$

hence the decaying solution is in the form of

$$z(\tau) = a(\tau)\cos(\Phi(\tau)) \cong a\mathrm{e}^{-\kappa\varepsilon\zeta\tau}\cos\left((\kappa + \varepsilon\Delta\kappa)\tau + \varphi_0\right), \tag{A.19}$$

where $\varepsilon\delta \ll 1$

$$\kappa = \frac{\omega_n}{\Omega_0} = \frac{\omega_n(1-\varepsilon\Delta)}{\Omega}, \tag{A.20}$$

multiplying both sides by $1 + \varepsilon\Delta$

$$\kappa(1+\varepsilon\Delta) = \frac{\omega_n(1-\varepsilon\Delta)}{\Omega}(1+\varepsilon\Delta), \tag{A.21}$$

results in

$$\kappa(1+\varepsilon\Delta) = \frac{\omega_n(1-\varepsilon^2\Delta^2)}{\Omega}, \tag{A.22}$$

when $\varepsilon\delta \ll 1$

$$\kappa(1+\varepsilon\Delta) \approx \frac{\omega_n}{\Omega}. \tag{A.23}$$

Hence, substituting $\kappa(1+\varepsilon\Delta) \approx \frac{\omega_n}{\Omega}$ into Eq. (A.19) yields

$$z(\tau) = a(\tau)\cos(\Phi(\tau)) \cong a\mathrm{e}^{-\kappa\varepsilon\zeta\tau}\cos\left(\frac{\omega_n}{\Omega}\tau + \varphi_0\right), \tag{A.24}$$

and in the time domain, where $(\tau = \Omega t)$

$$z\left(t\right) \cong a\mathrm{e}^{-\varepsilon\zeta\omega_n t}\cos\left(\omega_n t+\varphi\right). \tag{A.25}$$

where a and φ are the amplitude of the solution and they are obtained from the initial conditions.

A.2 Second condition: $\kappa = \frac{1}{2}$ ($\Omega_0 = 2\omega_n$), bounded and unbounded solutions

For the second condition when $\kappa = \frac{1}{2}$, $a'\left(\tau\right)$ and $\varphi'\left(\tau\right)$ can be found

$$a'\left(\tau\right) = -a\kappa\varepsilon\zeta + \mathcal{O}(\varepsilon^2), \tag{A.26}$$

and

$$\varphi'\left(\tau\right) = \kappa\varepsilon\Delta - \frac{1}{4}\kappa\varepsilon\delta + \mathcal{O}(\varepsilon^2). \tag{A.27}$$

Here the polar coordinate (a, φ) form is converted into the rectangular form (x, y). It is assumed that

$$x = a\cos\left(\varphi\right), \tag{A.28}$$

$$y = a\sin\left(\varphi\right), \tag{A.29}$$

taking derivatives with respect to τ

$$x' = a'\cos\left(\varphi\right) - a\varphi'\sin\left(\varphi\right), \tag{A.30}$$

$$y' = a'\sin\left(\varphi\right) + a\varphi'\cos\left(\varphi\right). \tag{A.31}$$

Substituting Eqs. (A.26) and (A.27) into Eqs. (A.30) and (A.31) leads to a set of equations, which can be written in the matrix form as

$$\begin{Bmatrix} x' \\ y' \end{Bmatrix} = \begin{bmatrix} -\kappa\varepsilon\zeta & -\kappa\varepsilon\Delta - \frac{1}{4}\kappa\varepsilon\delta \\ +\kappa\varepsilon\Delta - \frac{1}{4}\kappa\varepsilon\delta & -\kappa\varepsilon\zeta \end{bmatrix} \begin{Bmatrix} x \\ y \end{Bmatrix} \tag{A.32}$$

The solution is found from the eigenvalues as

$$\lambda_{1,2} = -\kappa\varepsilon\zeta \pm \frac{1}{4}\kappa\varepsilon\left(-16\Delta^2 + \delta^2\right)^{1/2} + \mathcal{O}(\varepsilon^2). \tag{A.33}$$

A.2.1 Bounded steady-state solutions

If the eigenvalues are complex ($\Delta^2 > \frac{\delta^2}{16}$) then the bounded steady-state solutions exist

$$z\left(t\right) \cong c_1 \cos\left(\frac{1}{2}\sqrt{\varepsilon^2\left(\Delta^2-\frac{1}{16}\delta^2\right)}\omega_n t\right) - c_2 \sin\left(\frac{1}{2}\sqrt{\varepsilon^2\left(\Delta^2-\frac{1}{16}\delta^2\right)}\omega_n t\right), \tag{A.34}$$

c_1 and c_2 are obtained from the initial conditions.

A.2.2 Unbounded solutions

If the eigenvalues are real ($\Delta^2 < \frac{\delta^2}{16}$) then the unbounded solutions exist

$$z\left(t\right) \cong \mathrm{e}^{-\varepsilon\zeta\omega_n t}\left(c_3\mathrm{e}^{2\lambda_1\omega_n t} + c_4\mathrm{e}^{2\lambda_2\omega_n t}\right), \tag{A.35}$$

c_3 and c_4 are obtained from the initial conditions.

A.3 Instability criteria

The first instability region is obtained from Eq. (A.33) when the eigenvalues are real and positive, and

$$\mid \Delta \mid < \sqrt{-\zeta^2+\frac{\delta^2}{16}} \tag{A.36}$$

should be satisfied. Substituting $\varepsilon\Delta = 1 - \frac{\Omega}{\Omega_0}$, Eq. (A.36) yields

$$2-2\varepsilon\sqrt{-\zeta^2+\frac{\delta^2}{16}} < \frac{\Omega}{\omega_n} < 2+2\varepsilon\sqrt{-\zeta^2+\frac{\delta^2}{16}}. \tag{A.37}$$

Rewriting Eq. (A.37) for $\varepsilon\delta$

$$\varepsilon\delta = \frac{2}{\omega_n}\sqrt{\Omega^2-4\Omega\omega_n+4\varepsilon^2\zeta^2\omega_n+4\omega_n^2}. \tag{A.38}$$

Appendix B

The method of averaging to study a nonlinear parametrically excited system

The method of averaging is considered to study the Nonlinear Parametrically Excited (NPE) system introduced in Section 3.4. Eq. (3.27) is normalized by the time scaling $\tau = \Omega t$ and is differentiated with respect to τ. The prime $(.)'$ represents a quantity differentiated with respect to τ. Normalization in this way results in

$$z'' + \frac{2\varepsilon\zeta\omega_n}{\Omega} z' + \frac{\omega_n^2}{\Omega^2} \left(1 + \varepsilon\delta \cos\left(\tau\right)\right) z + \frac{\omega_n^2}{\Omega^2} (\varepsilon\alpha + \varepsilon\gamma \cos\left(\tau\right)) z^3 = 0. \tag{B.1}$$

The complementary solution of this final simplified nonlinear equation is a linear combination of $\cos\left(\Phi\left(\tau\right)\right)$ and $\sin\left(\Phi\left(\tau\right)\right)$,

$$z\left(\tau\right) = a\left(\tau\right) \cos\left(\Phi\left(\tau\right)\right), \tag{B.2}$$

Substituting Eq. (B.2) and its derivative with respect to τ (Eq. (A.8)) into Eq. (B.1) results in an equation which can be solved for $a'\left(\tau\right)$ and $\varphi'\left(\tau\right)$. $a'\left(\tau\right)$ and $\varphi'\left(\tau\right)$ are the averaged over assuming $a\left(\tau\right)$ and $\varphi\left(\tau\right)$ change slowly. $a'\left(\tau\right)$ and $\varphi'\left(\tau\right)$ are the averaged over one period $T = \frac{2\pi}{\Omega}$. The resulting averaged equation can be integrated with respect to τ to find $a\left(\tau\right)$ and $\varphi\left(\tau\right)$ for a given κ and reference frequency Ω_0. The steady-state behaviour of the system can be recovered from the set of $a'\left(\tau\right)$ and $\varphi'\left(\tau\right)$ by setting $(a', \varphi') = (0, 0)$ and solving for steady-state values of a and φ. This approach is similar to the method of averaging used for the linear parametrically excited model.

B.1 First condition: $\kappa \neq \frac{1}{2}$ and $\Omega_0 \neq 2\omega_n$, damped response

Solving Eq. (B.1) with the method of averaging when $\kappa \neq \frac{1}{2}$ ($\Omega_0 \neq 2\omega_n$), results in $a'(\tau)$ and $\varphi'(\tau)$ as follows:

$$a'(\tau) = -\varepsilon\frac{\zeta\omega_n}{\Omega}a + \mathcal{O}(\varepsilon^2), \tag{B.3}$$

$$\varphi'(\tau) = \kappa\varepsilon\Delta + \frac{3\varepsilon\alpha\omega_n^2}{8\kappa\Omega^2}a^2 + \mathcal{O}(\varepsilon^2), \tag{B.4}$$

Hence, the solution based on the first approximation in Eq. (B.2) is

$$z\,(\tau) = a\cos\,(\Phi) \cong a\mathrm{e}^{-\varepsilon\frac{\zeta\omega_n}{\Omega}}, \tag{B.5}$$

a and Φ are constant. In the time domain, where $\kappa\tau = \omega_n t$ Eq. (B.5) gives

$$z\,(t) = a\mathrm{e}^{-\varepsilon\zeta\omega_n t}, \tag{B.6}$$

which is a decaying solution [3]. This is the solution of the system when the system is not excited at twice the natural frequency hence, there is no parametric amplification and the response decays.

B.2 Second condition: $\kappa = \frac{1}{2}$ and $\Omega_0 = 2\omega_n$, steady-state response

Solving Eq. (B.1) with the method of averaging when $\kappa = \frac{1}{2}$ ($\Omega_0 = 2\omega_n$), results in

$$a'(\tau) = a\left(\frac{\varepsilon a^2\,\gamma}{16}\sin\,(2\,\varphi) - \frac{\varepsilon\zeta\omega_n}{\Omega} + \frac{\varepsilon\delta}{8}\sin\,(2\,\varphi)\right) + \mathcal{O}(\varepsilon^2), \tag{B.7}$$

$$\varphi'(\tau) = \frac{1}{2}\,\varepsilon\,\Delta + \frac{\varepsilon a^2\,\gamma}{16}\,\cos\,(2\varphi) + \frac{3\varepsilon a^2\,\alpha}{16} + \frac{\varepsilon\,\delta}{8}\,\cos\,(2\,\varphi) + \mathcal{O}(\varepsilon^2), \tag{B.8}$$

where $\varepsilon\Delta = 1 - \frac{\Omega}{2\omega_n}$. The steady-state solutions, a and φ, are given by $a'(\tau) = \varphi'(\tau) = 0$. If $a = 0$ in Eq. (B.7) is zero, then $a'(\tau) = 0$ and this means $z(\tau) = 0$.

The trivial solutions of Eq. (B.1) are introduced when $a = 0$. Hence, Eq. (B.1) can be considered without the effect of nonlinear terms. For the non-trivial solutions of Eq. (B.1) when $a \neq 0$, Eq. (B.7) becomes

$$\frac{\varepsilon a^2\,\gamma}{16}\sin\,(2\,\varphi) - \frac{\varepsilon\zeta\omega_n}{\Omega} + \frac{\varepsilon\delta}{8}\sin\,(2\,\varphi) + \mathcal{O}(\varepsilon^2) = 0, \tag{B.9}$$

and $\sin(2\varphi)$ and $\cos(2\varphi)$ are

$$\sin(2\varphi) = \frac{8\zeta\omega_n}{\Omega(\frac{1}{2}a^2\gamma + \delta)}. \tag{B.10}$$

$$\cos(2\varphi) = \pm\left(1 - \left(\frac{8\zeta\omega_n}{\Omega(\frac{1}{2}a^2\gamma + \delta)}\right)^2\right)^{\frac{1}{2}}. \tag{B.11}$$

When $\varphi'(\tau) = 0$, from Eq. (B.8)

$$\frac{1}{2}\,\varepsilon\,\Delta + \frac{\varepsilon a^2\,\gamma}{16}\,\cos\left(2\,\varphi\right) + \frac{3\varepsilon a^2\,\alpha}{16} + \frac{\varepsilon\,\delta}{8}\,\cos\left(2\,\varphi\right) = 0. \tag{B.12}$$

Substituting Eq. (B.11) into Eq. (B.12) yields the following relation for $\varepsilon\Delta$

$$\varepsilon\Delta = \pm\left(1 - \left(\frac{8\zeta\omega_n}{\Omega(\frac{1}{2}a^2\gamma + \delta)}\right)^2\right)^{\frac{1}{2}}\left(\frac{\varepsilon a^2\gamma}{4} + \frac{\varepsilon\delta}{4}\right) - \left(\frac{3\varepsilon\alpha a^2}{8}\right), \tag{B.13}$$

where $\varepsilon\Delta = 1 - \frac{\Omega}{2\omega_n}$. This equation can be solved for a to be used for amplitude-frequency relation. If we solve this equation for a, two values of amplitudes will be found. Hence, this nonlinear parametrically excited system has two non-trivial solutions with different amplitudes.

Eq. (B.13) is solved for a, and two amplitudes can be found as a_1 and a_2. These amplitudes change with the parametric frequency. The amplitude-frequency relations from Eq. (B.13) are

$$a_1 = \sqrt{\frac{-4\varepsilon^2\,\gamma\,\delta\, - 12\varepsilon\,\alpha\,\left(\frac{\Omega}{\omega_n}\right) + 24\varepsilon\,\alpha\, + 2\left(\frac{\omega_n}{\Omega}\right)\,(\mathrm{j}_1 + \mathrm{j}_2)}{4\varepsilon^2\,\gamma^2 - 9\varepsilon^2\,\alpha^2}}, \tag{B.14}$$

$$a_2 = \sqrt{\frac{-4\varepsilon^2\,\gamma\,\delta\, - 12\varepsilon\,\alpha\,\left(\frac{\Omega}{\omega_n}\right) + 24\varepsilon\,\alpha\, - 2\left(\frac{\omega_n}{\Omega}\right)\,(\mathrm{j}_1 + \mathrm{j}_2)}{4\varepsilon^2\,\gamma^2 - 9\varepsilon^2\,\alpha^2}}, \tag{B.15}$$

and where j_1 and j_2 are

$$\mathrm{j}_1 = \sqrt{9\varepsilon^4\left(\frac{\omega_n}{\Omega}\right)^2\alpha^2\delta^2 + 24\varepsilon^3\,\gamma\left(\frac{\omega_n}{\Omega}\right)^3\alpha\,\delta\, + 16\varepsilon^2\,\gamma^2\left(\frac{\omega_n}{\Omega}\right)^4}, \tag{B.16}$$

$$\mathrm{j}_2 = \sqrt{256\varepsilon^4\,\gamma^2\zeta^2 - 48\varepsilon^3\,\gamma\left(\frac{\omega_n}{\Omega}\right)^2\alpha\,\delta\, - 576\varepsilon^4\,\alpha^2\zeta^2 - 64\varepsilon^2\,\gamma^2\left(\frac{\omega_n}{\Omega}\right)^3 + 64\varepsilon^2\,\gamma^2\left(\frac{\omega_n}{\Omega}\right)^2}. \tag{B.17}$$

a_1 is the stable solution and a_2 is the unstable solution. The phase of the solutions φ can be found from Eq. (B.10)

$$\varphi = \frac{1}{2}\arcsin\left(\frac{8\zeta\omega_n}{\Omega(\frac{1}{2}a^2\gamma + \delta)}\right). \tag{B.18}$$

B.3 Stability of the steady-state solutions of a nonlinear parametrically excited system

The solution of linear parametrically excited system is stable if it decays in time and is unstable otherwise [122, 123]. However, for a nonlinear system, such as the nonlinear parametrically excited system the stable and unstable solutions are defined differently from the linear system. To study the stability of the steady-state solution of a nonlinear system, for example Eq. (B.1) when $\alpha \neq 0$ and $\gamma \neq 0$, we must consider the small variation which can be added to the amplitude and the phase and then analyse the state of the solutions [3]. Hence, let averaged a to be $a + u$ and averaged φ to be $\varphi + v$, and substituting them into Eq. (B.7) and Eq. (B.8) results in a set of equations, which can be linearised by ignoring higher terms of u, v and uv. After linearising the set of equations are

$$\begin{Bmatrix} u' \\ v' \end{Bmatrix} = \begin{bmatrix} 0 & \varepsilon(\frac{\delta}{4}a + \frac{\gamma}{4}a^3)\cos(2\varphi) \\ \frac{3\varepsilon\alpha a}{8} & -\varepsilon(\frac{\delta}{4} + \frac{\gamma}{4}a^2)\sin(2\varphi) \end{bmatrix} \begin{Bmatrix} u \\ v \end{Bmatrix} \tag{B.19}$$

and the corresponding eigenvalues can be written as

$$\begin{aligned} \lambda_1, \lambda_2 = &-\frac{\varepsilon}{2}\left(\frac{\delta}{4} + \frac{\gamma}{4}a^2\right)\sin(2\varphi) \\ &\pm \frac{1}{2}\sqrt{\left(\varepsilon\left(\frac{\delta}{4} + \frac{\gamma}{4}a^2\right)\sin(2\varphi)\right)^2 + \left(\frac{3\varepsilon^2\alpha}{2}\left(\frac{\delta}{2}a^2 + \frac{\gamma}{4}a^4\right)\right)\cos(2\varphi)}. \end{aligned} \tag{B.20}$$

and replacing $\sin(2\varphi)$ by $\frac{8\zeta\omega_n}{\Omega(\frac{1}{2}a^2\gamma+\delta)}$ from Eq. (B.10) in Eq. (B.20), results in:

$$\begin{aligned} \lambda_1, \lambda_2 = &-\frac{\varepsilon}{2}\left(\frac{\delta}{4} + \frac{\gamma}{4}a^2\right)\left(\frac{8\zeta\omega_n}{\Omega(\frac{1}{2}a^2\gamma + \delta)}\right) \\ &\pm \frac{1}{2}\sqrt{\left(\varepsilon\left(\frac{\delta}{4} + \frac{\gamma}{4}a^2\right)\left(\frac{8\zeta\omega_n}{\Omega(\frac{1}{2}a^2\gamma + \delta)}\right)\right)^2 + \left(\frac{3\varepsilon^2\alpha}{2}\left(\frac{\delta}{2}a^2 + \frac{\gamma}{4}a^4\right)\right)\cos(2\varphi)}. \end{aligned} \tag{B.21}$$

The steady-state phase is derived from Eq. (B.10) and Eq. (B.11), and the solutions are $z\left(\tau\right) = a\cos\left(\kappa\tau + \varphi\right)$ when $\kappa = \frac{1}{2}$. The stability of the parametrically excited system with nonlinear parameter Eq. (3.26) can be found by using the eigenvalues shown in Eq. (B.21). $\left(\varepsilon\left(\frac{\delta}{4} + \frac{\gamma}{4}a^2\right)\left(\frac{8\zeta\omega_n}{\Omega(\frac{1}{2}a^2\gamma+\delta)}\right)\right)^2$ in Eq. (B.21) is positive and negligible when ζ is small. Due to this, the following statements hold when $\zeta \neq 0$:

- If $\cos(2\varphi) > 0$, then the eigenvalues can be positive real and negative real, hence an unstable solution exists.
- If $\cos(2\varphi) < 0$, then eigenvalues are imaginary and have negative real parts, hence a stable solution exists.
- If $\cos(2\varphi) = 0$, one of the eigenvalues is negative and real and the other one is zero. The steady-state solution represented by the point with vertical tangent, which bounds the upper and lower curve, is stable [6].

In order to find the bifurcation point for highly damped NPE system $\cos(2\varphi) = 0$ is considered. Substituting $\cos(2\varphi) = 0$ in Eq. (B.11) and solving for $\frac{\Omega}{\omega_{\mathrm{n}}}$ yields

$$\frac{\Omega}{\omega_{\mathrm{n}}} = \frac{8\zeta}{\frac{1}{2}a^2\gamma + \delta}. \tag{B.22}$$

This is the frequency at which the bifurcation can happen. For the parametrically excited system the damping ratio has to be large ($\zeta \gg \frac{\delta}{4}$), otherwise the stable and unstable solution do not meet at the bifurcation point.

The amplitude-frequency relation can present the behaviour of the nonlinear system based on the amplitude of the steady-state response and the parametric frequency. These amplitudes Eq. (B.14) and Eq. (B.15) are the function of nonlinear terms, such as cubic stiffness α and cubic parametric stiffness nonlinearity γ. Based on the stability of the non-trivial solutions, the solutions are

- $z_1(t) = a_1 \cos\left(\frac{\Omega}{2}t + \varphi\right)$ when $\varphi > 0$ or $\varphi = 0$, which is stable.
- $z_2(t) = a_2 \cos\left(\frac{\Omega}{2}t + \varphi\right)$ when $\varphi < 0$, which is unstable.

B.4 Undamped case, $\zeta = 0$

When the damping ratio is zero, Eq. (B.10) and Eq. (B.11), becomes $\sin(2\varphi) = 0$ and $\cos(2\varphi) = \pm 1$, hence the phase is $\varphi = \frac{\pi}{2}$ and 0. In this case the non-trivial solutions of the systems based on the approximate solutions ($z(\tau) = a\cos(\kappa\tau + \varphi)$) for $\kappa = \frac{1}{2}$ are

$$z(\tau) = -a\sin\left(\frac{\tau}{2}\right), \text{ and } \quad z(\tau) = a\cos\left(\frac{\tau}{2}\right), \tag{B.23}$$

and in the time domain t, where $\kappa\tau = \omega_n t$, the solutions are

$$z(t) = -a\sin\left(\frac{\Omega}{2}t\right), \quad \text{and} \quad z(t) = a\cos\left(\frac{\Omega}{2}t\right). \tag{B.24}$$

These are two solutions of the undamped parametric system with nonlinear parameters, where one is stable and the other is unstable. To find the stability of each solution, eigenvalues of the linearised system are considered.

The eigenvalues (from Eq. (B.21)) when $\zeta = 0$ and $\sin(2\varphi) = 0$ can be calculated

$$\lambda_{1,2} = \pm\frac{1}{2}\sqrt{\varepsilon^2\left(\frac{\delta}{4} + \frac{\gamma}{4}a^2\right)^2 + \left(\frac{3\varepsilon^2\alpha}{2}\left(\frac{\delta}{2}a^2 + \frac{\gamma}{4}a^4\right)\right)\cos(2\varphi)}. \tag{B.25}$$

In Eq. (B.25), $\cos(2\varphi)$ can be calculated from Eq. (B.11). $\cos(2\varphi) = \pm 1$ is calculated from Eq. (B.11). When $\cos(2\varphi) = 1$ this makes the eigenvalues to have a real and positive solution which shows the solution is unstable when $\varphi = 0$. When $\cos(2\varphi) = -1$ then the eigenvalues become imaginary and this shows a stable periodic solution. In summary:

- When $\varphi = \frac{\pi}{2}$, $\cos(2\varphi) = -1$, $\lambda_1 = -\lambda_2$ and complex, hence the stable solution is $z\left(t\right) = -a\sin\left(\frac{\Omega}{2}t\right)$.
- When $\varphi = 0$, $\cos(2\varphi) = 1$, $\lambda_1 < 0$ and $\lambda_2 > 0$ and real, hence the unstable solution is $z\left(t\right) = a\cos\left(\frac{\Omega}{2}t\right)$.

B.4.1 Case 1, $\zeta = 0$, $\alpha \neq 0$ and $\gamma = 0$

The amplitude of the response can be found by solving Eq. (B.13) for a, considering $\zeta = 0$, $\alpha \neq 0$ and $\gamma = 0$ two solutions are obtained

$$a_1 = \frac{1}{3\varepsilon\alpha}\sqrt{12\varepsilon\alpha\left(\frac{\Omega}{\omega_n}\right) - 24\varepsilon\alpha + 6\varepsilon^2\delta\alpha}, \tag{B.26}$$

and

$$a_2 = \frac{1}{3\varepsilon\alpha}\sqrt{12\varepsilon\alpha\left(\frac{\Omega}{\omega_n}\right) - 24\varepsilon\alpha - 6\varepsilon^2\delta\alpha}. \tag{B.27}$$

Considering the former condition for stability of the non-trivial solutions, the stable and unstable solutions are

- When $\varphi = \frac{\pi}{2}$, the stable solution is $z_1\left(t\right) = -a_1\sin\left(\frac{\Omega}{2}t\right)$.
- When $\varphi = 0$, the unstable solution is $z_2\left(t\right) = a_2\cos\left(\frac{\Omega}{2}t\right)$.

B.4.2 Case 2, $\zeta = 0$, $\alpha \neq 0$ and $\gamma \neq 0$

The amplitude of the response can be found by solving Eq. (B.13) for a, considering $\zeta = 0$, $\alpha \neq 0$ and $\gamma \neq 0$ two solutions are obtained

$$a_1 = \sqrt{-\frac{4\varepsilon^2\delta\gamma + 12\varepsilon\alpha\left(\frac{\Omega}{\omega_n}\right) - 24\varepsilon\alpha + \left(6\varepsilon^2\delta\alpha + 8\varepsilon\gamma\left(\frac{\Omega}{\omega_n}\right) - 16\varepsilon\gamma)\right)}{4\varepsilon^2\gamma^2 - 9\varepsilon^2\alpha^2}}, \tag{B.28}$$

and

$$a_2 = \sqrt{-\frac{4\varepsilon^2\delta\gamma + 12\varepsilon\alpha\left(\frac{\Omega}{\omega_n}\right) - 24\varepsilon\alpha - \left(6\varepsilon^2\delta\alpha + 8\varepsilon\gamma\left(\frac{\Omega}{\omega_n}\right) - 16\varepsilon\gamma)\right)}{4\varepsilon^2\gamma^2 - 9\varepsilon^2\alpha^2}}. \tag{B.29}$$

Similar to the previous case, based on the stability of the non-trivial solutions, the stable and unstable solutions are

- When $\varphi = \frac{\pi}{2}$, the stable solution is $z_1\left(t\right) = -a_1\sin\left(\frac{\Omega}{2}t\right)$.
- When $\varphi = 0$, the unstable solution is $z_2\left(t\right) = a_2\cos\left(\frac{\Omega}{2}t\right)$.

B.5 Damped case, $\zeta \neq 0$

When the damping is included, from Eq. (B.10) and Eq. (B.11) the phase can be calculated and the solutions would be $z(\tau) = a\cos(\kappa\tau + \varphi)$ for the case ($\kappa = \frac{1}{2}$). In the case that two amplitudes (a_1 and a_2) are found for the response, that means the system has two solutions $z(\tau)_1 = a_1\cos(\kappa\tau + \varphi)$ and $z(\tau)_2 = a_2\cos(\kappa\tau + \varphi)$. One of the solutions can be stable and the other one is the unstable solution.

B.5.1 Stability of non-trivial solutions, damped case $\zeta \neq 0$ and $\alpha \neq 0$ and $\gamma = 0$

The eigenvalues (Eq. (B.21)) when $\zeta \neq 0$ and $\gamma = 0$, are

$$\lambda_{1,2} = \frac{1}{8}\delta\sin(2\varphi) \pm \frac{1}{2}\sqrt{\frac{\varepsilon^2\delta^2}{16}\sin^2(2\varphi) + \frac{3}{4}\varepsilon^2\alpha\delta a\cos(2\varphi)}. \tag{B.30}$$

Substituting the Eq. (B.10) into Eq. (B.30) yields

$$\lambda_{1,2} = -\varepsilon\frac{\zeta\omega_n}{\Omega} \pm \frac{1}{2}\sqrt{\frac{4\varepsilon^2\zeta^2\omega_n^2}{\Omega^2} + \frac{3}{4}\varepsilon^2\alpha\delta a^2\cos(2\varphi)}. \tag{B.31}$$

The part $\frac{4\varepsilon^2\zeta^2\omega_n^2}{\Omega^2}$ in Eq. (B.31) is always positive, hence if

- $\cos(2\varphi) > 0$ then the eigenvalues can be positive real and negative real ($\lambda_1 > 0$ and $\lambda_2 < 0$), hence an unstable solution exists.
- $\cos(2\varphi) < 0$ then eigenvalues are imaginary with positive real and negative real part ($\lambda_1 = -\lambda_2$ and complex), hence a stable solution exists.
- $\cos(2\varphi) = 0$ then the eigenvalues are negative and real (λ_1, $\lambda_2 < 0$), hence a stable solution exists.

B.5.2 Non-trival solutions, $\zeta \neq 0$, $\alpha \neq 0$ and $\gamma = 0$

The amplitude of the response can be found by solving Eq. (B.13) for a, considering $\zeta \neq 0$, $\alpha \neq 0$ and $\gamma = 0$ two solutions are obtained

$$a_1 = \frac{1}{3\varepsilon\alpha}\sqrt{12\varepsilon\alpha\left(\frac{\Omega}{\omega_n}\right) - 24\varepsilon\alpha + 6\left(\frac{\omega_n}{\Omega}\right)\sqrt{\varepsilon^4\delta^2\alpha^2\left(\frac{\Omega}{\omega_n}\right)^2 - 64\varepsilon^4\alpha^2\zeta^2}}, \tag{B.32}$$

and

$$a_2 = \frac{1}{3\varepsilon\alpha}\sqrt{12\varepsilon\alpha\left(\frac{\Omega}{\omega_n}\right) - 24\varepsilon\alpha - 6\left(\frac{\omega_n}{\Omega}\right)\sqrt{\varepsilon^4\delta^2\alpha^2\left(\frac{\Omega}{\omega_n}\right)^2 - 64\varepsilon^4\alpha^2\zeta^2}}. \tag{B.33}$$

Based on the stability of the non-trivial solutions, the stable and unstable solutions are

- When $\varphi = \frac{\pi}{2}$, the stable solution is $z_1\left(t\right) = -a_1 \cos\left(\frac{\Omega}{2}t + \varphi\right)$.
- When $\varphi = 0$, the unstable solution is $z_2\left(t\right) = a_2 \cos\left(\frac{\Omega}{2}t + \varphi\right)$.

B.5.3 Stability of non-trivial solutions, damped case $\zeta \neq 0$, $\alpha \neq 0$ and $\gamma \neq 0$

Based on the eigenvalues Eq. (B.21) the stability of the parametrically excited system with the nonlinear parameter from Eq. (3.26) can be found. The part $\varepsilon^2 \left(\frac{\delta}{4} + \frac{\gamma}{4}a^2\right)^2$ in Eq. (B.21) is always positive hence, if

- $\cos(2\varphi) > 0$ then the eigenvalues can be positive real and negative real, hence an unstable solution exists.
- $\cos(2\varphi) < 0$ then eigenvalues are imaginary with positive real and negative real part, hence a stable solution exists.
- $\cos(2\varphi) = 0$ then the eigenvalues are negative and real, hence a stable solution exist.

Appendix C

The method of harmonic balance

C.1 The method of harmonic balance for solving a linear parametrically excited system system

The Linear Parametrically Excited (LPE) system introduced in Section 3.2 is studied with the method of harmonic balance.

C.1.1 Free vibration case, instability criteria, low number of terms

The stability boundaries of the Mathieu equation, Eq. (3.2) can be found by considering the solution as

$$z(t) = A_1 \cos\left(\frac{\Omega t}{2}\right) + B_1 \sin\left(\frac{\Omega t}{2}\right). \tag{C.1}$$

Substituting the trial $z(t)$ Eq. (C.1) into Eq. (3.2) and some trigonomerty yields

$$\begin{aligned} -\frac{1}{4}\,A_1\,\Omega^2\cos\left(\frac{\Omega t}{2}\right) - \frac{1}{4}\,B_1\,\Omega^2\sin\left(\frac{\Omega t}{2}\right) - \varepsilon\,\zeta\,\omega_n\,A_1\,\Omega\,\sin\left(\frac{\Omega t}{2}\right) + \varepsilon\,\zeta\,\omega_n\,B_1\,\Omega\,\cos\left(\frac{\Omega t}{2}\right) \\ + \frac{1}{2}\,A_1\,\delta\,\varepsilon\,{\omega_n}^2\cos\left(\frac{\Omega t}{2}\right) + \frac{1}{2}\,A_1\,\delta\,\varepsilon\,{\omega_n}^2\cos\left(\frac{3\Omega t}{2}\right) + \frac{1}{2}\,B_1\,\delta\,\varepsilon\,{\omega_n}^2\sin\left(\frac{3\Omega t}{2}\right) \\ - \frac{1}{2}\,B_1\,\delta\,\varepsilon\,{\omega_n}^2\sin\left(\frac{\Omega t}{2}\right) + A_1\,\cos\left(\frac{\Omega t}{2}\right){\omega_n}^2 + B_1\,\sin\left(\frac{\Omega t}{2}\right){\omega_n}^2 = 0. \end{aligned} \tag{C.2}$$

The solutions with frequency higher than $\frac{\Omega}{2}$ in Eq. (C.2) are neglected hence this is simplified to

$$\begin{aligned} \cos\left(\frac{\Omega t}{2}\right)\left(-\frac{1}{4}\,A_1\,\Omega^2 + \varepsilon\,\zeta\,\omega_n\,B_1\,\Omega + \frac{1}{2}\,A_1\,\delta\,\varepsilon\,{\omega_n}^2 + A_1\,{\omega_n}^2\right) \\ + \sin\left(\frac{\Omega t}{2}\right)\left(-\frac{1}{4}\,B_1\,\Omega^2 - \varepsilon\,\zeta\,\omega_n\,A_1\,\Omega - \frac{1}{2}\,B_1\,\delta\,\varepsilon\,{\omega_n}^2 + B_1\,{\omega_n}^2\right) = 0. \end{aligned} \tag{C.3}$$

Equating the coefficient of $\cos\left(\frac{\Omega t}{2}\right)$ and $\sin\left(\frac{\Omega t}{2}\right)$ from Eq. (C.3) yields to two sets of equations

$$\left(-\frac{1}{4}\,\Omega^2 + \frac{1}{2}\delta\,\varepsilon\,{\omega_n}^2 + {\omega_n}^2\right) A_1 + \varepsilon\,\zeta\,\omega_n\,\Omega B_1 = 0, \tag{C.4}$$

$$-\varepsilon\,\zeta\,\omega_n\,\Omega A_1 + \left(-\frac{1}{4}\,\Omega^2 - \frac{1}{2}\delta\,\varepsilon\,{\omega_n}^2 + {\omega_n}^2\right) B_1 = 0, \tag{C.5}$$

and in matrix form

$$\begin{bmatrix} \mathrm{L11} & \mathrm{L12} \\ -\mathrm{L12} & \mathrm{L22} \end{bmatrix} \times \begin{bmatrix} A_1 \\ B_1 \end{bmatrix} = \begin{bmatrix} 0 \\ 0 \end{bmatrix} \tag{C.6}$$

$$\mathrm{L11} = -\frac{1}{4}\,\Omega^2 + \frac{1}{2}\delta\,\varepsilon\,{\omega_n}^2 + {\omega_n}^2, \tag{C.7}$$

$$\mathrm{L12} = \varepsilon\,\zeta\,\omega_n\,\Omega, \tag{C.8}$$

$$\mathrm{L22} = -\frac{1}{4}\,\Omega^2 - \frac{1}{2}\delta\,\varepsilon\,{\omega_n}^2 + {\omega_n}^2, \tag{C.9}$$

setting the determinant of the matrix $\mathbf{L}$ equal to zero gives the instability equation, and solving it for $\varepsilon\delta$ yields

$$\varepsilon\delta = \frac{2}{\omega_n}\sqrt{\Omega^2 - 4\Omega\omega_n + 4\varepsilon^2\zeta^2\omega_n + 4\omega_n^2}. \tag{C.10}$$

C.1.2 Instability criteria, high number of terms

To study the odd-occurrence stability regions, periodic solutions of period $2T$, $T = \frac{2\pi}{\Omega}$ are considered. To determine the even occurrence stability boundaries, periodic solutions of period T, $T = \frac{2\pi}{\Omega}$ must be investigated.

Periodic solutions of period $2T$ can be expressed as a Fourier series,

$$\begin{aligned} z(t) = \sum_{m=0}^{M} A_{2m}\cos\left(\frac{2m\pi t}{T}\right) + B_{2m}\sin\left(\frac{2m\pi t}{T}\right) \\ = \sum_{m=1}^{M} A_{2m}\cos\left(\frac{2m\Omega t}{2}\right) + B_{2m}\sin\left(\frac{2m\Omega t}{2}\right), \end{aligned} \tag{C.11}$$

where A_{2m} and B_{2m} are the even coefficient of the Fourier series, and M is the number of terms. Substituting Eq. (C.11) into Eq. (3.2) and setting the coefficients of the trigonometric terms to zero leads to a set of equations for the transition curves. The non-trivial solution of this set results in the stability threshold, which describes a relation between Ω and $\varepsilon\delta$. Similarly, periodic solutions of period T can be expressed as a Fourier series,

$$\begin{aligned} z(t) = \sum_{m=1}^{M} A_{2m-1} \cos\left(\frac{(2m-1)\pi t}{T}\right) + B_{2m-1} \sin\left(\frac{(2m-1)\pi t}{T}\right) \\ = \sum_{m=1}^{M} A_{2m-1} \cos\left(\frac{(2m-1)\Omega t}{2}\right) + B_{2m-1} \sin\left(\frac{(2m-1)\Omega t}{2}\right), \end{aligned} \quad \text{(C.12)}$$

where A_{2m-1} and B_{2m-1} are the odd coefficients of the Fourier series, and M is the number of terms. Using the same procedure for periodic solutions of period $2T$ leads to another set of equations, which represents a set of lines in the Strutt diagram for the Mathieu equation [9].

C.1.3 MAPLE Code for generating the odd and even matrices

```
>restart:
```

FinalN is the number of terms in harmonic balance method.

```
>FinalN:=20
```

f is the governing differential equation. Eq. (3.2).

```
>f1 := expand(f)
>f2 := combine(f1, trig)
>for m to FinalN do SIN[m] := coeff(f2, sin((1/2)*m*Omega*t)) end do
>for m to FinalN do COS[m] := coeff(f2, cos((1/2)*m*Omega*t)) end do
>for n to (1/2)*FinalN do for m to (1/2)*FinalN do M[n, m] := coeff(SIN[2*n-1], a[2*m-1]) end do end do
>for n to (1/2)*FinalN do for m to (1/2)*FinalN do M[n, m+(1/2)*FinalN] := coeff(SIN[2*n-1], b[2*m-1]) end do end do
>for n to (1/2)*FinalN do for m to (1/2)*FinalN do M[n+(1/2)*FinalN, m] := coeff(COS[2*n-1], a[2*m-1]) end do end do
>for n to (1/2)*FinalN do for m to (1/2)*FinalN do M[n+(1/2)*FinalN, m+(1/2)*FinalN] := coeff(COS[2*n-1], b[2*m-1]) end do end do
>for n to FinalN do for m to FinalN do M[n, m] end do end do
>A := Matrix(FinalN, FinalN)
>for i to FinalN do for j to FinalN do A[i, j] := M[i, j] end do end do
>with(LinearAlgebra)
>det := Determinant(A)
```

Odd matrix.

```
>Podd := det
>COS[0] := (coeff(f2, a[0])-DELTA*k1*cos(Omega*t))*a[0]+(1/2)*DELTA*k1*a[2]
```

```
>SIN[0] := 0
>for m to FinalN do SIN[m] := coeff(f2, sin((1/2)*m*Omega*t)) end do
>for m to FinalN do COS[m] := coeff(f2, cos((1/2)*m*Omega*t)) end do
>for n to (1/2)*FinalN do for m from 0 to (1/2)*FinalN do M[n, m+1] := coeff(SIN[2*n], a[2*m]) end do end do
>for n to (1/2)*FinalN do for m to (1/2)*FinalN do M[n, m+(1/2)*FinalN+1] := coeff(SIN[2*n], b[2*m]) end do end do
>for n from 0 to (1/2)*FinalN do for m from 0 to (1/2)*FinalN do M[n+(1/2)*FinalN+1, m+1] := coeff(COS[2*n], a[2*m]) end do end do
>for n from 0 to (1/2)*FinalN do for m to (1/2)*FinalN do M[n+(1/2)*FinalN+1, m+(1/2)*FinalN+1] := coeff(COS[2*n], b[2*m]) end do end do
>for n to FinalN+1 do for m to FinalN+1  do M[n, m] end do end do
>B := Matrix(FinalN+1, FinalN+1)
>for i to FinalN+1 do for j to FinalN+1 do B[i, j] := M[i, j] end do end do
>det := Determinant(B)
```

Even matrix.

```
>Peven := det
```

C.1.4 Solution of a directly excited linear parametrically excited system

In order to find the response of Eq. (3.10) the method of harmonic balance can be applied. By assuming the response to a sinusoidal excitation is a sinusoid at the same frequency [9], the solution as a Fourier series results in

$$\begin{aligned} z(t) = A_0 \cos(\omega t) + B_0 \sin(\omega t) + \sum_{m=1}^{M} A_m \cos((\omega + m\Omega)t) + B_m \cos((\omega - m\Omega)t) \\ + C_m \sin((\omega + m\Omega)t) + D_m \sin((\omega - m\Omega)t). \end{aligned} \tag{C.13}$$

By substituting Eq. (C.13) into Eq. (3.10), the Fourier series coefficients can be found. The coefficients of sine and cosine of all harmonics are partitioned. For example, the number of terms $M = 6$ is considered to take into account the combined harmonics up to $\omega + 6\Omega$. For $M = 6$, a matrix of 26×26 is produced. Finding the determinant of the matrix leads to the coefficients of the combined harmonics. Putting each coefficient back to Eq. (C.13) gives the solution of Eq. (3.10).

C.2 The method of harmonic balance for a nonlinear parametrically excited system

The stability boundaries of Eq. (3.27) can be found by considering the solution as

$$z(t) = A_1 \cos\left(\frac{\Omega t}{2}\right) + B_1 \sin\left(\frac{\Omega t}{2}\right). \tag{C.14}$$

Substituting the trial $z(t)$ Eq. (C.14) into Eq. (3.27) yields

$$\begin{aligned}
&-\varepsilon\,\zeta\,\omega_n\,A_1\,\Omega\,\sin\left(\frac{\Omega\,t}{2}\right)+\varepsilon\,\zeta\,\omega_n\,B_1\,\Omega\,\cos\left(\frac{1}{2}\,\Omega\,t\right)\\
&+\frac{3}{4}\,{A_1}^2B_1\,\sin\left(\frac{3\Omega\,t}{2}\right)\alpha\,\varepsilon\,{\omega_n}^2+\frac{3}{4}\,{A_1}^2B_1\,\sin\left(\frac{\Omega\,t}{2}\right)\alpha\,\varepsilon\,{\omega_n}^2\\
&-\frac{3}{4}\,A_1\,{B_1}^2\cos\left(\frac{3}{2}\,\Omega\,t\right)\alpha\,\varepsilon\,{\omega_n}^2+\frac{3}{4}\,A_1\,{B_1}^2\cos\left(\frac{1}{2}\,\Omega\,t\right)\alpha\,\varepsilon\,{\omega_n}^2+\frac{3}{8}\,{A_1}^2B_1\,\gamma\,\varepsilon\,{\omega_n}^2\sin\left(\frac{5}{2}\,\Omega\,t\right)\\
&+\frac{3}{8}\,{A_1}^2B_1\,\gamma\,\varepsilon\,{\omega_n}^2\sin\left(\frac{3}{2}\,\Omega\,t\right)-\frac{3}{8}\,A_1\,{B_1}^2\gamma\,\varepsilon\,{\omega_n}^2\cos\left(\frac{5}{2}\,\Omega\,t\right)+\frac{3}{8}\,A_1\,{B_1}^2\gamma\,\varepsilon\,{\omega_n}^2\cos\left(\frac{3}{2}\,\Omega\,t\right)\\
&+B_1\,\sin\left(\frac{\Omega\,t}{2}\right){\omega_n}^2+A_1\,\cos\left(\frac{\Omega\,t}{2}\right){\omega_n}^2+\frac{1}{4}\,{A_1}^3\cos\left(\frac{3}{2}\,\Omega\,t\right)\alpha\,\varepsilon\,{\omega_n}^2+\frac{3}{4}\,{A_1}^3\cos\left(\frac{\Omega\,t}{2}\right)\alpha\,\varepsilon\,{\omega_n}^2\\
&-\frac{1}{4}\,{B_1}^3\sin\left(\frac{3}{2}\,\Omega\,t\right)\alpha\,\varepsilon\,{\omega_n}^2+\frac{3}{4}\,{B_1}^3\sin\left(\frac{\Omega\,t}{2}\right)\alpha\,\varepsilon\,{\omega_n}^2+\frac{1}{2}\,{A_1}^3\gamma\,\varepsilon\,{\omega_n}^2\cos\left(\frac{1}{2}\,\Omega\,t\right)\\
&+\frac{1}{8}\,{A_1}^3\gamma\,\varepsilon\,{\omega_n}^2\cos\left(\frac{5}{2}\,\Omega\,t\right)+\frac{3}{8}\,{A_1}^3\gamma\,\varepsilon\,{\omega_n}^2\cos\left(\frac{3}{2}\,\Omega\,t\right)-\frac{1}{8}\,{B_1}^3\gamma\,\varepsilon\,{\omega_n}^2\sin\left(\frac{5}{2}\,\Omega\,t\right)\\
&-\frac{1}{2}\,{B_1}^3\gamma\,\varepsilon\,{\omega_n}^2\sin\left(\frac{1}{2}\,\Omega\,t\right)+\frac{3}{8}\,{B_1}^3\gamma\,\varepsilon\,{\omega_n}^2\sin\left(\frac{3}{2}\,\Omega\,t\right)+\frac{1}{2}\,A_1\,\delta\,\varepsilon\,{\omega_n}^2\cos\left(\frac{\Omega\,t}{2}\right)\\
&+\frac{1}{2}\,A_1\,\delta\,\varepsilon\,{\omega_n}^2\cos\left(\frac{3\Omega\,t}{2}\right)+\frac{1}{2}\,B_1\,\delta\,\varepsilon\,{\omega_n}^2\sin\left(\frac{3\Omega\,t}{2}\right)-\frac{1}{2}\,B_1\,\delta\,\varepsilon\,{\omega_n}^2\sin\left(\frac{1}{2}\,\Omega\,t\right)\\
&-\frac{1}{4}\,A_1\,\Omega^2\cos\left(\frac{1}{2}\,\Omega\,t\right)-\frac{1}{4}\,B_1\,\Omega^2\sin\left(\frac{\Omega\,t}{2}\right)=0
\end{aligned} \tag{C.15}$$

The solutions with the frequency higher than $\frac{\Omega}{2}$ in Eq. (C.15) are neglected hence it is simplified to

$$\begin{aligned}
&\cos\left(\frac{\Omega t}{2}\right)\left(\varepsilon\,\zeta\omega_nB_1\Omega+\frac{3}{4}{A_1}^3\alpha\varepsilon{\omega_n}^2+\frac{1}{2}{A_1}^3\gamma\varepsilon{\omega_n}^2+\frac{1}{2}\,A_1\delta\varepsilon\,{\omega_n}^2+A_1{\omega_n}^2-\frac{1}{4}A_1\,\Omega^2\right)\\
&+\sin\left(\frac{\Omega t}{2}\right)\left(-\varepsilon\zeta\omega_nA_1\Omega+B_1{\omega_n}^2-\frac{1}{4}B_1\Omega^2+\frac{3}{4}{B_1}^3\alpha\varepsilon{\omega_n}^2-\frac{1}{2}\,{B_1}^3\gamma\varepsilon{\omega_n}^2-\frac{1}{2}\,B_1\delta\varepsilon{\omega_n}^2\right)=0
\end{aligned} \tag{C.16}$$

Equating the coefficient of $\cos\left(\frac{\Omega t}{2}\right)$ and $\sin\left(\frac{\Omega t}{2}\right)$ from Eq. (C.16) yields to two equations

$$\left(-\frac{1}{4}\,\Omega^2+\frac{1}{2}\delta\,\varepsilon\,{\omega_n}^2+\frac{3}{4}\,{A_1}^2\alpha\,\varepsilon\,{\omega_n}^2+\frac{1}{2}\,{A_1}^2\gamma\,\varepsilon\,{\omega_n}^2+{\omega_n}^2\right)A_1+\varepsilon\,\zeta\,\omega_n\,\Omega B_1=0, \tag{C.17}$$

$$-\varepsilon\,\zeta\,\omega_n\,\Omega A_1+\left(-\frac{1}{4}\Omega^2-\frac{1}{2}\delta\,\varepsilon\,{\omega_n}^2+\frac{3}{4}\,{B_1}^2\alpha\,\varepsilon\,{\omega_n}^2-\frac{1}{2}\,{B_1}^2\gamma\,\varepsilon\,{\omega_n}^2+{\omega_n}^2\right)B_1=0, \tag{C.18}$$

and in matrix form when the amplitude of the system is considered as $A_0 = B_0 = a$

$$\begin{bmatrix} \mathrm{L11} & \mathrm{L12} \\ -\mathrm{L12} & \mathrm{L22} \end{bmatrix} \times \begin{bmatrix} A_1 \\ B_1 \end{bmatrix} = \begin{bmatrix} 0 \\ 0 \end{bmatrix} \tag{C.19}$$

$$\mathrm{L11}=-\frac{1}{4}\,\Omega^2+\frac{1}{2}\delta\,\varepsilon\,{\omega_n}^2+\frac{3}{4}\,a^2\alpha\,\varepsilon\,{\omega_n}^2+\frac{1}{2}\,a^2\gamma\,\varepsilon\,{\omega_n}^2+{\omega_n}^2, \tag{C.20}$$

$$\mathrm{L12}=\varepsilon\,\zeta\,\omega_n\,\Omega, \tag{C.21}$$

$$\mathrm{L22}=-\frac{1}{4}\Omega^2-\frac{1}{2}\delta\,\varepsilon\,{\omega_n}^2+\frac{3}{4}\,a^2\alpha\,\varepsilon\,{\omega_n}^2-\frac{1}{2}\,a^2\gamma\,\varepsilon\,{\omega_n}^2+{\omega_n}^2, \tag{C.22}$$

setting the determinant of the matrix **L** equal to zero, gives the instability equation, and solving it for $\varepsilon\delta$ yields

$$\varepsilon\delta=-\varepsilon a^2\gamma+\frac{1}{2}\sqrt{\left(\frac{\Omega}{\omega_n}\right)^4-6\varepsilon\left(\frac{\Omega}{\omega_n}\right)^2a^2\alpha+64\varepsilon^2\zeta^2-8\left(\frac{\Omega}{\omega_n}\right)^2+24\varepsilon a^2\alpha+16} \tag{C.23}$$

C.2.1 Frequency response

For a nonlinear forced Mathieu equation

$$m\ddot{z}+\varepsilon c\dot{z}+\left(k_1+\varepsilon k_{\mathrm{p}1}\cos\left(\Omega t\right)\right)z+\left(\varepsilon k_3+\varepsilon k_{\mathrm{p}3}\cos\left(\Omega t\right)\right)z^3=\varepsilon F\cos(\omega t+\phi), \tag{C.24}$$

where F is the force, a trial solution $z(t) = a\cos\left(\omega\,t\right)$, for Eq. (C.24) is considered. Substituting the trial $z(t)$ into Eq. (C.24) yields

$$
\begin{aligned}
&- m_t\, a_0\, \omega^2 \cos(\omega\, t) - \varepsilon\, c_t\, a_0\, \omega\, \sin(\omega\, t) + k_1\, a_0\, \cos(\omega\, t) \\
&\quad + \frac{1}{2}\, k_{\mathrm{p}1}\, a_0\, \cos(\Omega\, t - \omega\, t) + \frac{1}{2}\, k_{\mathrm{p}1}\, a_0\, \cos(\Omega\, t + \omega\, t) + \frac{1}{4}\, k_3\, {a_0}^3 \cos(3\, \omega\, t) \\
&\quad + \frac{3}{8}\, k_3\, {a_0}^3 \cos(\omega\, t) + \frac{3}{8}\, k_{\mathrm{p}3}\, {a_0}^3 \cos(\Omega\, t - 3\, \omega\, t) + \frac{3}{8}\, k_{\mathrm{p}3}\, {a_0}^3 \cos(\Omega\, t + 3\, \omega\, t) \\
&\quad + \frac{3}{8}\, k_{\mathrm{p}3}\, {a_0}^3 \cos(\Omega\, t - \omega\, t) + \frac{3}{8}\, k_{\mathrm{p}3}\, {a_0}^3 \cos(\Omega\, t + \omega\, t) = \varepsilon\, F \cos(\omega\, t + \phi) \qquad \text{(C.25)}
\end{aligned}
$$

When $\Omega = 2\omega$, and the higher and lower terms are neglected and $\varepsilon F \cos(\omega t + \phi)$ in Eq. (C.25) is replaced by $\varepsilon F \cos(\omega t) \cos(\phi) - \varepsilon F \sin(\omega t) \sin(\phi)$, factorising Eq. (C.25) by $\cos(\omega t)$ and $\sin(\omega t)$ yields

$$\left(-m\omega^2 + k_1 + \frac{1}{2}\varepsilon k_{\mathrm{p}1} + \frac{3}{4}\varepsilon k_3 a^2 + \frac{1}{2}\varepsilon k_{\mathrm{p}3} a^2\right) a = \varepsilon F \cos(\phi) \tag{C.26}$$

$$\varepsilon c \omega a = \varepsilon F \sin(\phi) \tag{C.27}$$

squaring and adding Eq. (C.26) and Eq. (C.27) yields

$$\left(\left(-m\omega^2 + k_1 + \frac{1}{2}\varepsilon k_{\mathrm{p}1} + \frac{3}{4}\varepsilon k_3 a^2 + \frac{1}{2}\varepsilon k_{\mathrm{p}3} a^2\right)^2 + \varepsilon^2 c^2 \omega^2\right) a^2 = \varepsilon^2 F^2. \tag{C.28}$$

The expression for the gain of the system when $\varepsilon = 1$,

$$\left|\frac{a}{F}\right| = \frac{1}{\left(\left(-m\omega^2 + k_1 + \frac{1}{2}k_{\mathrm{p}1} + \frac{3}{4}k_3 a^2 + \frac{1}{2}k_{\mathrm{p}3} a^2\right)^2 + c^2\omega^2\right)^{\frac{1}{2}}}. \tag{C.29}$$

and the phase obtained from the ratio of Eq. (C.26) and Eq. (C.27)

$$\phi = \tan^{-1} \frac{-m\omega^2 + k_1 + \frac{1}{2}k_{\mathrm{p}1} + \frac{3}{4}k_3 a^2 + \frac{1}{2}k_{\mathrm{p}3} a^2}{-c\omega}. \tag{C.30}$$

From the complex composite FRF

$$\Lambda(\omega) = \frac{1}{-m\omega^2 + \mathrm{i}c\omega + k_1 + \frac{1}{2}k_{\mathrm{p}1} + \frac{3}{4}k_3 a^2 + \frac{1}{2}k_{\mathrm{p}3} a^2}. \tag{C.31}$$

The linearised system when $\varepsilon = 1$ is

$$m\ddot{z} + \varepsilon c\dot{z} + k_{\mathrm{eq}} z = \varepsilon F \cos(\omega t + \phi), \tag{C.32}$$

and the linearised stiffness when $\varepsilon = 1$ is

$$k_{\mathrm{eq}} = k_1 + \frac{1}{2}k_{\mathrm{p}1} + \frac{3}{4}k_3 a^2 + \frac{1}{2}k_{\mathrm{p}3} a^2. \tag{C.33}$$

Hence at the fixed level of excitation the FRF natural frequency is

$$\omega_N = \sqrt{\frac{k_1 + \frac{1}{2}k_{\mathrm{p1}} + \frac{3}{4}k_3 a^2 + \frac{1}{2}k_{\mathrm{p3}} a^2}{m}}. \tag{C.34}$$

Appendix D

The method of averaging for solving a nonlinear parametrically excited system subject to harmonic base excitations

Eq. (4.7) is normalised by time scaling $\tau = \Omega t$, and is expressed as derivatives with respect to τ instead of t. Prime $(.)'$ represents a quantity differentiated with respect to τ. Normalisation in this way results in

$$z'' + \frac{2\varepsilon\zeta\omega_n}{\Omega}z' + \frac{\omega_n^2}{\Omega^2}(1+\varepsilon\delta\cos(\tau))z + \frac{\omega_n^2}{\Omega^2}(\varepsilon\alpha+\varepsilon\gamma\cos(\tau))z^3 = \frac{1}{4}Y_0\cos(\frac{\tau}{2}+\phi). \tag{D.1}$$

To capture the system's near-resonance behaviour, the parametric frequency Ω varies around the reference frequency Ω_0; thus the detuning parameter Δ is introduced as $\Omega = \Omega_0\left(1-\varepsilon\Delta\right)$. If $\varepsilon = 0$, when the system is simplified to an undamped oscillator, the solutions of Eq. (D.1) are a linear combination of $\cos(\tau)$ and $\sin(\tau)$. This linear combination can be written as

$$z\left(\tau\right) = a\cos\left(\kappa\tau - \varphi\right) \tag{D.2}$$

where a and φ are the constant amplitude and the phase. The frequency ratio $\frac{\omega_n}{\Omega_0} = \kappa$ is used here for simplification.

If $\varepsilon \neq 0$, based on the "variation of constant" method of Lagrange, we can assume that the solution can still be written in the above form, but the amplitude and the phase a and φ are now functions of time [32]. With the averaging method, the solution of the weakly nonlinear problem is assumed to be similar in character to the linear one. Though, the amplitude a and phase φ are allowed to vary in time. Hence, the complementary solution of the final simplified nonlinear equation (Eq. (D.1)) is a linear combination of $\cos\left(\Phi\left(\tau\right)\right)$

and $\sin\left(\Phi\left(\tau\right)\right)$, which can be written as

$$z\left(\tau\right) = a\left(\tau\right)\cos\left(\Phi\left(\tau\right)\right), \tag{D.3}$$

where

$$\Phi\left(\tau\right) = \kappa\tau - \varphi\left(\tau\right), \tag{D.4}$$

and

$$z\left(\tau\right)' = a'\left(\tau\right)\cos\left(\Phi\left(\tau\right)\right) - a\left(\tau\right)\left(\kappa - \varphi'\left(\tau\right)\right)\sin\left(\Phi\left(\tau\right)\right). \tag{D.5}$$

Substituting $\Phi\left(\tau\right)$ and Eq. (D.5) into Eq. (D.1) results an equation which can be solved for $a'\left(\tau\right)$ and $\varphi'\left(\tau\right)$. From the averaging approximation, $a'\left(\tau\right)$ and $\varphi'\left(\tau\right)$ will be small since $\varepsilon \ll 1$, so that a and φ change much more slowly with τ than $\Phi\left(\tau\right)$ does. Hence, a and φ hardly change during one period of oscillating terms. From the approximation $a'\left(\tau\right)$ and $\varphi'\left(\tau\right)$ are replaced by their averaged values during one period of oscillation. Since, it is assumed that from the slow variations of a and φ, the rapid variations in $\Phi\left(\tau\right)$ terms can be neglected [124]. $a'\left(\tau\right)$ and $\varphi'\left(\tau\right)$ are averaged by assuming that $a\left(\tau\right)$ and $\varphi\left(\tau\right)$ are changing slowly. $a'\left(\tau\right)$ and $\varphi'\left(\tau\right)$ are averaged over one period $T = \frac{2\pi}{\Omega}$. The resulting averaged equation can be integrated with respect to τ to find the $a\left(\tau\right)$ and $\varphi\left(\tau\right)$ for a given κ and reference frequency Ω_0.

The average of $f(a, \Phi)$ is given by $\frac{1}{T}\int_0^T f(a, \Phi)\mathrm{d}\Phi$ where a and Φ are treated as constant during the period of integration. The steady-state behaviour of the system can be recovered from the set of $a'\left(\tau\right)$ and $\varphi'\left(\tau\right)$ by setting $(a', \varphi') = (0, 0)$ and solving for steady-state values of a and φ:

$$a'\left(\tau\right) = -\zeta a\frac{1}{\Omega} - \frac{1}{2}\delta a\frac{\omega_n^2}{\Omega^2}\sin(2\varphi) - \frac{1}{4}\gamma a^3\frac{\omega_n^2}{\Omega^2}\sin(2\varphi) + \frac{1}{4}Y_0\sin(\phi + \varphi) + \mathcal{O}(\varepsilon^2), \tag{D.6a}$$

$$a\varphi'(\tau) = -\frac{1}{2}\Delta a - \frac{1}{2}\delta a\frac{\omega_n^2}{\Omega^2}\cos(2\varphi) - \frac{3}{4}\alpha a^3\frac{\omega_n^2}{\Omega^2} - \frac{1}{2}\gamma a^3\frac{\omega_n^2}{\Omega^2}\cos(2\varphi) + \frac{1}{4}Y_0\cos(\phi + \varphi) + \mathcal{O}(\varepsilon^2). \tag{D.6b}$$

The resulting solution is an approximation of the original solution:

$$a = \frac{\Omega^2 Y_0\sqrt{\left(-p_1\sin(2\phi) + \zeta\right)^2 + \left(p_2 - p_3\cos(2\phi)\right)^2}}{8\omega_n^2\left(p_1^2(1 - \cos(2\phi)^2) + p_3^2\cos(2\phi)^2 - p_2^2 - \zeta^2\right)}, \tag{D.7}$$

$$\varphi = \frac{1}{2}\arctan\left(\frac{p_3\left(\zeta - \frac{1}{2a}Y_0\sin(\varphi + \phi)\right)}{p_1\left(p_2 - \frac{1}{2a}Y_0\cos(\varphi + \phi)\right)}\right), \tag{D.8}$$

where $p_1 = \frac{1}{4}\left(\delta + \frac{1}{2}\gamma a^2\right)$, $p_2 = \frac{3}{8}\alpha a^2 - \frac{\Omega}{2\omega_n} + 1$, and $p_3 = \frac{1}{4}\left(\delta + \gamma a^2\right)$. a represents the steady-state amplitude of non-trivial solutions.

D.1 Stability of solutions

The stability of the stationary solutions is determined by evaluating the Jacoubian eigenvalues. At a singular point (a, φ) the Jacoubian of the modulation equations Eq. (D.6) becomes:

$$\mathbf{J}(a,\varphi) = \begin{bmatrix} A_{11} & A_{12} \\ A_{21} & A_{22} \end{bmatrix} \quad \text{where,} \tag{D.9}$$

$$A_{11} = -\zeta\omega_{\mathrm{n}} - \frac{\omega_{\mathrm{n}}^2}{2\Omega}\delta\sin(2\varphi) - \frac{3\omega_{\mathrm{n}}^2}{4\Omega}\gamma a^2\sin(2\varphi). \tag{D.10a}$$

$$A_{12} = -\frac{3\omega_{\mathrm{n}}^2}{2\Omega}\alpha a - \frac{\omega_{\mathrm{n}}^2}{\Omega}\gamma a\cos(2\varphi) - \frac{1}{4a^2}Y_0\Omega\cos(\varphi+\phi). \tag{D.10b}$$

$$A_{21} = -\frac{\omega_{\mathrm{n}}^2}{\Omega}\delta a\cos(2\varphi) - \frac{\omega_{\mathrm{n}}^2}{2\Omega}\gamma a^3\cos(2\varphi). \tag{D.10c}$$

$$A_{22} = -\frac{\omega_{\mathrm{n}}^2}{\Omega}\delta\sin(2\varphi) - \frac{\omega_{\mathrm{n}}^2}{\Omega}\gamma a^2\sin(2\varphi) - \frac{1}{4a}Y_0\Omega\sin(\varphi+\phi). \tag{D.10d}$$

where the singular points a and φ are given by the solutions to Eq. (D.7), and Eq. (D.8). For the steady-state solutions $a'(\tau) = \varphi'(\tau) = 0$ the matrix D.9 is eliminated and the eigenvalues λ_{NPE}, as the solutions of $\mid \mathbf{J}(a,\varphi) - \lambda_{\mathrm{NPE}}\mathbf{I} \mid$, is found. A solution a is unstable if at least one eigenvalue has a positive real part, otherwise it is stable. For the Nonlinear Parametrically Excited (NPE) system with δ, α, and$\gamma \neq 0$ the equation which presents the eigenvalues is large and is not mentioned here.

For a base excited Duffing oscillator when δ, and γ in Eq. (D.1) are zero, the resulting solution is

$$a = \frac{\Omega^2 Y_0\sqrt{\zeta^2 + p_2^2}}{-8\omega_n^2\left(p_2^2 + \zeta^2\right)}, \tag{D.11}$$

$$\varphi = \arctan\left(\frac{\zeta}{p_2}\right) - \phi, \tag{D.12}$$

where $p_2 = \frac{3}{8}\alpha a^2 - \frac{\Omega}{2\omega_n} + 1$.

The eigenvalues of the Jacoubian matrix are found from:

$$\mathbf{J}(a,\varphi) = \begin{bmatrix} -\zeta & \left(1 - \frac{\Omega}{2\omega_n}\right) + \frac{3}{8}\alpha a^3 \\ \frac{1}{a}\left(1 - \frac{\Omega}{2\omega_n}\right) - \frac{9}{8}\alpha a & -\zeta \end{bmatrix}, \tag{D.13}$$

and the eigenvalues are

$$\lambda_{\mathrm{N}} = -\zeta \pm \frac{1}{8}\sqrt{-27\left(a^2\alpha - \frac{4\Omega}{3\omega_n} + \frac{8}{3}\right)\left(a^2\alpha - \frac{4\Omega}{9\omega_n} + \frac{8}{9}\right)}. \tag{D.14}$$

For a to be stable it is required that the eigenvalues can be imaginary positive or negative and negative real. A solution a is unstable if at least one eigenvalue has a positive real part. The unstable region where the eigenvalues are real positive are shown in the frequency response plots in Figs. 4.6a.

D.2 The solutions of the NPE system subject to harmonic base excitations with an electromagnetic system

Eq. (7.5) is solved in a similar manner to Eq. (4.7). The steady-state values of a and φ are

$$a'(\tau) = -\zeta_{\mathrm{m}} a\frac{1}{\Omega} - \frac{1}{2}\delta a\frac{\omega_n^2}{\Omega^2}\sin(2\varphi) - \frac{1}{4}\gamma a^3\frac{\omega_n^2}{\Omega^2}\sin(2\varphi) + \frac{1}{4}Y_0\sin(\phi+\varphi) - \frac{\zeta_{\mathrm{es}}\omega_n}{4\Omega}a^2 \\ - \frac{1}{256}\gamma_{\mathrm{es}} a^4\frac{\omega_n^2}{\Omega} + \mathcal{O}(\varepsilon^2), \tag{D.15}$$

$$a\varphi'(\tau) = -\frac{1}{2}\Delta a - \frac{1}{2}\delta a\frac{\omega_n^2}{\Omega^2}\cos(2\varphi) - \frac{3}{4}\alpha a^3\frac{\omega_n^2}{\Omega^2} - \frac{1}{2}\gamma a^3\frac{\omega_n^2}{\Omega^2}\cos(2\varphi) + \frac{1}{4}Y_0\cos(\phi+\varphi) \\ - \frac{1}{32}\delta_{\mathrm{es}} a\frac{\omega_n^2}{\Omega}\sin(2\varphi) - \frac{5}{256}\gamma_{\mathrm{es}} a^3\frac{\omega_n^2}{\Omega}\sin(2\varphi) + \mathcal{O}(\varepsilon^2). \tag{D.16}$$

The resulting solution is an approximation of the original solution:

$$a = \frac{\Omega^2 Y_0\sqrt{\left(-p_1\sin(2\phi) + \zeta_{\mathrm{m}} + \frac{1}{8}\zeta_{\mathrm{es}}a^2 - p_4\sin(\phi)\right)^2 + (p_2 - p_3\cos(2\phi))^2}}{8\omega_n^2\left(p_1^2(1-\cos(2\phi)^2) + p_3^2\cos(2\phi)^2 - p_2^2 - \zeta_{\mathrm{m}}^2 - \left(\frac{1}{8}\zeta_{\mathrm{es}}a^2\right)^2 + p_4^2\sin(\phi)^2\right)}, \tag{D.17}$$

where $p_1 = \frac{1}{4}\left(\delta + \frac{1}{2}\gamma a^2\right)$, $p_2 = \frac{3}{8}\alpha a^2 - \frac{\Omega}{2\omega_n} + 1$, and $p_3 = \frac{1}{4}\left(\delta + \gamma a^2\right)$. Parameters added as result of the induced current are ζ_{es}, and $p_4 = \frac{1}{4}\delta_{\mathrm{es}}\omega_n a^2 + \frac{1}{8}\gamma_{\mathrm{es}}\omega_n a^4$.

D.3 Backbone curve

A *backbone curve* corresponds to the solution of the nonlinear system on the hypothesis that both forcing and damping are zero, or equivalently, the base excitation compensates the damping forces in the system at those particular frequencies and amplitudes. A *backbone curve* is found for $\gamma = \zeta = \phi = 0$, when the parametric excitation is considered as an external force on the system which affects the *backbone curve*. The equation for the backbone curve is therefore,

$$\frac{1}{16}\delta^2 - \left(\frac{3}{8}\alpha a^2 - \left(\frac{\Omega}{2\omega_n} - 1\right)\right)^2 = 0. \tag{D.18}$$

Appendix E

Electromagnetic system and circuit diagrams

E.1 Output current programming by external voltage

The LAMBDA ZUP is a programmable DC power supply and is used to generate controllable DC/AC current from an input DC/AC voltage. For a given input voltage V_{in}, an output current I_{c} is generated by the LAMBDA ZUP. A voltage source variable from 0 to 4V, programs the output current proportionally from zero to full scale. Based on the programmable power supply manual, the maximum output current is $I_{\mathrm{out,max}} = 20\mathrm{A}$. Fig. E.1 shows the LAMBDA ZUP with input voltage V_{in} and output current I_{c} set-up.

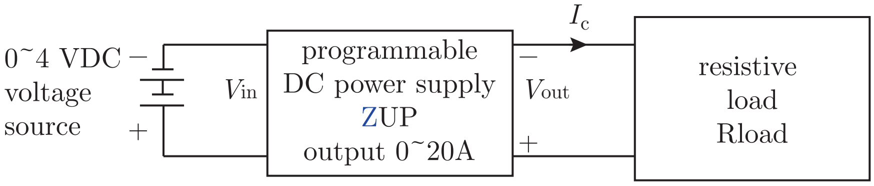

Fig. E.1. Schematic of generating controllable current from an input voltage.

For example, when the input voltage is set to 1V and the resistive load R_{load} connected to the LAMBDA ZUP is 1 Ohm, the current output is 25 percent of the maximum output current, and calculated from:

$$I_{\mathrm{c}} = \frac{V_{\mathrm{in}}}{V_{\mathrm{in,max}}} I_{\mathrm{out,max}}, \tag{E.1}$$

and

$$V_{\mathrm{out}} = I_{\mathrm{c}} R_{\mathrm{load}}. \tag{E.2}$$

Since the maximum output current is 20A, the output current I_{c} generated is calculated equal to 5A. This principle also applies when the input voltage varies in time. From

Fig. E.1 and based on the LAMBDA ZUP input configuration, it can be seen that differential input voltage is needed. A differential input is not connected to ground and is a difference between positive and negative voltage. Hence, to design the AC differential input voltage the circuit diagram presented in Fig. E.2 was considered.

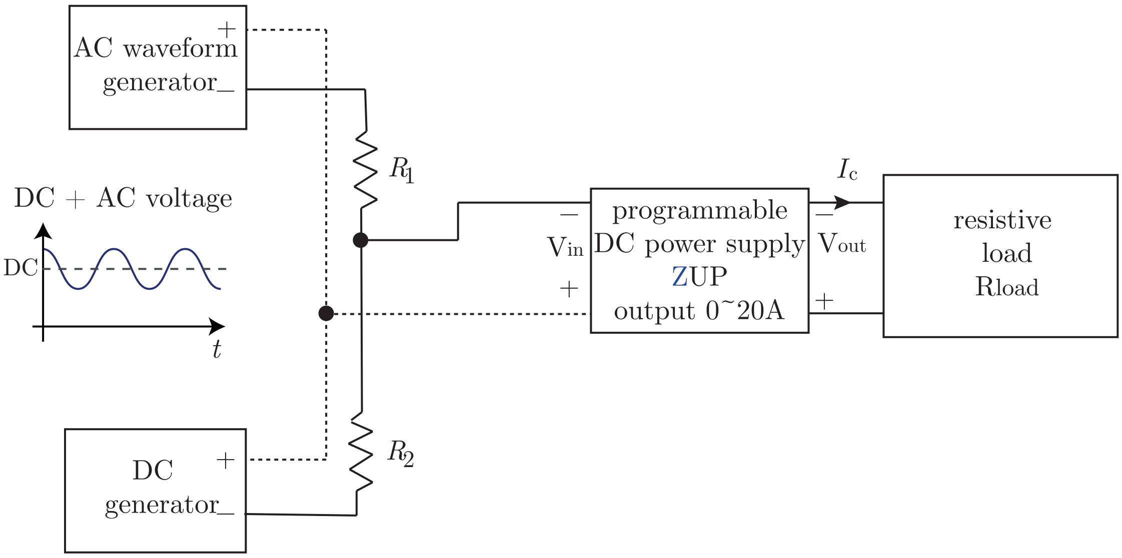

Fig. E.2. Generating AC and DC differential voltage for the LAMBDA ZUP power supply.

Resistor R_1 and R_2 are used for designing a voltage divider, hence the input voltage V_{in} is half of the voltage generated by the DC generator and AC wave generator. The input voltage is positive and varies only between 0 to 4 V, as a result of this a positive DC voltage is generated and the AC voltage is added to the DC signal. The peak amplitude of the AC voltage should not exceed the DC value, exceeding this value cuts the sinusoidal AC signal to be always positive.

E.2 Coil configurations and assumptions

The coils can be connected together in either a series connection, a parallel connection or combinations of both series and parallel together, to produce more complex networks whose overall inductance is a combination of the individual inductors. However, there are certain effects that depend on the application their configuration is important. In this thesis differentially coupled series inductors configuration is chosen because of the effect of electrical damping. This configuration is similar to connecting together resistors in series. However, when connecting together inductors in series they can be influenced by mutual inductance.

Mutually connected series inductors are classed as either aiding or opposing (see Fig. E.3) the total inductance depending on whether the coils are cumulatively coupled (in

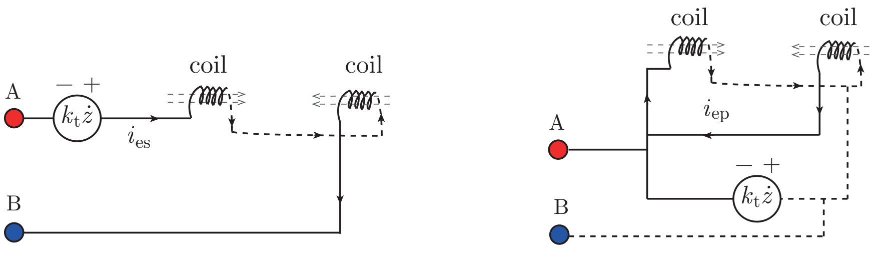

(a) (b)

Fig. E.3. (a) Coils in series opposing connection. (b) Coils in parallel opposing connection with a circulating current.

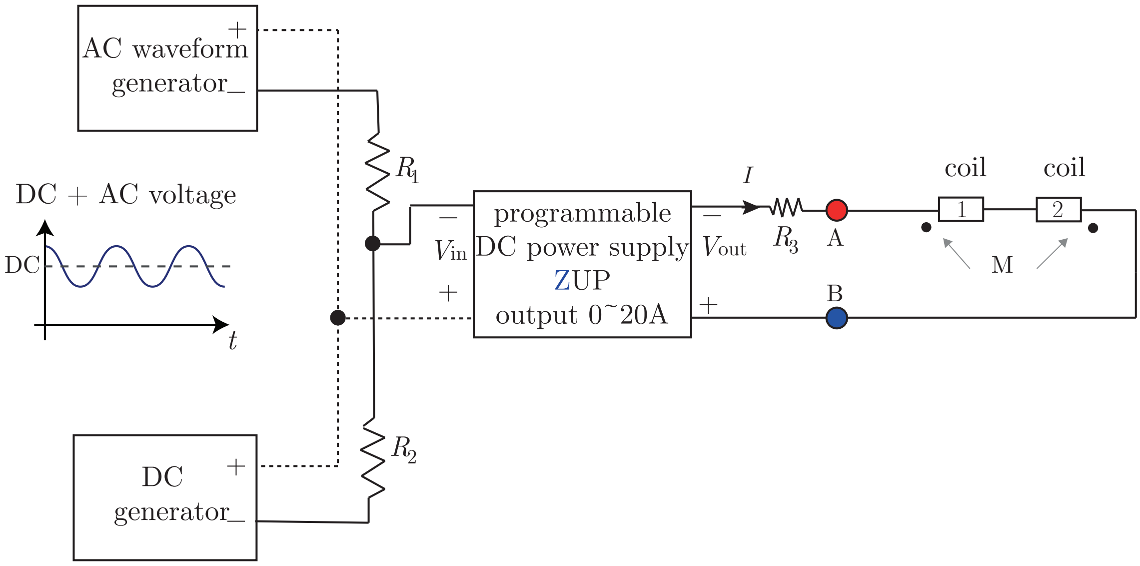

Fig. E.4. Series opposing connection coils connected to the LAMBDA ZUP with an extra resistance R_3 in series.

the same direction) or are differentially coupled (in opposite direction). When they are coupled in opposite directions the e.m.f that is induced into coil 1 by the effect of the mutual inductance M of coil 2 is in opposition to the self-induced e.m.f in coil 1 as now the same current passes through each coil in opposite directions. Figure E.4 shows the coils connected in series in opposing connection with an input current. Figure E.5 shows the coils connected in parallel in opposing connection with an input current. The mutual inductance in the coils connected in series or parallel is demonstrated in basic electronics textbooks [166].

When the coils are connected together in parallel so that the magnetic field of one links with the other, the effect of mutual inductance either increases or decreases the total inductance depending upon the amount of magnetic coupling that exists between the coils. The effect of this mutual inductance depends upon the distance between the coils and their orientation to each other. In this work the current carried in the coils has low frequency (less than 20 Hz), hence the inductance of the coil is neglected.

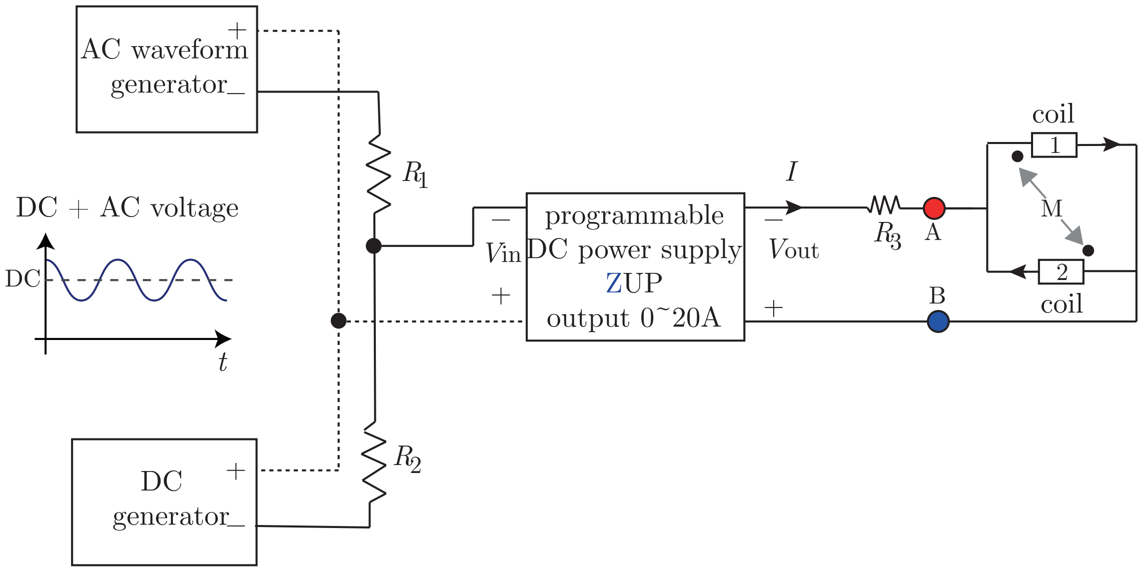

Fig. E.5. Parallel opposing connection coils connected to the LAMBDA ZUP with an extra resistance R_3 in series.

In coils connected in parallel opposing connection the circulating current can be observed [140]. The circulating current comes from induced current generated in each coil with induced voltage with same potential. Hence, the induced current circulates inside the coils connected in parallel. The circulating current result in increasing the magnetic field and also an increase in the damping of the cantilever beam. So the coils in opposing connections are not used for the electromagnetic system for generating time-varying stiffness.

E.3 Basic principles of a magnetic dipole

A force on a magnetic dipole due to a non-uniform magnetic field can be calculated [167]. The force on one magnet due to another magnet can be considered as an example to show how the magnetic force can be calculated. Moving the magnetic dipole from a region of low magnetic field to a region of high magnetic field causes the magnetic potential energy $U = -\boldsymbol{\mu}.\mathbf{B}$ to change [167]. $\boldsymbol{\mu}$ is the magnetic dipole moment and $\mathbf{B}$ is the magnetic field.

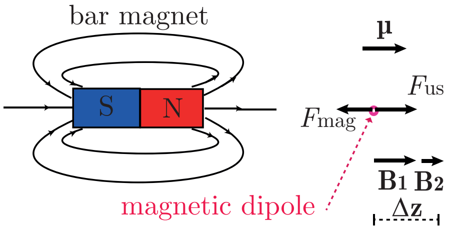

Fig. E.6. A bar magnet acts on a magnetic dipole.

The magnetic dipole moment $\boldsymbol{\mu}$ is the ratio between the maximum torque exerted on a magnet, current-carrying coil, or a moving charge situated in a magnetic field and the strength of that field. It is thus a measure of the strength of a magnetic or current-carrying coil. If the magnetic dipole is released from the rest position, the object moves to the position with lower potential energy and achieves higher kinetic energy. To prevent the kinetic energy from changing, the object should be moved at a slow constant speed. To have a constant kinetic energy, work needs to be done by applying some force. By calculating the work, the magnetic force on the object can be found. This magnetic force shows the force applied from one magnet to another [167]. A magnetic dipole aligned with the magnetic field made by a bar magnet is shown in Fig E.6, where $\Delta(.)$ represents the difference between the quantity between state 1 and 2, and F_{us} is an external force applied to move the magnetic dipole. The magnetic dipole is moved Δz by a larger force F_{us} to the right. Before moving the magnetic dipole the magnetic field was $\mathbf{B}_1$ and after moving the magnetic dipole the magnetic field is $\mathbf{B}_2$. Considering the change in distance between the bar magnet and the magnetic dipole, the magnetic field is moved from the higher magnetic field $\mathbf{B}_1$ to a lower magnetic field $\mathbf{B}_2$. Hence, the magnetic potential energy is increased from $-\boldsymbol{\mu} \cdot \mathbf{B}_1$ to less negative $-\boldsymbol{\mu}.\mathbf{B}_2$. This shows the work

$$F_{\mathrm{us}}\Delta z = \Delta U = (-\boldsymbol{\mu} \cdot \mathbf{B}_1) - (-\boldsymbol{\mu} \cdot \mathbf{B}_2) = -\boldsymbol{\mu} \cdot (\mathbf{B}_2 - \mathbf{B}_1) = -\boldsymbol{\mu} \cdot \Delta \mathbf{B}, \tag{E.3}$$

needs to be done. In Equation (E.3) the $-\boldsymbol{\mu} \cdot \Delta \mathbf{B}$ is positive because $\mathbf{B}_2 < \mathbf{B}_1$. The magnitude of the force exerted is

$$F_{\mathrm{us}} = \frac{\Delta U}{\Delta z} = \frac{-\boldsymbol{\mu} \cdot \Delta \mathbf{B}}{\Delta z} \to -\boldsymbol{\mu} \cdot \frac{\mathrm{d}\mathbf{B}}{dz}. \tag{E.4}$$

The force that the magnet exerts to the left on the magnetic dipole in the case of repulsion is numerically equal to the external force (In the case of repulsion the magnitude of the force is correct). This concept can be applied for the case of a current carrying coil with a magnetic field and a bar magnet.

E.4 Force on a magnet from a current loop

In electromagnetism, the Biot-Savart law describes the magnetic field generated by an electric current. From the Biot-Savart law each discrete element on the coil can generate its own magnetic field, which can be integrated parallel to the axis of the coil. Fig E.7 presents a current carrying coil and a dipole magnet in distance d from the centre of the coil.

From the Biot-Savart law, the differential contribution $\mathrm{d}\mathbf{B}$ to the magnetic field $\mathbf{B}$ from a differential length $\mathrm{d}\mathbf{l}$ of a coil with current I_c is given by

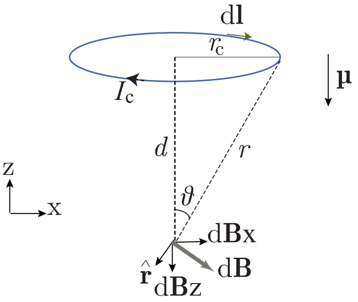

Fig. E.7. A current loop and a magnet seperated by distance d.

$$\mathrm{d}\mathbf{B} = \frac{\mu_0}{4\pi}\frac{I_c \mathrm{d}\mathbf{l} \times \hat{\mathbf{r}}}{r^2}, \tag{E.5}$$

where μ_0 is the permeability of free space, I_c is the current in the coil and r is the distance between a point on the coil and the magnet (see Fig. E.7). The magnetic field d**B** of each current segment I_cd**l** is perpendicular to the radius vector $\hat{\mathbf{r}}$

$$\mathrm{d}\mathbf{B} = \frac{\mu_0}{4\pi}\frac{I_c \mathrm{d}\mathbf{l}\sin(\frac{\pi}{2})}{r^2}, \tag{E.6}$$

and Eq. (E.6) is simplified to

$$\mathrm{d}\mathbf{B} = \frac{\mu_0}{4\pi}\frac{I_c \mathrm{d}\mathbf{l}}{r^2}. \tag{E.7}$$

The component of the differential magnetic field **B** in direction of **z** is

$$\mathrm{d}B_z = - \mid \mathrm{d}\mathbf{B} \mid \sin(\theta), \tag{E.8}$$

and substituting Eq. (E.8) into Eq. (E.7) yields

$$\mathrm{d}B_z = \frac{-\mu_0}{4\pi}\frac{I_c \mid \mathrm{d}\mathbf{l} \mid \sin(\theta)}{r^2}, \tag{E.9}$$

where $\sin(\theta) = \frac{r_c}{r}$ and r_c is the radius of the coil. Hence, Eq. (E.9) becomes

$$\mathrm{d}B_z = \frac{-\mu_0}{4\pi}\frac{r_c I_c \mathrm{d}l}{r^3}, \tag{E.10}$$

using Pythagoras' theorem Eq. (E.10) is expressed as

$$\mathrm{d}B_z = \frac{-\mu_0}{4\pi}\frac{r_c I_c \mathrm{d}l}{(d^2 + r_c^2)^{\frac{3}{2}}}, \tag{E.11}$$

where d is the distance between the centre of the coil and the centre of the dipole magnet. To find the total magnetic field the sum of all elements should be considered. Hence, the integration for the whole area of the coil is

$$\oint \mathrm{d}B_z = \oint \frac{-\mu_0}{4\pi} \frac{r_c I_c}{(d^2 + r_c^2)^{\frac{3}{2}}} \mathrm{d}l, \tag{E.12}$$

which is equal to,

$$B_z = \frac{-\mu_0}{2} \frac{r_c^2 I_c}{(d^2 + r_c^2)^{\frac{3}{2}}}. \tag{E.13}$$

For N turns in the coil, Eq. (E.12) becomes

$$B_z = \frac{-\mu_0 r_c^2 I_c N}{2(d^2 + r_c^2)^{\frac{3}{2}}}. \tag{E.14}$$

The force applied to the magnet F_z from the magnetic field generated by the pair of coils, can be found from Eq. (E.4) as

$$F_z = \frac{3 \mid \boldsymbol{\mu} \mid \mu_0 r_c^2 I_c N d}{2(d^2 + r_c^2)^{\frac{5}{2}}} = \frac{3\mu\mu_0 r_c^2 I_c N d}{2(d^2 + r_c^2)^{\frac{5}{2}}}. \tag{E.15}$$

E.5 Force applied to the pair of magnets from the coils connected in series

The magnetic field produced by two current carrying coils and two magnets can be calculated assuming that the coils are perfect and have identical solenoids and that the magnets constitute a magnetic dipole (the example in this thesis consists of two magnets attached on a cantilever beam). Fig. 5.3 shows two coils and the two attached magnets.

If the magnets and coils are repulsive, the magnets return to their equilibrium position, however when the magnets are not in the equilibrium position (z is the magnet displacement with respect to the equilibrium position) a greater force is generated from one set of current carrying coils than the other one. When the coils are carrying a DC current the magnets are under the constant force and to stay at the equilibrium position. When the coils are carrying an AC current as well as a DC current, the force on the magnets will change with time, as a result of the change in the magnetic field with the frequency of AC current but still the magnets are positioned at the equilibrium position.

The magnetic field B_z generated by the two pairs of coils and magnets at the centre of the cantilever beam, can be obtained from Biot-Savart law,

$$B_z(z) = -\frac{\mu_0 r_c^2 I_c N}{2((h+z)^2 + r_c^2)^{\frac{3}{2}}} - \frac{\mu_0 r_c^2 I_c N}{2((z-h)^2 + r_c^2)^{\frac{3}{2}}}, \tag{E.16}$$

where h is the distance between the centre of coil and the equilibrium position (see Fig. 5.3).

Taking derivatives of Eq. (E.16) respect to z results in,

$$\mathrm{d}B_z(z) = \frac{3\mu_0 r_c^2 I_c N(h+z)}{2((h+z)^2+r_c^2)^{\frac{5}{2}}} + \frac{3\mu_0 r_c^2 I_c N(z-h)}{2((z-h)^2+r_c^2)^{\frac{5}{2}}}. \tag{E.17}$$

The repulsive magnetic force F_e applied to the cantilever beam, which is calculated from $(F_e = -\boldsymbol{\mu} \cdot \frac{\mathrm{d}\mathbf{B}}{dz})$ is

$$F_e(z) = -\frac{3\mu\mu_0 r_c^2 I_c N(h+z)}{2((h+z)^2+r_c^2)^{\frac{5}{2}}} - \frac{3\mu\mu_0 r_c^2 I_c N(z-h)}{2((z-h)^2+r_c^2)^{\frac{5}{2}}}. \tag{E.18}$$

A magnetic dipole μ, is characterised by a magnetic dipole moment vector, which indicates the orientation and the strength of the magnetic field:

$$\mu = \frac{B_r V_m}{\mu_0} \tag{E.19}$$

where B_r is the residual magnetic flux density of the permanent magnet, V_m is the volume of magnet and μ_0 is the permeability of free space. The magnetic dipole moment is calculated based on the values in Table 5.1 is 3.08 Am^2.

Eq. (E.18) is simplified to

$$F_e(z) = -\frac{GI_c(h+z)}{((h+z)^2+r_c^2)^{\frac{5}{2}}} - \frac{GI_c(z-h)}{((z-h)^2+r_c^2)^{\frac{5}{2}}}, \tag{E.20}$$

where

$$G = \frac{3}{2}\mu\mu_0 r_c^2 N. \tag{E.21}$$

Using the Taylor expansion about $z = 0$

$$F_e(z) = F_e(0) + F_e(0)'z + \frac{1}{2}F_e''(0)z^2 + \frac{1}{6}F_e'''(0)z^3 + \mathcal{O}(z^4) \tag{E.22}$$

The force applied to the cantilever beam can be expressed as

$$F_e(z) = \mathrm{H}_1 I_c z + H_2 I_c z^3, \tag{E.23}$$

where H_1 and H_2 are

$$H_1 = \left(\frac{-2G}{(h^2+r_c{}^2)^{\frac{5}{2}}} + \frac{10Gh^2}{(h^2+r_c{}^2)^{\frac{7}{2}}} \right), \tag{E.24}$$

$$H_2 = \left(\frac{5G}{(r_\mathrm{c}^2+h^2)^{\frac{7}{2}}} - \frac{70Gh^2}{(r_\mathrm{c}^2+h^2)^{\frac{9}{2}}} + \frac{105Gh^4}{(r_\mathrm{c}^2+h^2)^{\frac{11}{2}}} \right). \tag{E.25}$$

E.6 Induced voltage generated by a disc magnet

Considering a disc magnet on the axis of coil in Fig. E.8 located at $z = 0$. A magnetic moment $\mu = \frac{V_\mathrm{m} B_\mathrm{r}}{\mu_0}\hat{\mathbf{e}}_\mathbf{z}$, where V_m is the volume of the magnet, B_r is the residual magnetic flux density, μ_0 is the permeability of free space and $\hat{\mathbf{e}}_\mathbf{z}$ is a unit vector pointing in the positive z direction [141]. The magnetic field generated between the magnet and the coil can be approximated as [141]

$$\mathbf{B}_{ez1} = \frac{V_\mathrm{m} B_\mathrm{r}}{4\pi}\left(\frac{3r(h-z)\hat{\mathbf{e}}_\mathbf{r} - \left(r^2 - 2(h-z)\right)\hat{\mathbf{e}}_\mathbf{z}}{(r^2 + (h-z)^2)^{\frac{5}{2}}}\right), \tag{E.26}$$

where $\hat{\mathbf{e}}_\mathbf{r}$ is a unit vector pointing in the positive r direction. When the magnet is moved along the axis of the coil, an electric field will be generated in the coil. This electric field is developed to oppose the motion of the magnets. The electric field generates an electric potential across the coils.

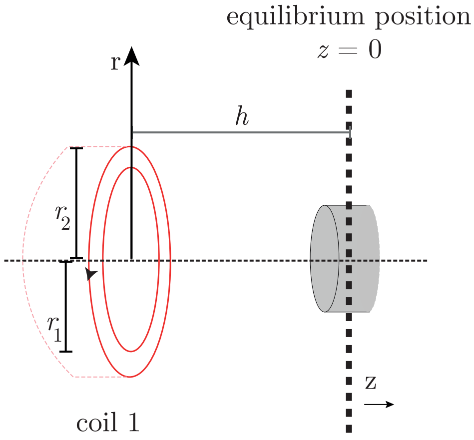

Fig. E.8. Diagram showing a coil and a magnet in a cylindrical coordinate system.

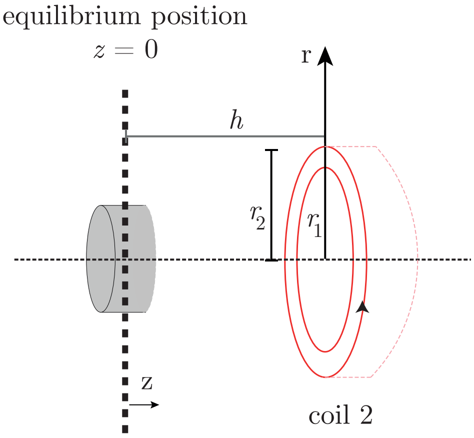

Fig. E.9. Diagram showing a coil and a magnet in a cylindrical coordinate system.

Faraday's Law of induction is applied and several assumptions are imposed in order to generate an approximate analytical expression. Based on Faraday's Law, any change of magnetic flux through a conductive loop of wire will cause a voltage to be induced in that loop. The magnetic flux is defined as [168]:

$$\phi_{\mathrm{m}} = \iint_A \mathbf{B}_{\mathrm{ez1}} \mathrm{d}A, \tag{E.27}$$

where A indicates the area enclosed by the wire loop and $\mathbf{B}_{\mathrm{ez1}}$ is the magnetic flux density generated by the magnet in the direction of z (see Fig. E.8). When the magnet moves from left to right, then the magnetic flux density in the direction of z is considered. Vertical motion of the magnets on the cantilever beam are considered negligible. The induced voltage is [141]

$$V_1 = \dot{\phi}_{\mathrm{m}}. \tag{E.28}$$

The induced voltage from a moving magnet and a coil from [141] is

$$V_1 = \dot{z} k_{\mathrm{t1}}. \tag{E.29}$$

where

$$k_{\mathrm{t1}} = \frac{\varsigma q_1}{(r_2 - r_1)(z_2 - z_1)} \left(\sum_{n,m=1}^{2} (-1)^{n+m} \ln(r_n + z''_{nm}) - \frac{r_n}{z''_{nm}} \right), \tag{E.30a}$$

$$z''_{nm} = \sqrt{r_n^2 + (z_m - (-z + h))^2}, \tag{E.30b}$$

where ς is the fill factor. The fill factor from [142] is

$$\varsigma = \frac{D_{\mathrm{w}}^2 l_{\mathrm{w}} N}{4(r_2^2 - r_1^2) h_{\mathrm{coil}}}, \tag{E.31}$$

where D_{w} is the coil diameter, l_{w} is the length of the wire in one rotation, N is the number of turns in coils, h_{coil} is the height of the coil, and r_2 and r_1 are the inner and outer radius of the coil respectively. Quantity q_1 is the conveniently defined parameter

$$q_1 = \frac{3}{2} V_{\mathrm{m}} B_{\mathrm{r}}, \tag{E.32}$$

where V_{m} is the volume of the magnet and B_{r} is the residual magnetic flux density.

In Fig. E.9 a moving magnet and a coil on its right side is considered. The induced voltage generated in coil 2 is

$$V_2 = \dot{z} k_{\mathrm{t2}}. \tag{E.33}$$

where

$$k_{\mathrm{t2}} = \frac{\varsigma q_1}{(r_2 - r_1)(z_2 - z_1)} \left(\sum_{n,m=1}^{2} (-1)^{n+m} \ln(r_n + z'_{nm}) - \frac{r_n}{z'_{nm}} \right), \tag{E.34a}$$

$$z'_{nm} = \sqrt{r_n^2 + (z_m - (z + h))^2}, \tag{E.34b}$$

When two coils are connected in series in opposing connection the total induced voltage is

$$V = V_2 - V_1. \tag{E.35}$$

E.7 Solutions of the system considering the effect of induced current

The equation of motion Eq. (5.23) which describes a SDOF model of a cantilever beam with an electromagnetic system which has coils connected in series when δ_{es} and γ_{es} are small values, is solved with an averaging method.
Solving the Eq. (5.23) with the method of averaging when $\kappa = \frac{1}{2}$ ($\Omega_0 = 2\omega_n$), results in

$$a'(\tau) = a \left(\frac{a^2\,\gamma}{16} \sin(2\,\varphi) - \frac{\zeta_{\mathrm{m}}\omega_n}{\Omega} + \frac{\delta}{8} \sin(2\,\varphi) - \frac{\zeta_{\mathrm{es}}\omega_n}{4\Omega} a^2 \right) + \mathcal{O}(\varepsilon^2), \tag{E.36}$$

$$\varphi'(\tau) = \frac{1}{2}\,\Delta + \frac{a^2\,\gamma}{8} \cos(2\,\varphi) + \frac{3a^2\,\alpha}{16} + \frac{\delta}{8} \cos(2\,\varphi) + \mathcal{O}(\varepsilon^2). \tag{E.37}$$

The amplitude of the response a is the amplitude of the periodic solutions and it can be found by rearranging and substituting Eq. (E.36) into Eq. (E.37) when $a'(\tau) = \varphi'(\tau) = 0$. Two nontrivial solutions, stable and unstable solutions are found, however since they are long mathematical terms, they are not included in this thesis.

E.8 The effects of electrical damping in coils connected in parallel opposing connection

The effect of electrical damping in coils connected in series opposing is presented in Section 5.4.1. The coils in this configuration have less effect on the damping of the cantilever beam with an electromagnetic system compared to the parallel configuration. The effect of induced current i_{ep}, in the coils connected in parallel opposing and resistive load, R_3, on electrical damping is studied experimentally. The mechanical damping ratio, ζ_{m}, is measured for the cantilever beam without the electromagnetic systems. The magnets are attached on the beam but the coils are removed. The impact test is done to find the mechanical damping ratio, ζ_{m}, from the peak-amplitude method of the first natural frequency [144]. The mechanical damping ratio is assumed to be constant for all tests and was measured as $\zeta_{\mathrm{m}} = 0.003$. The electrical damping ratio, ζ_{ep}, generated as a result of the electromagnetic system is measured from $\zeta_{\mathrm{ep}} = \zeta - \zeta_{\mathrm{m}}$, where ζ is the total damping and it was measured by impact tests with the peak-amplitude method.

The electrical damping is measured when two parallel coils are connected to load R_3 (see Fig. E.5). Strong electrical damping can be seen when two coils are close to each other. Fig. E.10 shows the total damping ratio of the cantilever beam when two parallel coils are in open circuit and the case in which they are connected to the load. From Fig. E.12 it can be seen that the first natural frequency of the cantilever beam with two parallel coils in open circuit is less than the first natural frequency when the coils are attached to the load (When the coils are close to each other, $h < 0.03$m). From these results, we can understand that to reduce the effect of electrical damping in different position h, increasing the coil resistance or the resistive load is beneficial.

The total damping ratio ζ and the first and second natural frequencies, ω_{n} and ω_{n2} were measured for several system configurations (when different DC current was generated into coils) as plotted in Figs. E.10, E.11, and E.12. For the open circuit test, the coils were in parallel; however they were not connected to the load R_3 and the LAMBDA ZUP. In Fig. E.5 points A and B show where the coils are open circuit. In Figs. E.10, E.11, and E.12, it is shown as "open circuit".

When two parallel coils are open circuit, as a result of the circulating induced current and the coils small internal resistance, a large electrical damping ζ_{ep} is expected. The circulating current in the coils in parallel opposing connection can be seen in the circuit configuration shown in Fig. E.3. Also, increasing the DC current generated by the LAMBDA ZUP and the distance between the coils can change the electrical damping. The repulsion force applied to the cantilever beam increases as DC current increases. The cantilever beam then is forced to stay in its equilibrium position, and its motion is reduced. Hence, the induced current generated by the moving magnet decreases as the DC current increases. Consequently, the electrical damping is eliminated as the DC current is increased (see Fig. E.10). Also, when the half distance between the coils h, is increased the effect of the magnetic flux density is reduced. Fig. E.10 shows that increasing the distance h, reduces the total damping ratio. In Fig. E.10 each block of green color, corresponds to one experimental result. Since, there are 9 positions and 9 different current plus the open circuit case, in total 90 blocks of experimental results are shown.

In this experiment, the small magnetic flux density generated by the moving magnet does not change the cantilever beam stiffness, the first and second natural frequency significantly. Increasing the DC current generated by the LAMBDA ZUP, increases the electromagnetic force and stiffness of the cantilever beam. Increasing the stiffness of the

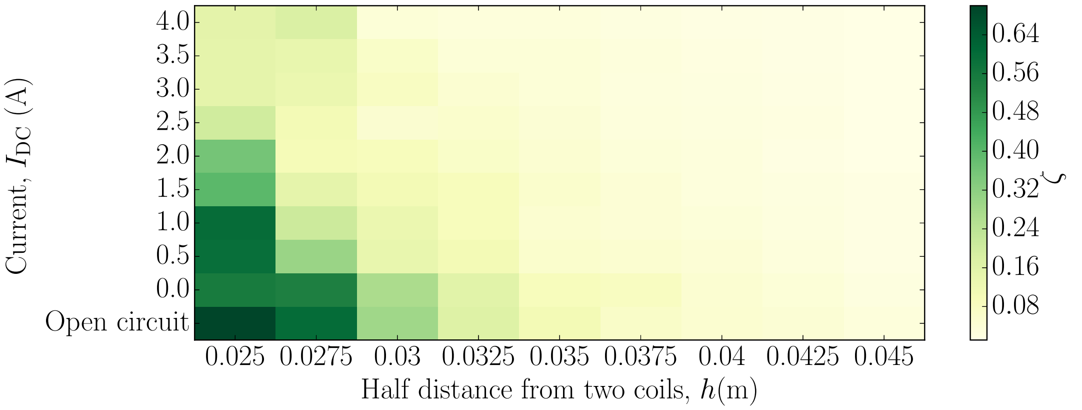

Fig. E.10. Experimental results showing the damping ratio ζ from the FRF and the peak-amplitude method for different DC currents and positions h.

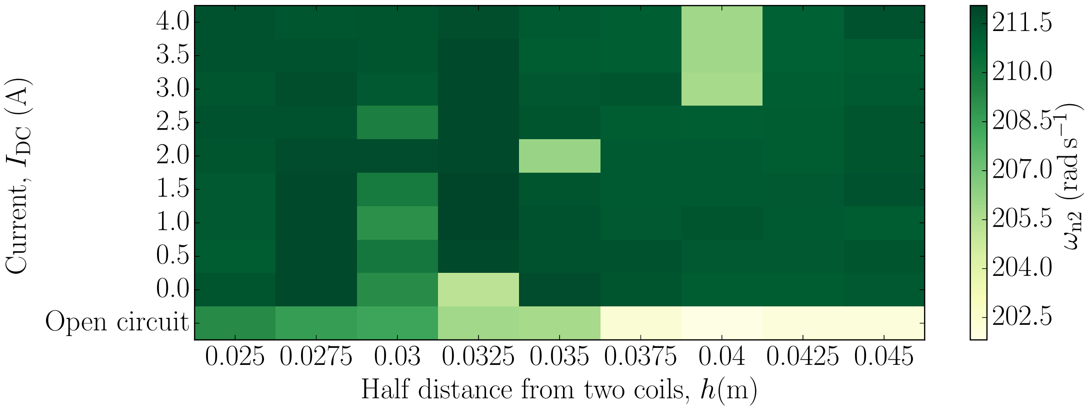

Fig. E.11. Experimental results showing the second natural frequency from the FRF for different DC currents and positions h.

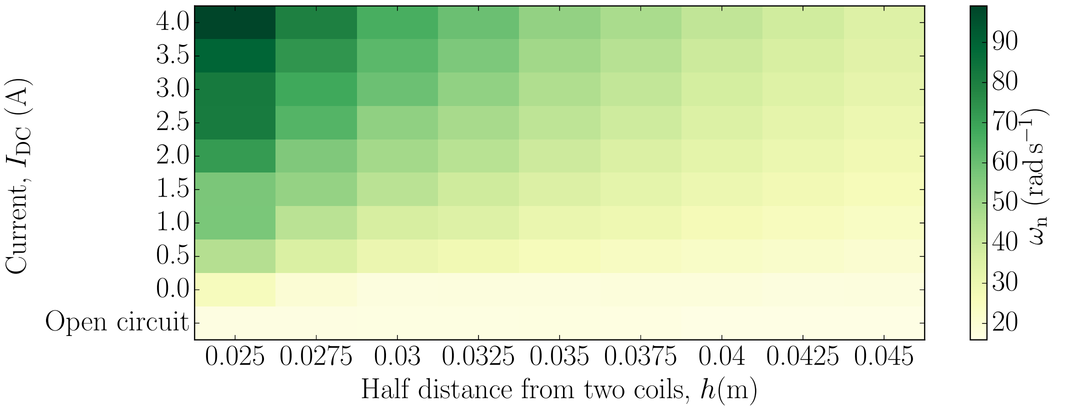

Fig. E.12. Experimental results showing the first natural frequency from the FRF for different DC currents and positions h.

cantilever beam can change the natural frequencies. The electromagnetic system to be placed in a position of the cantilever beam which has the lowest effect on the second natural frequency to satisfy the SDOF approximation. It can be seen from Fig. E.11 that the second natural frequency does not change when the DC current or the distance between the coils are varied. However, the first natural frequency is increased when the DC current is increased or the distance between the coils h are reduced. Fig. E.12 shows the first natural frequency for different DC current and different positions between the coils h.

Appendix F

Rayleigh energy method used to determine fundamental frequencies

F.1 Fundamental frequency of a fixed-free cantilever beam

The cantilever beam with constant supported spring k_{ext} and added mass m_{m} at position l_1 is shown in Figure F.1.

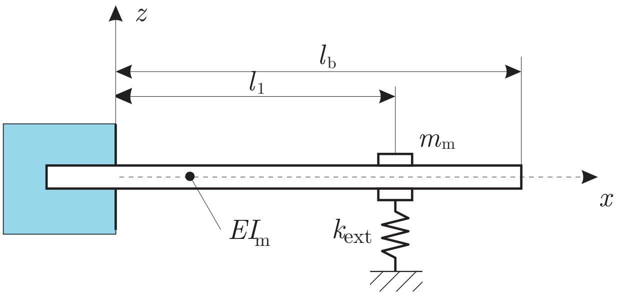

Fig. F.1. Schematic of the cantilever beam model with constant supported spring k_{ext}.

The cantilever beam has the mode shape

$$\phi(x) = \left(\frac{\cos\left(\frac{2\pi l_b}{\lambda_b}\right) + \cosh\left(\frac{2\pi l_b}{\lambda_b}\right)}{\sin\left(\frac{2\pi l_b}{\lambda_b}\right) - \sinh\left(\frac{2\pi l_b}{\lambda_b}\right)}\right)\left(\sin\left(\frac{2\pi x}{\lambda_b}\right) - \sinh\left(\frac{2\pi x}{\lambda_b}\right)\right) + \sin\left(\frac{2\pi x}{\lambda_b}\right) - \sinh\left(\frac{2\pi x}{\lambda_b}\right), \quad \text{(F.1)}$$

where $\left(\frac{2\pi l_b}{\lambda_b}\right) = 1.875$, and l_b is the length of the beam, and l_1 is the position of the spring. So the potential energy and kinetic energy can be written as

$$V = 0.5\, I_{\mathrm{m}} E \int_0^{l_b} \left(\frac{d^2}{dx^2}\phi\left(x\right)\right)^2 \mathrm{d}x + 0.5\, k_{\mathrm{ext}} \left(\phi\left(x\right)\right)^2, \quad \text{(F.2)}$$

$$T = 0.5\, m_{\mathrm{b}} \int_0^{l_b} \left(\phi\left(x\right)\right)^2 \mathrm{d}x + 0.5\, m_{\mathrm{m}}\, \left(\phi\left(x\right)\right)^2, \tag{F.3}$$

where E is the elastic modulus of the beam, I_{m} is the area moment of inertia ($I_m = \frac{1}{12} b_b t_b^3$) and b_b is the cantilever beam width and t_b is the cantilever beam thickness, m_{m} is the mass of two permanent magnet on beam. From $V_{\max} = T_{\max}$ in a free vibration, we can find $\omega_n^2 = \frac{V_{\max}}{T_{\max}}$ as

$$\omega_n = \sqrt{\frac{61.4 E I_{\mathrm{m}} + k_{\mathrm{ext}} D_1}{0.52 m_{\mathrm{b}} + m_{\mathrm{m}} D_1}}, \tag{F.4}$$

where

$$D_1 = 0.5 \left(-1.36 \cos\left(\frac{2\pi l_1}{\lambda_b}\right) + 1.36 \cosh\left(\frac{2\pi l_1}{\lambda_b}\right) + \sin\left(\frac{2\pi l_1}{\lambda_b}\right) - \sinh\left(\frac{2\pi l_1}{\lambda_b}\right) \right)^2. \tag{F.5}$$

Appendix G

Hilbert transform for determination of linear and nonlinear damping coefficients

G.1 Introduction to the Hilbert transform

A practical use of the Hilbert transform to find the damping factor is introduced here. One way of finding the Hilbert transform is from the Fourier transform of the given signal $\dot{z}(t)$. After rejecting the negative frequencies, the inverse Fourier transform can be calculated, and the result will be a complex signal where the real and the imaginary parts form a Hilbert transform pair. The second way of obtaining the Hilbert transform is a 90° phase shift of the original signal $\dot{z}(t)$ (see Fig. G.1 modified from [169]). The Hilbert transform can be explained as passing the original signal to a filter, that leaves its magnitude unchanged, but shifts the phase by 90° for positive frequencies.

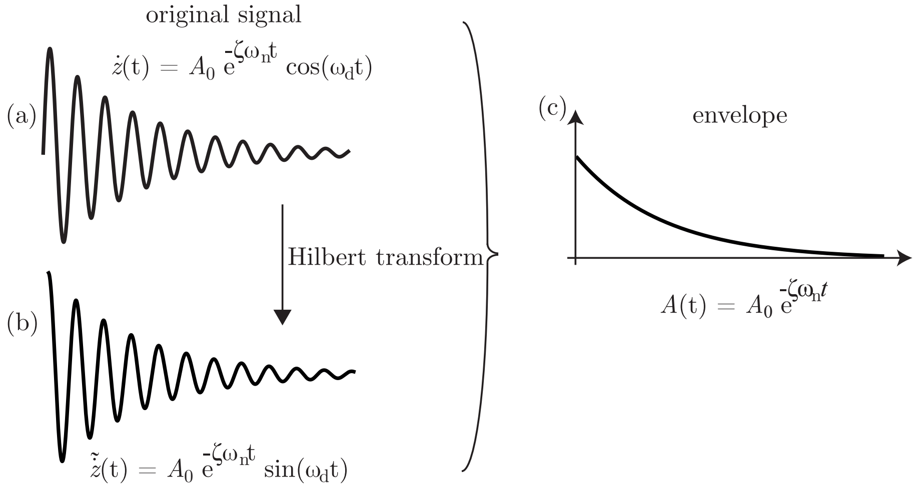

Fig. G.1. Schematic of the Hilbert transform damping analysis. The Hilbert transform allows estimation of the envelope of the decaying transient response from the original signal $\dot{z}(t)$ and the signal with 90° phase shift, $\tilde{\dot{z}}(t)$.

$\tilde{\dot{z}}(t)$ is $\dot{z}(t)$ shifted by 90°. For simplicity, the decaying transient signal, velocity signal can be introduced as

$$\dot{z}(t) = A_0 e^{-\zeta \omega_\mathrm{n} t} \cos(\omega_\mathrm{d} t), \tag{G.1}$$

where A_0 is the amplitude of the velocity signal, ζ is the damping ratio, ω_n is the undamped natural frequency and ω_d is the damped natural frequency. The Hilbert transform of $\dot{z}(t)$, is the signal shifted by 90°

$$\tilde{\dot{z}}(t) = A_0 e^{-\zeta \omega_\mathrm{n} t} \sin(\omega_\mathrm{d} t). \tag{G.2}$$

The analytic signal based on Hilbert transform is the sum of the real part plus the imaginary part (i is the imaginary unit)

$$g(t) = \dot{z}(t) + \mathrm{i}\,\tilde{\dot{z}}(t). \tag{G.3}$$

The magnitude of the analytic signal can be directly calculated from $\dot{z}(t)$ and $\tilde{\dot{z}}(t)$

$$A(t) = \sqrt{\dot{z}^2(t) + \tilde{\dot{z}}^2(t)}. \tag{G.4}$$

In phasor form

$$g(t) = A(t) e^{\mathrm{i}\theta(t)}. \tag{G.5}$$

Based on Bendat and Piersolb [147, 170] nomenclature, $A(t)$ is the envelope signal of $\dot{z}(t)$, and $\theta(t)$ is the instantaneous phase signal of $\dot{z}(t)$. The instantaneous phase and frequency are explained by Smith and Wereley [147]. The envelope is a exponential function of time

$$A(t) = A_0 e^{-\zeta \omega_n t}. \tag{G.6}$$

The envelope can be shown in a logarithmic amplitude scale, thus the analytical expressions below are expressed based on Eq. (G.6)

$$\log_{10} A(t) = \log_{10} A_0 e^{-\zeta \omega_n t}, \tag{G.7}$$

where the exponential curve $A(t)$, determined by a decay rate $\zeta\omega_n$ is a linear decay [146]. Hence, the instantaneous damping ratio can be found from rewriting Eq. (G.7) as

$$\zeta = -\frac{1}{\omega_n} \frac{\mathrm{d}\left(\log_{10} \frac{A(t)}{A_0}\right)}{\mathrm{d}t}. \tag{G.8}$$

Appendix H

Determination of the phase difference between the shaker acceleration and the current in the coils

H.1 Methodology

In order to find the phase difference between the shaker acceleration and the current in the coils Fourier analysis is employed. The acceleration (acceleration of the shaker plate) signal and the current signal (input current in coils) are expressed as a series of sine and cosine signals.

The acceleration signal, $\ddot{z}(t)$, is a periodic signal with period T_{acc}, and is represented by the Fourier series

$$\ddot{z}(t) = Y_0 + a_{\mathrm{acc},1}\cos\left(\frac{\Omega_1}{2}t\right) + a_{\mathrm{acc},2}\cos\left(\frac{\Omega_2}{2}t\right) + ... \\ + b_{\mathrm{acc},1}\sin\left(\frac{\Omega_1}{2}t\right) + b_{\mathrm{acc},2}\sin\left(\frac{\Omega_2}{2}t\right) + ... \quad \text{(H.1)}$$

where

$$\Omega_1 = \frac{4\pi}{T_{\mathrm{acc}}}, \text{ and } \Omega_{\mathrm{n}} = n\Omega_1. \quad \text{(H.2)}$$

The coefficients $a_{\mathrm{acc,n}}$, and $b_{\mathrm{acc,n}}$ are found based on [145]:

$$a_{acc,n} = \frac{2}{T_{\mathrm{acc}}}\int_{-\frac{T_{\mathrm{acc}}}{2}}^{\frac{T_{\mathrm{acc}}}{2}} \ddot{z}(t)\cos\left(\frac{\Omega_n}{2}t\right)\mathrm{d}t, \quad \text{(H.3)}$$

$$b_{acc,n} = \frac{2}{T_{\text{acc}}} \int_{-\frac{T_{\text{acc}}}{2}}^{\frac{T_{\text{acc}}}{2}} \ddot{z}(t) \sin\left(\frac{\Omega_n}{2}t\right) \text{d}t. \tag{H.4}$$

Based on the coefficients of the Fourier series the phase can be found as $\phi_1 = \tan^{-1}(\frac{b_{acc,n}}{a_{acc,n}})$ [145]. The current signal, $I_0(t)$, is a periodic signal with period T, it is represented by the Fourier series

$$\begin{aligned} I_0(t) = I_{\text{DC}} + a_1\cos(\Omega_1 t) + a_2\cos(\Omega_2 t) + ... \\ + b_1\sin(\Omega_1 t) + b_2\sin(\Omega_2 t) + ... \end{aligned} \tag{H.5}$$

where

$$\Omega_1 = \frac{2\pi}{T}, \text{ and } \Omega_{\text{n}} = n\Omega_1. \tag{H.6}$$

The coefficients a_{n}, and b_{n} are found based on [145]:

$$a_{\text{n}} = \frac{2}{T}\int_{-\frac{T}{2}}^{\frac{T}{2}} I_0(t)\cos(\Omega_n t)\text{d}t, \tag{H.7}$$

$$b_{\text{n}} = \frac{2}{T}\int_{-\frac{T}{2}}^{\frac{T}{2}} I_0(t)\sin(\Omega_n t)\text{d}t. \tag{H.8}$$

Based on the coefficients of the Fourier series the phase can be found as $\phi_2 = \tan^{-1}(\frac{b_{\text{n}}}{a_{\text{n}}})$ [145]. The process of finding the phase of the acceleration with respect to the current signal is:

1. **For measured current signal, find $a_{\text{acc,1}}$ and $b_{\text{acc,1}}$** for the acceleration signal, and a_1 and b_1 for the current signal. To do this, the integral in Eqs. H.3 and H.4 numerically with the trapezoidal method is evaluated.
2. **Use a_{acc1} and b_{acc1} to find ϕ_1, which is the phase of the acceleration signal compare to a cosine wave of the same frequency $\frac{\Omega}{2}$.**
3. **Use a_1 and b_1 to find ϕ_2, which is the phase of the current signal compare to a cosine wave of the same frequency Ω.**
4. **Subtract twice the ϕ_1 from the ϕ_2 to find the phase of the acceleration with respect to the current signal. The phase difference is then rotated to satisfy $-180° < \phi \leq 180°$.**

In Chapter 4 it is shown that the current signal has zero phase with respect to a cosine wave with the same frequency. The acceleration signal has phase ϕ with respect to a cosine wave with the same frequency. The frequency of the acceleration is also considered to be half of the current signal frequency. Throughout this thesis, when the phase difference between the acceleration signal and the current signal is considered, phase ϕ is mentioned. However, the current signals recorded experimentally do not have phase zero with respect to a cosine wave of the same frequency in all time. In order to compare the analytical and experimental results, the phase difference calculated from the measured acceleration and the current is presented based on ϕ.

Bibliography

[1] Zaghari B., Ghandchi Tehrani M., and Rustighi E. Mechanical modelling of a vibration energy harvester with time-varying stiffness. In *EURODYN 2014: 9th International Conference on Structural Dynamics*, 2014.

[2] Zaghari B., Rustighi E., and Ghandchi Tehrani M. Experimental study on harvesting energy from a parametrically excited system. In *MoViC2014: The 12th International Conference on Motion and Vibration Control*, 2014.

[3] Zaghari B., Rustighi E., and Ghandchi Tehrani M. An experimentally validated parametrically excited vibration energy harvester with time-varying stiffness. In *SPIE Smart Structures and Materials+ Nondestructive Evaluation and Health Monitoring*. International Society for Optics and Photonics, 2015.

[4] Zaghari B., Rustighi E., and Ghandchi Tehrani M. Dynamic response of a nonlinear parametrically excited system subject to harmonic base excitation. *Journal of Physics: Conference Series*, 744(1):012125, 2016.

[5] Fey R.H.B., Mallon N.J., Kraaij C.S., and Nijmeijer H. Nonlinear resonances in an axially excited beam carrying a top mass: simulations and experiments. *Nonlinear dynamics*, 66(3):285–302, 2011.

[6] Xie W.C. *Dynamic stability of structures.* Cambridge University Press, 2006.

[7] Bolotin V.V. *The dynamic stability of elastic systems.* Holden-Day, San Francisco, 1964.

[8] Giraldo-Londoño O. and Aristizábal-Ochoa J.D. Dynamic stability of slender columns with semi-rigid connections under periodic axial load: verification and examples. *Dyna*, 81(185):66–72, 2014.

[9] Nayfeh A.H. and Mook D.T. *Nonlinear oscillations.* John Wiley & Sons, 2008.

[10] DeMartini B., Moehlis J., Turner K., Rhoads J.F., Shaw S., and Zhang W. Modeling of parametrically excited microelectromechanical oscillator dynamics with application to filtering. In *Proceedings of the Fourth IEEE Conference on Sensors*, pages 345–348. IEEE, 2005.

[11] Hu Z., Gallacher B.J., Burdess J.S., Fell C.P., and Townsend K. A parametrically amplified MEMS rate gyroscope. *Sensors and Actuators A: Physical*, 167(2):249–260, 2011.

[12] Jia Y., Yan J., Soga K., and Seshia A.A. A parametrically excited vibration energy harvester. *Journal of Intelligent Material Systems and Structures*, 25(3):278–289, 2013.

[13] Dohnal F. and Mace B.R. Amplification of damping of a cantilever beam by parametric excitation. In *Proceedings-CD MOVIC 2008*. Institute of Applied Mechanics, 2008.

[14] Schmidt E., Paradeiser W., Dohnal F., and Ecker H. Prototype design and experimental verification of an electromagnetic actuator for parametric stiffness excitation. In *23rd Canadian Conference on Electrical and Computer Engineering (CCECE)*, pages 1–5. IEEE, 2010.

[15] Chen C.C. and Yeh M.K. Parametric instability of a beam under electromagnetic excitation. *Journal of sound and vibration*, 240(4):747–764, 2001.

[16] Yeh M.K. and Kuo Y.T. Dynamic instability of composite beams under parametric excitation. *Composites science and technology*, 64(12):1885–1893, 2004.

[17] Iakubovich V.A. and Starzhinski V.M. *Linear differential equations with periodic coefficients*, volume 2. Wiley, 1975.

[18] Cartmell M.P. *Introduction to linear, parametric and nonlinear vibrations.* Chapman and Hall London, 1990.

[19] Hsu C.S. On the parametric excitation of a dynamic system having multiple degrees of freedom. *Journal of Applied Mechanics*, 30(3):367–372, 1963.

[20] Kniffka T.J. *Numerical, semi-analytical and analytical approaches for investigating parametrically excited non-linear systems.* PhD thesis, Faculty of mechanical and industrial engineering, TU Wien, Austria, 2016.

[21] Faraday M. On a peculiar class of acoustical figures; and on certain forms assumed by groups of particles upon vibrating elastic surfaces. *Philosophical Transactions of the Royal Society of London*, 121:299–340, 1831.

[22] Lord Rayleigh F.R.S. On maintained vibrations. *The London, Edinburgh, and Dublin Philosophical Magazine and Journal of Science*, 15(94):229–235, 1883.

[23] M. Farkas. *Periodic motions*, volume 104. Springer Science & Business Media, 2013.

[24] Sinha S.C. and Butcher E.A. Symbolic computation of fundamental solution matrices for linear time-periodic dynamical systems. *Journal of Sound and Vibration*, 206(1):61–85, 1997.

[25] Mathieu É. Mémoire sur le mouvement vibratoire d'une membrane de forme elliptique. *Journal de mathématiques pures et appliquées*, 13:137–203, 1868.

[26] Hill G.W. On the part of the motion of the lunar perigee which is a function of the mean motions of the sun and moon. *Acta mathematica*, 8(1):1–36, 1886.

[27] Poincaré H. *Théorie mathématique de la lumiere*. Gauthier Villars, 1892.

[28] Floquet G. Sur les équations différentielles linéaires à coefficients périodiques. In *Annales scientifiques de l'École normale supérieure*, volume 12, pages 47–88, 1883.

[29] Lyapunov A.M. Sur une série relative a la théorie des équations différentielles linéaires avec coeficient périodiques. *Comptes Rendus de l'Académie des Sciences, Paris*, 123:1248–1252, 1896.

[30] Clairaut A.C. Mémoire sur l'orbite apparente du soleil autour de la terre, en ayant égard aux perturbations produites par des actions de la lune et des planètes principales. *Hist. Acad. Sci. Paris*, pages 52–564, 1754.

[31] Lagrange J.L. *Mécanique analytique*, volume 1. Mallet-Bachelier, 1853.

[32] Verhulst F. *Nonlinear differential equations and dynamical systems*. Springer Science & Business Media, 1996.

[33] Sun J.Q. and Luo A.C.J. *Bifurcation and chaos in complex systems*, volume 1. Elsevier, 2006.

[34] Murdock J.A. *Perturbations: theory and methods*, volume 27. Siam, 1999.

[35] Nayfeh A.H. *Introduction to perturbation techniques*. John Wiley & Sons, 2011.

[36] Sinha S.C. and Wu D.H. An efficient computational scheme for the analysis of periodic systems. *Journal of Sound and Vibration*, 151(1):91–117, 1991.

[37] Rand R.H. Lecture notes on nonlinear vibrations, 2005.

[38] King M.R. and Mody N.A. *Numerical and statistical methods for bioengineering: applications in MATLAB*. Cambridge University Press, 2010.

[39] Govaerts W., Kuznetsov Yu. A., De Witte V., Dhooge A., Meijer H.G.E., Mestrom W., Riet A.M., and Sautois B. MATCONT and CL MATCONT: Continuation toolboxes in MATLAB. *Gent University and Utrech University, Technical Report*, 2011.

[40] Jones E., Oliphant T., Peterson P., et al. SciPy: Open source scientific tools for Python, 2001.

[41] Chatjigeorgiou I.K. and Mavrakos S.A. Nonlinear resonances of parametrically excited risers numerical and analytic investigation for $\omega = 2\omega_1$. *Computers & structures*, 83(8):560–573, 2005.

[42] Sparks C.P. *Fundamentals of marine riser mechanics: basic principles and simplified analyses*. PennWell Books, 2007.

[43] Patel M.H. and Seyed F.B. Review of flexible riser modelling and analysis techniques. *Engineering structures*, 17(4):293–304, 1995.

[44] Froude W. *On the rolling of ships*. Institution of Naval Architects, 1861.

[45] Fossen T.I. and Nijmeijer H. *Parametric resonance in dynamical systems*. Springer Science & Business Media, 2011.

[46] Masoud Z.N., Nayfeh A.H., and Mook D.T. Cargo pendulation reduction of ship-mounted cranes. *Nonlinear Dynamics*, 35(3):299–311, 2004.

[47] Benton M. and Seireg A. Simulation of resonances and instability conditions in pinion-gear systems. *Journal of Mechanical Design*, 100(1):26–32, 1978.

[48] Lin J. and Parker R.G. Planetary gear parametric instability caused by mesh stiffness variation. *Journal of Sound and vibration*, 249(1):129–145, 2002.

[49] de Sá Caetano E. *Cable vibrations in cable-stayed bridges*, volume 9. IABSE, 2007.

[50] Abdel-Ghaffar A.M. and Khalifa M.A. Importance of cable vibration in dynamics of cable-stayed bridges. *Journal of Engineering Mechanics*, 117(11):2571–2589, 1991.

[51] Lu K.C., Wang Y., Lynch J.P., Loh C.H., Chen Y.J., Lin P.Y., and Lee Z.K. Ambient vibration study of Gi-Lu cable-stay bridge: application of wireless sensing units. In *Smart Structures and Materials*. International Society for Optics and Photonics, 2006.

[52] Gonzalez-Buelga A., Neild S.A., Wagg D.J., and Macdonald J.H.G. Modal stability of inclined cables subjected to vertical support excitation. *Journal of Sound and Vibration*, 318(3):565–579, 2008.

[53] Nayfeh A.H. and Pai P.F. *Linear and nonlinear structural mechanics*. John Wiley & Sons, 2008.

[54] Kovacic I. and Cartmell M.P. Special issue on parametric excitation: Applications in science and engineering. In *Proceedings of the Institution of Mechanical Engineers, Part C: Journal of Mechanical Engineering Science*, pages 1909–1911, 2012.

[55] Gu M., Xiang H.F., and Chen A.R. A practical method of passive TMD for suppressing wind-induced vertical buffeting of long-span cable-stayed bridges and its application. *Journal of Wind Engineering and Industrial Aerodynamics*, 51(2):203–213, 1994.

[56] Jensen C.N., Nielsen S.R., and Sørensen J.D. Optimal damping of stays in cable-stayed bridges for in-plane vibrations. *Journal of Sound and vibration*, 256(3):499–513, 2002.

[57] Galeazzi R., Blanke M., and Poulsen N.K. Parametric roll resonance detection on ships from nonlinear energy flow indicator. In *7th IFAC Symposium on Fault Detection, Supervision and Safety of Technical Processes*, 2009.

[58] Rhoads J.F., Miller N.J., Shaw S.W., and Feeny B.F. Mechanical domain parametric amplification. *Journal of Vibration and Acoustics*, 130(6):061006, 2008.

[59] Mumford W.W. Some notes on the history of parametric transducers. *Proceedings of the IRE*, 48(5):848–853, 1960.

[60] Louisell W.H. *Coupled mode and parametric electronics.* Wiley, 1960.

[61] Chivukula V.B. and Rhoads J.F. Microelectromechanical bandpass filters based on cyclic coupling architectures. *Journal of Sound and Vibration*, 329(20):4313–4332, 2010.

[62] DeMartini B.E., Rhoads J.F., Turner K.L., Shaw S.W., and Moehlis J. Linear and nonlinear tuning of parametrically excited MEMS oscillators. *Microelectromechanical Systems, Journal of*, 16(2):310–318, 2007.

[63] Rhoads J.F., Shaw S.W., Turner K.L., and Baskaran R. Tunable microelectromechanical filters that exploit parametric resonance. *Journal of Vibration and Acoustics*, 127(5):423–430, 2005.

[64] Rhoads J.F., Shaw S.W., Turner K., Moehlis J., DeMartini B.E., and Zhang W. Generalized parametric resonance in electrostatically actuated microelectromechanical oscillators. *Journal of Sound and Vibration*, 296(4):797–829, 2006.

[65] Welte J., Kniffka T.J., and Ecker H. Parametric excitation in a two degree of freedom MEMS system. *Shock and Vibration*, 20(6):1113–1124, 2013.

[66] Ghandchi Tehrani M. and Kalkowski M.K. Active control of parametrically excited systems. *Journal of Intelligent Material Systems and Structures*, 2015.

[67] Yabuno H. and Nayfeh A.H. Nonlinear normal modes of a parametrically excited cantilever beam. *Nonlinear Dynamics*, 25(1-3):65–77, 2001.

[68] Rugar D. and Grütter P. Mechanical parametric amplification and thermomechanical noise squeezing. *Physical Review Letters*, 67(6):699, 1991.

[69] Lee Y., Pai P.F., and Feng Z.C. Nonlinear complex response of a parametrically excited tuning fork. *Mechanical Systems and Signal Processing*, 22(5):1146–1156, 2008.

[70] Baskaran R. and Turner K. Mechanical domain non-degenerate parametric resonance in torsional mode micro electro mechanical oscillator. In *TRANSDUCERS 2003, The 12th International Conference on Solid-State Sensors, Actuators and Microsystems*, volume 1, pages 863–866. IEEE, 2003.

[71] Abou-Rayan A.M., Nayfeh A.H., Mook D.T., and Nayfeh M.A. Nonlinear response of a parametrically excited buckled beam. *Nonlinear Dynamics*, 4(5):499–525, 1993.

[72] Daqaq M.F. and Bode D. Exploring the parametric amplification phenomenon for energy harvesting. *Proceedings of the Institution of Mechanical Engineers, Part I: Journal of Systems and Control Engineering*, 225(4):456–466, 2011.

[73] Dohnal F., Ecker H., and Springer H. Enhanced damping of a cantilever beam by axial parametric excitation. *Archive of Applied Mechanics*, 78(12):935–947, 2008.

[74] Crespo da Silva M.R.M. and Glynn C.C. Nonlinear flexural-flexural-torsional dynamics of inextensional beams: Equations of motion. *Journal of Structural Mechanics*, 6(4):437–448, 1978.

[75] Crespo da Silva M.R.M. and Glynn C.C. Nonlinear flexural-flexural-torsional dynamics of inextensional beams: Forced motions. *Journal of Structural Mechanics*, 6(4):449–461, 1978.

[76] Nayfeh A.H. and Pai P.F. Non-linear non-planar parametric responses of an inextensional beam. *International Journal of Non-Linear Mechanics*, 24(2):139–158, 1989.

[77] Carvalho E.C., Gonçalves P.B., Rega G., and Del Prado Z.J. Influence of axial loads on the nonplanar vibrations of cantilever beams. *Shock and Vibration*, 20(6):1073–1092, 2013.

[78] Stabler C. Parametric instabilities for vibratory energy harvesting under harmonic, time-varying frequency, and random excitations. Master's thesis, Clemson University, 2010.

[79] Daqaq M.F., Stabler C., Qaroush Y., and Seuaciuc-Osorio T. Investigation of power harvesting via parametric excitations. *Journal of Intelligent Material Systems and Structures*, 20(5):545–557, 2009.

[80] Ghaderi P. and Dick A.J. Parametric resonance based piezoelectric micro-scale resonators: modeling and theoretical analysis. *Journal of Computational and Nonlinear Dynamics*, 8(1):011004, 2013.

[81] Dolev A. and Bucher I. Tuneable, non-degenerated, nonlinear, parametrically-excited amplifier. *Journal of Sound and Vibration*, 361:176–189, 2016.

[82] Han Q., Jianjun W., and Qihan L. Experimental study on dynamic characteristics of linear parametrically excited system. *Mechanical Systems and Signal Processing*, 25(5):1585–1597, 2011.

[83] Cugat O., Delamare J., and Reyne G. Magnetic micro-actuators and systems (MAGMAS). *Transactions on Magnetics*, 39(6):3607–3612, 2003.

[84] Husain A.H., Postma H.W.C., Huang X.M.H., Drake T., Barbic M., Scherer A., and Roukes M.L. Nanowire-based very-high-frequency electromechanical resonator. *Applied Physics Letters*, 83(6):1240–1242, 2003.

[85] Rhoads J.F., Kumar V., Shaw S.W., and Turner K.L. The non-linear dynamics of electromagnetically actuated microbeam resonators with purely parametric excitations. *International Journal of Non-Linear Mechanics*, 55:79–89, 2013.

[86] Kumar V., Sabater A., and Rhoads J.F. Dynamics of coupled electromagnetically-actuated microbeams. In *Proceedings of the 2011 NSF Engineering Research and Innovation Conference, Atlanta, Georgia*, 2011.

[87] Rhoads J.F and Shaw S.W. The impact of nonlinearity on degenerate parametric amplifiers. *Applied Physics Letters*, 96(23):234101, 2010.

[88] Krylov S., Gerson Y., Nachmias T., and Keren U. Excitation of large-amplitude parametric resonance by the mechanical stiffness modulation of a microstructure. *Journal of Micromechanics and Microengineering*, 20(1):015041, 2009.

[89] Zhu D., Tudor M.J., and Beeby S.P. Strategies for increasing the operating frequency range of vibration energy harvesters: a review. *Measurement Science and Technology*, 21(2):022001, 2010.

[90] Tang L., Yang Y., and Soh C.K. Toward broadband vibration-based energy harvesting. *Journal of Intelligent Material Systems and Structures*, 21(18):1867–1897, 2010.

[91] Cammarano A., Neild S.A., Burrow S.G., and Inman D.J. The bandwidth of optimized nonlinear vibration-based energy harvesters. *Smart Materials and Structures*, 23(5):055019, 2014.

[92] Jang S.J., Rustighi E., Brennan M.J., Lee Y.P., and Jung H.J. Design of a 2DOF vibrational energy harvesting device. *Journal of Intelligent Material Systems and Structures*, 22(5):443–448, 2011.

[93] Berdy D.F., Jung B., Rhoads J.F., and Peroulis D. Wide-bandwidth, meandering vibration energy harvester with distributed circuit board inertial mass. *Sensors and Actuators A: Physical*, 188:148–157, 2012.

[94] Abdelkefi A., Nayfeh A.H., and Hajj M.R. Global nonlinear distributed-parameter model of parametrically excited piezoelectric energy harvesters. *Nonlinear Dynamics*, 67(2):1147–1160, 2012.

[95] Jia Y., Yan J., Soga K., and Seshia A.A. Parametrically excited MEMS vibration energy harvesters with design approaches to overcome the initiation threshold amplitude. *Journal of Micromechanics and Microengineering*, 23(11):114007, 2013.

[96] Harne R.L., Sun A., and Wang K.W. An investigation on vibration energy harvesting using nonlinear dynamic principles inspired by trees. In *SPIE Smart Structures and Materials+ Nondestructive Evaluation and Health Monitoring*, pages 94310L–94310L. International Society for Optics and Photonics, 2015.

[97] Jia Y., Yan J., Soga K., and Seshia A.A. Parametric resonance for vibration energy harvesting with design techniques to passively reduce the initiation threshold amplitude. *Smart Materials and Structures*, 23(6):065011, 2014.

[98] Jia Y. and Seshia A.A. An auto-parametrically excited vibration energy harvester. *Sensors and Actuators A: Physical*, 220:69–75, 2014.

[99] Jia Y., Yan J., Soga K., and Seshia A.A. Multi-frequency operation of a MEMS vibration energy harvester by accessing five orders of parametric resonance. *Journal of Physics: Conference Series*, 476:012126, 2013.

[100] Daqaq M.F., Renno J.M., Farmer J.R., and Inman D.J. Effects of system parameters and damping on an optimal vibraiton-based energy harvester. In *Proceedings of 48th AIAA/ASME/ASCE/AHS/ASC Structures, Structural Dynamics and Materials Conference*. American Institute of Aeronautics and Astronautics, 2007.

[101] Jia Y. and Seshia A.A. Directly and parametrically excited bi-stable vibration energy harvester for broadband operation. In *The 17th International Conference on Solid-State Sensors, Actuators and Microsystems (TRANSDUCERS & EUROSENSORS XXVII)*, pages 454–457. IEEE, 2013.

[102] Tondl A. On the interaction between self-excited and parametric vibrations. In *Monographs and Memoranda of the National Research Institute for Machine Design*, volume 25, Prague, 1978.

[103] Tondl A. To the problem of quenching self-excited vibrations. *Acta technica ČSAV*, 43(1):109–116, 1998.

[104] Pumhössel T., Hehenberger P., and Zeman K. Reduced-order modelling of self-excited, time-periodic systems using the method of proper orthogonal decomposition and the Floquet theory. *Mathematical and Computer Modelling of Dynamical Systems*, 20(6):528–545, 2014.

[105] Dohnal F. Suppressing self-excited vibrations by synchronous and time-periodic stiffness and damping variation. *Journal of sound and vibration*, 306(1):136–152, 2007.

[106] Dohnal F. *Damping of Mechanical Vibrations by Parametric Excitation: Parametric Resonance and Anti-resonance*. Sudwestdeutscher Verlag fur Hochschulschriften, 2009.

[107] Dohnal F. and Markert R. Enhancement of external damping of a flexible rotor in active magnetic bearings by time-periodic stiffness variation. *Journal of System Design and Dynamics*, 5(5):856–865, 2011.

[108] Chasalevris A. and Dohnal F. A journal bearing with variable geometry for the suppression of vibrations in rotating shafts: simulation, design, construction and experiment. *Mechanical Systems and Signal Processing*, 52:506–528, 2015.

[109] Dohnal F. Experimental studies on damping by parametric excitation using electromagnets. *Proceedings of the Institution of Mechanical Engineers, Part C: Journal of Mechanical Engineering Science*, 226(8):2015–2027, 2012.

[110] Pumhössel T. and Ecker H. Active damping of vibrations of a cantilever beam by axial force control. In *ASME 2007 International Design Engineering Technical Conferences and Computers and Information in Engineering Conference*, pages 117–127. American Society of Mechanical Engineers, 2007.

[111] Pumhössel T., Hehenberger P., and Zeman K. Preserving stability properties in reduced models of time-periodic systems using proper orthogonal decomposition. In *ASME 2011 International Mechanical Engineering Congress and Exposition*, pages 897–906. American Society of Mechanical Engineers, 2011.

[112] Dohnal F. and Tondl A. Using time-periodicity for inducing energy transfer between vibration modes. In *ASME 2013 International Design Engineering Technical Conferences and Computers and Information in Engineering Conference*. American Society of Mechanical Engineers, 2013.

[113] Sanders J.A., Verhulst F., and Murdock J. *Averaging methods in nonlinear dynamical systems*, volume 59. Springer, 2007.

[114] Wagg D. and Neild S. *Nonlinear vibration with control.* Springer, 2014.

[115] Zhang W., Baskaran R., and Turner K.L. Effect of cubic nonlinearity on auto-parametrically amplified resonant MEMS mass sensor. *Sensors and Actuators A: Physical*, 102(1):139–150, 2002.

[116] Cveticanin L. and Kovacic I. Parametrically excited vibrations of an oscillator with strong cubic negative nonlinearity. *Journal of Sound and Vibration*, 304(1):201–212, 2007.

[117] Prakash G., Raman A., Rhoads J.F., and Reifenberger R.G. Parametric noise squeezing and parametric resonance of microcantilevers in air and liquid environments. *Review of Scientific Instruments*, 83(6):065109, 2012.

[118] Verhulst F. Perturbation analysis of parametric resonance. In *Encyclopedia of Complexity and Systems Science*, pages 6625–6639. Springer, 2009.

[119] Zounes R.S. and Rand R.H. Transition curves for the quasi-periodic mathieu equation. *SIAM Journal on Applied Mathematics*, 58(4):1094–1115, 1998.

[120] Blaquiere A. *Nonlinear system analysis.* Elsevier, 2012.

[121] Levine W.S. *Control system fundamentals.* CRC press, 1999.

[122] Khalil H.K. and Grizzle J.W. *Nonlinear systems*, volume 3. Prentice hall New Jersey, 1996.

[123] Sastry S. *Nonlinear systems: analysis, stability and control*, volume 10. Springer New York, 1999.

[124] Thompson J.M. and Stewart H.B. *Nonlinear dynamics and chaos.* John Wiley & Sons, 2002.

[125] Nayfeh A.H. and Balachandran B. *Applied nonlinear dynamics: analytical, computational and experimental methods.* John Wiley & Sons, 2008.

[126] Hagedorn P. Non-linear oscillations. *Clarendon Press, Oxford and New York*, 1, 1981.

[127] Minorsky N. *Nonlinear oscillations.* van Nostrand, 1962.

[128] Bittanti S. and Colaneri P. *Periodic systems: filtering and control.* Springer Science & Business Media, 2008.

[129] Ye Y. and Lo C.L. *Theory of limit cycles*, volume 66. American Mathematical Soc., 1986.

[130] Peters D.A. Fast Floquet theory and trim for multi-bladed rotorcraft. *Journal of the American Helicopter Society*, 39(4):82–89, 1994.

[131] Panardo I. Stability of periodic systems and Floquet theory. Master's thesis, Università degli Studi di Padova, 2014.

[132] Hale J. K. and H. Koçak. *Dynamics and bifurcations*, volume 3. Springer Science & Business Media, 2012.

[133] Kniffka T.J. and Ecker H. Observations regarding numerical results obtained by the Floquet-method. In *ASME 2013 International Design Engineering Technical Conferences and Computers and Information in Engineering Conference*. American Society of Mechanical Engineers, 2013.

[134] Lazarus A. and Thomas O. A harmonic-based method for computing the stability of periodic solutions of dynamical systems. *Comptes Rendus Mécanique*, 338(9):510–517, 2010.

[135] van der Pol B. and Strutt M.J.O. II. on the stability of the solutions of Mathieu's equation. *The London, Edinburgh, and Dublin Philosophical Magazine and Journal of Science*, 5(27):18–38, 1928.

[136] Acar G. and Feeny B.F. Floquet-based analysis of general responses of the Mathieu equation. *Journal of Vibration and Acoustics*, 138(4):041017, 2016.

[137] Thomsen J.J. *Vibrations and Stability, Order and Chaos.* McGraw-Hill Companies, 2013.

[138] Neumeyer S., Van Gastel M.H.M., Sorokin V.S., and Thomsen J.J. Frequency detuning effects for parametrically and directly excited elastic structures. In *Proceedings of 5th ECCOMAS Thematic Conference on Computational Methods in Structural Dynamics and Earthquake Engineering*, pages 1–7, 2015.

[139] Kovacic I. and Brennan M.J. *The Duffing equation: Nonlinear oscillators and their behaviour.* John Wiley & Sons, 2011.

[140] Hammond P. *Electromagnetism for engineers.* Oxford university press, 2005.

[141] Sneller A.J. and Brian P.M. On the nonlinear electromagnetic coupling between a coil and an oscillating magnet. *Journal of Physics D: Applied Physics*, 43(29):295005, 2010.

[142] Joyce B.S. Development of an electromagnetic energy harvester for monitoring wind turbine blades. Master's thesis, Virginia Polytechnic Institute and State University, 2011.

[143] Cammarano A., Neild S.A., Burrow S.G., Wagg D.J., and Inman D.J. Optimum resistive loads for vibration-based electromagnetic energy harvesters with a stiffening nonlinearity. *Journal of Intelligent Material Systems and Structures*, 2014.

[144] Ewins D.J. *Modal testing: theory and practice*, volume 15. Research studies press Letchworth, 1984.

[145] Thomson W. *Theory of vibration with applications*. CRC Press, 1996.

[146] Feldman M. Hilbert transform in vibration analysis. *Mechanical systems and signal processing*, 25(3):735–802, 2011.

[147] Smith C.B. and Wereley N.M. Transient analysis for damping identification in rotating composite beams with integral damping layers. *Smart materials and structures*, 5(5):540, 1996.

[148] Feldman M. *Hilbert transform applications in mechanical vibration.* Wiley Online Library, 2011.

[149] Schafer R.W. What is a savitzky-golay filter? *Signal Processing Magazine, IEEE*, 28(4):111–117, 2011.

[150] Savitzky A. and Golay M.J.E. Smoothing and differentiation of data by simplified least squares procedures. *Analytical chemistry*, 36(8):1627–1639, 1964.

[151] Raskin J.P., Brown A.R., Khuri-Yakub B., and Rebeiz G.M. A novel parametric-effect MEMS amplifier. *Microelectromechanical Systems, Journal of*, 9(4):528–537, 2000.

[152] Hamdan M.N., Al-Qaisia A.A., and Al-Bedoor B.O. Comparison of analytical techniques for nonlinear vibrations of a parametrically excited cantilever. *International Journal of Mechanical Sciences*, 43(6):1521–1542, 2001.

[153] Krauss R.W. and Nayfeh A.H. Comparison of experimental identification techniques for a nonlinear sdof system. In *Proceedings of the 17th International Modal Analysis Conference*, pages 1182–1187, 1999.

[154] Lee C., Stamp D., Kapania N.R., and Mur-Miranda J.O. Harvesting vibration energy using nonlinear oscillations of an electromagnetic inductor. In *SPIE*, pages 76830Y–76830Y. International Society for Optics and Photonics, 2010.

[155] Tang B., Brennan M.J., Lopes V., da Silva S., and Ramlan R. Using nonlinear jumps to estimate cubic stiffness nonlinearity: An experimental study. *Proceedings of the Institution of Mechanical Engineers, Part C: Journal of Mechanical Engineering Science*, 2015.

[156] Malatkar P. *Nonlinear vibrations of cantilever beams and plates.* PhD thesis, Virginia Polytechnic Institute and State University, 2003.

[157] Anderson T.J., Nayfeh A.H., and Balachandran B. Experimental verification of the importance of the nonlinear curvature in the response of a cantilever beam. *Journal of Vibration and Acoustics*, 118(1):21–27, 1996.

[158] Timoshenko S. and Young D.H. Elements of strength of materials. 1968.

[159] Kumar V., Miller J.K., and Rhoads J.F. Nonlinear parametric amplification and attenuation in a base-excited cantilever beam. *Journal of Sound and Vibration*, 330(22):5401–5409, 2011.

[160] Upadhyaya S.K., Rand R.H., and Cooke J.R. Dynamics of fruit tree trunk impact. *Transactions of the ASAE*, 24(4):846–0855, 1981.

[161] Blekhman I.I. Vibrational dynamic materials and composites. *Journal of Sound and Vibration*, 317(3):657–663, 2008.

[162] Blekhman I.I. and Sorokin V.S. On the separation of fast and slow motions in mechanical systems with high-frequency modulation of the dissipation coefficient. *Journal of Sound and Vibration*, 329(23):4936–4949, 2010.

[163] Jensen J.S., Tcherniak D.M., and Thomsen J.J. Stiffening effects of high-frequency excitation: experiments for an axially loaded beam. *Journal of applied mechanics*, 67(2):397–402, 2000.

[164] Thomsen J.J. Some general effects of strong high-frequency excitation: stiffening, biasing and smoothening. *Journal of Sound and Vibration*, 253(4):807–831, 2002.

[165] Thomsen J.J. Slow high-frequency effects in mechanics: problems, solutions, potentials. *International Journal of Bifurcation and Chaos*, 15(09):2799–2818, 2005.

[166] Patrick D.R. and Fardo S.W. *Electricity and electronics fundamentals.* The Fairmont Press, Inc., 2008.

[167] Cutnell J.D. and Kenneth W. *Physics.* John Wiley & Sons, 2009.

[168] Spreemann D. and Manoli Y. *Electromagnetic vibration energy harvesting devices: Architectures, design, modeling and optimization*, volume 35. Springer, 2012.

[169] Bendat J.S. *The Hilbert transform and applications to correlation measurements.* Brüel & Kjaer, 1991.

[170] Bendat J.S. and Piersol A.G. *Random data: analysis and measurement procedures*, volume 729. John Wiley & Sons, 2011.